REPUBLIC OF TÜRKİYE
MUĞLA SITKI KOÇMAN UNIVERSITY
GRADUATE SCHOOL OF NATURAL AND APPLIED SCIENCES

DEPARTMENT OF GEOLOGICAL ENGINEERING

CHARACTERISTICS, GENESIS AND TRIGGERS FOR THE FORMATION OF HOD MADEN Au-Cu MINERALIZATION SYSTEM, NE TURKEY

PHD THESIS

MUSTAFA ERDE BİLİR

SEPTEMBER 2023
MUĞLA

M. E. BİLİR GEOLOGICAL ENGINEERING PHD THESIS MUĞLA 2023

REPUBLIC OF TÜRKİYE
MUĞLA SITKI KOÇMAN UNIVERSITY
GRADUATE SCHOOL OF NATURAL AND APPLIED SCIENCES

DEPARTMENT OF GEOLOGICAL ENGINEERING

CHARACTERISTICS, GENESIS AND TRIGGERS FOR THE FORMATION OF HOD MADEN Au-Cu MINERALIZATION SYSTEM, NE TURKEY

PHD THESIS

MUSTAFA ERDE BİLİR

SEPTEMBER 2023
MUĞLA

MUGLA SITKI KOÇMAN UNIVERSITY

Graduate School of Natural and Applied Sciences

APPROVAL OF THESIS

The thesis submitted by **MUSTAFA ERDE BİLİR** with the title of "**CHARACTERISTICS, GENESIS AND TRIGGERS FOR THE FORMATION OF HOD MADEN Au-Cu MINERALIZATION SYSTEM, NE TURKEY"** has been unanimously accepted by the jury members on the 24th of August, 2023 to fulfill the requirements for the degree of Doctor of Philosophy in the Department of Geological Engineering.

THESIS JURY MEMBERS

Prof. Dr. Tolga OYMAN **(Head of Jury)** Signature:

Department of Geological Engineering,
Dokuz Eylül University, İzmir _____

Prof. Dr. İlkay KUŞCU **(Supervisor)** Signature:

Department of Geological Engineering,
Muğla Sıtkı Koçman University, Muğla _____

Assoc. Prof. Dr. Ceren KÜÇÜKUYSAL **(Member)** Signature:

Department of Geological Engineering,
Muğla Sıtkı Koçman University, Muğla _____

Prof. Dr. Gonca KUŞCU **(Member)** Signature:

Department of Geological Engineering,
Muğla Sıtkı Koçman University, Muğla _____

Assist. Prof. Dr. Ali İMER **(Member)** Signature:

Department of Geological Engineering,
Middle East Technical University, Ankara _____

APPROVAL OF HEAD OF THE DEPARTMENT

Prof. Dr. Semih GÜRSU Signature:

Head of Department, Geological Engineering _____

Prof. Dr. İlkay KUŞCU Signature:

Supervisor, Department of Geological Engineering _____

Date of Defense: 24/08/2023

I hereby declare that all information in this document has been obtained and presented in accordance with academic rules and ethical conduct. I also declare that, as required by rules and conduct, I have fully cited and referenced all material and results that are not original to this work.

Mustafa Erde BİLİR

24/08/2023

ABSTRACT

CHARACTERISTICS, GENESIS AND TRIGGERS FOR THE FORMATION OF HOD MADEN Au-Cu MINERALIZATION SYSTEM, NE TURKEY

Mustafa Erde BİLİR

Doctor of Philosophy (PhD)

Graduate School of Natural and Applied Sciences

Department of Geological Engineering

Supervisor: Prof. Dr. İlkay KUŞCU

September 2023, 143 pages

Hod Maden Au-Cu deposit is located in eastern Pontides, in northeastern Turkey, and represents one of the highest-grade gold-copper (approximately 4 Moz @11.1 g/t AuEq) discoveries made globally in recent years. It is hosted by steeply east dipping Late Cretaceous andesitic to dacitic-rhyodacitic lava flows, volcaniclastic and volcano-sedimentary sequences of Çatak and Kızılkaya formations which host several Kuroko-type volcanogenic massive sulfide (VMS) and epithermal deposits throughout the region. Although Hod Maden shares similar host rock, stratigraphy, and age characteristics with these deposits, it differs significantly in terms of its elevated gold grades and unique mineralization/alteration styles. Thus, this study aims to investigate the mineralization nature, and the origin and evolution of the ore-bearing hydrothermal fluids through field mapping, drill core logging, petrographic investigation, short-wave infrared (SWIR), EPMA (electron probe microanalyzer), QEMSCAN (quantitative evaluation of minerals by scanning electron microscopy) work as well as U-Pb and Ar-Ar geochronology, and stable isotope (S-, O-, and H-isotope) analyses.

Hod Maden consists of various mineralization styles including massive sulfide to semi-massive sulfide lenses and stockwork quartz-sulfide (pyrite-chalcopyrite ± sphalerite) veins. The ore zones form three distinct ore bodies that are from north to south, Main Zone, South Zone and Old Workings Zone. Main Zone consists gold and copper sulfide (pyrite-chalcopyrite)-quartz veins and zones of disseminated to semimassive and massive sulfides. The ore zone is spatially associated with jasper-bearing, chlorite and zeolite altered amygdaloidal andesite breccia with occasional hyaloclastite and sericite (fine-grained muscovite and K-illite) and clay (Mg-illite, kaolinite-dickite) altered spherulitic, amygdaloidal dacite breccia units. A late, intense anhydrite phase overprints the pre-existing volcanic and hydrothermal alteration textures. The orebody is bounded by the volcano-sedimentary sequences in east. South Zone consists of auriferous semimassive veins, zones of sulfide stringers and disseminated sulfides that are hosted in spherulitic/amygdaloidal, monomictic dacite breccia and mass flow deposits. Quartz-pyrite-chalcopyrite-sphalerite veins and clasts replaced by sulfides form the

mineralized bodies. The alteration consists of an assemblage of sericite (fine-grained muscovite, K- illite), clay (dickite, kaolinite, halloysite, montmorillonite) and late calcite, dolomite and anhydrite overprint. Old workings zone consists of copper and zinc sulfide (chalcopyrite-pyrite-sphalerite)-quartz veins. The ore zone is hosted in amygdaloidal andesite breccia and rhyodacitic dome with banded lava flow and pyroclastic products (pumice-bearing crystal tuff). Quartz-sulfide veins are accompanied by pervasive chlorite, sericite and occasional dolomite, epidote, rhodochrosite alteration.

The volcanic textures of the host rocks including (i) spherulitic texture, replacements of radiating fibers of crystals by later sericite, chlorite and sulfides; (ii) hyaloclastites or false vitriclastic textures (hydraulic fragmentation of quenched lava flows); (iii) amygdaloidal texture, infilling of vugs and replacement of lithic clasts by chlorite, quartz, carbonates and zeolites; (iv) subaqueous mass flow deposits with dacitic lithic clasts and sulfide clasts; (v) presence of "tetsusekiei" (or jasper-hematite); and hydrothermal alteration features such as spatial zonation of Fe-rich chlorites and zeolites, and the late anhydrite phase overprinting gold-copper mineralization provide a better understanding toward the formation of seafloor/subseafloor hydrothermal alteration and mineralization.

Hydrothermal alteration mineralogy is mainly controlled by the host rock composition (chloritic alteration with andesitic host or sericitic-clay alteration with dacitic host). High grade Au mineralization is associated with the hydrothermal alteration sequence starting with an (i) early stage pervasive fine-grained quartz and chlorite/clay (K-illite, kaolinite) alteration cut by (ii) fine-grained quartz veinlets followed by (iii) comb coarse-quartz veins bearing pyrite and chalcopyrite and with the (iv) late stage anhydrite, epidote and carbonate phase as overprint or open space filling.

With respect to the presence of various mineralization/alteration styles and host rock lithologies in Hod Maden deposit the ore zones form three distinct ore bodies that are from north to south, Main Zone, South Zone and Old Workings Zone. New zircon U-Pb dating clarifies that columnar dacites (evaluated as the same volcanic phase with the host dacite breccias at the South Zone) formed at 84.78 $\pm$ 0.43 Ma while the rhyodacitic unit of Old Workings Zone has been dated at 84.00 $\pm$ 0.44 Ma. In addition, the volcanic clasts of a red conglomerate unit of Öğdem Formation, a marker horizon in the region, yielded the age of 163.65 $\pm$ 0.69 Ma.

The majority of the sulfur isotopic compositions (δ^{34}S values) of sulfide minerals (chalcopyrite, pyrite, sphalerite and galena) record minor deviations between -0.81 and +3.33 ‰ VCDT and represents a magmatic source (magmatic water and/or seawater interaction with pre-existing host volcanic rocks). The δ^{34}S values of sulfate minerals (anhydrite) display variations between 17.06 and 19.93 ‰ VCDT and overlap with the sulfur isotopic composition of Late Cretaceous seawater sulfate.

$\delta^{18}O_{water}$ and δD_{water} values of the hydrothermal fluids in equilibrium with chlorite and sericite are calculated using mineral-water fractionation equations. Fluid signatures indicate the fluid responsible for chlorite and sericite assemblages was evolved from Cretaceous seawater as a result of fluid-rock interactions and a possible magmatic water input. Chlorite-rich Main Zone alteration phases have $\delta^{18}O_{water}$ between -2.7

to +4.3 ‰ and δD_{water} ‰ values between -33 to -3.

Keywords: Late Cretaceous, Submarine volcanic rock textures, Çatak, Kızılkaya, Evliyatepe, U-Pb geochronology, Ar-Ar geochronology, Lithogeochemistry, S-isotope, O-isotope, H-isotope, Au-rich VMS deposits, gold, copper, Hod Maden, Eastern Pontides, Turkey

ÖZET

HOD MADEN Au-Cu CEVHERLEŞMESİ SİSTEMİNİN KARAKTERİ, KÖKENİ VE OLUŞUM MEKANİZMASI, KD TÜRKİYE

Mustafa Erde BİLİR

Doktora Tezi

Fen Bilimleri Enstitüsü

Jeoloji Mühendisliği Anabilim Dalı

Danışman: Prof. Dr. İlkay KUŞCU

Eylül 2023, 143 sayfa

Hod Maden Au-Cu yatağı, kuzeydoğu Türkiye'de doğu Pontidlerde yer alır ve son yıllarda dünya çapında en yüksek tenörlü altın-bakır (yaklaşık 4 Moz @11.1 g/t Au eşleniği) keşiflerinden birini temsil eder. Doğu Pontidler boyunca birçok Kuroko-tipi volkanojenik masif sülfit (VMS) ve epitermal yatağı da barındıran Geç Kretase yaşlı Çatak ve Kızılkaya formasyonlarının andezitik-dasitik-riyodasitik lav akıntıları, volkaniklastikleri ve volkanosedimanter sekansları tarafından barındırılır. Hod Maden diğer yataklarla benzer ana kaya ve stratigragiyi paylaşmasına rağmen, yüksek altın tenörü ve özgün cevherleşme/alterasyon özellikleriyle diğerlerinden ayrılır. Bu nedenle, arazi haritalaması, karot loglaması, petrografik analiz, kısa-dalga kızılötesi (SWIR), elektronprob mikroanaliz (EPMA), QEMSCAN (minerallerin taramalı elektron mikroskobu ile kuantitatif değerlendirilmesi) çalışmaları ile, U-Pb ve Ar-Ar jeokronolojisi ve duraylı izotop (S-, O-, and H-izotopu) verileri kullanılarak cevherleşmenin doğasını belirlemeyi ve cevher içeren hidrotermal akışkanların kaynağı ve evrimini ifade etmeyi amaçlar.

Hod Maden, masif ve yarı masif sülfit mercekleri ve ağsı kuvars-sülfit (pirit-kalkopirit ± sfalerit) damarlarını içeren birçok cevherleşme stili içerir. Cevherli kütleler kuzeyden güneye Ana Zon, Güney Zon ve Eski İşletmeler Zonu olmak üzere üç ayrı cevher zonu oluşturur. Ana Zon altın ve bakır sülfit (pirit-kalkopirit)-kuvars damarları ile saçınımlı, yarı masif ve masif sülfit zonlarından oluşur. Cevher zonu mekânsal olarak özellikle jasper içeren, klorit ve zeolit alterasyonlu yer yer hyaloklastik özellik gösteren amigdüllü andezit breş ile serizit (ince taneli muskovit ve K-illit) ve kil (Mg-illit, kaolinit-dikit) alterasyonlu sferülitik/amigdüllü dasit breş birimleriyle ilişkilidir. Geç evre, yoğun anhidrit fazı volkanik ve önceki evre hidrotermal alterasyon dokularını siler veya ornatır şekildedir. Cevher kütlesi doğuda volkanosedimanter sekanslarla sınırlanır. Güney Zon altınca zengin yarı masif damarlar, ağsı ve saçınımlı sülfit zonlarını içerir ve sferülitik/amigdüllü, monomiktik dasit breş ve kütle akması yataklarınca barındırılır. Kuvars-pirit-kalkopirit-sfalerit damarları ve klastların üzerine gelişen sülfitler cevher kütlelerini oluşturur. Alterasyon serizit (ince taneli muskovit, K-illit), kil (dikit, kaolen, halloysit, montmorillonit) ve geç evre kalsit, dolomit ve anhidritlerce

karakterize edilir. Eski İşletmeler Zonu cevheri bakır ve çinko sülfit (kalkopirit-pirit-sfalerit)-kuvars damarlarını içerir. Cevher amigüllü andezit breş ile akma bandı dokusu da gösteren riyodasit domu ve piroklastik ürünleri (pümis içeren kristal tüf) içindedir. Kuvars-sülfit damarları yaygın klorit, serizit ve yer yer dolomit, epidot ve rodokrozit alterasyonuyla ilişkilidir.

Cevher ile ilişkili volkanik kayaç dokuları: (i) ışınsal kristal fiberlerin serizit, klorit ve sülfitlerce üzerlendiği sferülitik doku; (ii) lav akıntılarının deniz suyunda ani soğuma ile hidrolik olarak parçalanmasıyla oluşan hyaloklastikler veya yalancı (yanlış) vitriklastik doku; (iii) kayaç boşluklarının klorit, kuvars, karbonat ve zeolitlerce dolduğu amigdül doku; (iv) dasitik litik ve sülfit klastlı denizaltı kütle akması yatakları; (v) "tetsusekiei" (veya jasper-hematit) varlığı; ile demirce zengin kloritler ve zeolitlerin mekânsal dağılımı ve altın-bakır cevherleşmesini üzerleyen geç evre anhidrit fazı gibi belirleyici hidrotermal alterasyon özellikleri deniz tabanında/deniz tabanı altında gerçekleşen hidrotermal alterasyon ve cevherleşme süreçlerinin daha iyi anlaşılmasını sağlayan önemli çıktılardır.

Hod Maden Au-Cu yatağı, kuzeydoğu Türkiye'de doğu Pontidlerde yer alır ve son yıllarda dünya çapında en yüksek tenörlü altın-bakır (yaklaşık 4 Moz @11.1 g/t Au eşleniği) keşiflerinden birini temsil eder. Doğu Pontidler boyunca birçok Kuroko-tipi volkanojenik masif sülfit (VMS) ve epitermal yatağı da barındıran Geç Kretase yaşlı Çatak ve Kızılkaya formasyonlarının andezitik-dasitik-riyodasitik lav akıntıları, volkaniklastikleri ve volkanosedimanter sekansları tarafından barındırılır. Hod Maden yüksek altın tenörü ve özgün cevherleşme/alterasyon özellikleriyle bölgedeki benzer ana kaya ve stratigrafiyi paylaştığı diğer yataklardan ayrılır. Dolayısı ile, bu çalışma cevherleşmenin doğasını belirlemek ve cevher içeren hidrotermal akışkanların kaynağı ve evrimini ifade etmek adına oldukça önemli bir rol oynar.

Hidrotermal alterasyon mineralojisi çoğunlukla ana kaya kompozisyonunca (andezitik ana kayalarda kloritik, dasitik ana kayalarda serizitik alterasyon) kontrol edilir. Yüksek tenörlü altın cevherleşmesi (i) erken evre yaygın ince taneli kuvars ve klorit/kil (K-illit, kaolinit) alterasyonunu kesen (ii) ince taneli kuvars damarcıklarını ve onu takip eden (iii) iri taneli tarak dokulu pirit ve kalkopirit içeren kuvars damarları ile (iv) geç evre üzerleyen şekilde veya boşluk dolgusu şeklinde gelişen anhidrit, epidot ve karbonat fazının temsil ettiği hidrotermal alterasyon süreçleriyle ilişkilidir.

Hod Maden yatağında birçok cevherleşme/alterasyon stili ve ana kaya litolojilerinin ışığında kuzeyden güneye Ana Zon, Güney Zon ve Eski İşletmeler Zonu olmak üzere üç ayrı cevher zonu tanımlanmıştır. Volkanik kayaçlarda gerçekleştirilen U-Pb zirkon jeokronoloji ve hem Ana Zon hem de Güney Zondaki cevherleşmelerden elde edilen serizitler üzerinde gerçekleştirilen Ar-Ar jeokronolojisi, Hod Maden altın-bakır yatağının oluşumunda Geç Kretase volkanik ve hidrotermal aktivitesinin sorumlu olduğu görüşünü destekler.

Sülfit minerallerinden (kalkopirit, pirit, sfalerit ve galen) elde edilen sülfür izotopik kompozisyonlarının çoğunluğu (δ^{34}S değerleri) -0.81 ve +3.33 ‰ VCDT (Viyana Canon-Diablo Troilite) aralığında değişir ve bir magmatik kökeni (magmatik su ve/veya deniz suyunun var olan ana kaya volkanik kayaçlarla etkileşimi) ifade eder. Sülfat (anhidrit) minerallerinden elde edilen δ^{34}S değerleri 17.06 ve 19.93 ‰ VCDT

aralığındadır ve Geç Kretase deniz suyu değerleriyle örtüşmektedir.

Mineral-su fraksiyonlanma denklemleri kullanılarak hidrotermal akışkan ile denge halinde olan klorit ve serizitlerden $\delta^{18}O_{su}$ ve δD_{su} değerleri hesaplanmıştır. Akışkan imzaları, klorit ve serizit topluluklarını oluşturan akışkanın kayaç etkileşimi ve muhtemel magmatik su katkısı ile Kretase deniz suyundan evrildiğini gösterir. Kloritçe zengin Ana Zon alterasyon fazları +1.7 ile +4.7 ‰ aralığında $\delta^{18}O_{su}$ ve -8 ile -24 ‰ aralığında δD_{su} değerlerine sahiptir.

Anahtar kelimeler: Geç Kretase, Denizaltı volkanik kayaç dokuları, Çatak, Kızılkaya, Evliyatepe, U-Pb jeokronolojis, Ar-Ar jeokronolojisi, Litojeokimya, S-izotopu, O-izotopu, H-izotopu, Altınca zengin VMS yatakları, Altın, Bakır, Hod Maden, Doğu Pontidler, Türkiye



To my family...

ACKNOWLEDGEMENT

Firstly, I would like to express my sincere gratitude to my advisor Prof. Dr. İlkay KUŞCU for the continuous support of my PhD study and related research, for his patience, motivation, and immense knowledge. His guidance helped me in all the time of research and writing of this thesis.

Besides my advisor, I would like to thank the my ”co-supervisor”: Prof. Dr. Robert MORITZ for his insightful comments and encouragement, but also for the hard question which incented me to widen my research from various perspectives. I could not have imagined having better advisors and mentors for my study.

I would also like to thank the rest of my research committee: Prof. Dr. Tolga Oyman, Assoc. Prof. Dr. Ceren KÜÇÜKUYSAL, and jury members Prof. Dr. Gonca KUŞCU and Assist. Prof. Dr. Ali İMER for their valuable suggestions and revisions on my thesis.

Financial support for this project was provided by Swiss National Faundation, Geneva-Switzerland.

To my partners in crime in Geneva: Sean (bless his heart) Gaynor, Clementine Antoine and Andre Paul, Martin, Melissa and Hugo from Isotope Research Group and Enzo, Frank, Ivano, Mara, Mateo, Zsofi, Erik, Francisco, Corin, Alessandro, Alex and Stefan from Maraîchers - many thanks for the memorable times. I must also mention Agathe and Antoine and for their help.

I would like to thank Aleksey Ulianov, Torsten Vennemann, Benita Putlitz and Jorge Spangenberg from University of Lausanne for U-Pb geochronology, H-, O- and S-isotope analyses, respectively; and from University of Geneva Richard Spikings for Ar geochronology and Florance Begue for EPMA work.

Thanks to Ebamüslüm TOPAL from Artmin Madencilik (and later SSR Mining) for introducing me the project site and continuous discussions on Hod Maden mineralization.

I thank my friends: Şafak Utku SÖNMEZ and Ali ALUÇ for the stimulating

discussions, for the sleepless nights we were working together before deadlines, and for all the fun we have had in the last years.

TABLE OF CONTENTS

ACKNOWLEDGEMENT . . . . . **xi**

TABLE OF CONTENTS . . . . . **xvi**

LIST OF TABLES . . . . . **xvii**

LIST OF FIGURES . . . . . **xxviii**

1. INTRODUCTION **1**

1.1. Geographic Setting 1

1.2. Previous Work 2

1.3. Purpose and Scope of the Study 3

2. METHODOLOGY **5**

2.1. Field Work 5

2.2. Leapfrog Modelling 6

2.3. Petrography 7

2.3.1. Shortwave infrared spectroscopy (SWIR) 8

2.3.2. Raman spectroscopy 9

2.3.3. Electron microprobe analysis (EPMA) 10

2.3.4. Quantitative evaluation of minerals by scanning electron microscopy (QEMSCAN) 11

2.4. Geochronology 11

2.4.1. In-situ U-Pb geochronology by laser ablation-inductively coupled plasma-mass spectroscopy (LA-ICP-MS) 11

2.4.2. Ar-Ar geochronology 14

2.5. Stable Isotopes 16

2.5.1. S-isotope analysis 16

2.5.2. O-isotope analysis 16

2.5.3. H-isotope analysis 17

2.6. Fluid Inclusion Petrography and Microthermometry 17

3. GEOLOGY OF THE PONTIDES **19**

3.1. Regional Geological Context of the Pontides 19

3.2. The Eastern Pontides 22

3.2.1. The late Cretaceous eastern Pontides magmatic arc 23
3.3. Geology and Magmatic-Tectonic Evolution of the Artvin District . . 24
4. GEOLOGY AND STRATIGRAPHY OF THE HOD REGION 26
4.1. Berta Formation 29
4.2. Kırgülü Formation 29
4.3. Hızarlıdere Formation (Hızarlıdere Volcanics) 30
4.4. Öğdem Formation 30
4.5. Aşağımaden Formation 32
4.6. Çatak Formation 32
4.7. Kızılkaya Formation 33
4.7.1. Spherulitic dacite flows and breccia 33
4.7.2. Columnar jointed dacitic lava flows and pyroclastic rocks 34
4.7.3. Well-stratified dacite to volcanosedimentary rocks 34
4.7.4. Rhyodacite dome 35
4.8. Evliyatepe Formation 35
5. VOLCANIC ROCK TEXTURES IN HOD MADEN DEPOSIT 38
5.1. Spherulitic Texture 40
5.2. Hyaloclastites 42
5.3. Amygdaloidal Texture 43
5.4. Subaqueous Volcaniclastic Mass-Flow Deposits 45
5.5. Presence of Jasper-Hematite 46
6. HYDROTHERMAL ALTERATION 48
6.1. Hydrothermal Alteration at Main Zone 49
6.1.1. Early chlorite-rich alteration 49
6.1.2. Early sericite-rich alteration 51
6.1.3. Chlorite2 and quartz2 alteration 51
6.1.4. Sericite2 alteration 56
6.1.5. Clay and hematite-goethite alteration 56
6.1.6. Quartz4 and carbonate alteration 56
6.1.7. Late anhydrite and calcite overprint 59
6.1.8. Alteration trends at main zone 60
6.2. Hydrothermal Alteration at South Zone 69
6.2.1. Early sericite-rich alteration 69

6.2.2. Clay alteration 72
6.2.3. Zeolite alteration 72
6.2.4. Carbonate alteration 74
6.2.5. Late anhydrite overprint 75
6.2.6. Alteration trends at south zone 76
6.3. Hydrothermal Alteration at Old Workings Zone 80

7. CHLORITE MINERAL CHEMISTRY 85

8. MINERALIZATION 89
8.1. Main Zone Mineralization 89
8.1.1. Massive (to semi-massive) sulfide mineralization 90
8.1.2. Gold mineralization associated with chlorite2-rich alteration . . . 90
8.1.3. Gold mineralization associated with chalcopyrite-2 94
8.1.4. Gold mineralization associated with Fe-oxide assemblage 94
8.1.5. Geologic and geochemical profiles of main zone mineralization . 95
8.2. South Zone Mineralization 102
8.2.1. Geologic and geochemical profiles of south zone mineralization . 107
8.3. Old Workings Zone Mineralization 109

9. GEOCHRONOLOGY 113
9.1. U-Pb Geochronology 113
9.2. Ar-Ar Geochronology 115

10. STABLE ISOTOPES 117
10.1. Sulfur Isotope Analysis 117
10.2. Oxygen and Deuterium Isotope Analysis 119

11. FLUID INCLUSIONS 121

12. DISCUSSION 123
12.1. Revised Age of the Dacitic Units 123
12.2. Delineation of “Unnamed Volcanosedimentary Rocks” 123
12.3. Physico-Chemical Conditions of Gold Precipitation 124
12.4. Elevated Gold Grades of the Hod Maden Au-Cu Deposit 125
12.5. Mineral Deposit Type of Hod Maden Mineralization 126
12.6. Contribution to Exploration Programs Conducted in the Region . . . 128

13. CONCLUSIONS 129

REFERENCES **138**

APPENDICES **139**

CURRICULUM VITAE **140**

LIST OF TABLES

Table 5.1. Characteristics of facies in Hod Maden Deposit 39
Table 7.1. Average chlorite compositions and temperature calculations 86

LIST OF FIGURES

Figure 1.1. Geographic setting and location of the Hod Maden 1

Figure 1.2. (A) South-looking view of mineralized zones of Hod Maden deposit including main zone, south zone and the old workings zone from north to south. (B) Northeast-looking view of the main zone and the south zone 2

Figure 2.1. Field input data on sample locations and mapping informations in GISKit software 6

Figure 2.2. Geological model of Hod Maden deposit (A, B) and drill holes (C, D) on Leapfrog software 7

Figure 2.3. (A) Olympus automated stage scanning microscope and (B) Leica polarized microscope 7

Figure 2.4. (A) ASD TerraSpec® Halo Mineral Identifier instrument, (B) SWIR reading on Teraspec instrument and (C) drill core rock slab examples 8

Figure 2.5. LabRAM HR spectrometer (Horiba Jobin Yvon) equipment for Raman spectroscopy 9

Figure 2.6. JEOL 8200 superprobe instrument 10

Figure 2.7. (A) Hydraulic press for crushing and grinding the samples down to 300μm, (B) Wilfley table, (C) heavy liquid (MI) gravimetric separation setup, (D) hand picking zircons under binocular microscope 12

Figure 2.8. Scanning Electron Microscope JEOL JSM7001F and the cathodoluminescence images of zircon crystals acquired with this instrument 13

Figure 2.9. Sericite mineral separation methodology including (A) gravitational settling of water-mineral mixture, (B) addition of sodium hexametaphosphate, (C) siphoning of residual floating materials, (D) control panel for centrifuge parameters and (E) final sericite composite 15

Figure 2.10. (A) CO_2-laser ablation system with Pt-sample holder and chlorite sample during ablation in the view, (B) CO_2-laser fluorination line, (C) trapped O_2 17

Figure 2.11. (A) Double-polished fluid inclusion section (EB181) view under binocular microscope, (B) a single euhedral quartz crystal (181-Q1) containing fluid inclusions, (C) Z-stack photomicrograph of a particular area (181-Q1-R2) 18

Figure 2.12. THMSG 600 Linkam heating-freezing stage mounted on a DMLB Leica microscope 18

Figure 3.1. (A) Tectonic units of Turkey (Okay and Tüysüz, 1999), (B) Simplified geological map of the eastern Pontides (1:500,000 scale; modified after (MTA, 2002)) and spatial distribution of porphyry, epithermal and VMS deposits 20

Figure 3.2. Geological map of the Artvin district (1:500,000 scale; modified after (MTA, 2002; Ustaömer et al., 2013)) 25

Figure 4.1. Generalized stratigraphic section of Hod region (modified after (Konak and Hakyemez, 2009; Kanar, 2016)) 27

Figure 4.2. Geological map of the Hod region and the schematic northwest-southeast cross section through Hod Maden Au-Cu deposit (modified after (Şatır and Ereren, 1976; Callan, 2013; Kanar, 2016; Bozkurt, 2017; Topal and Tezcan, 2018)) 28

Figure 4.3. Field photographs from Hod region: (A) Öğdem Formation, (B) Öğdem Formation, (C) Çatak Formation, (D) Çatak Formation, amygdaloidal andesite with quartz (qtz), chlorite (chl), zeolite (zeo), vermiculite (vrm) and carbonate (ca) amygdales; E) intense chlorite altered andesite breccia, (F) spherulitic dacite with pervasive sericite alteration, (G) columnar dacite, notice the horizontal elongation of the columns; (H) dacite porphyry, (I) northwest-looking view of volcanosedimentary sequence of Kızılkaya Formation in the west, Hod East Fault Zone (HEFZ) and Evliyatepe Formation in the east, (J) altered rhyodacite; (K) Evliyatepe Formation. 32

Figure 4.4. Thin section photomicrographs of selected lithologies from Hod region: A) pervasively silicified (qtz) and montmorillonite (mm) altered volcaniclastic rock of Kızılkaya Formation; B) dacite from the volcanosedimentary sequence of Kızılkaya Formation, displaying trachytic texture –plagioclases (pl) forming flow lines- and embayment in quartz (qtz), notice the chlorite (chl) alteration in the groundmass, C) amygdaloidal chlorite (chl) altered basalt from Evliyatepe Formation, notice that vermiculite (vrm) and calcite (ca) fills the amygdales and occupy the cores of plagioclases (pl) displaying sieve texture; D) Euhedral pyroxene (px) of a basaltic dike displaying sericite (ser) and calcite (ca) alteration; E) pseudomorphic calcite (ca) after hornblende (hbl), and plagioclase (pl) from an andesitic rock of Evliyatepe Formation. 37

Figure 5.1. Photomicrograph of diagnostic extinction crosses observed in the spherulites replaced by sericite, XPL; Main Zone, EB232, HTD018-253.5m 40

Figure 5.2. Representative examples from drill core samples, photomicrographs and SEM images of samples displaying spherulitic texture. (A) Main Zone, HTD029-370.5m, dacite breccia with spherulite-bearing clasts; (B) South Zone, EB070, HTD021-6.5m, dacite breccia with spherulitic texture and pervasive sericite alteration, (C) and (D) South Zone, EB124, HTD021-215.9m, spherulites replaced by sphalerite, pyrite, chalcopyrite, dolomite and quartz in PPL and XPL, respectively; (E) Main Zone, EB232, HTD018-253.5m, dacite breccia with spherulites replaced by sericite and pyrite, PPL and SEM images. Abbreviations: qtz: quartz, py: pyrite, ser: sericite, ca: carbonate, cp: chalcopyrite, sl: sphalerite, dol: dolomite. 41

Figure 5.3. Photomicrographs of hyaloclastites observed in Main Zone, EB193, HTD029-487.2m. Notice the cuspate shape or curviplanar edges of andesite clasts and glass shards. Abbreviations: chl: chlorite, Mg-ill: Mg-illite, qtz: quartz, phe: phengite 42

Figure 5.4. Examples from Main Zone samples displaying amygdaloidal texture. (A) EB043, HTD090-299.9m, full thin section scan under PPL; (B) in PPL and (C) in XPL of sample EB043, concentrically zoned quartz and chlorite amygdales; (D) EB178, HTD029-71.8m, drill core sample with concentrically zoned chlorite, quartz, epidote and sericite amygdales; (E) EB178, full thin section scan in XPL; (F) in PPL and (G) in XPL photomicrograph of an amygdale filled by chlorite, quartz, epidote and calcite; (H) in PPL and (G) in XPL photomicrograph of amygdales with concentric zonation of chlorite-sericite and chlorite-quartz. Abbreviations: qtz: quartz, chl: chlorite, anh: anhydrite, py: pyrite, cp: chalcopyrite, ser: sericite, cal: calcite, ep: epidote 44

Figure 5.5. Representative amygdaloidal plagioclase porphyry, sample EB022, from Evliyatepe Formation displaying concentic zonation of calcite-chlorite; (A) Hand sample, (B) Photomicrograph in PPL and (C) Photomicrograph in XPL. Abbreviations: qtz: quartz, chl: chlorite, cal: calcite, ep: epidote, pl: plagioclase 45

Figure 5.6. (A) An illustration depicting a speculative interpretation of the origin of massive sulfide clasts in a submarine volcaniclastic mass-flow deposit in the Mount Read Volcanics, western Tasmania (McPhie et al., 1993); (B) Drill core samples showing submarine volcaniclastic mass-flow deposit with chalcopyrite and pyrite clasts in the South Zone mineralization of Hod Maden deposit. Notice the pervasive sericite and nontronite alteration accompanied by quartz alteration. Abbreviations: py: pyrite, cp: chalcopyrite, ser: sericite, non: nontronite, qtz: quartz 46

Figure 5.7. Representative examples with jasper-hematite. (A) Drill core sample with patches of jasper-hematite accomapiend by quartz, black chlorite, chalcopyrite, pyrite and sphalerite with late anhydrite veinlets. (B) Drill core sample with jasper-hematite hosting sulfides and cut by late anhydrite veinlets. (C) Outcrop photo of andesite breccia with vein-type jasper-hematite. It is cut by a quartz-sphalerite-chalcopyrite-pyrite vein. (D) Drill core sample with jasper-hematite occupying the interstital spaces in the pillow-like structures of andesite breccia. Abbreviations: jsp: jasper-hematite, py: pyrite, cp: chalcopyrite, sl: sphalerite, qtz: quartz, chl: chlorite, hm: hematite, anh: anhydrite 47

Figure 6.1. A cross section across the Main Zone showing the spatial distribution of lithological units, Au, Cu and Zn ore zones and associated hydrothermal alteration assemblages. Notice the each petrographic sample indicates the present hydrothermal alterations and their temporal evolution from early to late phases. 50

Figure 6.2. (A-C) Hand samples from Main Zone displaying amygdaloidal andesite with early phase pervasive chlorite alteration accompanied by fine-grained quartz, vermiculite and cubic pyrite; (D-E) Drill core samples (EB212) from drill hole HTD30A-518.4m, targeting Main Zone mineralization with pervasive early chlorite alteration cut by quartz -sulfide veins and overprinted by anhydrite; (F-I) Photomicrographs of sample EB212 characterizing the light green color under PPL and dark brown to dark violet colors under XPL 52

Figure 6.3. Full thin section scan photomicrograph examples of samples displaying early sericite-quartz alteration (XPL), (A) EB230, HTD018-158m; (B) EB232, HTD018-253.5m 53

Figure 6.4. Drill core samples representing chlorite2-quartz2 alteration phase accompanied by chalcopyrite and Au mineralization; (A) HTD088-348m, 7.85 g/t Au and 4.01 %Cu, (B) HTD088-350.4m, 10.5 g/t Au and 1.67 %Cu, (C) HTD088-343m, 3.13 g/t Au and 4.59 %Cu (abbreviations are as in Figure 6.1) 54

Figure 6.5. Full thin section scan photomicrograph and scanning electon microscope (SEM) images of sample EB193 representing early chlorite-1 and mineralization phase chlorite-2 alterations; EB193, HTD029-487.2m. anh: anhydrite, chl: chlorite, cp: chalcopyrite, qtz: quartz 55

Figure 6.6. Photomicrographs representing sericite alteration postdating the chlorite alteration on andesite breccia, sample EB180, HTD029-154.1m; (A) Concentrically zoning of chlorite-sericite amygdales and selective sericite alteration on plagioclase phenocrysts (PPL), (A) Concentrically zoning of chlorite-sericite amygdales and selective sericite alteration on plagioclase phenocrysts (XPL), (C) Concentrically zoning of chlorite-sericite amygdales and selective sericite alteration on plagioclase phenocrysts (PPL), (D) Concentrically zoning of chlorite-sericite amygdales and selective sericite alteration on plagioclase phenocrysts (XPL), (E) Muscovite overprint on chlorite associated with pyrite mineralization (PPL), (F) Muscovite overprint on chlorite associated with pyrite mineralization (XPL). chl: chlorite, ms: muscovite, pl: plagioclase, py: pyrite, qtz: quartz 57

Figure 6.7. (A) Drill core sample from Main Zone mineralization representing clay and Fe-oxide overprint over pre-existing chlorite and sulfides, HTG02-35.4m, (B) Photomicrograph from sample EB041, HTD090-273m, showing saponite and hematite-goethite overprint on chalcopyrite-pyrite and chlorite assemblage (PPL), (C) Photomicrograph from sample EB041, HTD090-273m, showing saponite and hematite-goethite overprint on chalcopyrite-pyrite and chlorite assemblage (XPL), (D) Photomicrograph from sample EB039, HTD090-264m, representing kaolinite overprint on chlorite-2 alteration (PPL), (E) Photomicrograph from sample EB039, HTD090-264m, representing kaolinite overprint on chlorite-2 alteration (XPL). anh: anhydrite, chl: chlorite, cp: chalcopyrite, goe: goethite, hm: hematite, kao: kaolinite, py: pyrite, sap: saponite, qtz: quartz 58

Figure 6.8. Full thin section scan photomicrograph examples of samples displaying comb quartz4-carbonate veins (XPL), (A) EB181, HTD029-185.5m; (B) EB183, HTD029-224.7m. cp: chalcopyrite, cal: calcite, dol: dolomite, hs: halloysite, py: pyrite, qtz: quartz, ser: sericite 59

Figure 6.9. (A) Drill core sample and (B) the full thin section scan photomicrograph (XPL) of the sample EB039. It represents the late anhydrite phase overprinting the pre-existing early chlorite1-quartz-1, chlorite2-jasper-hematite-kaolinite-sulfide and quartz4 alterations. anh: anhydrite, cp: chalcopyrite, chl: chlorite, hm: hematite, jas: jasper, kao: kaolinite, py: pyrite, qtz: quartz 61

Figure 6.10. Alteration index (AI) versus chlorite-carbonate-pyrite index (CCPI) alteration box plot for drill core samples (HTD018) representing Main Zone mineralization, AI = 100 × (MgO + K_2O)/(MgO + K_2O + CaO + NaO) (Ishikawa et al., 1976), CCPI = 100 × (MgO + FeO)/(MgO + FeO + Na_2O + K_2O) (Large et al., 2001) 64

Figure 6.11. Alteration index (AI) versus chlorite-carbonate-pyrite index (CCPI) alteration box plot for drill core samples (HTD029) representing Main Zone mineralization, AI = 100 × (MgO + K_2O)/(MgO + K_2O + CaO + NaO) (Ishikawa et al., 1976), CCPI = 100 × (MgO + FeO)/(MgO + FeO + Na_2O + K_2O) (Large et al., 2001) 66

Figure 6.12. Alteration index (AI) versus chlorite-carbonate-pyrite index (CCPI) alteration box plot for drill core samples (HTD090) representing Main Zone mineralization, AI = 100 × (MgO + K_2O)/(MgO + K_2O + CaO + NaO) (Ishikawa et al., 1976), CCPI = 100 × (MgO + FeO)/(MgO + FeO + Na_2O + K_2O) (Large et al., 2001). anh: anhydrite, ca: carbonate, cal: calcite, chl: chlorite, dck: dickite, ep: epidote, dol: dolomite, ill: illite, kao: kaolinite, ms: muscovite, py: pyrite, sd: siderite, ser: sericite, ver: vermiculite, zeo: zeolite 68

Figure 6.13. A cross section across the South Zone showing the spatial distribution of lithological units, Au-Cu and Zn ore zones and associated hydrothermal alteration assemblages. Notice the each petrographic sample indicates the present hydrothermal alterations and their temporal evolution from early to late phases. 70

Figure 6.14. Full thin section scan photomicrograph examples of samples displaying early sericite-rich alteration accompanied by later kaolinite overprint (XPL), (A) EB075, HTD021-15.9m; (B) EB077, HTD021-17.4m. kao: kaolinite, qtz: quartz, ser: sericite 71

Figure 6.15. (A) Drill core sample from HTD021-201m representing clay alteration replacing pre-existing sericite alteration on dacite breccia. Notice the brown clay minerals replacing the beige sericite, (B) Full thin section scan photomicrograph (XPL) of sample EB118, HTD021-202.1m. Dark brown minerals are annotated as clay minerals and SWIR work provides the presence of kaolinite, dickite, palygorskite and rectorite. anh: anhydrite, ser: sericite. 73

Figure 6.16. Drill core sample, EB116 from HTD021-191.7 m, representing zeolite (laumontite)-bearing alteration associations replacing volcanosedimantary rock. Notice the presence of pre-existing pervasive sericite alteration and late crosscutting anhydrite veinlets. anh: anhydrite, ser: sericite, zeo: zeolite. 74

Figure 6.17. (A) Drill core sample from HTD027-126.5m representing coarse comb quartz (quartz-4)-dolomite-pyrite vein cutting the spherulitic dacite breccia and pre-existing sericite and kaolinite alteration, (B) Full thin section scan photomicrograph (XPL) of sample EB072, HTD021-10.7m, comb quartz4-dolomite-pyrite vein cutting pre-existing sericite. and kaolinite alterations. dol: dolomite, goe: goethite, hm: hematite, kao: kaolinite, qtz: quartz, ser: sericite 75

Figure 6.18. Full thin section scan photomicrograph examples of samples displaying late anhydrite overprint on sericite and clay altered volcanosedimentary rocks (XPL). (A) EB125ii, HTD021-221.4 m; (B) EB131, HTD021-237.6 m. anh: anhydrite, kao: kaolinite, qtz: quartz, ser: sericite, sl: sphalerite, vrm: vermiculite 77

Figure 6.19. Alteration index (AI) versus chlorite-carbonate-pyrite index (CCPI) alteration box plot for drill core samples (HTD021) representing South Zone mineralization, AI = $100 \times (MgO + K_2O)/(MgO + K_2O + CaO + Na_2O)$ (Ishikawa et al., 1976), CCPI = $100 \times (MgO + FeO)/(MgO + FeO + Na_2O + K_2O)$ (Large et al., 2001) 79

Figure 6.20. A cross section across the old workings zone showing the spatial distribution of lithological units, Au-Zn ore zones and associated hydrothermal alteration assemblages. Notice the each petrographic sample indicates the present hydrothermal alterations and their temporal evolution from early to late phases. Abbreviations: anh: anhydrite, ca: carbonate, cal: calcite, chl: chlorite, dol: dolomite, ep: epidote, ill: illite, mm: montmorillonite, plg: palygorskite, py: pyrite, rho: rhodochrosite, qtz: quartz, ser: sericite, vrm: vermiculite 81

Figure 6.21. (A-B) Drill core samples from drill hole HTD222-4.8 m and HTD222-143.8 m (sample EB249), respectively, targetting the old workings zone mineralization with early chlorite1-rich alteration overprinted by sericite1 and Mg-illite; (C-D) Photomicrographs of sample EB249 under PPL and XPL, respectively, displaying the early chlorite1 alteration on the groundmass of andesite porphyry clasts of andesite breccia and sericite1 alteration selectively pervasive on plagioclase phenocrysts and later Mg-illite overprint on the groundmass (abbreviations are as in Figure 6.20). 82

Figure 6.22. Sample EB163 displaying early pervasive chlorite1 and occasional selective sericite1 alteration on plagioclase phenocrysts cut by comb quartz4-dolomite-epidote-calcite vein, (A) Full thin section sketch, (B) Photomicrograph of the microfault displaying present hydrothermal alteration associations, XPL 83

Figure 6.23. Alteration index (AI) versus chlorite-carbonate-pyrite index (CCPI) alteration box plot for drill core samples (HTD222) representing old workings zone mineralization, AI = 100 × (MgO + K_2O)/(MgO + K_2O + CaO + Na_2O) (Ishikawa et al., 1976), CCPI = 100 × (MgO + FeO)/(MgO + FeO + Na_2O + K_2O) (Large et al., 2001) 84

Figure 8.1. (A) Deformed and brecciated massive sulfide mineralization consisting of pyrite and chalcopyrite, drill hole HTG02-79.2 m, (B) Brecciated semi-massive chalcopyrite-pyrite mineralization, drill hole HTD029-557.3 m. Notice that matrix is occupied by anhydrite. (C) Deformed and brecciated massive sulfide mineralization consisting of pyrite and chalcopyrite with anhydrite overprint occupying fractures, drill hole HTD05-149 m. Abbreviations: anh: anhydrite, cp: chalcopyrite, py: pyrite 91

Figure 8.2. Sample EB197, drill hole HTD029-507.1 m, representing Main Zone chalcopyrite2 (±pyrite3) mineralization associated with chlorite2-quartz2 phase and overprinted by anhydrite. Notice the presence of hematite. (A) drill core sample, (B, D) Photomicrograph in PPL and (C, E) in XPL. Abbreviations: anh: anhydrite, cp: chalcopyrite, chl: chlorite, hm: hematite, qtz: quartz 92

Figure 8.3. BSE and QEMSCAN images of gold grains characterizing main zone mineralization from selected composite samples representing drill hole intervals (Meng, 2019), (A) and (B) HTD110, 190-220 m, (C) HTD111, 358-370, (D) HTD110, 190-220 m 93

Figure 8.4. (A) Polished sample (EB197, HTD029-507.1 m) reflected light photomicrograph representing chalcopyrite2 replacing fractures along pyrite3 (B, C and D) BSE and QEMSCAN images of gold grains from composite samples from (B) HTD110-190-220 m, (C, D) HTD090-290-303 m representing main zone gold mineralization associated with chalcopyrite2 replacing pyrite3 95

Figure 8.5. (A, B) Polished samples (EB198, HTD029-521.7 m) reflected light photomicrographs representing main zone mineralization, goethite overprint on pre-existing pyrite3-chalcopyrite2 and chalcoyprite2, respectively. (C, D) BSE and QEMSCAN images of gold grains associated with goethite, siderite and quartz3 phases characterizing main zone mineralization from selected composite samples, HTD111, 358-370 96

Figure 8.6. Geologic and geochemical profiles of drill hole HTD018 (trace and legend shown on Fig. 6.1) that intersects Main Zone mineralization. The location and distribution of the analyzed samples and results are indicated by black horizontal lines. All the lithogeochemical data and Au, Ag, Cu, Zn and Pb assay values are from Artmin Madencilik. AI = alteration index (Ishikawa et al., 1976), CCPI = chlorite-carbonate-pyrite index (Large et al., 2001). 99

Figure 8.7. Geologic and geochemical profiles of drill hole HTD029 (trace and legend shown on Fig. 6.1) that intersects Main Zone mineralization. The location and distribution of the analyzed samples and results are indicated by black horizontal lines. All the lithogeochemical data and Au, Ag, Cu, Zn and Pb assay values are from Artmin Madencilik. AI = alteration index (Ishikawa et al., 1976), CCPI = chlorite-carbonate-pyrite index (Large et al., 2001). 100

Figure 8.8. Geologic and geochemical profiles of drill hole HTD090 (trace and legend shown on Fig. 6.1) that intersects Main Zone mineralization. The location and distribution of the analyzed samples and results are indicated by black horizontal lines. All the lithogeochemical data and Au, Ag, Cu, Zn and Pb assay values are from Artmin Madencilik. AI = alteration index (Ishikawa et al., 1976), CCPI = chlorite-carbonate-pyrite index (Large et al., 2001). 101

Figure 8.9. Sample EB124 from drill hole HTD021-215.9 m, representing South Zone galena-sphalerite-pyrite-chalcopyrite mineralization accompanied by quartz, dolomite and anhydrite replacing spherulitic dacite breccia, (A) drill core slab, (B) full thin section scan photomicrograph (PPL), (C) full thin section scan photomicrograph (XPL), (D) polished section, reflected light image. anh: anhydrite, cp: chalcopyrite, dol: dolomite, gn: galena, py: pyrite, sl: sphalerite 103

Figure 8.10. Sample EB079 from drill hole HTD021-20.3 m, representing South Zone sphalerite2-chalcopyrite2-pyrite4 mineralization associated with quartz4 and dolomite. (A) Polished sample, reflected light image, (B, C) Optical cathodoluminescence images. cp: chalcopyrite, dol: dolomite, py: pyrite, qtz: quartz, sl: sphalerite 105

Figure 8.11. BSE and QEMSCAN images of gold grains characterizing south zone mineralization from selected composite samples representing drill hole HTD196, 42-57 m (Meng, 2019), (A) Gold particles enclosed within pyrite3, (B) gold particles associated with chalcopyrite2 replaces pyrite3, (C) gold particles associated with chalcopyrite2 and sphalerite2?, (D) gold particles associated with quartz3-pyrite3-sericite2-kaolinite-iron oxide-siderite 106

Figure 8.12. Geologic and geochemical profiles of drill hole HTD021 (trace and legend shown on Fig. 6.13) that intersects South Zone mineralization. The location and distribution of the analyzed samples and results are indicated by black horizontal lines. All the lithogeochemical data and Au, Ag, Cu, Zn and Pb assay values are from Artmin Madencilik. AI = alteration index (Ishikawa et al., 1976), CCPI = chlorite-carbonate-pyrite index (Large et al., 2001). 108

Figure 8.13. Old workings zone mineralization occured as chlorite2-quartz2-pyrite3$\pm$chalcopyrite2 veins and patches replacing the chlorite1-altered andesite breccia, (A) drill core photo from HTD222-142.5 m, (B) Full thin section scan of sample EB162, (C-D) Photomicrographs of sample EB162, PPL. 110

Figure 8.14. Geologic and geochemical profiles of drill hole HTD222 (trace and legend shown on Fig. 6.20) that intersects old workings zone mineralization. The location and distribution of the analyzed samples and results are indicated by black horizontal lines. All the lithogeochemical data and Au, Ag, Cu, Zn and Pb assay values are from Artmin Madencilik. AI = alteration index (Ishikawa et al., 1976), CCPI = chlorite-carbonate-pyrite index (Large et al., 2001). 112

Figure 9.1. $^{206}Pb/^{238}U$ vs. $^{207}Pb/^{235}U$ Concordia, $^{206}Pb/^{238}U$ weighted mean histogram diagrams and zircon cathodoluminescence images with laser spot locations (orange circles), spot $^{206}Pb/^{238}U$ ages (orange if accepted, grey if outlying, and pale pink if discordant). Blue numbers indicate the zircon number (N) in the weighted mean age diagram). (A), (B) and (C) from the columnar dacite, EB056; (D), (E) and (F) from rhyodacite EB142; (G), (H) and (I) from red conglomerate unit with volcanic clasts 114

Figure 9.2. $^{40}Ar/^{39}Ar$ age spectra for analyzed sericite, (A-B) EB078, south zone mineralization; (C-D) EB232, main zone mineralization. MSWD: mean square of weighted deviates . 116

Figure 10.1. Histogram of measured $\delta^{34}S$ values in chalcopyrite, pyrite, sphalerite and anhydrite, CDT: Canyon Diablo Troilite . . . 118

Figure 10.2. Calculated $\delta^{18}O_{water}$ vs. δD_{water} of hydrothermal fluids responsible for chlorite1, chlorite2, sericite2, Mg-illite and kaolinite alterations, VSMOW: Vienna Standard Mean Ocean Water, Meteoric water line (Craig, 1961), felsic magmatic water (Taylor, 1992), primary magmatic water (Taylor, 1974), volcanic vapor (Giggenbach, 1992) 120

Figure 11.1. Primary and pseudo-secondary fluid inclusions in a quartz4 crystal of the comb quartz4 vein in sample EB181. Notice the euhedral habit and the growth zones of the quartz4 crystal. 122

1. INTRODUCTION

1.1. Geographic Setting

The Hod Maden, the study area is located in the northeastern Turkey, and is accessible from the Artvin, which is approximately 50 km away, or 130 km away from the Erzurum via Yusufeli (Artvin) (Fig. 1.1, 1.2). It covers an area of approximately 67 km^2 and situated in Artvin's 1/25000 scale F47c4, F47c3, G47b1 and G47b2 quadrangles.

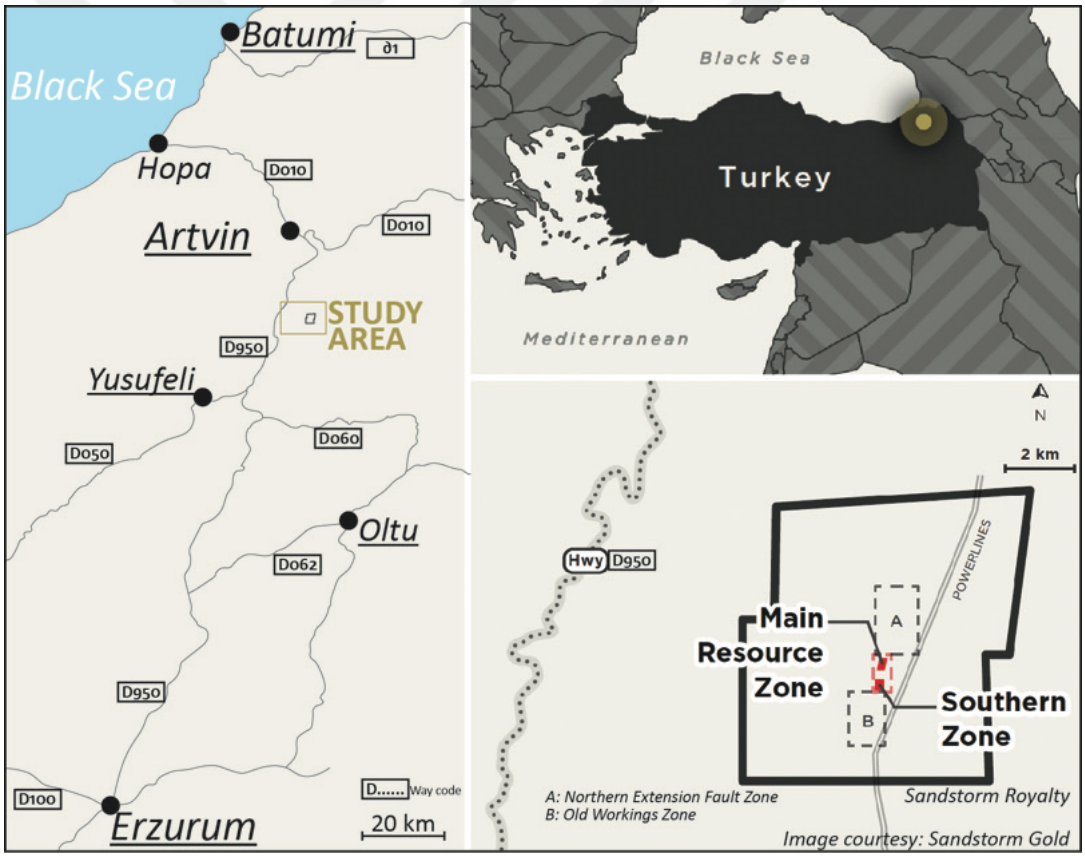


Figure 1.1. Geographic setting and location of the Hod Maden

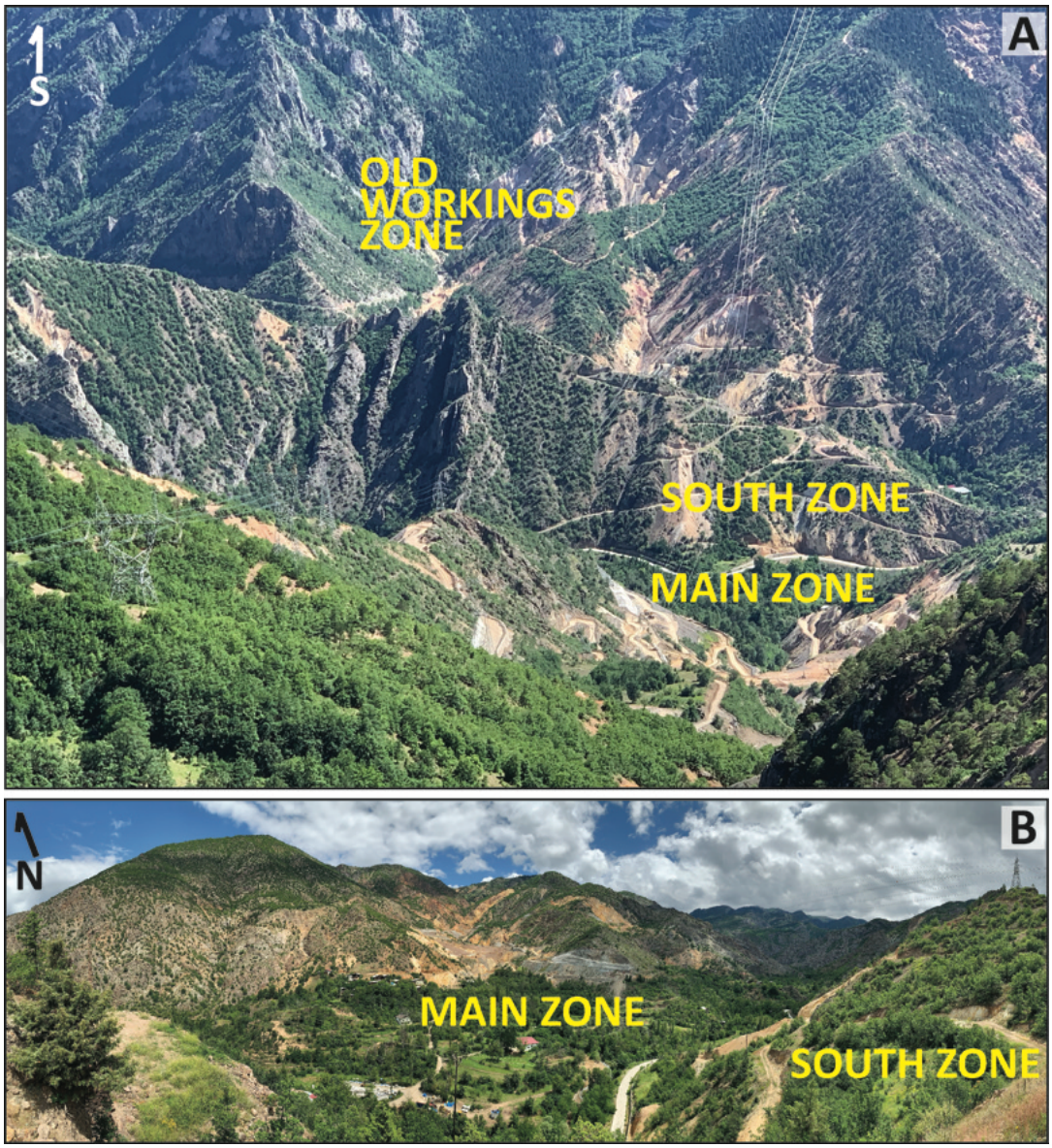


Figure 1.2. **A) South-looking view of mineralized zones of Hod Maden deposit including main zone, south zone and the old workings zone from north to south. (B) Northeast-looking view of the main zone and the south zone**

1.2. Previous Work

Prior to this study, Hod region was investigated by the Turkish Mineral Research and Exploration Directorate (MTA) in several studies, including (Ovalıoğlu, 1966; Doyuran, 1970; Şatır and Ereren, 1976; Çekiç et al., 1984; Kandemir et al., 2017). However, from 1991 onwards, mining companies such as Anglo American, Teck (Cominco), and AMG (later Aegean Metals and Mediterranean Resources) have been involved in exploration activities. In 2014, Lidya Madencilik discovered one of the

most significant gold-copper deposits (∼4 Moz @ 11.1 g/t AuEq; Alizade and Aksoy, 2019), Hod Maden, in the world in recent years. Since then, the Hod region gained considerable attention from mining companies' exploration departments, leading to a surge in interest in the area.

1.3. Purpose and Scope of the Study

Hod Maden and its vicinity is one of the ideal locations to observe and study the main lithologic and volcano-stratigraphic features of eastern part of the eastern Pontides as it comprises Jurassic and Cretaceous volcanic and sedimentary sequences. To gain a deeper comprehension of the geological nature of the region, revised geological map and stratigraphic section of the study area are prepared and characteristic features of lithological units are reported. The first objective of this study is to contribute to the existing knowledge on the regional geology by combining the previously published technical reports and scientific papers with new data obtained from field geological mapping and petrographic investigation carried out during this research.

In recent years, Hod Maden deposit and its surrounding region gained considerable attention from mining companies' exploration departments, leading to a surge in interest in the area. Therefore, the second objective is to provide field geologists with exploration tools, methodologies and vectors by delineating lithological units, defining textural characteristics, clarifying stratigraphic relationships and elaborating descriptive implications between volcanism and ore forming processes.

The main objective of this study is to determine the nature and type of mineralization by identifying and clarifying the origin and evolution of the ore-bearing hydrothermal fluids and the triggers and mechanisms for high-grade gold and copper ore precipitation. To achieve these objectives, in the scope of this research, field work, petrography, radiogenic and stable isotope analyses were performed and each of these methods are explained in the following chapter.

According to Moritz et al. (2016, 2020) and Grosjean et al. (2022), there is a close connection between the Cretaceous magmatic (particularly submarine volcanism) and metallogenic evolutions in the northern Lesser Caucasus and the eastern

Pontides of Turkey. Hence, the results of this study will be crucial in correlating the geologic and metallogenic picture of the Lesser Caucasus and the eastern Pontides.

2. METHODOLOGY

This chapter plays a crucial role in providing an understanding of the scope and context of the thesis. By detailing the methods used to address geological problems associated with the Hod Maden mineralization, the subsequent results of each method or analytical work were analyzed and discussed. This information will also be used in future studies to expand upon the existing data or to fill the gaps in knowledge. In addition, this chapter instills confidence in the acquired data sets, as it outlines the conditions, processes, and analytical parameters of each data. This information will be useful for other researchers who may wish to use this work in future studies or replicate the analyses.

2.1. Field Work

The fieldwork for this study took place at the Hod Maden camp in the Artvin, spanning the fall of 2018 and the summer of 2019. A total of thirteen weeks were dedicated to the field works. The field work activities include field mapping, logging drill cores, and collecting samples. The analytical work was primarily carried out at the University of Geneva (UNIGE, Switzerland) and the University of Lausanne (UNIL, Switzerland).

The field mapping campaign was focused on differencing the main lithologies (volcanic facies) and their spatial distribution. The drill-core logging was for the identification of the mineralized zones exhibiting ore minerals, hydrothermal alteration minerals, distinctive volcanic and mineralization textures, as well as deformation events. The field data was collected as georeferenced point data using a GISKIT software, and was stored in digital format (Fig. 2.1.). During the field work activities, a total of 284 rock samples were collected from the outcrops during the mapping and drill-core logging campaigns. Afterward, these samples were subdivided into distinct groups for petrographical, mineral chemistry, and isotope

analytical purposes. Each sample was assigned a unique sample ID, which was further divided into multiple sub-samples (e.g., 100i, 100ii, and so forth) for more specific investigations. Sample list including sample ID, sample type (outcrop or drill core), depth (if drill core sample), coordinates (easting-northing in WGS84 datum), completed analytical work on that particular sample, field and drill core photos and notes/explanation is given in Appendix-A1 as a list and as a ”Notion” database format.

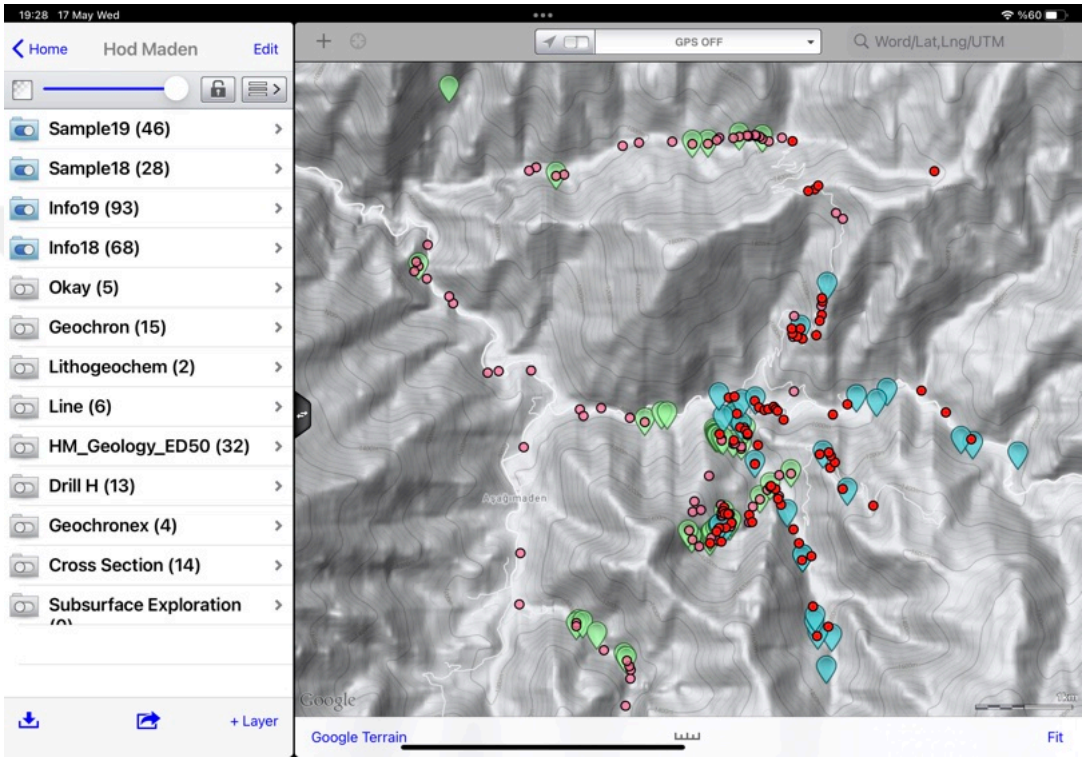


Figure 2.1. Field input data on sample locations and mapping informations in GISKit software

2.2. Leapfrog Modelling

A 3D geological map of Hod region is created by modeling lithological units and structural elements, which incorporates the drill hole data to display hydrothermal alteration, volcanic and ore textures, and metal grades distribution (Fig. 2.2.). The model is built using various imported data, such as georeferenced maps, elevation grid data, GIS vector data, lithological data, and digitized drillcore logs. The data is validated before building the model to accurately represent the Hod geology.

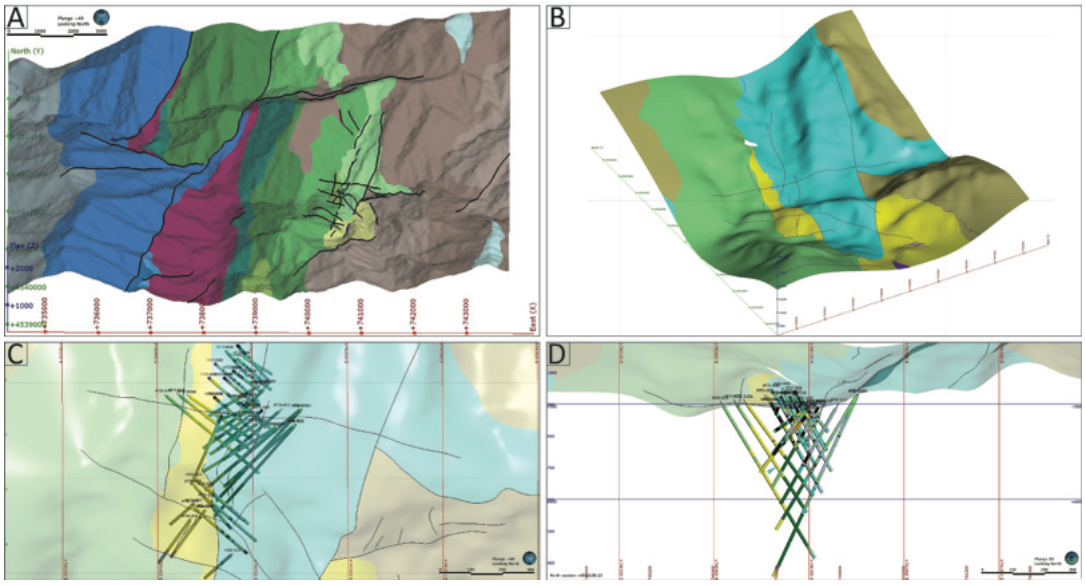


Figure 2.2. **Geological model of Hod Maden deposit (A, B) and drill holes (C, D) on Leapfrog software**

2.3. Petrography

The rock samples representing the volcanic rocks, ore zones and associated alteration zones collected for petrographic analysis, were used to identify mineral assemblages, hydrothermal alteration, host rock and ore textures through transmitted and reflected light microscopy (Fig. 2.3.). All petrographic work was conducted at MSKÜ and UNIGE and the detailed petrographic report for each sample are given in Appendix-A2.

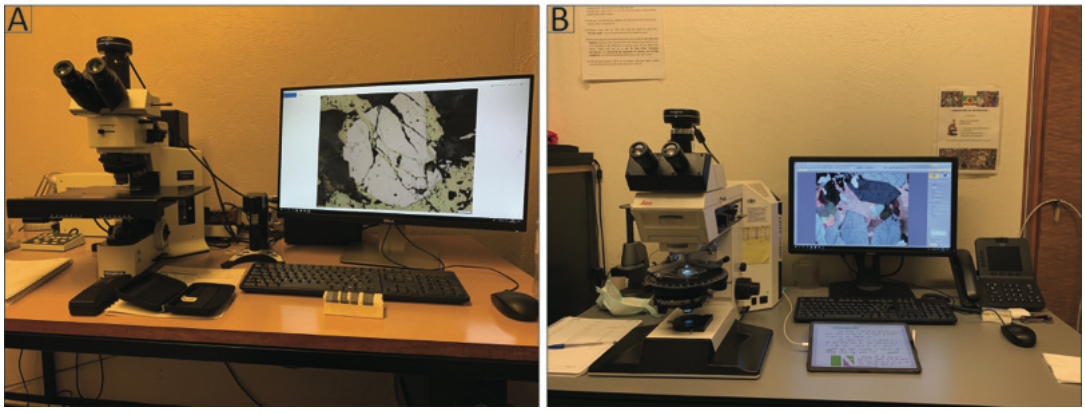


Figure 2.3. **(A) Olympus automated stage scanning microscope and (B) Leica polarized microscope**

2.3.1. Shortwave infrared spectroscopy (SWIR)

A total of 253 rock slabs mainly from the drill cores and surface rock samples were used for the identification of the composition of the hydrothermal alteration mineralogy using SWIR spectroscopy (N:492 spot reading). The analysis was conducted using a ASD TerraSpec® Halo Mineral Identifier instrument (Fig. 2.4. A) at the UNIGE. The level of confidence in the identified minerals is denoted by a rating of one to three stars (Fig. 2.4. B). Raman Spectroscopy and microprobe techniques were used to verify the SWIR spectral results for chlorite, sericite and illite, where applicable. These results, combined with petrographic and drill core findings, were used to construct a hydrothermal alteration model for the Hod Maden mineralization. The results of SWIR analysis are given in Appendix-A3.

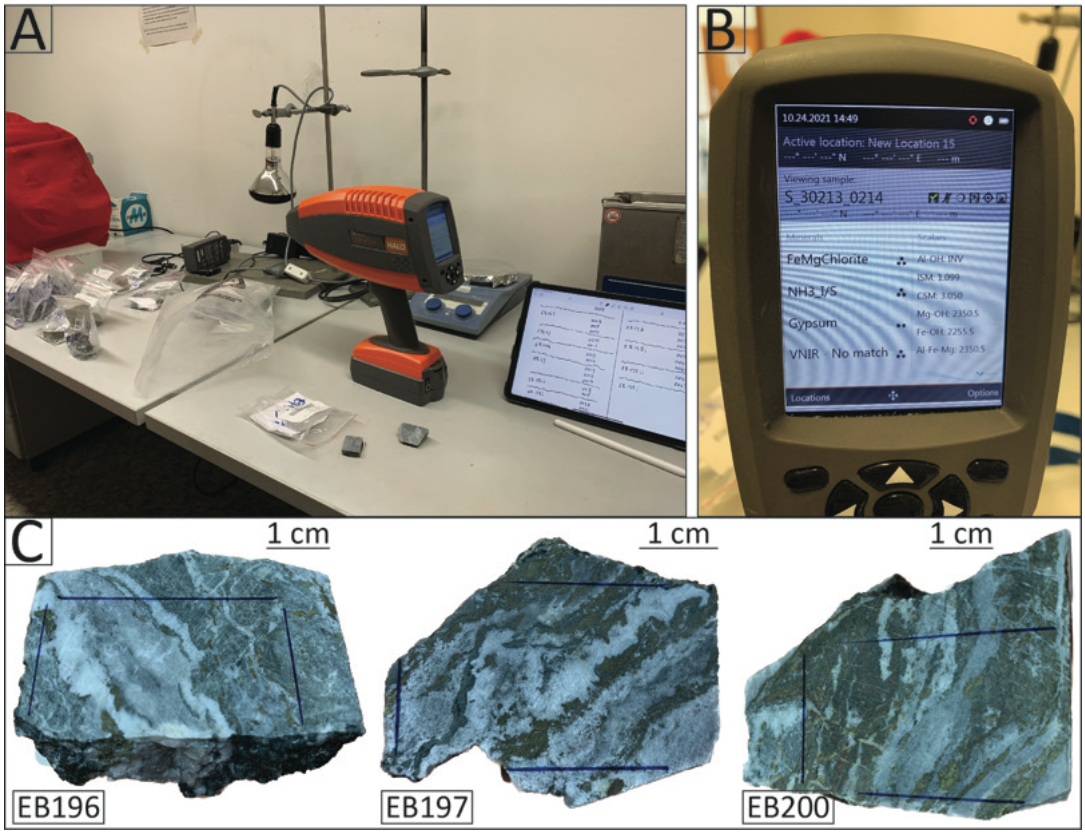


Figure 2.4. **(A) ASD TerraSpec® Halo Mineral Identifier instrument, (B) SWIR reading on Teraspec instrument and (C) drill core rock slabs examples**

2.3.2. Raman spectroscopy

A total of 37 samples are measured and evaluated by the author using Raman spectroscopy at UNIGE. Raman spectra were obtained using a LabRAM HR spectrometer (Fig. 2.5.) (Horiba Jobin Yvon) equipped with a 600 g.mm^{-1} grating and an edge filter. The confocal hole aperture had a diameter of 500 μm, and the slit aperture was set to 100 μm. An excitation beam was generated by a Stabilite 2017 Ar+ laser (Spectra Physics, Newport Corporation) operating at a wavelength of 542 nm and a power output of 200 mW. The laser beam was focused on the sample using a 100x objective from Olympus. The acquisition time and number of accumulations were adjusted to optimize the signal-to-noise ratio (S/N), aiming for a value below 1%. Although the precise limits of detection and absolute concentrations of trace gases could not be determined, the relative proportions of gas species were estimated qualitatively using the peak area, acquisition time, and the specific scattering cross-section of each peak. The LabSpec software Schrötter and Klöckner (1979) provided by Burke (2001) was utilized for these calculations.

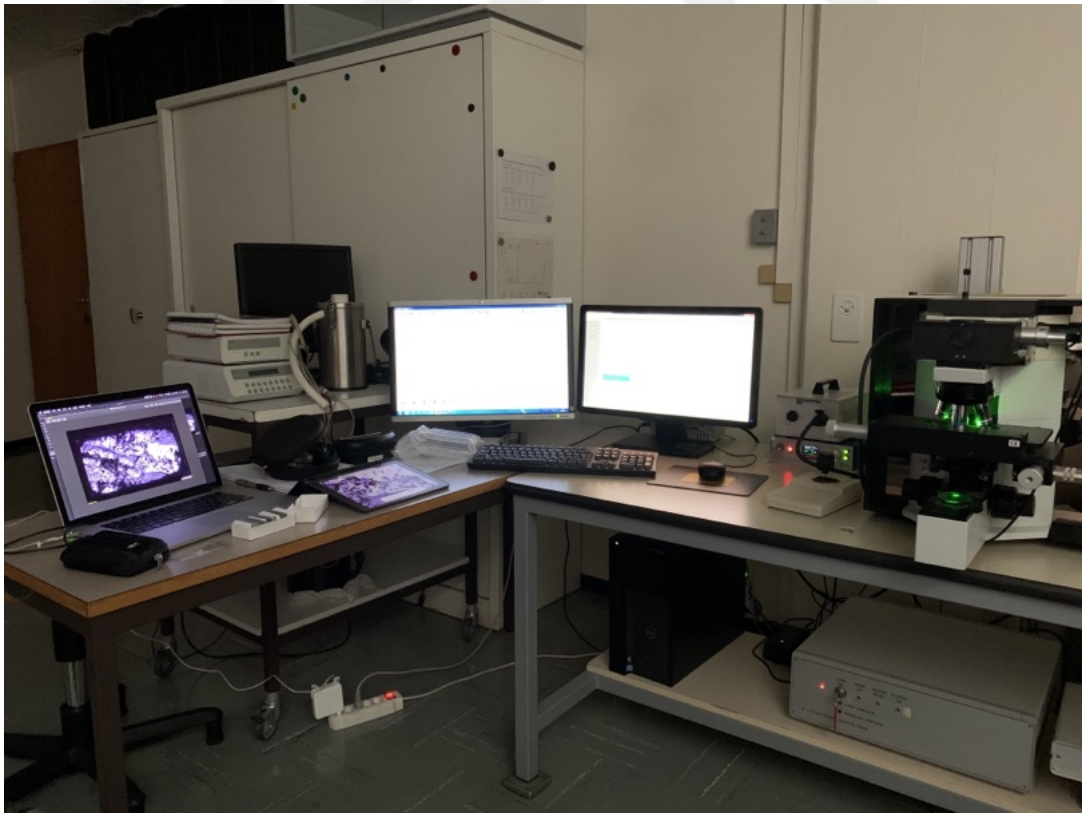


Figure 2.5. LabRAM HR spectrometer (Horiba Jobin Yvon) equipment for Raman spectroscopy

2.3.3. Electron microprobe analysis (EPMA)

The element compositions of chlorite, sericite, and sphalerite were determined by conducting quantitative point analyses using Wavelength Dispersive Spectroscopy (WDS) on a JEOL 8200 Superprobe at the UNIGE (Fig. 2.6.). The analyses were performed by the author under the supervision of Florence Bégué and with the help of Enzo-Enrico Cacciatore and Zsófia Palos. The analyses were carried out with a 15 kV accelerating voltage, a probe current of 20 nA, and a beam size of 1 μm. Generally, the error estimates for major element oxides were found to be less than $\pm 1\%$. Standards used: albite (Na), andalusite (Al), orthoclase (K), wollastonite (Si, Ca), olivine (Mg), fayalite (Fe), Mg-Mn-Ti oxide (Ti, Mn), Cr_2O_3 (Cr). The results of EPMA analyses consitisting of element compositions and microprobe beam locations along with additional photomicrographs and average composition tables were given in Appendix-B1 and Appendix-B2, respectively.



Figure 2.6. JEOL 8200 superprobe instrument

2.3.4. Quantitative evaluation of minerals by scanning electron microscopy (QEMSCAN)

QEMSCAN analyses were performed and reported by ALS Metallurgy Mineralogy (Meng, 2019). Seventy-one gold/copper-bearing samples (P_{80} 106 μm) from the Hod Maden variability test program were submitted for quantitative mineralogical analysis by QEMSCAN. Each sample was riffle split to produce sub-samples of suitable size for making QEMSCAN polished sections. Each sub-sample was mixed with size-graded, high purity graphite to ensure particle separation and discourage density segregation. The sample graphite mixtures were then set into moulds using a two-part epoxy resin, producing a representative sub-sample or randomly orientated particles. After curing, the resin blocks were cut back to expose a fresh surface and progressively ground and fine-polished. Passing QA/QC checks, the sections were then carbon coated for electron beam conductivity and presented to the QEMSCAN for analysis. Each block was analyzed using QEMSCAN, Field Scan (FS) mode at 6 μm pixel spacing. Bright phase search for minerals with high atomic density and strong electron backscatter response, including gold-rich mineral phases was undertaken using the Trace Mineral search (TMS) analysis for each block. Spot analysis of all identified grains was undertaken by standard-less quantification using Energy Dispersive Spectrometry (EDS). The particles measured during the TMS scan were mapped with 1 μm spacing.

2.4. Geochronology

2.4.1. In-situ U-Pb geochronology by laser ablation-inductively coupled plasma-mass spectroscopy (LA-ICP-MS)

U-Pb geochronology analyses were performed by the author at the UNIL under the supervision of Alexey Ulianov. Three samples of magmatic rocks (EB056: dacite porphyry from columnar-jointed dacite; EB142: rhyodacite lava flow; and EB275: mafic porphyritic volcanic rock clasts in the red conglomerate) were analyzed for U-Pb dating using LA-ICP-MS.

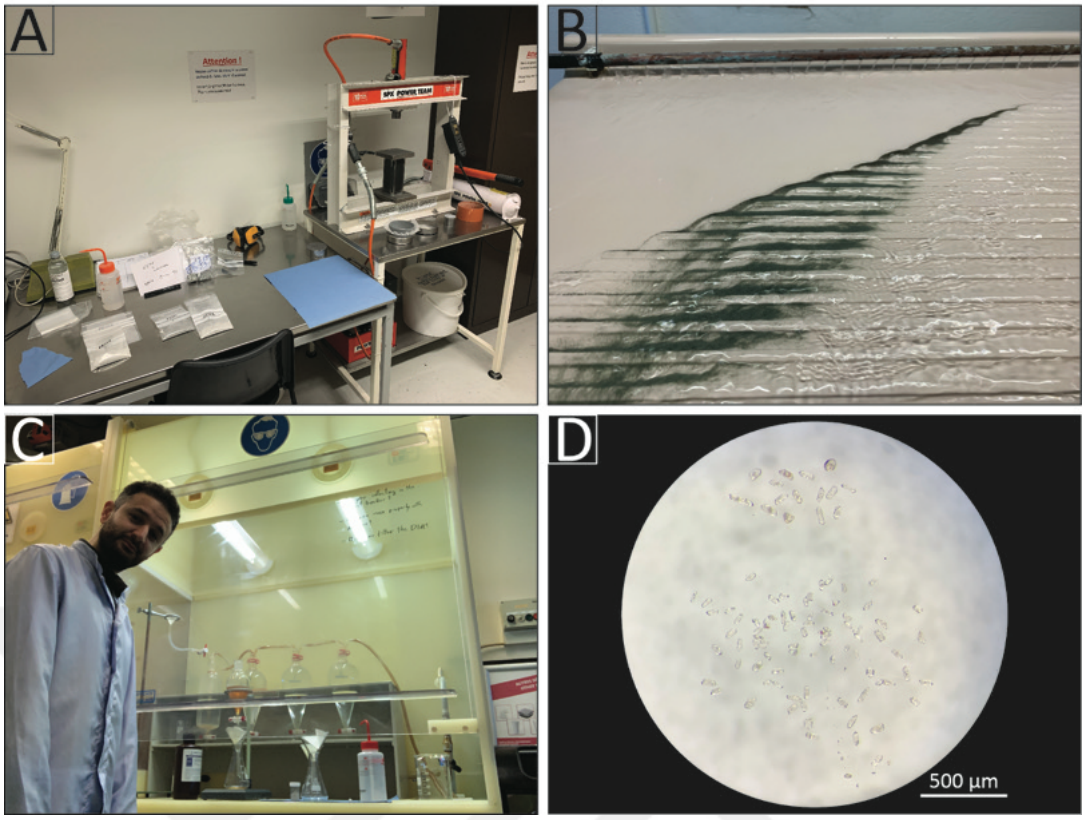


Figure 2.7. (A) Hydraulic press for crushing and grinding the samples down to 300μm, (B) Wilfley table, (C) heavy liquid (MI) gravimetric separation setup, (D) hand picking zircons under binocular microscope

The zircon crystals within these samples were extracted by crushing and grinding the whole-rock samples to a particle size of 300 μm using a hydraulic press and sieving (Fig. 2.7. A). The separation of zircon crystals was accomplished through the utilization of a Wilfley table (Fig. 2.7. B) and heavy liquid gravimetric separation (Fig. 2.7. C). Selection of euhedral to subhedral zircon crystals was conducted by handpicking them from the heavy fraction under a binocular microscope (Fig. 2.7. D). For the purpose of determining the U-Pb geochronology using LA-ICP-MS, the zircon crystals were carefully selected and affixed to an epoxy resin block. Subsequently, zircon imaging was conducted at the University of Geneva using the JEOL JSM7001F scanning electron microscope equipped with a cathodoluminescence detector (Fig. 2.8.). This imaging process aimed to identify the growth zones within the zircons, detect any existing inherited cores, and provide insights into the crystal textures. Such information proved instrumental in accurately determining the suitable locations for laser ablation during the analysis.

The in-situ U-Pb dating of zircon performed on an ICP-MS instrument (Element

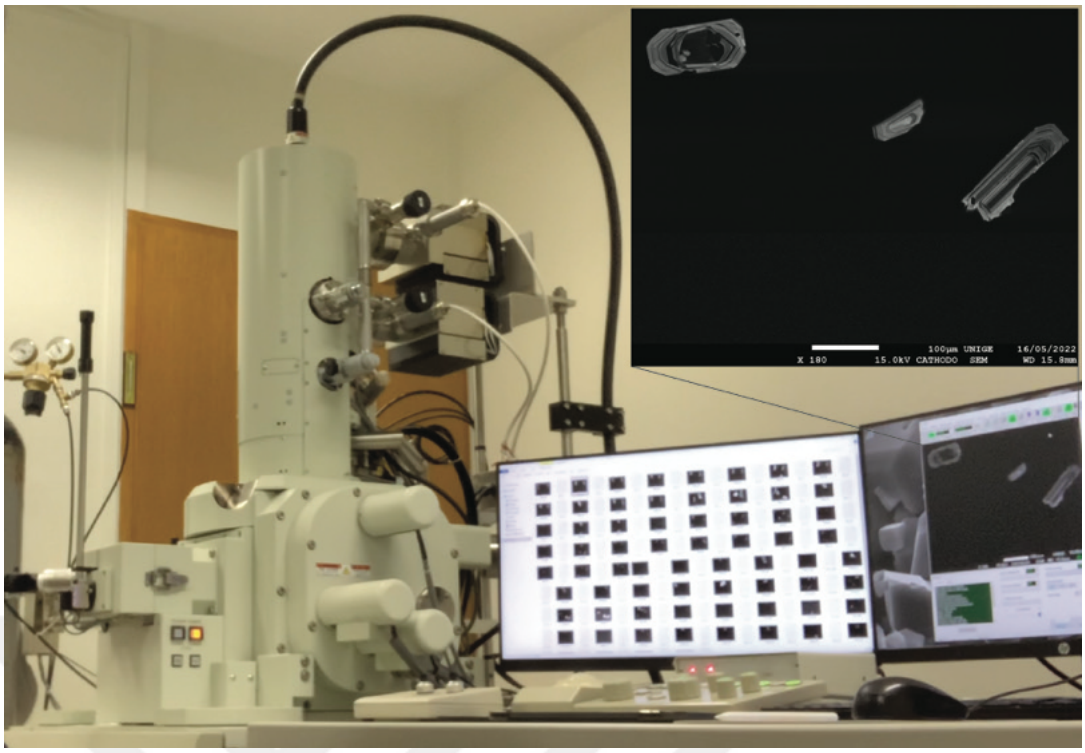


Figure 2.8. Scanning Electron Microscope JEOL JSM7001F and the cathodoluminescence images of zircon crystals acquired with this instrument

XR, Thermo Fisher Scientific) coupled with an ASI (Australian Scientific Instruments) RESOlution 193 nm ArF excimer laser system (ESI). The analytical procedure involved a pulse repetition rate of 10 Hz, an on-sample energy density of 6 J/cm^2, and conditions that closely resembled those described by (Ulianov et al., 2012). The analytical spot diameter was set to 20 μm. GJ-1 (Griffin et al., 2004; Jackson et al., 2004) and Plešovice (Sláma et al., 2008) were used as reference zircons for instrument calibration and accuracy control (QA/QC), respectively. The intensity versus time data were obtained manually and corrected for spikes, and then reduced using LAMTRACE software. Concordia diagrams with 2σ error ellipses were drawn and ^{206}Pb/^{238}U weighted mean ages were calculated with Isoplot. Any discordant or outlier zircon ages were excluded from the calculations, and only concordant ages were used to determine the weighted mean age. To determine the weighted mean age, we used single spot analysis that overlapped within error with the youngest significant PDC peak, while maintaining a statistically representative number of analyses (n) and a mean square weighted deviation (MSWD) that was as low as possible and close to 1. The obtained age is an average age of crystallization given with a calculated propagated 2 standard deviation number (2σ). The

propagated 2σ was calculated considering the standard deviation from the standard sample (GJ-1) measurements used for each sample. The weighted mean average ages, their 2σ and MSWD are presented in the corresponding sections in this thesis (see Chapter 9).

2.4.2. Ar-Ar geochronology

The Ar-Ar geochronology methodology involves several steps, including mineral separation, sample preparation, irradiation, and measurement. The author conducted the mineral separation at the Samples Preparation Laboratory at the UNIGE and then submitted the samples to Richard Spikings for further preparation. Subsequently, the samples were sent to Oregon State University (OSU) for irradiation.

Sericite concentrates were extracted from mineralized drill core slabs. First sample (EB232 from drill hole HTD018) represents the spherulitc dacite with sericite alteration from the Main Zone mineralization and the second sample (EB078 from drill hole HTD021) represents a sericite-pyrite vein crosscutting sericite altered dacite breccia from the South Zone mineralization. Each sample has two aliquots having different size fractions.

The samples underwent a crushing process using a hydraulic press and were subsequently ground using an agate mill. The resulting materials from each sample were combined with water in a ratio of 1 to 10 and sodium hexametaphosphate was added to facilitate flocculation of fine-grained particles that have negative surface charges and to suspend the clay fraction particle size, $\leq$ 2 µm. (Fig. 2.9. A, B). After stirring, the samples were allowed to gravitational settling for a duration of 10 hours (Fig. 2.9. A). The residual floating materials were siphonaged from the beaker and trensferred into centrifuge tubes (Fig. 2.9. C). The tubes were then centrifuged at a speed of 1000 rpm for 3 minutes at a temperature of 20°C (Fig. 2.9. D, E). Following this, the samples were dried for 15 hours (Fig. 2.9. E). The compositions of the samples were identified as composites of muscovite and K-illite using the Terraspec instrument subsequent to the mineral separation procedure.

A total of four sericite aliquots (EB078A is $\geq$ 2 µm, 7.2 mg; EB078B is $\leq$ 2 µm,



Figure 2.9. Sericite mineral separation methodology including (A) gravitational settling of water-mineral mixture, (B) addition of sodium hexametaphosphate, (C) siphoning of residual floating materials, (D) control panel for centrifuge parameters and (E) final sericite composite

276.1 mg; EB232A is $\geq$ 2 µm, 15.0 mg; and EB232B is $\leq$ 2 µm, 107.6 mg) were wrapped in Cu foil, and stacked inside a silica-glass tube, along with Fish Canyon Tuff sanidine (28.201 $\pm$ 0.046 Ma; (Kuiper et al., 2008)). The tube was irradiated at the shielded CLICIT position at the Oregon State University TRIGA reactor for 18 hours. The samples were pre-degassed at a laser power of 0.56 W to remove extraneous Ar from the grain surfaces, using a 55 W, CO2-IR laser (Photon Machines Inc.). The samples were subsequently step-heated with typically 12-18 individual degassing increments. The liberated gas was cleaned via a cold finger held at 130 °C, and hot GP50 (ST101) and cold NP10 (ST101) getters. Ar isotopes were multi-collected in a single step using a Thermo Fisher multi-collector Argus VI mass ($^{40\text{-}37}$Ar were collected on Faradays equipped with 1E13 ohm resistors, and ^{36}Ar was collected with the CDD). Data were reduced using ArArCalc (Koppers, 2002). Mass discrimination and Faraday/CDD yields were continually monitored and corrections were made as a function of gas intensity.

2.5. Stable Isotopes

2.5.1. S-isotope analysis

Sulfides (pyrite, chalcopyrite, sphalerite and galena) and sulfates (anhydrite) were analyzed at the stable isotope laboratory of the UNIL under the supervision of Jorge Spangenberg. Minerals were separated using a Dremel microdrill. After separation, samples wereweighed into tin capsules. The list of samples with amount (μg) and δ^{34}S (per mil VCDT) values as well as calibration/normalization standards used for sulfur isotope analysis at the UNIL-IDYST (Spangenberg et al., 2022) are given in Appendix-C1.

2.5.2. O-isotope analysis

The oxygen isotope compositions of chlorite, sericite, Mg-illite and kaolinite and whole-rock samples were analyzed by the author at the stable isotope laboratory of the UNIL under the supervision of Benita Putlitz. Minerals were extracted from the twin rock slab used for thin and polished sections by micro drilling (Dremel) or by a liquid suspension circuit. The analysis involved a CO_2-laser fluorination line coupled to a Finnigan MAT 253 mass spectrometer. The method used was similar to that described by (Sharp, 1990) and (Rumble and Hoering, 1994), with further details provided in (Kasemann et al., 2001). Approximately 0.5 to 4 mg of samples were loaded onto a Pt sample holder. To remove any adsorbed water, the samples were dried in an oven at 180 °C for 24-48 hours and then subjected to vacuum pumping for at least 10 hours. Following pre-fluorination cycles, the samples were heated using a CO_2-laser (Fig. 2.10. A) in the presence of pure F_2 at a pressure of 50 mbars. Excess F_2 was separated from O_2 by converting it to Cl_2 using KCl at 150 °C (Fig. 2.10. B). The extracted O_2 was collected on a molecular sieve (Fig. 2.10. C) and introduced into the gas source mass spectrometer through an inlet. The oxygen isotope compositions were reported using the standard δ-notation relative to VSMOW, expressed in permil (‰) (see Appendix-C2). The replicate analyses of the standard used (LS-1 qtz) exhibited an average precision of ± 0.1‰.

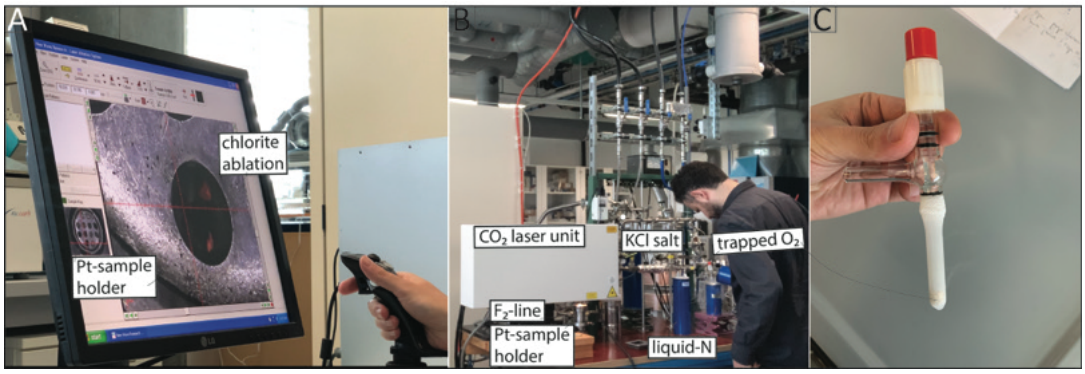


Figure 2.10. **(A) CO_2-laser ablation system with Pt-sample holder and chlorite sample during ablation in the view, (B) CO_2-laser fluorination line, (C) trapped O_2**

2.5.3. H-isotope analysis

Measurements of hydrogen isotopic ratios were performed using 1-4 mg of chlorite, sericite, Mg-ill, kaolinite and whole-rock samples at the stable isotope laboratory of the UNIL by Laszio Kocsis under supervision of Torsten Vennemann on a Thermo high-temperature conversion elemental analyzer (TC/EA) coupled to a Thermo MAT 253 mass spectrometer in continuous flow mode. Repeated measurements of standards and unknowns resulted in an uncertainty of ±3 ‰ in δD values. The results including unknown sample and standard amount (μg), wt% water, δD VSMOV values of unknowns and standards are given in Appendix-C3.

2.6. Fluid Inclusion Petrography and Microthermometry

The selection of samples was carried out following a comprehensive petrographic study, with a focus on large, euhedral quartz crystals and sphalerites displaying yellow to light-brown colors. The author prepared a total of 15 double-polished sections with a thickness of approximately $\sim$150μm at the sample preparation lab at MSKÜ, while Jean-Marie Boccard at UNIGE prepared an additional five double-polished sections with a thickness of around $\sim$135μm (Fig. 2.11. A). For fluid inclusion petrography, a Leica polarized microscope equipped with 50x objectives was used. Once the fluid inclusion assemblages (FIA) were identified, several photomicrographs were captured at varying z-values (representing depth and

focus) to generate a stacked photomicrograph that enabled the examination of all the FIAs situated at different depths (Fig. 2.11. B, C).

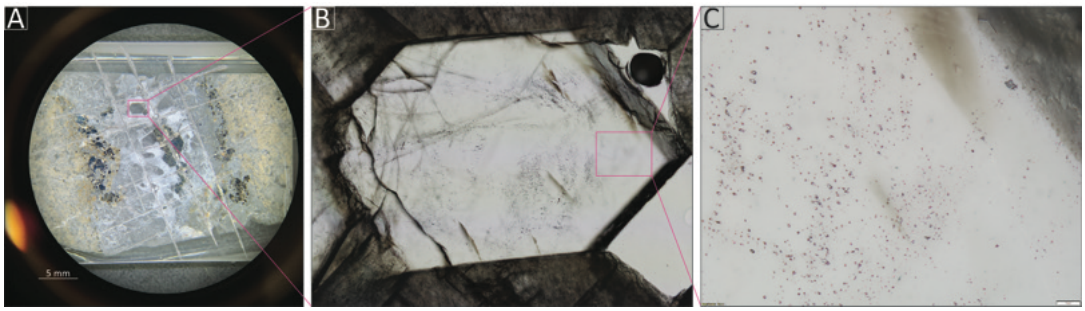


Figure 2.11. **(A) Double-polished fluid inclusion section (EB181) view under binocular microscope, (B) a single euhedral quartz crystal (181-Q1) containing fluid inclusions, (C) Z-stack photomicrograph of a particular area (181-Q1-R2)**

Microthermometric measurements were performed using a THMSG 600 Linkam heating-freezing stage mounted on a DMLB Leica microscope at the UNIGE. Calibrations were made using SynFluid standards at -56.6°C, 0.0°C, and 374.1°C (Sterner and Bodnar, 1984). All inclusions were evaluated as part of the NaCl-H2O system, and salinity in wt % NaCl eq.

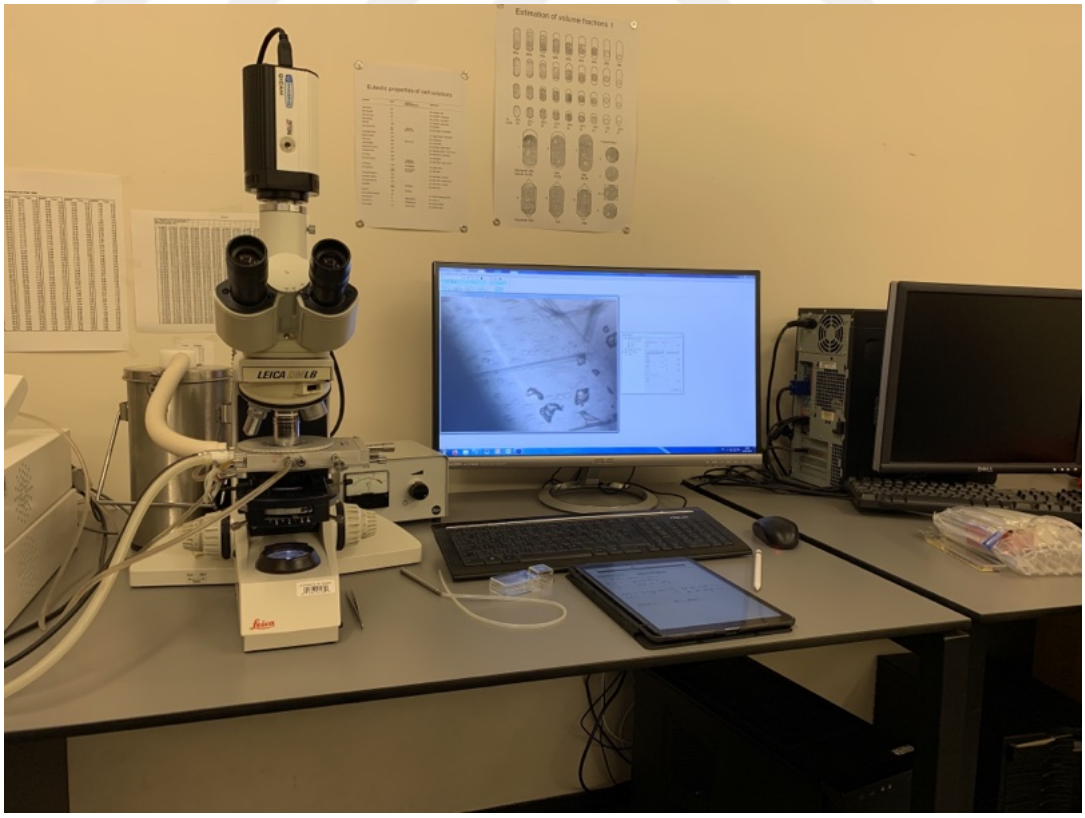


Figure 2.12. **THMSG 600 Linkam heating-freezing stage mounted on a DMLB Leica microscope**

3. GEOLOGY OF THE PONTIDES

3.1. Regional Geological Context of the Pontides

The Pontides is an important orogenic belt of about 1000 km long running from Bulgaria across the Black Sea coast of Turkey towards the Lesser Caucasus in Georgia and Armenia (Fig. 3.1. A). It forms the westernmost segment of the eastern Tethyan orogenic belt between the Rhodopes in the west and the Caucasus in the east. The geological entity of the Pontides was shaped by the closure of the PaleoTethyan and NeoTethyan Oceans (e.g., Şengör and Yilmaz, 1981; Okay et al., 1994). The Pontides is bordered to the south by the ophiolitic rocks, mélanges, and accretionary complexes collectively forming the collisional suture zone (Fig. 3.1. A, B).

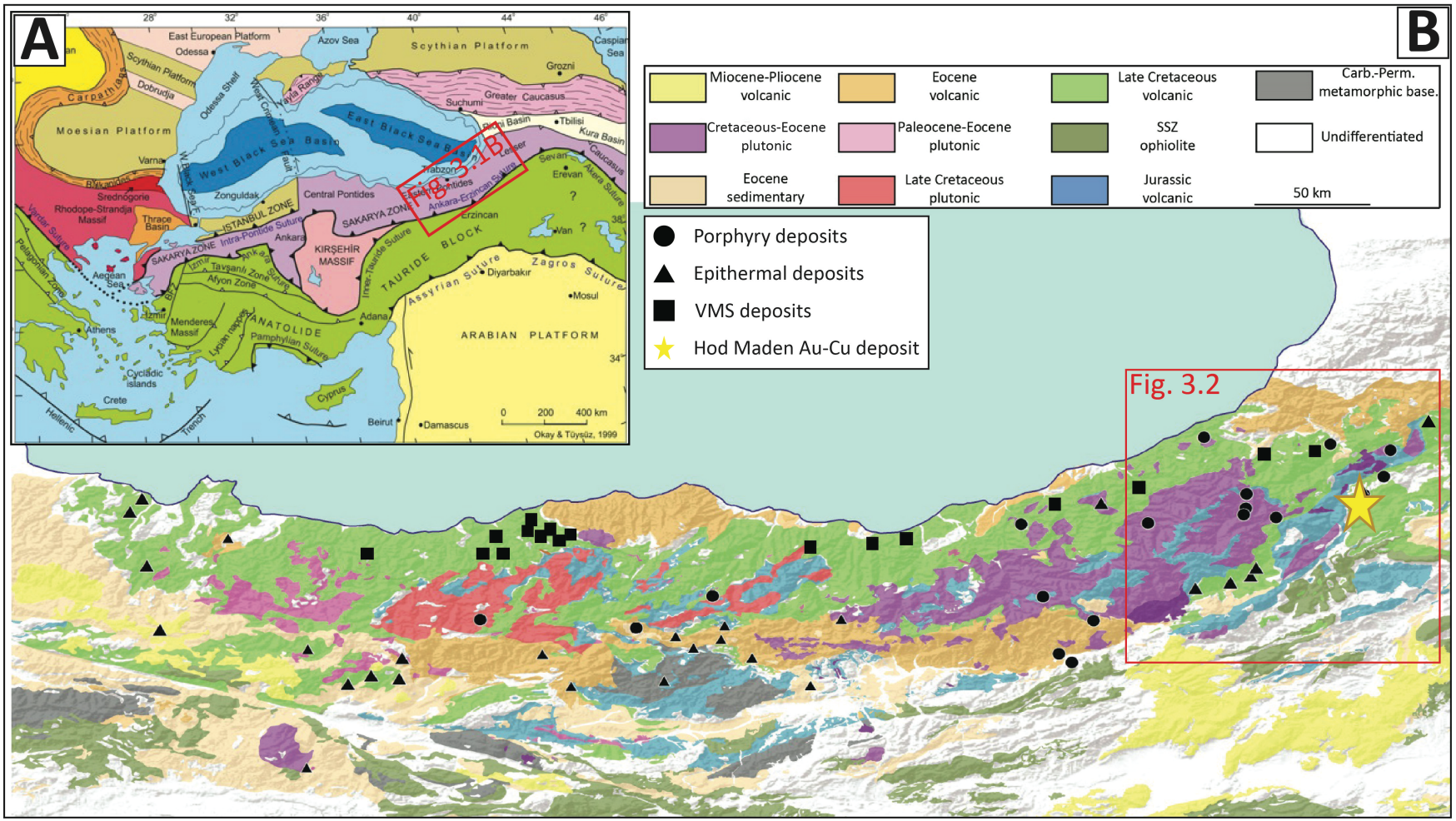


Figure 3.1. **(A) Tectonic units of Turkey (Okay and Tüysüz, 1999), (B) Simplified geological map of the eastern Pontides (1:500,000 scale; modified after (MTA, 2002)) and spatial distribution of porphyry, epithermal and VMS deposits**

The Pontides is comprised of three crystalline tectonostratigraphic terranes. These are from west to east, the Strandja, massif, Istanbul-Zonguldak, and Sakarya zones. The boundary between the İstanbul-Zonguldak and Sakarya zones, has long been a subject of debate, and is marked by the Intra-Pontide Suture (Şengör and Yilmaz, 1981; (Fig. 3.1 A). The Strandja massif refers to the Variscan metamorphic basement overlain by a Triassic-Jurassic continental to shallow marine sedimentary sequence. It respresents the part of the Rhodope and Serbo-Macedonian massifs(Okay, 2008; Fig. 3.1. A). The İstanbul zone is composed of Ordovician to Carboniferous sedimentary sequence unconformably resting on the pre-Cambrian metamorphic rocks (Okay, 1989). The Sakarya zone forms the main entity of the Pontides, and extends from the Aegean in the west to the Eastern Pontides. It consists of a pre-Jurassic crystalline basement unconformably overlain by the Mesozoic to Cenozoic sedimentary and volcanic succession composed of magmatic arc sequences and post-collisional volcano-sedimantary sequences (Okay et al., 2020). The crystalline basement contains three distinct rock types; high grade Variscan metamorphic rocks, Carbonifeous metagranites, and upper Triassic low-grade metamorphic oceanic subduction-accretion complex, the Karakaya Complex (Karakaya) (Okay, 2008; Okay et al., 2020).

The tectonostratigraphic terranes in the Pontides were accreted to form a single continental fragment during the closure of the NeoTethys ocean since the late Triassic that also coeval with the opening of the Black Sea during mid Cretaceous (Okay et al., 2020). A continuous northward subduction of the İzmir-Ankara ocean under the Pontides from the Late Triassic to the Late Cretaceous and Neogene has been recently proposed by (Okay et al., 2020). This closure resulted in the generation of the Mesozoic to Cenozoic sedimentary and volcanic succession composed of magmatic arc sequences and post-collisional volcano-sedimentary sequences. Okay et al. (2020) suggested that despite the continuous northward subduction of the İzmir-Ankara ocean, the accretion was episodic in the Late Triassic-Jurassic and Late Cretaceous intervening episodes of subduction-erosion possibly during the Early Cretaceous. The geological records of the Mesozoic and Neogene subductions are well preserved in the eastern Pontides (Fig. 3.1. B) where numerous mineral deposits were widely generated.

3.2. The Eastern Pontides

The eastern Pontides mimics the geologic and tectonic events from the opening to the closure of the İzmir-Ankara ocean that finally generated the Ankara-Erzincan suture. The Eastern Pontides is composed of the basement rocks, the magmatic rocks, the nappes, and the sedimentary basins. The basement rocks are represented by the Mesozoic carbonates, the Tokat Massif in the West and the Agvanis-Pulur Massif in the East (Fig. 3.1. B).

The Mesozoic and Cenozoic magmatic rocks of the eastern Pontides include volcano-plutonic associations (Fig. 3.1. B) , and are exposed along the Black Sea coast from Georgia to the Sredna Gora in the Bulgaria. They contain sequence of submarine lavas, pyroclastic rocks and intercalated sediments and plutonic rock. These magmatic associations are product of Jurassic and Cretaceous arc magmatism, and middle Eocene post-collisonal magmatism now preserved as E-W trending belts. The Jurassic magmatic associations consisting of volcanic and plutonic rocks are commonly identified in the southern part of the eastern Pontides whereas those of the Late Cretacous and Eocene age are clustered at the central and northern part of the eastern Pontides (Fig. 3.1. B).

The Mesozoic magmatic associations have the characteristics of the Andean-type magmatic arc (Kaygusuz et al., 2010; Nikishin et al., 2015; Alkan et al., 2019). Despite the magmatic arc is accepted to be started to develop during the late Triassic Okay et al. (2020), no magmatic association of this age is exposed in the eastern Pontides. However, the commonplace of the abundant detrital magmatic zircon population in the Triassic subduction-accretion complexes and in the Jurassic sandstones (Akdoğan et al., 2018; Ustaömer et al., 2016), is ascribed to the presence of a subaerial Triassic magmatic arc located to the north of the present Black Sea (Okay and Nikishin, 2015). The arc magmatism between Jurassic and late Cretaceous are well preserved in the Pontides. The arc magmatism was halted in the Maastrichtian (Şengör and Yilmaz, 1981; Okay and Nikishin, 2015). However, it is accepted that the collision between the Pontides and the Anatolides-Taurides commenced in the Late Palaeocene-Early Eocene (Okay, 2008). The collision was followed by uplift and extensive erosion leading to a episode of sedimentation and

magmatism in the middle Eocene (Okay, 2008).

3.2.1. The late Cretaceous eastern Pontides magmatic arc

The Late Cretaceous magmatic arc in the eastern Pontides was developed during Turonian, (ca. 90 Ma; Robinson et al., 1995; Okay and Şahintürk, 1997). The magmatism appears to be episodic with early phase of extensive volcanism and sedimentation, later accompanied by relatively later phase of plutonism. Large number of volcanogenic massive sulfide (VMS) deposits, porphyry Cu-Mo, epithermal Au systems are associated with the early volcanic and subvolcanic and late plutonic associations, respectively in the eastern Pontides (e.g. Akıncı, 1984; Kuşcu et al., 2019). The volcanic rocks are clustered in two subparallel belts based on their geographic distribution in the eastern Pontides (Fig. 3.1. B); the northern and the southern volcanic belts.

The northern volcanic belt consists of basalt and basaltic andesite alternating with pyroclastic and volcanosedimentary rocks of Turonian-Lower Campanian age (Kandemir et al., 2019; Yılmaz et al., 2022). They display geochemical characteristics of volcanic arc lavas (Yılmaz et al., 1997; Çiftçi and Hagni, 2005; Eyüboğlu, 2010; Nikishin et al., 2013; Aydın et al., 2016). The southern volcanic belt is almost parallel to the northern one. This belt consists of several types of volcanic rocks including calc-alkaline basaltic lava, andesite-dacite lava and associated pyroclastic rocks. This belt is said to be formed during the Late Campanian-Maastrichtian (Eyuboglu et al., 2011). The andesitic lavas are the predomint rock type in the southern belt more prominent. Some adakite-like rock associations are also present in this belt ((Eyuboglu et al., 2011; Karslı et al., 2011).

The plutonic rock associations in the eastern Pontides form approximately E-W trending bodies of granitic plutons. They are formed by the multiple magma injections into the earlier volcanic-volcanosedimentary associations during the Late Cretaceous and middle Eocene (Yılmaz and Boztuğ, 1996; Kaygusuz and Aydınçakır, 2011). The plutonic rocks at the north are late Cretaceous in age (88-76 Ma; Boztuğ et al., 2004; Temizel and Kurt, 2019; Kuşcu et al., 2019). The plutonic rocks at the central part of the eastern Pontides consists of middle Eocene plutons

with ages clustering between (ca.44 and 39 Ma;Topuz et al., 2005; Karslı et al., 2011; Kuşcu et al., 2019).

3.3. Geology and Magmatic-Tectonic Evolution of the Artvin District

The geology of the Artvin district is shaped by successive events consisting of subduction, collision and post-collision. The subduction due to the closure of the NeoTethyan oceanic lithosphere was initiated during the Jurassic and continued towards the end of the Campanian. The subduction resulted in generation of arc magmatism accompanied by sedimentation (Kandemir et al., 2019; Aydın et al., 2020). According to Kandemir et al. (2019) and Aydın et al. (2020), the Cretaceous subduction-related arc magmatism in the Artvin district spanned between Turonian and late Campanian as a submarine volcanosedimentary sequence. In response to subduction, collision and post-collisional events, various magmatic suites were emplaced into heterogeneous pre-Jurassic basement and Jurassic to mid-Cretaceous volcanic and sedimentary sequences from Late Cretaceous to Middle Eocene (Fig. 3.2.). The volcanic, volcano-plutonic and volcanoclastic rock association in the Artvin district represent a segment of world famous Western Tethyan Metallogenic belt, and are associated with volcanogenic massive sulfide (VMS) deposits (Cu, Pb, Zn, ±Au), porphyry Cu and porphyry Cu-Mo and epithermal Au and epithermal Au-Ag-Pb-Zn deposits. The Hod maden, the study area, lies within the Artvin district, and comprises Jurassic and Cretaceous volcanosedimentary units. This study is focused on the Late Cretaceous arc sequences in the Hod Maden region.

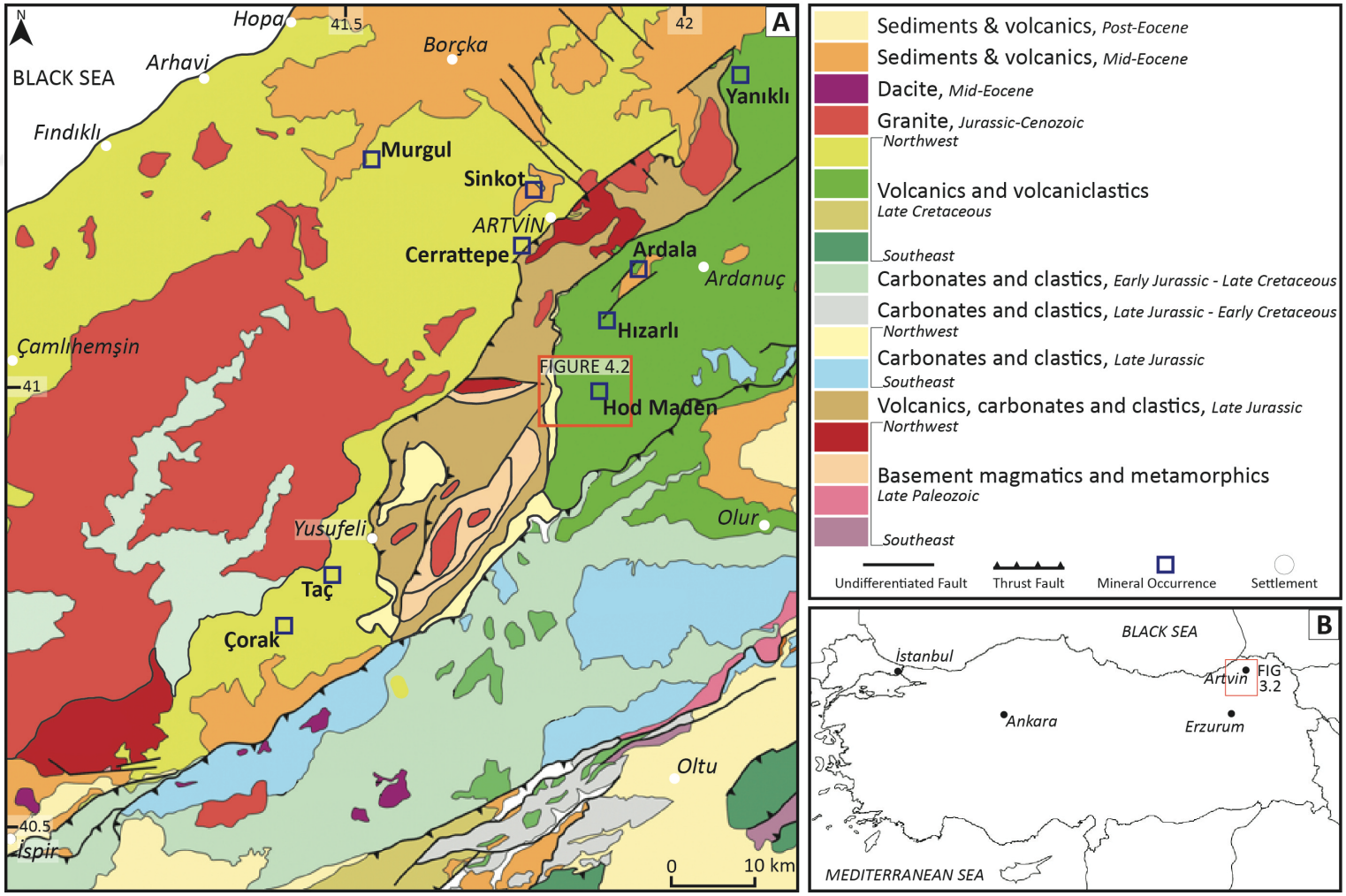


Figure 3.2. **Geological map of the Artvin district (1:500,000 scale; modified after (MTA, 2002; Ustaömer et al., 2013))**

4. GEOLOGY AND STRATIGRAPHY OF THE HOD REGION

If an observer were to view the Hod region from outer space, the most striking feature, visible after pushing aside the belts of white-grey clouds, would be the steeply dipping stratigraphy. This stratigraphic succession comprises (i) Liassic Berta Formation, (ii) Dogger Kırgülü Formation and (iii) Hızarlıdere Formation (Hızarlıdere volcanics), (iv) Malm-Lower Cretaceous Öğdem Formation and (v) İnanlı Limestone Member, (vi) Lower Cretaceous Aşağımaden Formation, (vii) Turonian Çatak Formation, (viii) Santonian Kızılkaya Formation and (ix) Santonian-Campanian Evliyatepe Formation. (Konak and Hakyemez, 2009) briefly explains the geology as follows: The initial succession, Liassic-Dogger in age, is composed of pelitic rocks and lava flows with pyroclastic interlayers. Conglomerates and sandstones, which overlie the volcanics unconformably, comprise limestone lenses. Upper Cretaceous volcanic rocks and volcanosedimentary units bearing limestone and mudstone interbeds are situated on the top of the succession. Here, we introduce the revised stratigraphy (Fig. 4.1.) and its correlation with the surrounding regions. In addition, we present a geological map (Fig. 4.2.) that illustrates the spatial distribution of structural elements and the following lithological units:

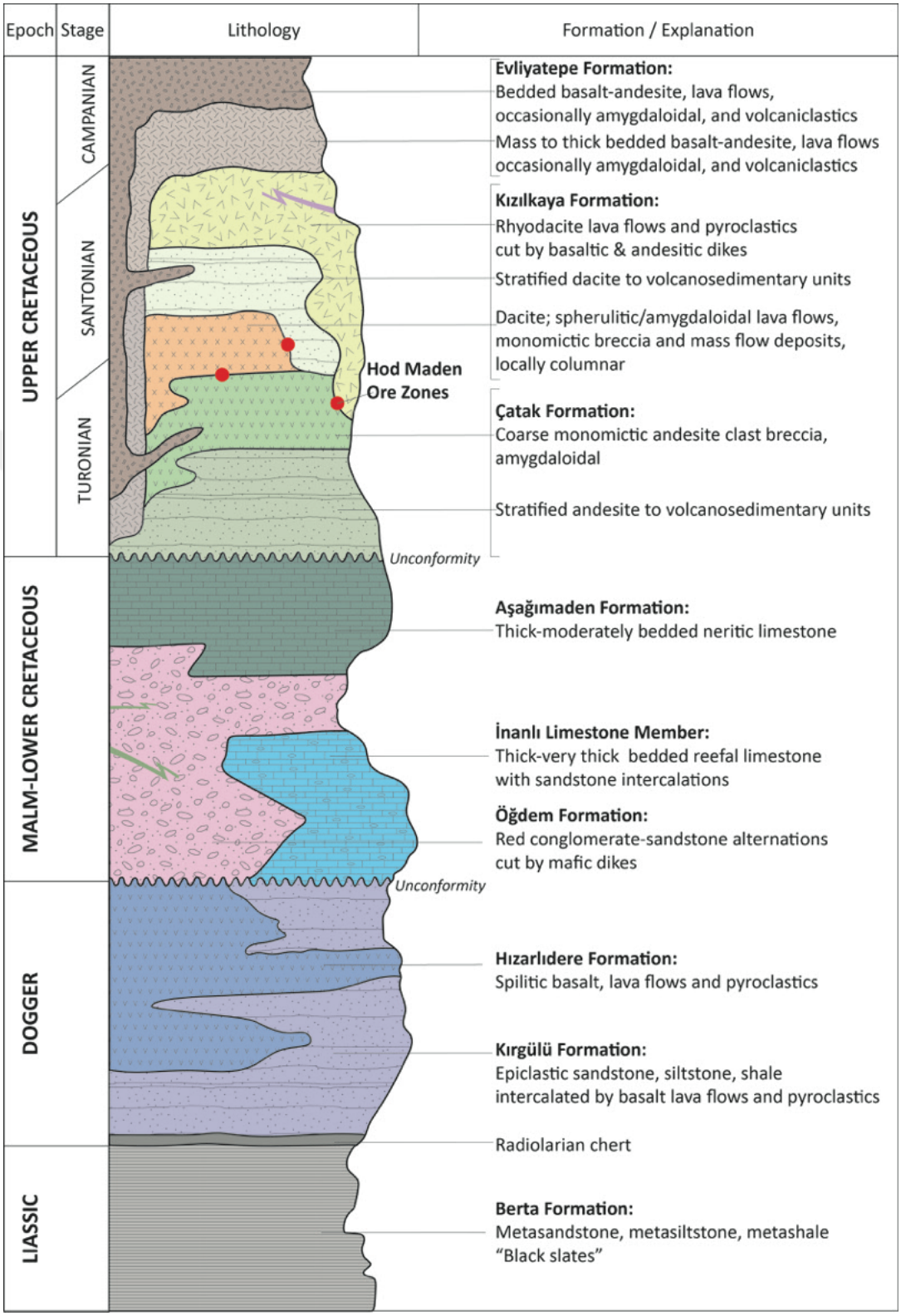


Figure 4.1. Generalized stratigraphic section of Hod region (modified after (Konak and Hakyemez, 2009; Kanar, 2016))

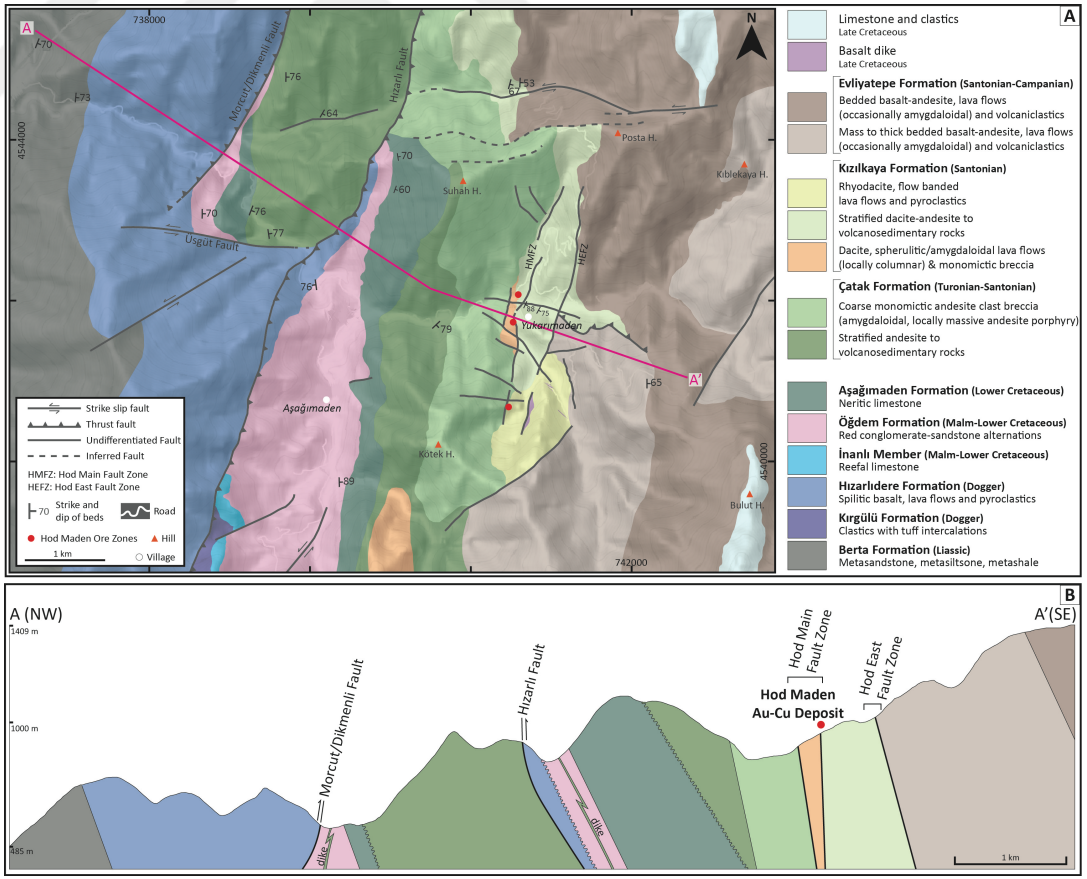


Figure 4.2. **Geological map of the Hod region and the schematic northwest-southeast cross section through Hod Maden Au-Cu deposit (modified after (Şatır and Ereren, 1976; Callan, 2013; Kanar, 2016; Bozkurt, 2017; Topal and Tezcan, 2018))**

4.1. Berta Formation

Konak et al. (2009) reports that the road cut reveals the steeply northeast dipping black slates (low degree metamorphics) intercalated with black siltstones and fine-grained black sandstones. It is observed that the sequence is strongly deformed by shear zones and by small scale folds. Despite the fact that basalt and andesites dominate the beginning of the road section, towards east most of the section consists of sedimentary rocks. According to Konak et al. (2009) they are representing an anoxic turbiditic series. In the most eastern part, red to green, medium bedded radiolarian cherts and siliceous mudstones overlie the greyish green siltstones and shale. Liassic age from mudstones and cherts in this section of the Berta formation were obtained based on radiolarian faunas (Soycan, 2017). The radiolarian cherts are overlain by the volcanic rocks which dominate the upper part of the Lower to Middle Jurassic sequence and named as Hızarlıdere Formation (or Hızarlıdere volcanics).

4.2. Kırgülü Formation

The formation is named after Kırgülü Village that is located south to the study area. Konak and Hakyemez (2009) reports that Kırgülü Formation is characterized by thin-moderately bedded, grey-green colored, turbiditic sandstone-siltstone alternations with intercalations of basaltic lava flow and pyroclastics formed in a submarine slope. Sandstones are moderately bedded, occasionally thick-bedded and formed by volcanic clasts. The unit comprises grey and red chert, and marn with chert intercalations as well as basalt, spilitic basalt and pyroclastics at the upper part. However, in the study area, the contact between Kırgülü Formation and Hızarlıdere volcanics is tectonic. The age of the unit is stated as Dogger or older based on radiolarian faunas and stratigraphic relationships (Konak and Hakyemez, 2009).

4.3. Hızarlıdere Formation (Hızarlıdere Volcanics)

The formation is named after Hızarlıdere Valley (where it is observed best) that is located north to the study area. The unit is mainly composed of mafic lava flows and pyroclastics and spilitic basalts. In addition, chert bands are present locally. Kanar (2016) reports that cherts are red, dark grey-blackish and forms thin bands (2-3 cm) within the lava flows. Greenish and brownish color indicates weak chlorite and iron-oxide alteration. It is also reported that in Hızarlıdere Valley, pillow basalts are observed with pillow sizes changing from 10-60 cm (Kanar, 2016). Presence of pillow basalts reveals that the volcanic activity occurred in submarine environment. Basalts display porphyritic texture (Fig. 4.3. A) with plagioclase and clinopyroxene phenocrysts. Konak et al. (2001) states that the volcanic rocks are calc-alkaline-tholeiitic in composition and the age of the unit is Liassic-Dogger. The unit is overlain by Öğdem Formation unconformably.

4.4. Öğdem Formation

Volcanic rocks of Hızarlıdere Formation are unconformably overlain by thickly bedded conglomerates which are red-crimson colored, thick bedded, poorly sorted and clast to matrix supported. Clasts are originated predominantly from basalts and andesites of Hızarlıdere Formation (Fig. 4.3. A). The unit is occasionally cut by mafic dikes and sills. The conglomerates are intercalated by sandstones and shales (Fig. 4.3. B) which are regarded to be formed in a shallow marine environment. Therefore, it is suggested that the Öğdem Formation was formed during a transition from a continental to a shallow marine environment during Malm-Early Cretaceous (Konak et al., 2009). Limestone bands and lenses are present in both the lower and upper parts of the Öğdem Formation. According to Konak and Hakyemez (2009), the reefal limestones in the lower and upper part of the Öğdem Formation are defined as the İnanlı Limestone Member, while the neritic limestones in the most upper part are referred to the Aşağımaden Formation.


A
B
C
D
qtz
chl rim
zeo, vrm, ca
E
jas, hm
qtz
black chl
green chl
andesite
breccia
cp, py
F
1 cm
ser
cp, py
dol
qtz
G
H
amph
bt
pl
qtz
I
Kızılkaya F.
HEFZ
Evliya
Tepe F.
J
qtz
chl, ep,
vrm, Mg-ill
K
chl rim
qtz core

Figure 4.3. Field photographs from Hod region: (A) Öğdem Formation, volcanic clast of Hızarlıdere Formation in the red conglomerate; (B) Öğdem Formation, steeply east dipping sandstone and shale levels; (C) Çatak Formation, well-stratified, volcanogenic, green-purple colored, carbonate-bearing claystone; (D) Çatak Formation, amygdaloidal andesite with quartz (qtz), chlorite (chl), zeolite (zeo), vermiculite (vrm) and carbonate (ca) amygdales; (E) intense chlorite altered andesite breccia hosting bands of black chlorite (chl), quartz (qtz), chalcopyrite (cp), pyrite (py), jasper (jas) and hematite (ht), HTD05-157m @ 88g/t Au and 2.46% Cu, 13m interval between 150-163m; (F) Kızılkaya Formation, spherulitic dacite with pervasive sericite alteration and spherules replaced by chalcopyrite (cp), pyrite (py), quartz (qtz), dolomite (dol); (G) Kızılkaya Formation, columnar dacite, notice the horizontal elongation of the columns; (H) dacite porphyry with large quartz (qtz) phenocrysts accompanied by plagioclase (pl), amphibole (amph) and biotite (bt); (I) northwest-looking view of volcanosedimentary sequence of Kızılkaya Formation in the west, Hod East Fault Zone (HEFZ) and Evliyatepe Formation in the east, notice the intense clay alteration along the HEFZ; (J) quartz (qtz), chlorite (chl), epidote (ep), vermiculite (vrm) and Mg-illite (Mg-ill) altered rhyodacite; (K) Evliyatepe Formation, amygdaloidal basalt, notice concentrically zoned chlorite (chl) at the rim and quartz (qtz) at the core of the amygdale.

4.5. Aşağımaden Formation

The formation is named after Aşağımaden Village which is located in the lower central part of the study area. It is almost vertically dipping towards east, moderate to thick bedded and is characterized by dark grey color. Occasionally, karstic features are present. (Kanar, 2016) and (Konak and Hakyemez, 2009) reports that Aşağımaden Formation is formed in beach-shelf environment during Early Cretaceous (Valanginian) based on the fauna. The unit overlies Öğdem Formation conformably and it is overlain by Çatak Formation unconformably.

4.6. Çatak Formation

The units forming the Çatak Formation are (i) stratified basalt, andesite and volcanosedimentary rocks overlying Aşağımaden Formation unconformably and (ii) amygdaloidal andesite porphyry and monomictic andesite clast breccia forming the western margin of Hod Maden mineralization. They define the onset of Late Cretaceous arc volcanism during Turonian-Santonian (Kandemir et al., 2019). Çatak formation overlies red conglomerates of Öğdem Formation and neritic limestones of Aşağımaden Formation, unconformably. (Kanar, 2016) reports that this

unconformity is transgressive and the unit is formed in continental to shallow marine environment. The succession starts with well-stratified, volcanogenic, green-purple colored (Fig. 4.3. C), carbonate-bearing claystone and basalt-andesite intercalations. As volcanic activity soars, the succession is dominated by basaltic and andesitic lava flows. The most significant characteristics of these rocks are amygdaloidal texture, chlorite and zeolite alteration accompanied by weak silicification and pervasive pyrite dissemination (Fig. 4.3. D). The unit is observed as monomictic andesite clast breccia towards east where the deformation and hydrothermal alteration intensity increases closer to Hod Main Fault Zone. High-grade gold and copper mineralization of Hod Maden deposit is hosted by jasper-hematite-bearing andesitic breccia with intense chlorite alteration (Fig. 4.3. E).

4.7. Kızılkaya Formation

Kızılkaya Formation overlies Çatak Formation conformably. The contacts between the volcanic rocks of Çatak Formation and Kızılkaya Formation are observed as either magmatic superimposition or as tectonic. It is characterized by felsic to intermediate subvolcanic intrusions, lava flows and pyroclastics. Stratified clastic volcanosedimentary rocks of dacitic origin with local limestone beds develop in the upper part of the sequence as volcanic activity ceases. The volcanic rocks of Kızılkaya Formation in the study area comprise (i) spherulitic/amygdaloidal dacite lava flows (Fig. 4.3. F), as well as monomictic dacite breccia and mass flow deposits; (ii) columnar dacite (Fig. 4.3. G); (iii) well-stratified dacite to volcanosedimentary units with local limestone beds; and (iv) flow-banded (locally spherulitic) rhyodacitic lava flows and pyroclastics.

4.7.1. Spherulitic dacite flows and breccia

The unit is exposed to the surface in between andesite breccia unit of Çatak Formation and stratified dacite to volcanosedimentary unit of Kızılkaya Formation. It hosts the high-grade gold-copper mineralization. Spherulitic texture is significant

as it represents quenching of dacitic lava flow due to sea-water interaction and formation of very thin radiating arrays of K-feldspar and plagioclase. The feldspars are either altered into sericite or replaced completely by hydrothermal quartz, carbonates and sulfides (Fig. 4.3. F). The present hydrothermal alteration associations consists of sericite (fine-grained muscovite, K- illite), clay minerals (dickite, kaolinite, halloysite, montmorillonite) and late calcite, dolomite and anhydrite overprint.

4.7.2. Columnar jointed dacitic lava flows and pyroclastic rocks

The unit is exposed in the southern part of the study area. Columnar dacites are considered to be formed either at a subaerial part of the Late Cretaceous sea environment, or at an active feeder zone in a submarine setting. Cooling surfaces of the dacite columns are near vertical and they are parallel to the stratification of volcanic and sedimentary sequences in the region (Fig. 4.3. G). Dacites display porphyritic texture with large quartz phenocrysts and plagioclases and mafic minerals (biotite, amphibole; Fig. 4.3. H). Sericitization on plagioclase phenocrysts and weak chlorite alteration on mafic minerals and groundmass are present.

4.7.3. Well-stratified dacite to volcanosedimentary rocks

Volcanosedimentary rocks with local limestone beds are exposed in the central part of the Late Cretaceous succession (Fig. 4.3. I). The unit is characterized by volcanic siltstones and sandstones (Fig. 5A), fine to coarse-grained lithic fragment-bearing and crystal-rich tuffs and dacitic lava flows. Dacitic lava flows display porphyritic and trachytic texture, embayment in quartz phenocrysts and sieve texture in plagioclase phenocrysts (Fig. 4.4. B). Selective sericite alteration on plagioclase and pervasive chlorite alteration on the groundmass are present. Thin limestone horizons locally occur in the sequence. (Şatır and Ereren, 1976) reports the inoceramus-bearing limestone bed in the succession along the Belizor stream indicating Late Cretaceous formation of this sequence. This volcanosedimentary unit is bounded by Hod Main Fault Zone in the west and Hod East Fault Zone in the

east. Therefore, the rocks are deformed and altered intensely. The volcanosedimentary rocks are the main host for the stratabound zinc mineralization.

4.7.4. Rhyodacite dome

Flow-banded rhyodacite with local auto-breccia facies forms a dome morphology. It is characterized by quartz phenocrysts and greenish color groundmass due to the chlorite, vermiculite and Mg-illite alteration (Fig. 4.3. J). The dome appears to intrude the stratified volcanosedimentary rocks and the andesite breccia in the west. The contact between the andesite breccia is an ore zone with significant copper, zinc and gold mineralization characterized by quartz-chalcopyrite-sphalerite-pyrite veins with accompanied chlorite (andesitic host), sericite (rhyodacite host), quartz, epidote, calcite and rhodochrosite alteration. In the northwestern flank of the dome, auto-breccia facies and pyroclastic products of rhyodacite volcanism are observed. Several andesitic to basaltic dikes cut the rhyodacite dome. They are characterized by relatively fresh euhedral pyroxene phenocrysts and pervasive sericite and carbonate alteration on plagioclase phenocrysts and on the groundmass (Fig. 4.4. D).

4.8. Evliyatepe Formation

The formation is named after Evliya Hill, located to the southeast of the study area. Precise age relations with the adjacent rhyodacite dome and volcanosedimentary stratigraphy are poorly constrained due to tectonic contacts and intense hydrothermal alteration along the East Fault Zone (EFZ) (Fig. 4.3. I). The unit is characterized by basaltic to andesitic lava flows and volcaniclastics. Amygdaloidal texture is significant on lavas as the vugs are occupied by chlorite, quartz, vermiculite, zeolites and carbonates (Fig. 4.3. K, Fig. 4.4. C). Plagioclase phenocrysts of lavas often display sieve texture and occasionally overprinted by sericite. Mafic phenocrysts such as pyroxene and amphibole, on the other hand, are either relatively fresh or completely overprinted by secondary minerals (Fig. 4.4. E).

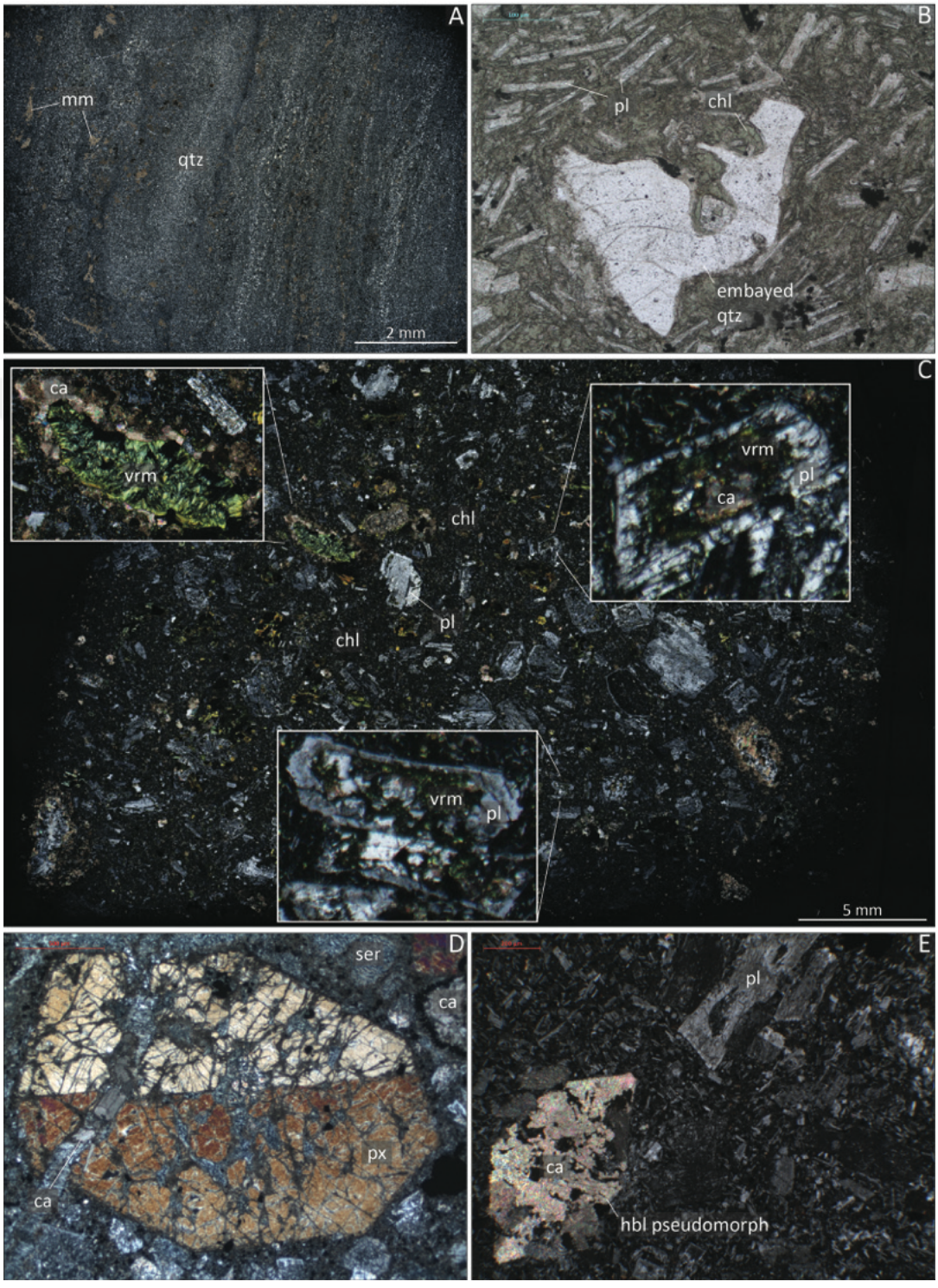

A
mm
qtz
2 mm
B
pl
chl
embayed
qtz
C
ca
vrm
chl
vrm
pl
ca
pl
chl
vrm
pl
5 mm
D
ser
ca
px
ca
E
pl
ca
hbl pseudomorph

Figure 4.4. Thin section photomicrographs of selected lithologies from Hod region: (A) pervasively silicified (qtz) and montmorillonite (mm) altered volcaniclastic rock (dacitic composition) of Kızılkaya Formation; (B) dacite from the volcanosedimentary sequence of Kızılkaya Formation, displaying trachytic texture –plagioclases (pl) forming flow lines- and embayment in quartz (qtz), notice the chlorite (chl) alteration in the groundmass, C) amygdaloidal chlorite (chl) altered basalt from Evliyatepe Formation, notice that vermiculite (vrm) and calcite (ca) fills the amygdales and occupy the cores of plagioclases (pl) displaying sieve texture; D) Euhedral pyroxene (px) of a basaltic dike displaying sericite (ser) and calcite (ca) alteration; E) pseudomorphic calcite (ca) after hornblende (hbl), and plagioclase (pl) from an andesitic rock of Evliyatepe Formation.

(Konak and Hakyemez, 2009) reports this unit as spilitic basalt lava flows and agglomerate with an age of Santonian-Campanian.

5. VOLCANIC ROCK TEXTURES IN HOD MADEN DEPOSIT

The dedicated chapter on textures of volcanic rocks in the Hod Maden deposit serves to characterize both the volcanic rocks hosting high-grade gold and copper mineralization (additional zinc-rich zones) and barren volcanic rocks. This investigation of volcanic textures further allows for the interpretation of the volcanic environment and geological processes during the formation of these rocks.

The initial step involved conducting field observations on volcanic rock outcrops, where the lithological boundaries between different units were examined. Hand samples were collected and described, and the presence of phenocrysts was identified if present. Hydrothermal alteration minerals were also documented. Subsequently, drill cores were logged to investigate the changes that occurred at deeper levels. The presence of specific textures and alteration assemblages was compared with the varying grades of gold, copper, and zinc. Finally, representative samples were selected for petrographic analysis. This involved examining both the textures of the volcanic rocks and the features of hydrothermal alteration. As a result, the spatial and temporal relationship between volcanic rocks exhibiting distinct textures and specific alteration phases was determined.

The volcanic textures and lithofacies characteristics of the host volcanic rocks (Table 5.1) including (i) spherulitic texture, replacements of radiating fibers of crystals by later sericite and sulfides; (ii) hyaloclastites or false vitriclastic textures (hydraulic fragmentation of quenched lava flows); (iii) amygdaloidal texture, infilling of vugs and replacement of lithic clasts by chlorite, quartz, carbonates and zeolites; (iv) subaqueous mass flow deposits with dacitic lithic clasts and sulfide clasts; (v) presence of “tetsusekiei” (or jasper-hematite); and hydrothermal alteration features such as spatial zonation of Fe-rich chlorites and zeolites, and the late anhydrite phase overprinting gold-copper mineralization provide a better understanding toward the formation of seafloor/subseafloor hydrothermal alteration and mineralization.

Table 5.1. Characteristics of facies in Hod Maden Deposit

Formation	Facies	Lithofacies Characterization / Textures	Mineralogy/Components	Alteration	Interpretation
Çatak	andesite	amygdaloidal	jasper, phenocrysts and clasts	chlorite-rich	coherent facies of lavas, hyaloclastite and autobreccia
Kızılkaya	dacite	spherulitic, densely microspherulitic, monomictic breccia	phenocrysts and clasts	sericite-rich	cryptodome, synvolcanic sills
Kızılkaya	dacite	columnar joints	phenocrysts	fresh, weakly altered	synvolcanic intrusion, submarine feeder tube?
Kızılkaya	volcanosedimentary rocks	graded, stratified	dacite and sulfide clasts	sericite-rich	mass-flow deposits
Kızılkaya	rhyodacite	flow-banded	phenocrysts, clasts	pervasive silicification	coherent facies of lavas, dome, blocky flow banded ryhodacite breccia
Evliyatepe	andesite and basalt	amygdaloidal, glomeroporphyritic	phenocrysts	chlorite-rich	coherent facies of lavas
Evliyatepe	basalt	columnar joints	plagioclase phenocrysts	weak alteration	synvolcanic intrusion, submarine feeder tube?
Evliyatepe?	basalt	dike	olivine, pyroxene and plagioclase phenocrysts	late calcite overprint	dike

5.1. Spherulitic Texture

Spherulites are clusters of needle-like or acicular crystal fibers that emanate from a central point, typically exhibiting a spherical shape (although rarely perfectly spherical). The presence of spherulitic texture is indicative of the former presence of glass and, indirectly, the rapid cooling of lava (quenching). In Hod Maden deposit, spherulites are interpreted to be formed as a result of the abrupt temperature decrease due to the subaquous/subseafloor interaction of glassy dacitic lavas and sea water.

When spherulites are examined under crossed polarized light (XPL), an ”extinction cross” is frequently observed. This phenomenon occurs due to the different optical vibration orientations of the individual crystal fibers within the spherulite. These crystal fibers, primarily composed of feldspars and quartz, can be replaced by secondary minerals like sericite through hydrothermal alteration processes, while the characteristic ”extinction cross” feature remains intact (Fig. 5.1).

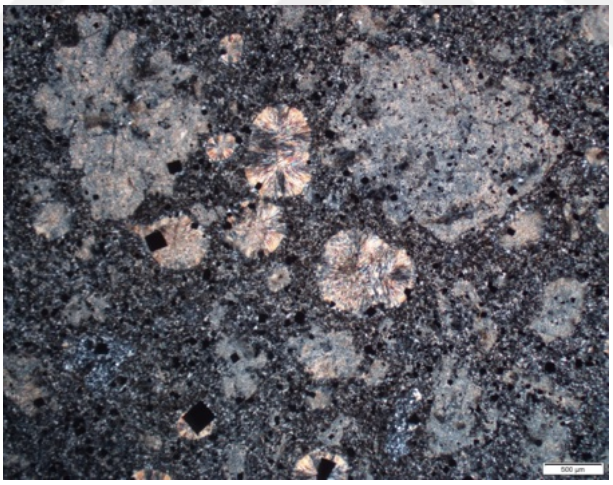


Figure 5.1. Photomicrograph of diagnostic extinction crosses observed in the spherulites replaced by sericite, XPL; Main Zone, EB232, HTD018-253.5m

In Hod Maden deposit, spherulitc texture is observed in dacitic lava flows and monomictic dacite breccia (with clasts displaying spherulitic texture) both in Main Zone and South Zone. They are identified as spherulitic texture right away during drill core logging as they display near-perfect spherical shape (Fig. 5.2 A, B). Spherulites are assumed to be formed with feldspar and quartz reflecting felsic to indermediate composition of the dacitic lavas and later replaced by sericite (K-illite

and/or fine-grained muscovite), quartz, dolomite and sulfides including pyrite, chalcopyrite and sphalerite. In South Zone, spherulites are often replaced by sphalerite and dolomite (Fig. 5.2 C,D) whereas in Main Zone, sericite accompanied by cubic pyrite dissemination predominate the spherulites (Fig. 5.2 E).

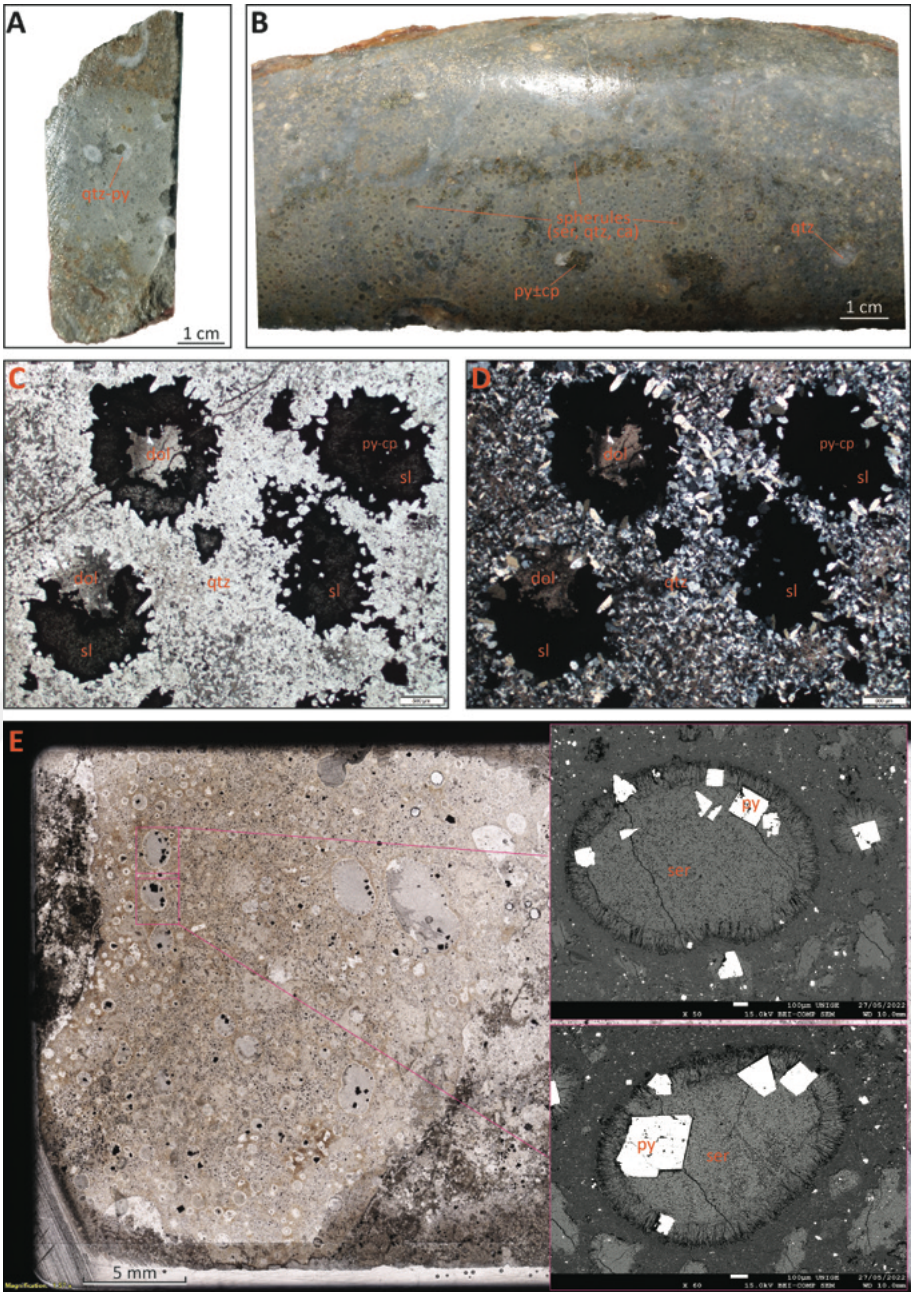


Figure 5.2. Representative examples from drill core samples, photomicrographs and SEM images of samples displaying spherulitic texture. (A) Main Zone, HTD029-370.5m, dacite breccia with spherulite-bearing clasts; (B) South Zone, EB070, HTD021-6.5m, dacite breccia with spherulitic texture and pervasive sericite alteration, (C) and (D) South Zone, EB124, HTD021-215.9m, spherulites replaced by sphalerite, pyrite, chalcopyrite, dolomite and quartz in PPL and XPL, respectively; (E) Main Zone, EB232, HTD018-253.5m, dacite breccia with spherulites replaced by sericite and pyrite, PPL and SEM images. Abbreviations: qtz: quartz, py: pyrite, ser: sericite, ca: carbonate, cp: chalcopyrite, sl: sphalerite, dol: dolomite.

5.2. Hyaloclastites

The term ”hyaloclastite” is employed to describe clastic aggregates resulting from the non-explosive fracturing and disintegration of rapidly cooled lavas and intrusions (cf. Rittmann, 1962; Silvestri, 1963; Pichler, 1965; Honnorez and Kirst, 1975; Yamagishi, 1987). This term encompasses both unconsolidated clastic aggregates and their lithified counterparts. The fragmentation process occurs due to thermal stress accumulated during rapid cooling and the strain imposed by the brittle outer portions of lava flows and intrusions as the more ductile interior continues to deform (Pichler, 1965; Kokelaar, 1986). Hyaloclastite can form from magmas spanning a wide compositional range, from basalt to rhyolite. Our current understanding of quench fragmentation processes primarily stems from investigations of ancient submarine volcanic sequences, supplemented in recent times by the observation and sampling of hyaloclastite on modern ocean floors (McPhie et al., 1993).

Glass shards may be an important component of autoclastic deposits, especially hyaloclastite. Shards generated by quench fragmentation have blocky, cuneiform or splintery shapes, and surfaces are planar or curviplanar (McPhie et al., 1993; Fig. 5.3 A,C). Hyaloclastite shards are typically non-vesicular or poorly vesicular, and shard surfaces cut across vesicles.

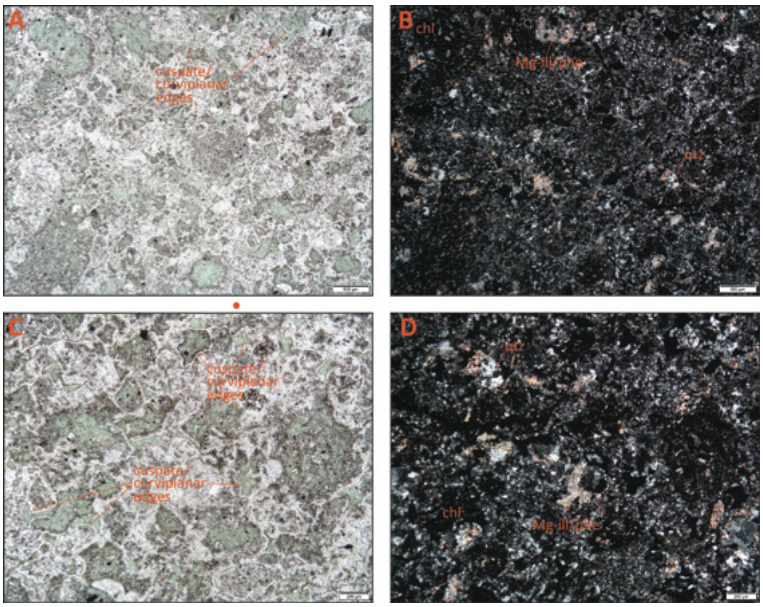


Figure 5.3. Photomicrographs of hyaloclastites observed in Main Zone, EB193, HTD029-487.2m. Notice the cuspate shape or curviplanar edges of andesite clasts and glass shards. Abbreviations: chl: chlorite, Mg-ill: Mg-illite, qtz: quartz, phe: phengite

5.3. Amygdaloidal Texture

Volatiles released from lavas and shallow intrusions gather in bubbles known as vesicles, which can become permanently trapped and preserved upon solidification. Amygdales represent former vesicles that have been partly or fully filled with secondary minerals. The term originates from the Latin word ”amygdala,” meaning almond, which describes the typical shape of a filled vesicle. The shape and size of amygdales can range from rounded to elongated and from a few millimeters to several centimeters. Rocks containing amygdales are referred to as amygdaloidal. Typically, amygdales form after the rock has been emplaced and are often associated with low-temperature alteration processes. They frequently exhibit concentric zoning (McPhie et al., 1993). In Hod Maden, andesitic to basaltic lavas emplaced both in the stratigraphic footwall (Çatak Formation) and stratigraphic hangingwall (Evliyatepe Formation) display amygdaloidal texture.

In the Main Zone, the andesitic lavas and breccias exhibit a distinctive amygdaloidal texture characterized by concentric zonation. In sample EB043 (Fig. 5.4 A), which represents the andesite breccia of the Çatak Formation, the amygdales display concentric zoning and contain chlorite and quartz, accompanied by disseminated pyrite (Fig. 5.4 B,C). Whereas, in sample EB178 (Fig. 5.4 D), representing andesite porphyry of Çatak Formation, the amygdales exhibit a wider variety of hydrothermal alteration minerals. The concentric zoning in this case can consist of chlorite-quartz-epidote-calcite (Fig. 5.4 F,G), chlorite-sericite (Fig. 5.4 H,I), or chlorite-quartz (Fig. 5.4 H,I).

Andesitic to basaltic volcanic rocks (plagioclase porphyry) of Evliyatepe Formation in the stratigraphic hangingwall display amygdaloidal texture with concentric zoning of calcite and chlorite (Fig. 5.4 A,B,C). In other outcrops, andesitic-basaltic lavas are observed to exhibit concentrically zoned amygdales with chlorite-quartz, quartz-chlorite or quartz-chlorite-quartz.

A notable observation is the presence of extinction crosses within chlorite-filled amygdales (Fig. 5.4 C). These crosses are interpreted to form subsequent to the development of ”varioles,” which are radial or sheaf-like clusters of plagioclase and pyroxene. These structures resemble spherulites but are limited to mafic volcanic

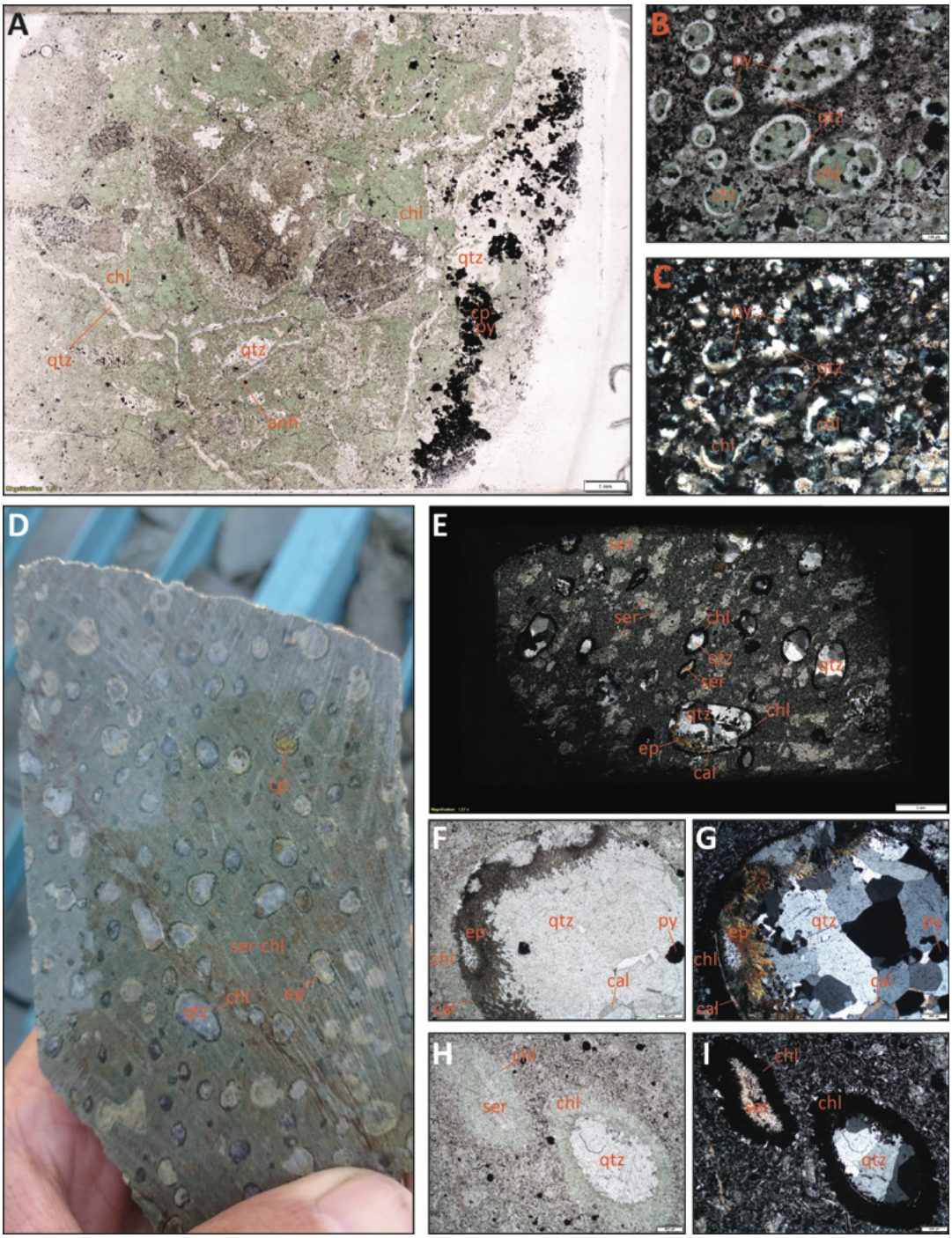


Figure 5.4. **Examples from Main Zone samples displaying amygdaloidal texture. (A) EB043, HTD090-299.9m, full thin section scan under PPL; (B) in PPL and (C) in XPL of sample EB043, concentrically zoned quartz and chlorite amygdales; (D) EB178, HTD029-71.8m, drill core sample with concentrically zoned chlorite, quartz, epidote and sericite amygdales; (E) EB178, full thin section scan in XPL; (F) in PPL and (G) in XPL photomicrograph of an amygdale filled by chlorite, quartz, epidote and calcite; (H) in PPL and (G) in XPL photomicrograph of amygdales with concentric zonation of chlorite-sericite and chlorite-quartz. Abbreviations: qtz: quartz, chl: chlorite, anh: anhydrite, py: pyrite, cp: chalcopyrite, ser: sericite, cal: calcite, ep: epidote**

facies (Fowler et al., 1987).

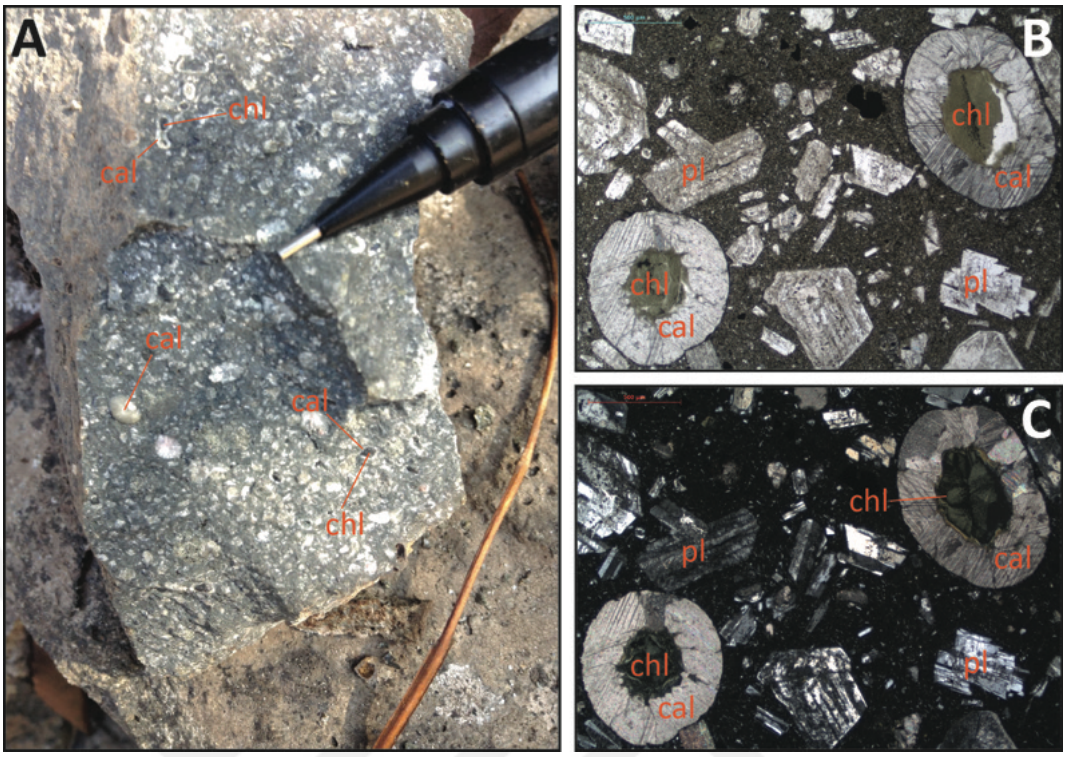


Figure 5.5. **Representative amygdaloidal plagioclase porphyry, sample EB022, from Evliyatepe Formation displaying concentic zonation of calcite-chlorite; (A) Hand sample, (B) Photomicrograph in PPL and (C) Photomicrograph in XPL. Abbreviations: qtz: quartz, chl: chlorite, cal: calcite, ep: epidote, pl: plagioclase**

5.4. Subaqueous Volcaniclastic Mass-Flow Deposits

The significance of examining clast populations within mass-flow deposits becomes evident when considering the presence of clasts originating from massive sulfide deposits. Such occurrences are frequently observed in submarine volcaniclastic mass-flow deposits within sequences hosting massive sulfide mineralization, as exemplified by Mount Read Volcanics, western Tasmania (Fig. 5.6 A, McPhie et al., 1993) and this study (Fig. 5.6 B). These clasts are interpreted to be originated from the massive sulfide deposit at the source of the mass flow (as illustrated in Fig. 5.6). The distance of transportation depends on the clast size and the characteristics of the host mass flow.

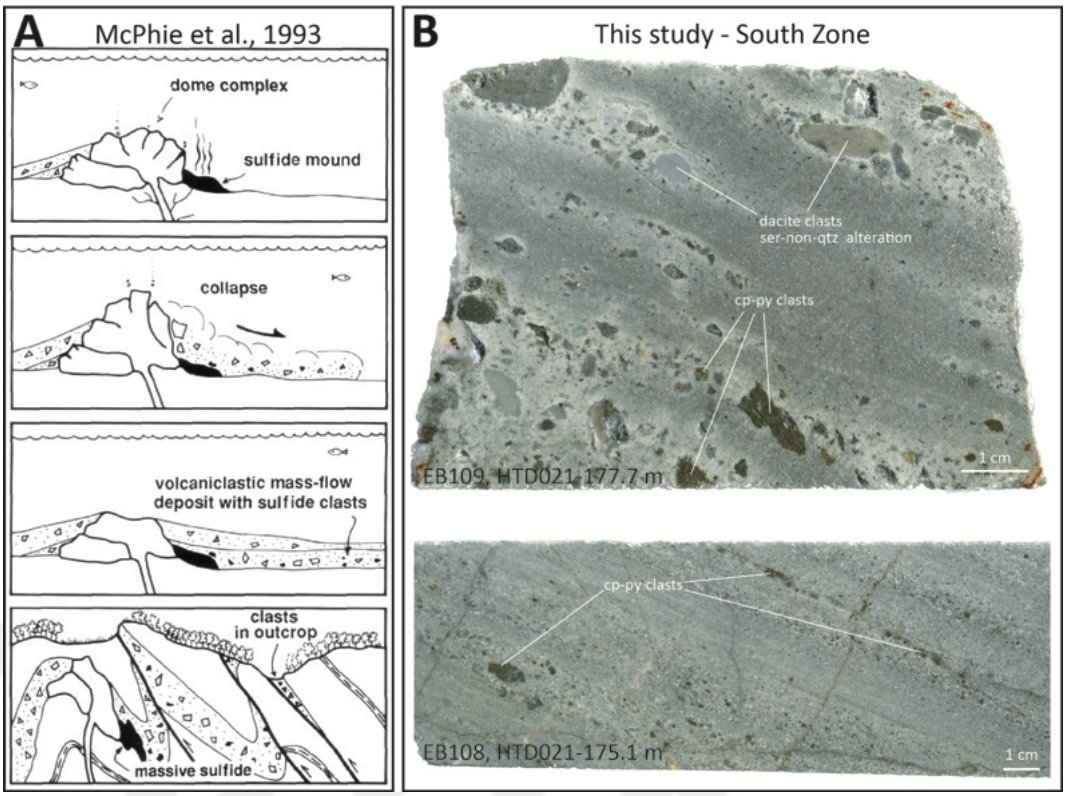


Figure 5.6. **(A) An illustration depicting a speculative interpretation of the origin of massive sulfide clasts in a submarine volcaniclastic mass-flow deposit in the Mount Read Volcanics, western Tasmania (McPhie et al., 1993); (B) Drill core samples showing submarine volcaniclastic mass-flow deposit with chalcopyrite and pyrite clasts in the South Zone mineralization of Hod Maden deposit. Notice the pervasive sericite and nontronite alteration accompanied by quartz alteration. Abbreviations: py: pyrite, cp: chalcopyrite, ser: sericite, non: nontronite, qtz: quartz**

5.5. Presence of Jasper-Hematite

Jasper-hematite (hematitic chert, tetsusekiei) formations are significant horizons or zones found in various volcanogenic massive sulfide (VMS) districts worldwide. These units often serve as key indicators of mineralization and can be located stratigraphically above, below, within, or along the strike of orebodies (Galley et al., 2007; Hollis et al., 2015). Examples include the Fukuzawa Mine in Japan (Kalogeropoulos and Scott, 1983; Tsutsumi and Ohmoto, 1983), the Abitibi greenstone belt in Canada (Genna et al., 2014), the Iberian pyrite belt (Leistel et al., 1997), the Urals (Herrington et al., 2005; Maslennikov et al., 2012), and the Bathurst Mining Camp in Canada (Peter and Goodfellow, 1996).

Jasper-hematites in the Hod Maden deposit are the result of the replacement of glassy

lavas below or at the seafloor. These formations are found in the andesitic lava flows and andesite breccias of the Çatak Formation. Their reddish to orangish color is due to the presence of finely dispersed hematite (cryptocrystalline hematite embedded in a silica matrix). Jasper-hematites are observed as patches (Fig. 5.7 A,B), veins (Fig. 5.7 C) and infillings between interstitial spaces in the pillow-like structures of the andesite breccia (Fig. 5.7 D).

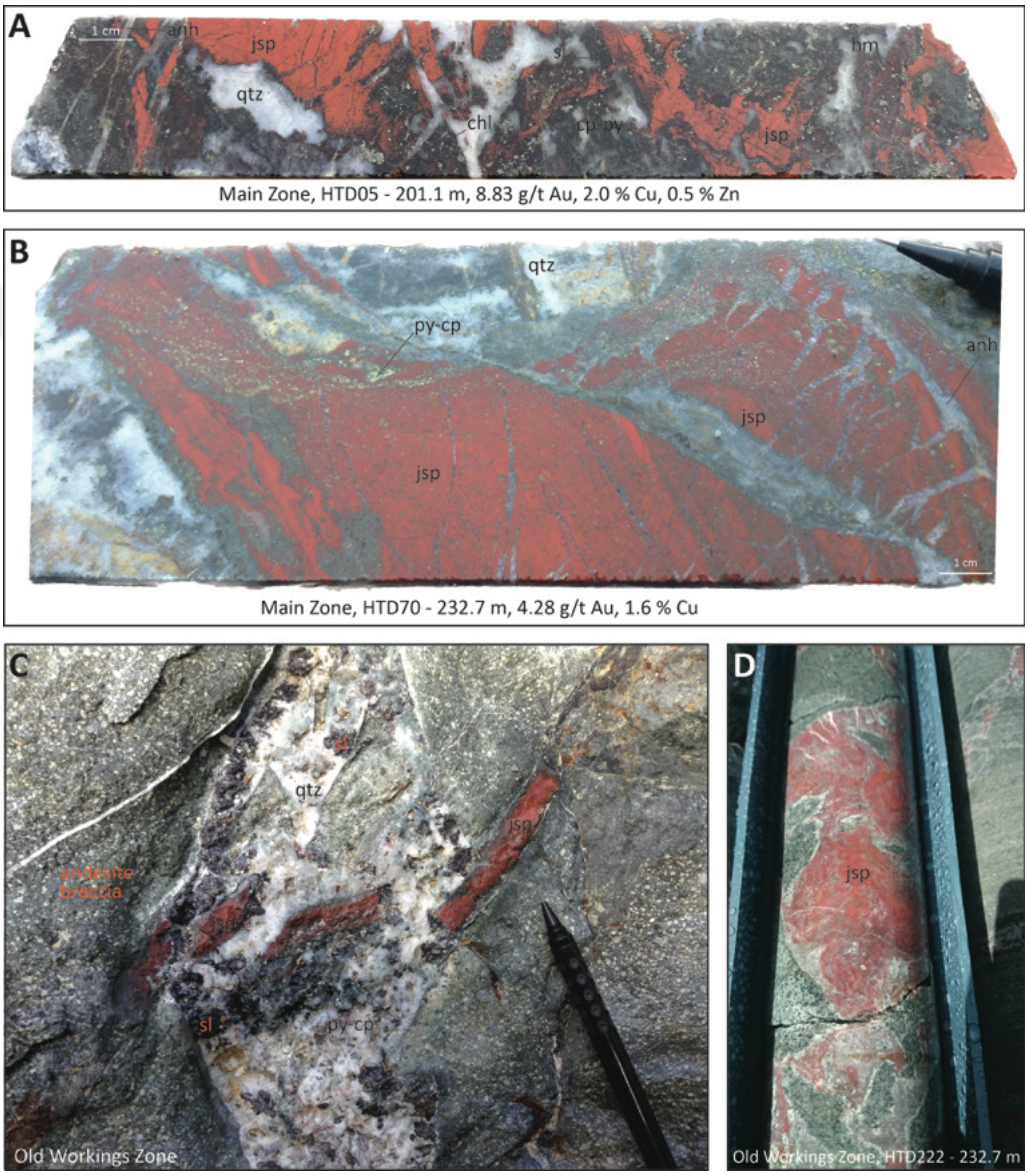


Figure 5.7. Representative examples with jasper-hematite. (A) Drill core sample with patches of jasper-hematite accomapiend by quartz, black chlorite, chalcopyrite, pyrite and sphalerite with late anhydrite veinlets. (B) Drill core sample with jasper-hematite hosting sulfides and cut by late anhydrite veinlets. (C) Outcrop photo of andesite breccia with vein-type jasper-hematite. It is cut by a quartz-sphalerite-chalcopyrite-pyrite vein. (D) Drill core sample with jasper-hematite occupying the interstital spaces in the pillow-like structures of andesite breccia. Abbreviations: jsp: jasper-hematite, py: pyrite, cp: chalcopyrite, sl: sphalerite, qtz: quartz, chl: chlorite, hm: hematite, anh: anhydrite

6. HYDROTHERMAL ALTERATION

The petrographic examination of the submarine volcanic host rocks reveals the characteristics of the hydrothermal alteration identified in the Hod maden deposit. The examination of spatial patterns of alterations across the deposit has been conducted despite the intricate overlapping relationships among hydrothermal alteration minerals. Furthermore, the main focus was on investigating the temporal relationships between the submarine volcanic activity, phases of alteration, the mineralization event, and subsequent late overprinting events. Hence, cross sections showing lithologies, ore zones and associated hydrothermal alterations were prepared for each mineralization zone in the deposit including the main, south and Russian galleries. These cross sections also include the traces of drill holes with sample locations on which petrographic analyses have been conducted. Each sample was studied in detail to construct the temporal relationships between the phases of the hydrothermal alteration. The hydrothermal alteration in each ore zone exhibits distinct chemical and textural characteristics. Therefore, the composition and spatial distribution of alteration assemblages were described in relation to the specific ore zones they are associated with. Furthermore, the temporal evolution of hydrothermal alteration phases within each ore zone will be discussed.

In addition to the petrographic characteristics of the alterations, whole rock geochemistry of altered volcanic host rocks were also presented to better understand the geochemical composition and extent of hydrothermal alteration. Assessing the geochemical characteristics of hydrothermal alteration is valuable because these alteration patterns often cover a larger area than the actual ore deposit and can be difficult to detect. By calculating geochemical alteration indices and molar element ratios based on major element data as well as taking paragenetic sequence of hydrothermal alteration assemblages, the geochemical signature and temporal evolution of hydrothermal alteration was evaluated at the Hod Maden deposit.

6.1. Hydrothermal Alteration at Main Zone

Hydrothermal alteration at the Main Zone is not clearly visible due to the an overburden and dense vegetation. Therefore, it was studied through samples from 3 drill holes (HTD018, HTD029 and HTD090) targeting the high-grade Au-Cu mineralization and accompanying Zn-rich zones. Petrographic examination of these samples enabled the construction of a geologic cross section showing the spatial distribution of the host submarine volcanic rocks, Au, Cu and Zn ore zones and associated hydrothermal alteration assemblages (Fig. 6.1). Each sample for petrographic analysis reports the available hydrothermal alteration assemblages and their temporal association with respect to each other. The alterations in the main zone are hosted by andesite breccia, dacite breccia and volcanosedimentary rocks. The hydrothermal alteration assemblages associated with the Main Zone mineralization form two groups as early and late phases of alteration. The early phase includes (i) early chlorite-rich (chlorite1) alteration on andesite breccia and (ii) early sericite-rich (sericite1) alteration on dacite; overprinted by late phases including (iv) mineralization phase (syn-mineral) chlorite (chlorite2) and quartz2 alteration; (v) sericite2 alteration; (vi) clay and Fe-oxide alteration accompanied by quartz3; (vii) quartz4 and carbonate alteration and (viii) late overprinting anhydrite and calcite alterations.

6.1.1. Early chlorite-rich alteration

The earliest hydrothermal alteration phase observed on andesitic rocks in the Main Zone is characterized by the presence of fine-grained chlorite (chlorite1), zeolites (mostly chabazite, laumontite), and fine-grained quartz (quartz1). Field observations indicate that the chlorites have a light green color and possess a fine-grained texture. The chlorite1 alteration is commonly observed in andesitic rocks that exhibit submarine volcanic textures, including hyaloclastites and amygdaloidal textures. This chlorite1 alteration is widespread and affects the original volcanic texture of the host rocks, which can still be observed (Fig. 6.2 A-E). Alongside chlorite1, quartz1 is also commonly found in this pervasive alteration assemblage.

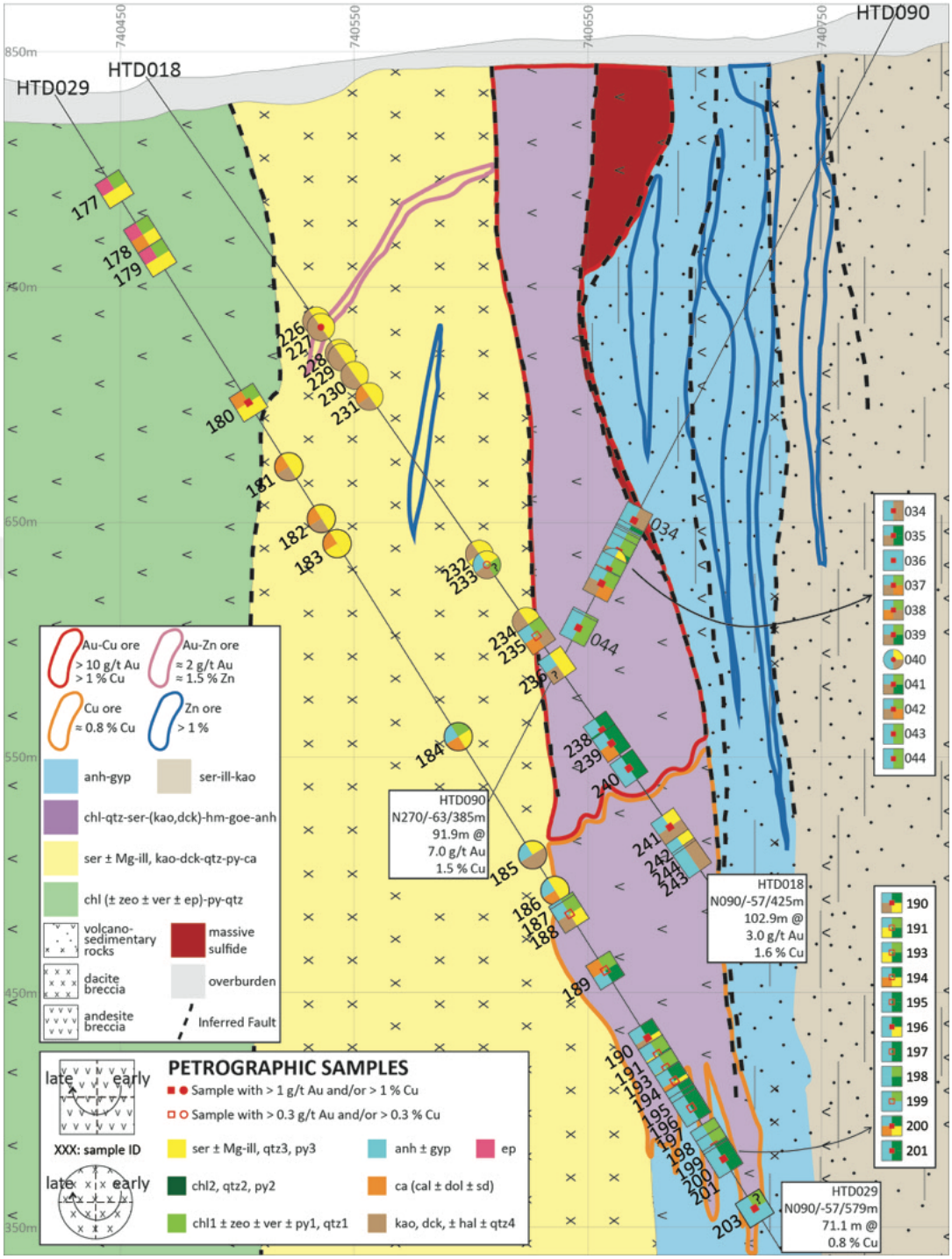


Figure 6.1. A cross section across the Main Zone showing the spatial distribution of lithological units, Au, Cu and Zn ore zones and associated hydrothermal alteration assemblages. Notice the each petrographic sample indicates the present hydrothermal alterations and their temporal evolution from early to late phases.

Disseminated pyrite is also frequently present (Fig. 6.2. C). The alteration can be easily identified in the field by the green coloration of the altered rocks and the distinct light green color visible under plane polarized light (PPL) when examining thin sections using a polarized microscope (Fig. 6.2 F,H). When viewed under cross

polarized light (XPL), chlorites exhibit colors ranging from dark brown and dark blue to dark violet (Fig. 6.2 G,I).

6.1.2. Early sericite-rich alteration

Early sericite-rich alteration assemblage is characterized by pervasive sericite (sericite1) characterized by fine-grained muscovite and K-illite, pervasive fine-grained quartz (quartz1) and pyrite (pyrite1) dissemination. This assemblage was formed spatially associated with dacite. In hand sample, this alteration is observed in light grey to light yellow in color. If dacite is observed as a subvolcanic intrusion then sericite1 is observed as replacing the phenocrysts and groundmass while quartz1 accompanies sericite1 on the groundmass (Fig. 6.3. A). However, as the dacite is present mostly as monomictic matrix-supported dacite breccia, the early sericite-rich alteration assemblage alters both dacite clasts and the groundmass. Occasionally, the dacite breccia clasts display original submarine volcanic textures of dacite including spherulitic texture and sericite1 can be observed as replacements of radiating crystal fibers of former feldspars forming spherulitic texture (Fig. 6.3. B).

6.1.3. Chlorite2 and quartz2 alteration

Drill core logging, geochemical analyses and petrographic examination of gold and copper-rich intervals/ore zones reveal that there is a spatial and temporal association between chlorite2-quartz2 alteration and high-grade Au-Cu mineralization. Therefore, an additional effort was made to clarify this association via detailed petrography. Drill core investigation of host andesitic rocks with a naked eye or with a hand lens suggests that early chlorite1 alteration associated with andesite breccia is light green in color and fine grained while chlorite2 associated high grade Cu-Au mineralization is black to dark green in color (logged as ”black chlorites”) and coarser-grained (Fig. 6.4).

The notable distinction between chlorite1 and chlorite2 is evident in thin sections. Chlorite1 is fine-grained, while chlorite2 is coarser and exhibits flaky texture (Fig.

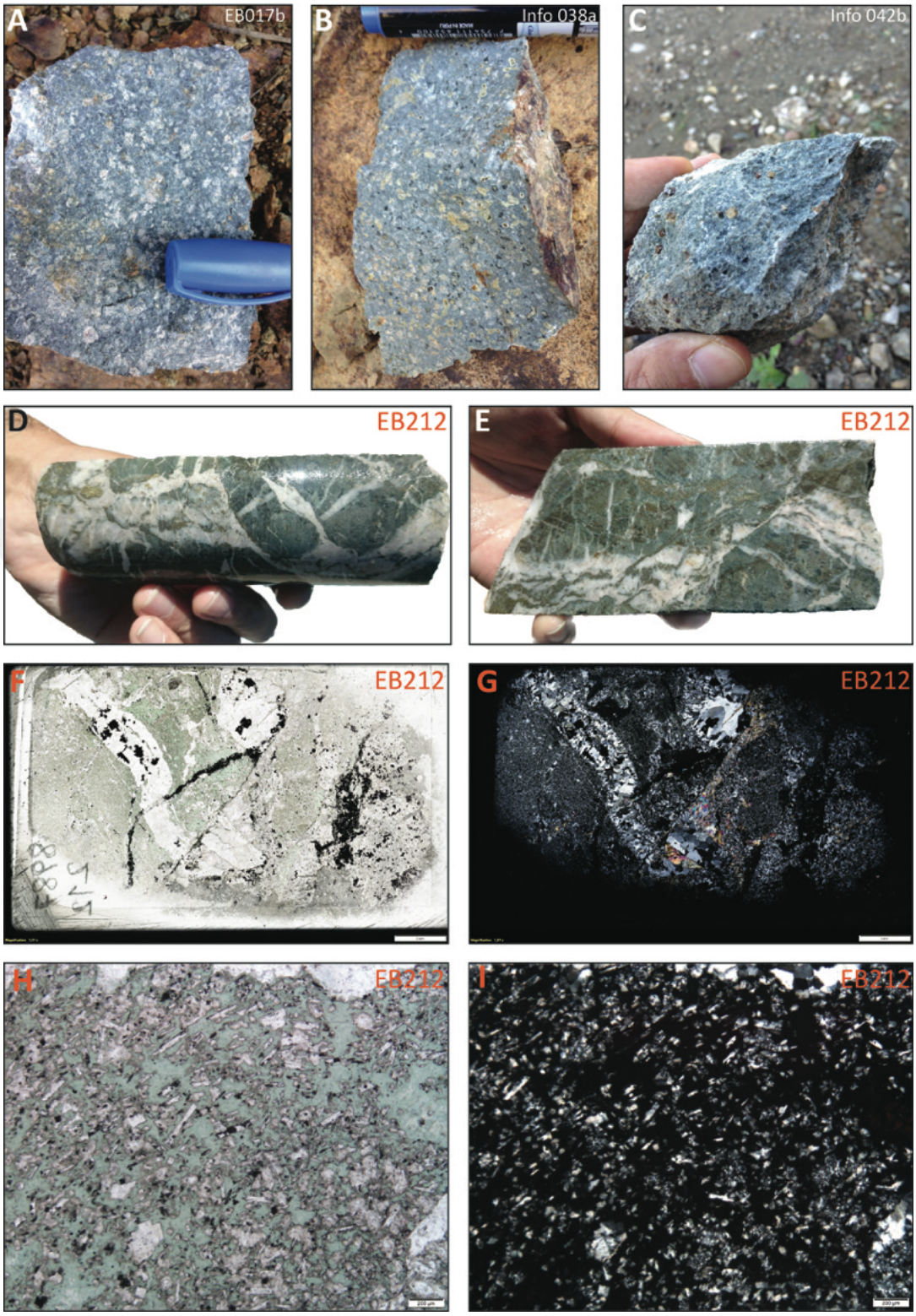


Figure 6.2. **(A-C) Hand samples from Main Zone displaying amygdaloidal andesite with early phase pervasive chlorite alteration accompanied by fine-grained quartz, vermiculite and cubic pyrite; (D-E) Drill core samples (EB212) from drill hole HTD30A-518.4m, targeting Main Zone mineralization with pervasive early chlorite alteration cut by quartz -sulfide veins and overprinted by anhydrite; (F-I) Photomicrographs of sample EB212 characterizing the light green color under PPL and dark brown to dark violet colors under XPL**

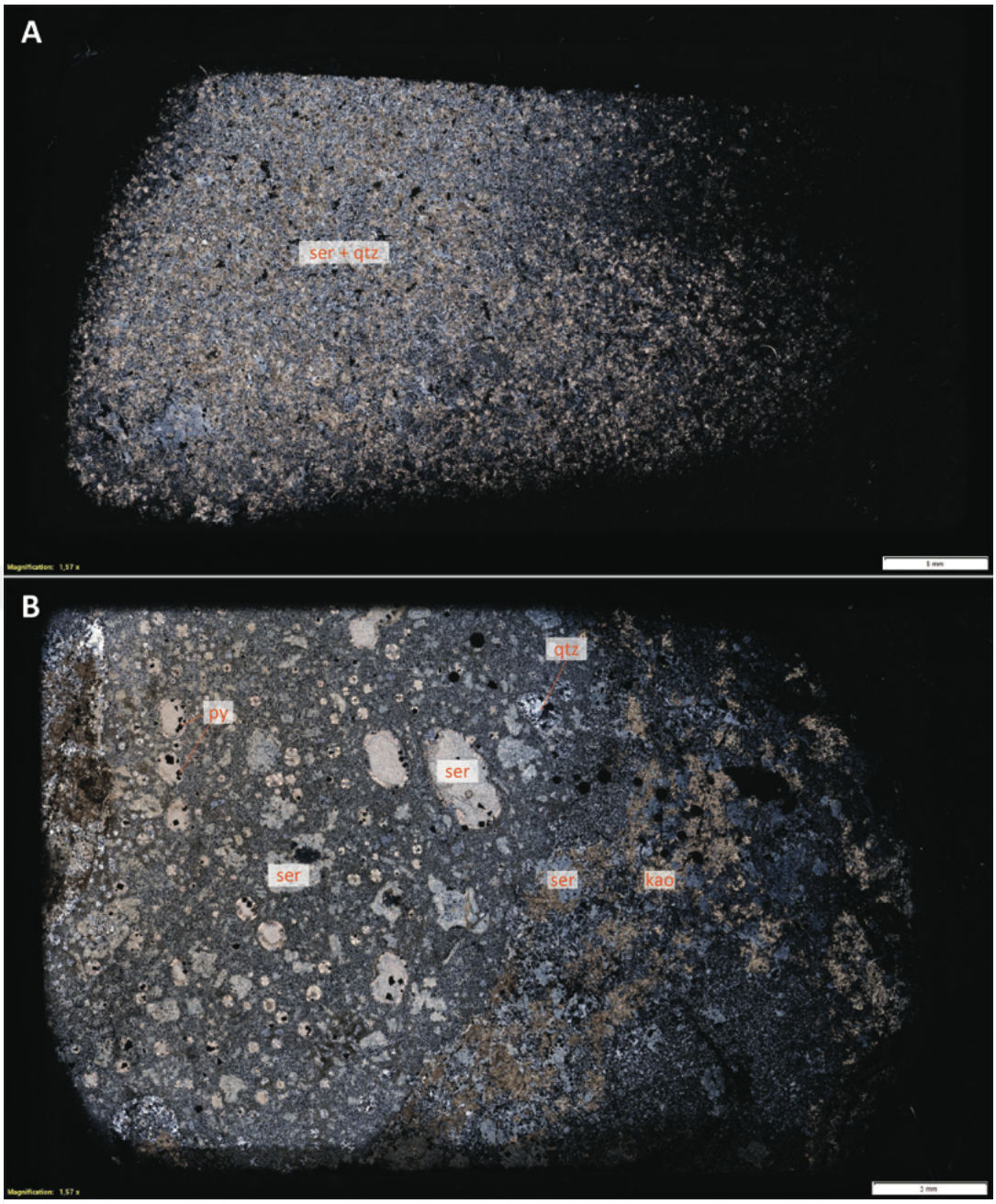


Figure 6.3. Full thin section scan photomicrograph examples of samples displaying early sericite-quartz alteration (XPL), (A) EB230, HTD018-158m; (B) EB232, HTD018-253.5m

6.5). These two types of chlorites may coexist , and chlorite2 appears to cut across the chlorite1 if both are present in the same sample (Fig. 6.5). Chlorite2 is spatially and temporally associated with quartz2 and high-grade chalcopyrite $\pm$ pyrite (Fig. 6.5). Scanning electron microscope images (Fig. 6.5) also highlight the flaky nature of chlorite2 and spatial association between high-grade gold-copper mineralization and chlorite2.

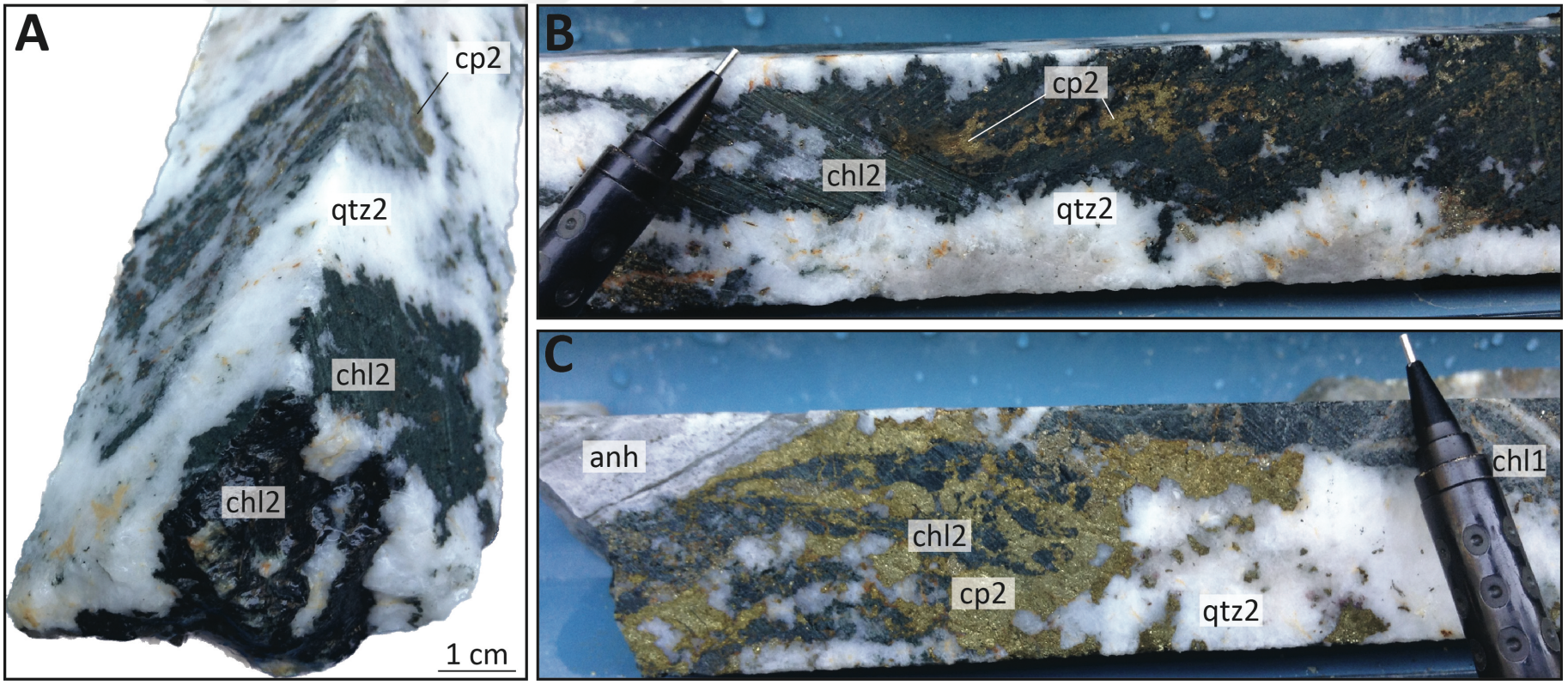


Figure 6.4. **Drill core samples representing chlorite2-quartz2 alteration phase accompanied by chalcopyrite and Au mineralization; (A) HTD088-348m, 7.85 g/t Au and 4.01 %Cu, (B) HTD088-350.4m, 10.5 g/t Au and 1.67 %Cu, (C) HTD088-343m, 3.13 g/t Au and 4.59 %Cu (abbreviations are as in Figure 6.1)**

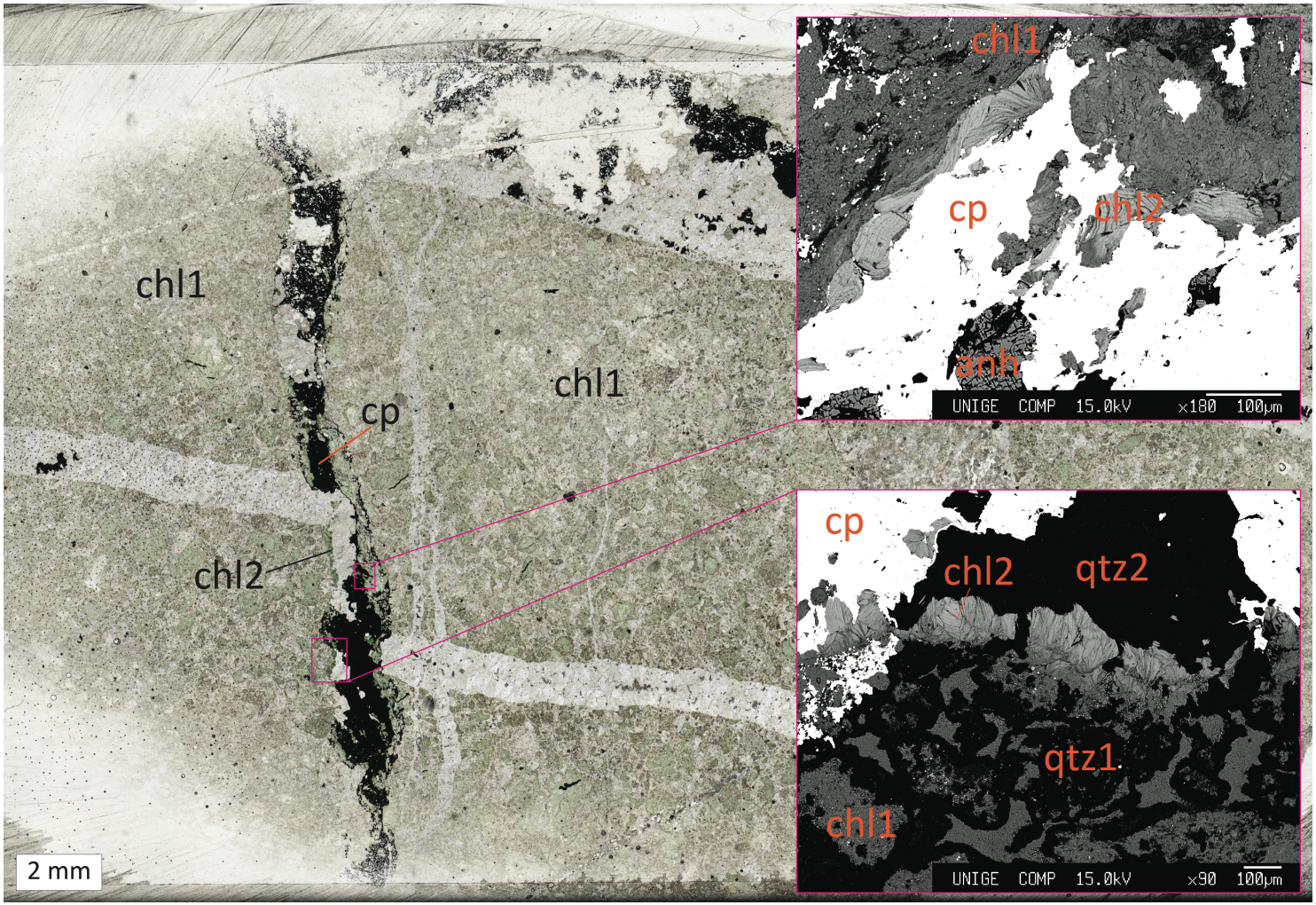


Figure 6.5. **Full thin section scan photomicrograph and scanning electon microscope (SEM) images of sample EB193 representing early chlorite-1 and mineralization phase chlorite-2 alterations; EB193, HTD029-487.2m. anh: anhydrite, chl: chlorite, cp: chalcopyrite, qtz: quartz**

6.1.4. Sericite2 alteration

Sericite2 alteration, occurring after the earlier chlorite alteration (both chlorite1 and chlorite2), is identifiable either as chlorite-sericite amygdales showing concentric zoning or as selectively pervasive sericite alteration on plagioclase phenocrysts (Fig. 6.6 A-D). Additionally, sericite2 alteration can be observed overprinting the earlier chlorite2-chalcopyrite2 patches (Fig. 6.6 E, F). When comparing sericite1 and sericite2 alterations, a notable difference is the higher crystallinity of sericite2 crystals, identified as muscovite due to this characteristic. As the intensity of hydrothermal alteration increases in the high-grade gold and copper ore zones, the sericite2 alteration is thought to be completely altered into the clay minerals, predominantly kaolinite and dickite.

6.1.5. Clay and hematite-goethite alteration

Earlier chlorite2 and sericite-rich alterations associated with sulfides, predominantly pyrite1-3 and chalcopyrite2 are altered into clay and Fe-oxide phases, arguably due to the changes in the physico-chemical conditions of the hydrothermal system such as pH and the oxidation state. As a consequence, clay minerals, predominantly kaolinite and dickite, additionally saponite are observed to overprint/replace the earlier chlorite and sericite-rich alterations, while hematite and goethite are observed as patches over the sulfide minerals (Fig. 6.7). Quartz3 phase, characterized by medium-grained quartz patches is temporally associated with this clay-hematite-goethite phase.

6.1.6. Quartz4 and carbonate alteration

Quartz4 and carbonate alteration represent one of the latest hydrothermal alteration phases identified in the Main Zone mineralization. It is characterized by the occurrence of very coarse-grained quartz veins mostly with a comb texture, accompanied by carbonate minerals, mainly dolomite, calcite, and siderite. This phase is the final alteration event that includes mineralization in the form of quartz-carbonate-pyrite-chalcopyrite veins. Petrographic investigation reveals that

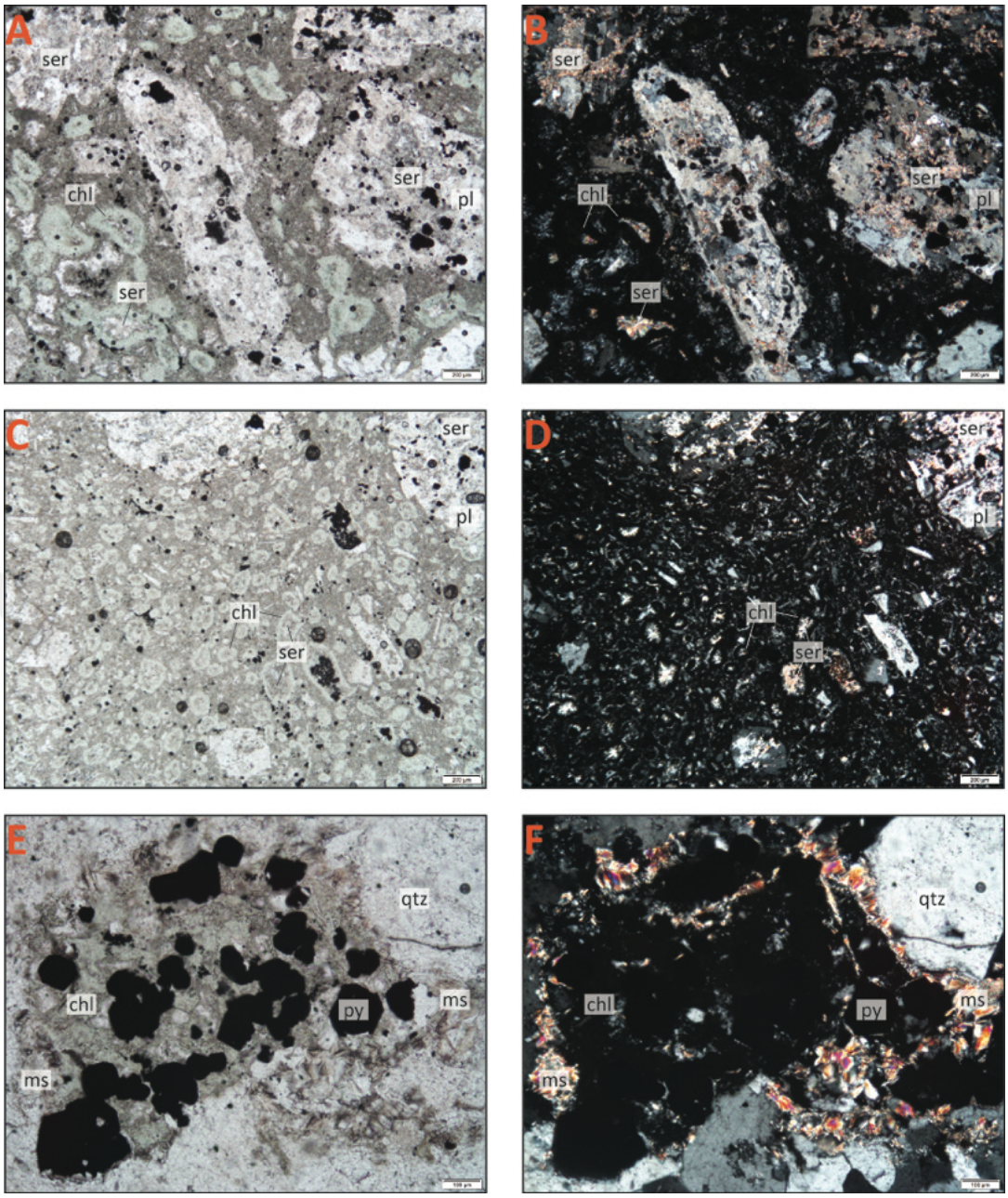


Figure 6.6. Photomicrographs representing sericite alteration postdating the chlorite alteration on andesite breccia, sample EB180, HTD029-154.1m; (A) Concentrically zoning of chlorite-sericite amygdales and selective sericite alteration on plagioclase phenocrysts (PPL), (A) Concentrically zoning of chlorite-sericite amygdales and selective sericite alteration on plagioclase phenocrysts (XPL), (C) Concentrically zoning of chlorite-sericite amygdales and selective sericite alteration on plagioclase phenocrysts (PPL), (D) Concentrically zoning of chlorite-sericite amygdales and selective sericite alteration on plagioclase phenocrysts (XPL), (E) Muscovite overprint on chlorite associated with pyrite mineralization (PPL), (F) Muscovite overprint on chlorite associated with pyrite mineralization (XPL). chl: chlorite, ms: muscovite, pl: plagioclase, py: pyrite, qtz: quartz

quartz4-carbonate veins crosscut all the pre-existing alteration phases such as early sericite-quartz1 phase and pervasive clay alterations (Fig. 6.8). Carbonate minerals are predominantly dolomite. It is an important observation to highlight the presence

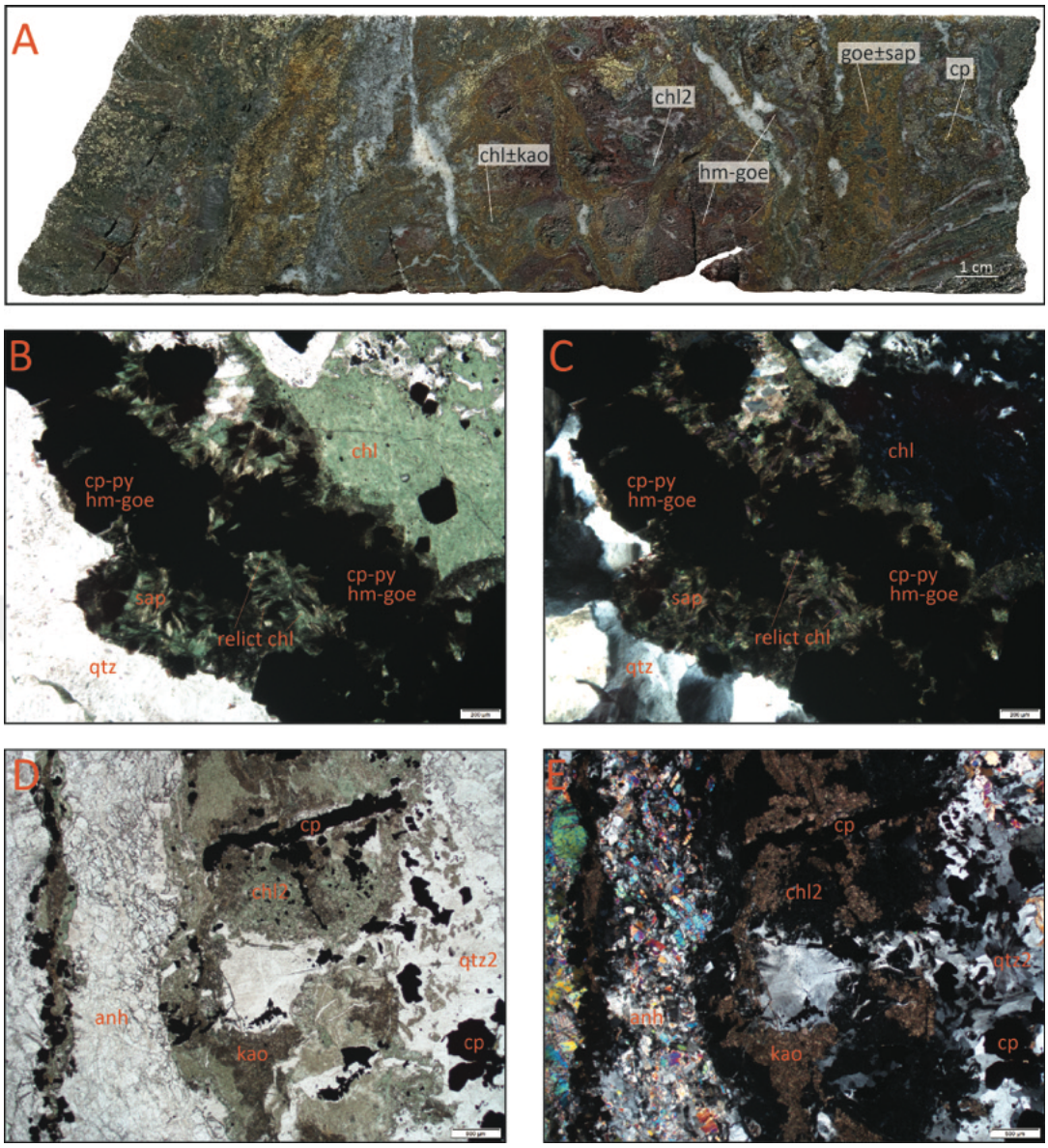


Figure 6.7. **(A) Drill core sample from Main Zone mineralization representing clay and Fe-oxide overprint over pre-existing chlorite and sulfides, HTG02-35.4m, (B) Photomicrograph from sample EB041, HTD090-273m, showing saponite and hematite-goethite overprint on chalcopyrite-pyrite and chlorite assemblage (PPL), (C) Photomicrograph from sample EB041, HTD090-273m, showing saponite and hematite-goethite overprint on chalcopyrite-pyrite and chlorite assemblage (XPL), (D) Photomicrograph from sample EB039, HTD090-264m, representing kaolinite overprint on chlorite-2 alteration (PPL), (E) Photomicrograph from sample EB039, HTD090-264m, representing kaolinite overprint on chlorite-2 alteration (XPL). anh: anhydrite, chl: chlorite, cp: chalcopyrite, goe: goethite, hm: hematite, kao: kaolinite, py: pyrite, sap: saponite, qtz: quartz**

of late stage Mg-metasomatism. Dolomite crystals occupy the interstitial spaces between euhedral to subhedral quartz crystals (Fig. 6.8) accompanied by chalcopyrite ± pyrite.

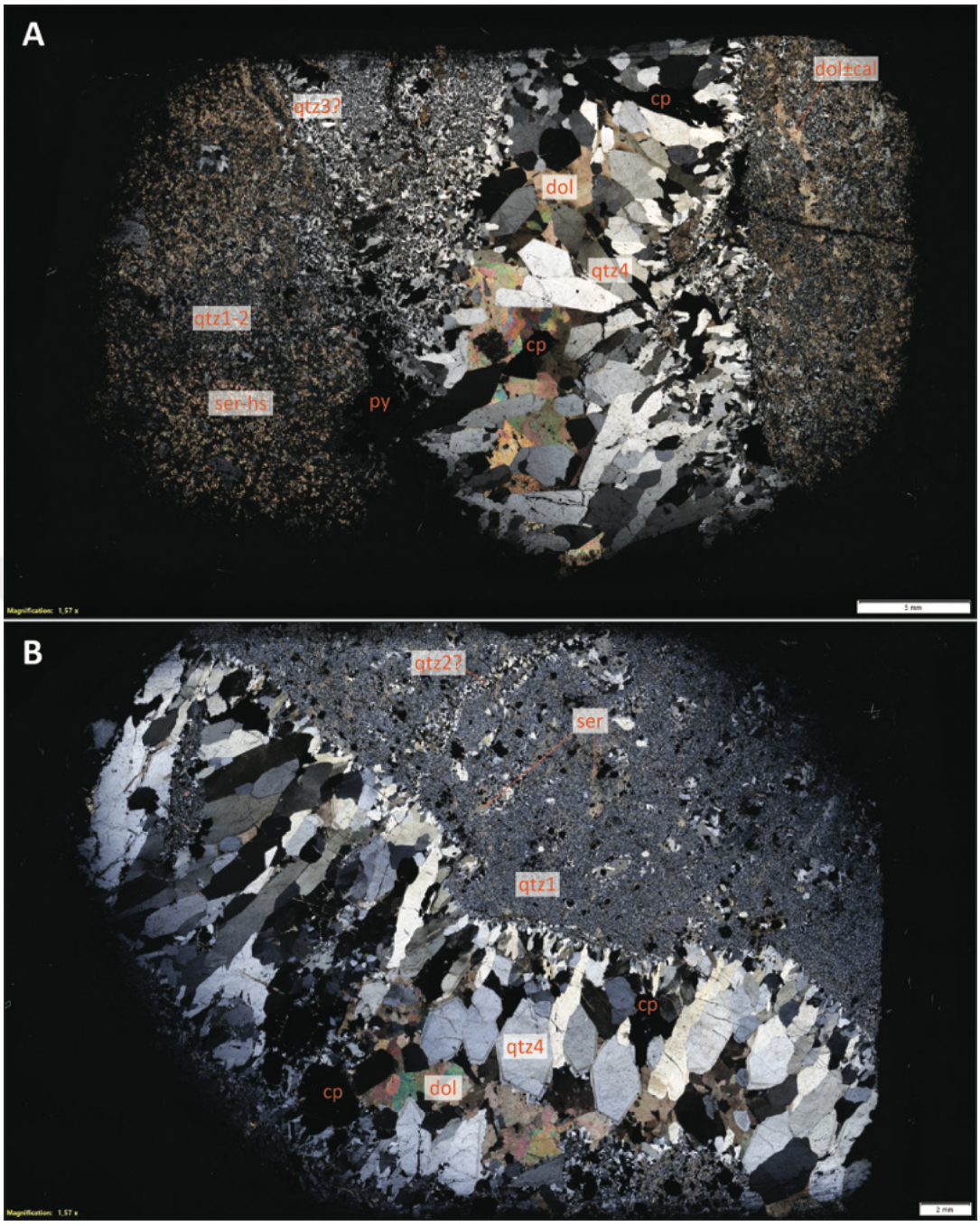


Figure 6.8. Full thin section scan photomicrograph examples of samples displaying comb quartz4-carbonate veins (XPL), (A) EB181, HTD029-185.5m; (B) EB183, HTD029-224.7m. cp: chalcopyrite, cal: calcite, dol: dolomite, hs: halloysite, py: pyrite, qtz: quartz, ser: sericite

6.1.7. Late anhydrite and calcite overprint

Anhydrite alteration is highly noticeable as it crosscuts all the pre-existing hydrothermal alteration phases. It can be observed as an intense and pervasive alteration that completely replaces the earlier associations, or as veins, veinlets, and open spaces fillings. The presence of calcite also indicates late-stage

Ca-metasomatism, occurring alongside anhydrite. Calcite crystals are also found as open space fillings or as veinlets. Another important aspect of the anhydrite overprint is that it dilutes the high-grade gold and copper ore zones. When anhydrite alteration occurs intensely and pervasively, the gold and copper grades decrease significantly. However, if the original texture of the host volcanic rock and the presence of pre-existing hydrothermal alteration phases are preserved (Fig. 6.9), then anhydrite alteration can serve as a valuable indicator for mineralization.

6.1.8. Alteration trends at main zone

To track and visualize the chemical and mineralogical changes associated with the hydrothermal alteration, a graphic method is utilized by creating a box plot which combines two alteration indices, Ishikawa alteration index (AI, Ishikawa et al., 1976) and the chlorite-carbonate-pyrite index (CCPI, Large et al., 2001). These indices are calculated by the whole rock major element lithogeochemical data and the formulas given in the equations 6.1 and 6.2.

$$\mathrm{AI} = 100 \cdot (\mathrm{MgO} + \mathrm{K_2O}) \,/\, (\mathrm{MgO} + \mathrm{K_2O} + \mathrm{Na_2O} + \mathrm{CaO}) \tag{6.1}$$

$$\mathrm{CCPI} = 100 \cdot (\mathrm{FeO} + \mathrm{MgO}) \,/\, (\mathrm{FeO} + \mathrm{MgO} + \mathrm{Na_2O} + \mathrm{K_2O}) \tag{6.2}$$

AI and CCPI values were calculated for each sample with detailed petrographic examination that represents the hydrothermal alteration and associated mineralization in Main Zone. Hydrothermally altered samples define a trend toward particular directions in the alteration index box depending on the chemical and mineralogical changes (Fig. 6.10, 6.11, 6.12). These trends are defined with respect to the least altered host volcanic rocks with andesitic (AI= 20-50, CCPI= 60-80) and dacitic (AI= 20-50, CCPI= 40-60) compositions. Relative significance of minerals such as chlorite, sericite and pyrite produces trends to the right on the alteration box plot, whereas calcite, epidote and anhydrite alterations define trends to the left on the alteration box plot (Fig. 6.10, 6.11, 6.12). Through petrographic examination of each sample and the use of alteration indices, a more comprehensive understanding

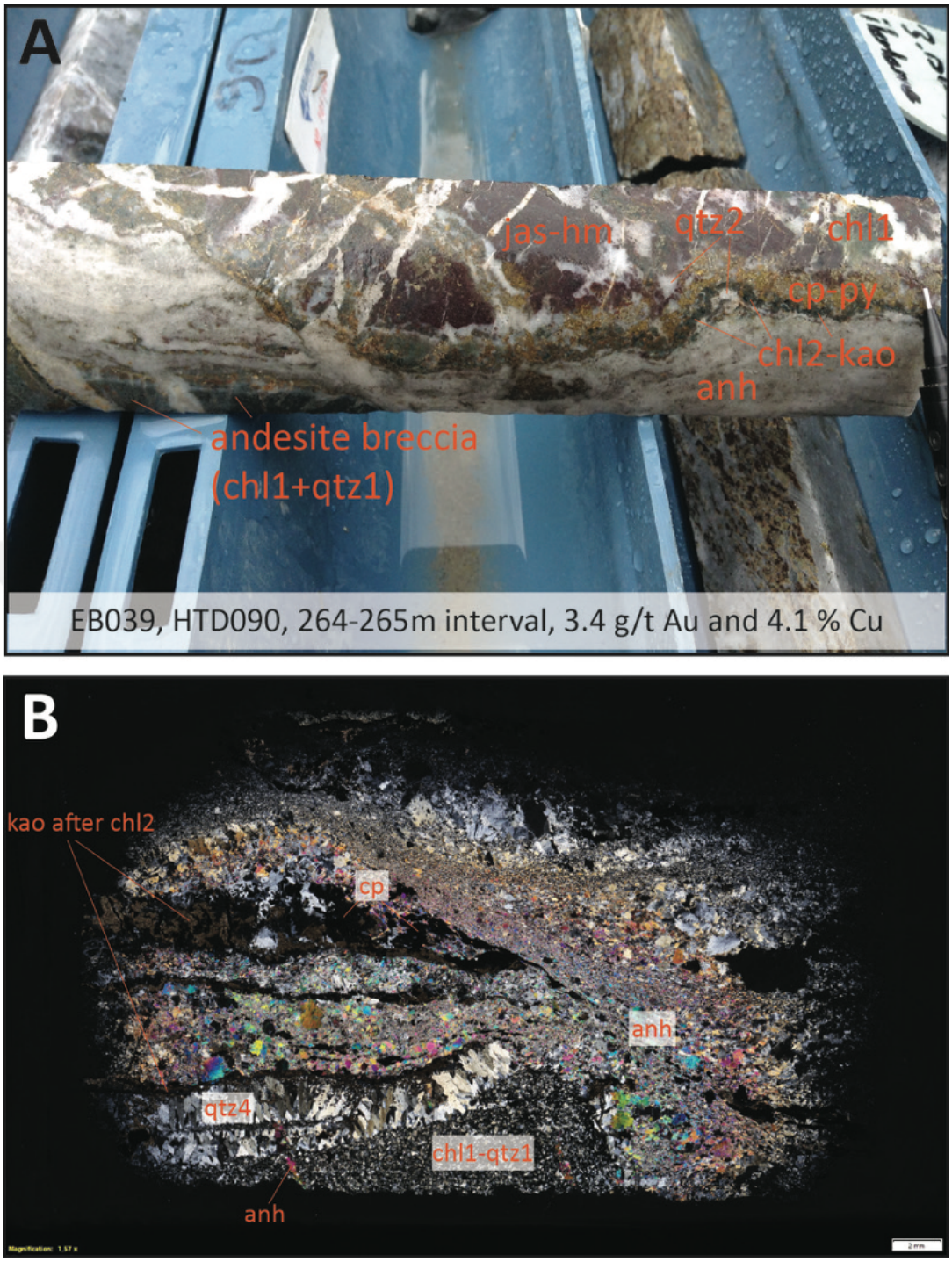


Figure 6.9. **(A) Drill core sample and (B) the full thin section scan photomicrograph (XPL) of the sample EB039. It represents the late anhydrite phase overprinting the pre-existing early chlorite1-quartz-1, chlorite2-jasper-hematite-kaolinite-sulfide and quartz4 alterations. anh: anhydrite, cp: chalcopyrite, chl: chlorite, hm: hematite, jas: jasper, kao: kaolinite, py: pyrite, qtz: quartz**

of the temporal evolution of the hydrothermal alteration assemblages is achieved. Additionally, the gold, copper, and zinc grades corresponding to each 1-meter drill core interval represented by the samples are taken into account. By combining these

data, the chemical and mineralogical changes, along with mineralization, are effectively contextualized in terms of both time and space.

A geological cross section was constructed to illustrate the Main Zone mineralization. This cross section incorporates three drill holes, namely HTD018, HTD029, and HTD090. Petrographic examination and lithogeochemical assessment of the drill core samples were conducted, and the results were integrated into their respective drill holes to demonstrate the spatial arrangement of the hydrothermal alteration assemblages (Fig. 6.1). Then, alteration box plots were prepared to highlight the mineralogical and chemical changes in time.

The evolution of hydrothermal processes in Main Zone is revealed through the petrographic examination and the distribution of samples from drill hole HTD018 in the alteration box plot. The least altered andesitic rocks are altered into early phase chlorite1, zeolite, pyrite1 and quartz1. This process results in an increase in Mg and Fe composition, while Na and Ca are depleted. Chlorite1-rich alteration phase can be followed by either chlorite2-rich alteration accompanied by quartz2 and pyrite2 or sericite-rich alteration. Chlorite-2 rich alteration accompanied by sulfides brings about an increase in especially Fe and Mg and loss of Na and Ca. Consequently, the AI and CCPI values increase, and the alteration trend shifts towards the upper right corner of the alteration box plot, highlighting the intensity of the alteration. On the other hand, sericite-rich alteration causes a depletion in Mg, Fe, Na, and Ca values, with an increase in K content. As a result, the alteration trend moves towards the bottom right corner of the alteration box plot. The clay alteration, represented by minerals such as kaolinite, dickite, $\pm$ halloysite, $\pm$ vermiculite and $\pm$ saponite along with the presence of accompanying quartz, overprints the existing chlorite and sericite-rich alteration assemblages. This leads to shifts in the CCPI values both upwards and downwards. The late-stage calcite and anhydrite overprinting phases are noteworthy as they indicate Ca-metasomatism. These processes contribute to an increase in Ca and $\pm$ Mg, in case of the dolomite precipitation, which results in an alteration trend shift towards the upper left corner of the alteration box plot. It is important to highlight the presence of high-grade gold-bearing samples with chlorite-2 alterations located in the upper left corner of the plot due to the influence of overprinting carbonate and anhydrite phases (Fig. 6.10).

Least altered dacitic rocks altered into early phase sericite, quartz and pyrite. It leads to gain in K and and loss of Na, Ca, Mg and Fe. As a result, the alteration trend shifts to the right in the alteration box plot (Fig. 6.10). Following clay alteration characterized by kaolinite, dickite, and accompanying ± halloysite overprints the sericite-rich alteration and causes the alteration trend to move towards upwards as the rock exhibits a sharp decrease in K (Fig. 6.10).

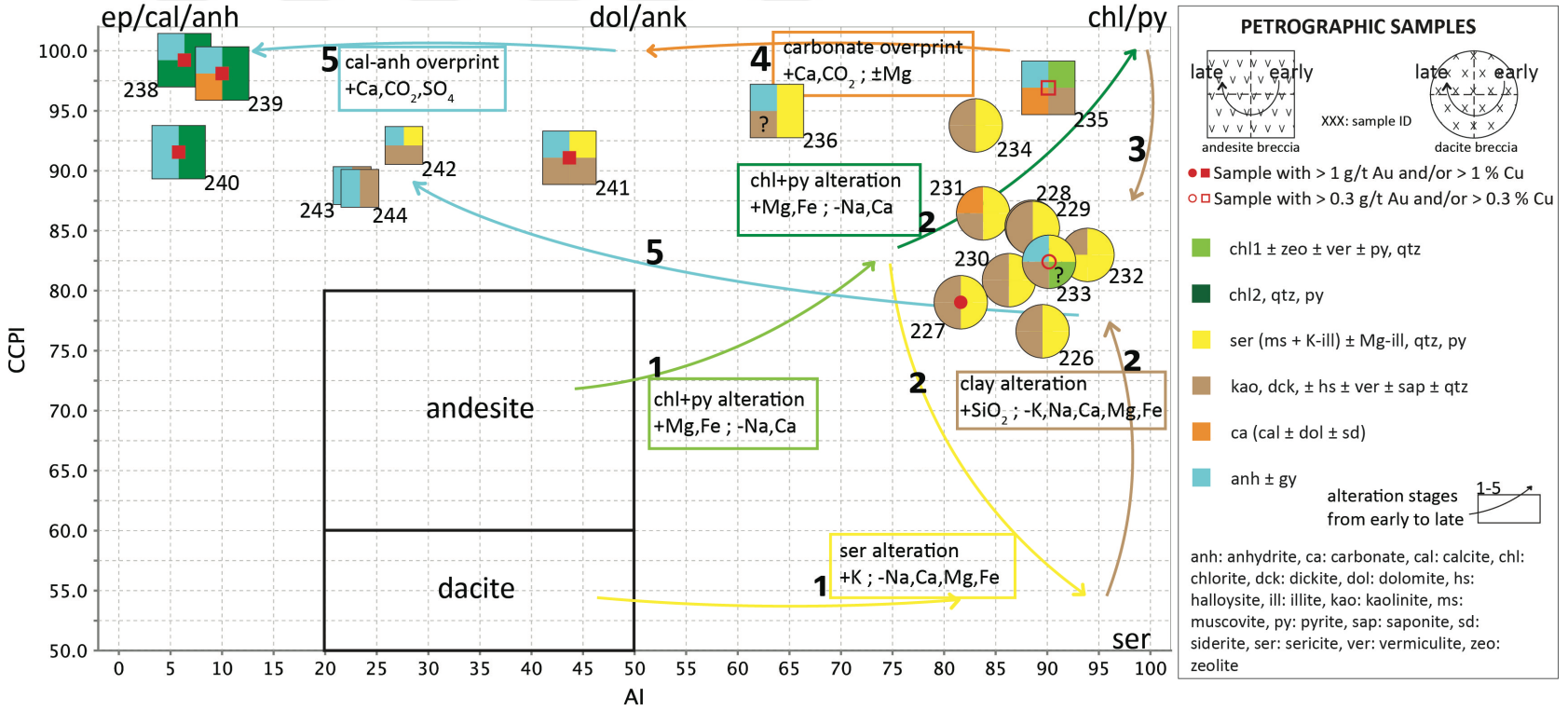


Figure 6.10. Alteration index (AI) versus chlorite-carbonate-pyrite index (CCPI) alteration box plot for drill core samples (HTD018) representing Main Zone mineralization, AI = 100 × (MgO + K_2O)/(MgO + K_2O + CaO + NaO) (Ishikawa et al., 1976), CCPI = 100 × (MgO + FeO)/(MgO + FeO + Na_2O + K_2O) (Large et al., 2001)

Sample distribution of drill hole HTD029 in the alteration box plot resembles to the characteristic of HTD018 alteration trends (Fig. 6.10, 6.11). That is expected as both of the drill holes target the similar host rocks and alteration zones with a few differences. It is evident that samples from HTD029 with high-grade gold and copper mineralization are concentrated in the upper left part of the alteration box plot (Fig. 6.11). The mineralization is hosted by andesite breccia and the associated alteration is characterized by early (i) chlorite1-rich alteration, (ii) chlorite2-rich alteration accompanied by pyrite and chalcopyrite, (iii) kaolinite and dickite alteration accompanied by halloysite, vermiculite and saponite, and late phase (iv) carbonate and (v) anhydrite overprint. Shallow intervals of this drill hole represents barren andesite with early chlorite and sericite alteration overprinted by calcite and epidote. Presence of late calcite and epidote causes a shift in the alteration trend towards upper left part of the alteration box plot due to the addition of Ca and Fe^{3+} (Fig. 6.11).

Dacite on the other hand, is altered into (i) sericite-rich assemblage which are later replaced by (ii) clay minerals, predominantly kaolinite and dickite. Sericite-rich alteration results in an increase in K and a depletion in Na, Ca, Mg and Fe. This causes the altertion trend to shift towards right-hand side as AI increases (Fig. 6.11). The influence of clay alteration, however, causes an abrupt decrease in K that leads the CCPI values go up and the alteration trend shifts towards upwards (Fig. 6.11). Clay alteration is followed by carbonate, predominantly dolomite and calcite and late anhydrite overprinting events that results in a shift in the alteration trend towards the upper left part of the alteration box plot (Fig. 6.11).

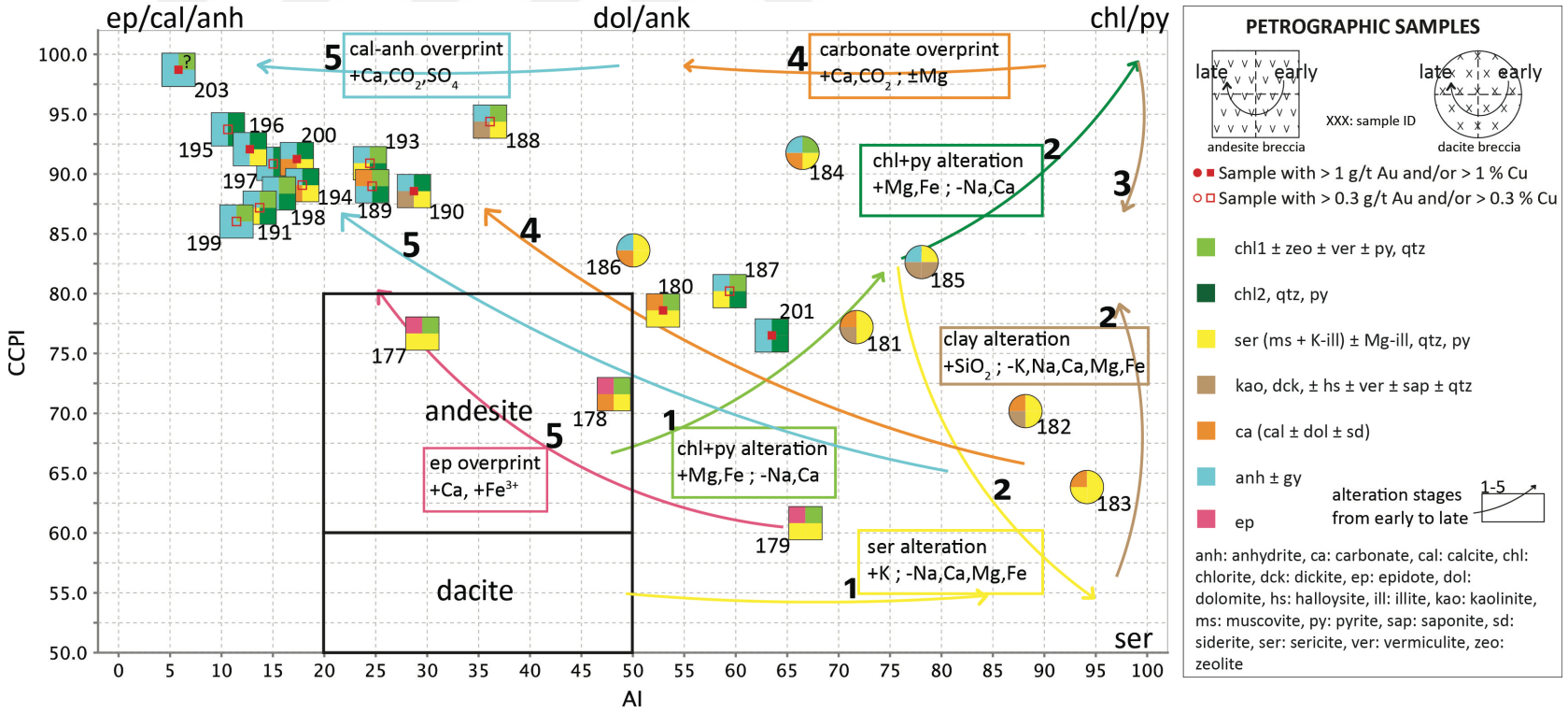


Figure 6.11. Alteration index (AI) versus chlorite-carbonate-pyrite index (CCPI) alteration box plot for drill core samples (HTD029) representing Main Zone mineralization, AI = 100 × (MgO + K_2O)/(MgO + K_2O + CaO + NaO) (Ishikawa et al., 1976), CCPI = 100 × (MgO + FeO)/(MgO + FeO + Na_2O + K_2O) (Large et al., 2001)

Samples taken from HTD090 represents the very high-grade Au and Cu mineralization interval of the Main Zone with gold grades up to 66.1 g/t and copper grades up to 4.1 %. In the alteration box plot, all the samples are accumulated in the upper left corner (Fig. 6.12). That is because of the subsequent hydrothermal alteration events consisting of (i) early chlorite1-rich alteration; (ii) chlorite2-rich alteration accompanied by sulfides; (ii) clay alteration characterized by kaolinite, dickite, ±halloysite, ±vermiculite and ±saponite; and late phase overprinting (iv) carbonate and (v) anhydrite phases. Firstly, the alteration trend shifts towards upper right corner as chlorite and pyrite predominate the systems, then it moves downwards as clay alteration results in a depletion especially in Mg and Fe and in K, Ca and Na as well (Fig. 6.12). Finally, late phase carbonate, predominantly calcite and dolomite and anhydrite causes a shift in the alteration trend towards the upper left corner of the alteration box plot (Fig. 6.12).

The intensity of the hydrothermal alteration processes can be denoted from the trend shifts in the alteration box plot. As the unaltered host andesitic and dacitic volcanic rocks rests in the bottom of the plot, any intense alteration preocess accompanied by silicification and sulfide precipitation (pyrite, chalcopyrite and sphalerite in Hod Maden case) causes a shift toward upwards in the alteration plot. The predominant chlorite and sericite-rich alteration process accompanied by quartz and sulfides result in a shift towards the upper right corner due to an abrupt increase in Mg-Fe and K, and a depletion in Ca and Na. Therefore, the mineralized samples displaying intense hydrothermal alteration are expected to be located in the upper right part of the alteration box plot. However, the late overprinting events, carbonate and anhydrite precipitation in Hod Maden mineralization case, cause a shift towards left due to the addition of Ca to the system. In addition clay alteration also disturbs the cations which determine the AI and CCPI indices. Despite the late disturbance, the majority of the samples representing high-grade gold and copper mineralization with intense hydrothermal alteration are accumulated in the upper part of the alteration box plot (Fig. 6.10, 6.11, 6.12).

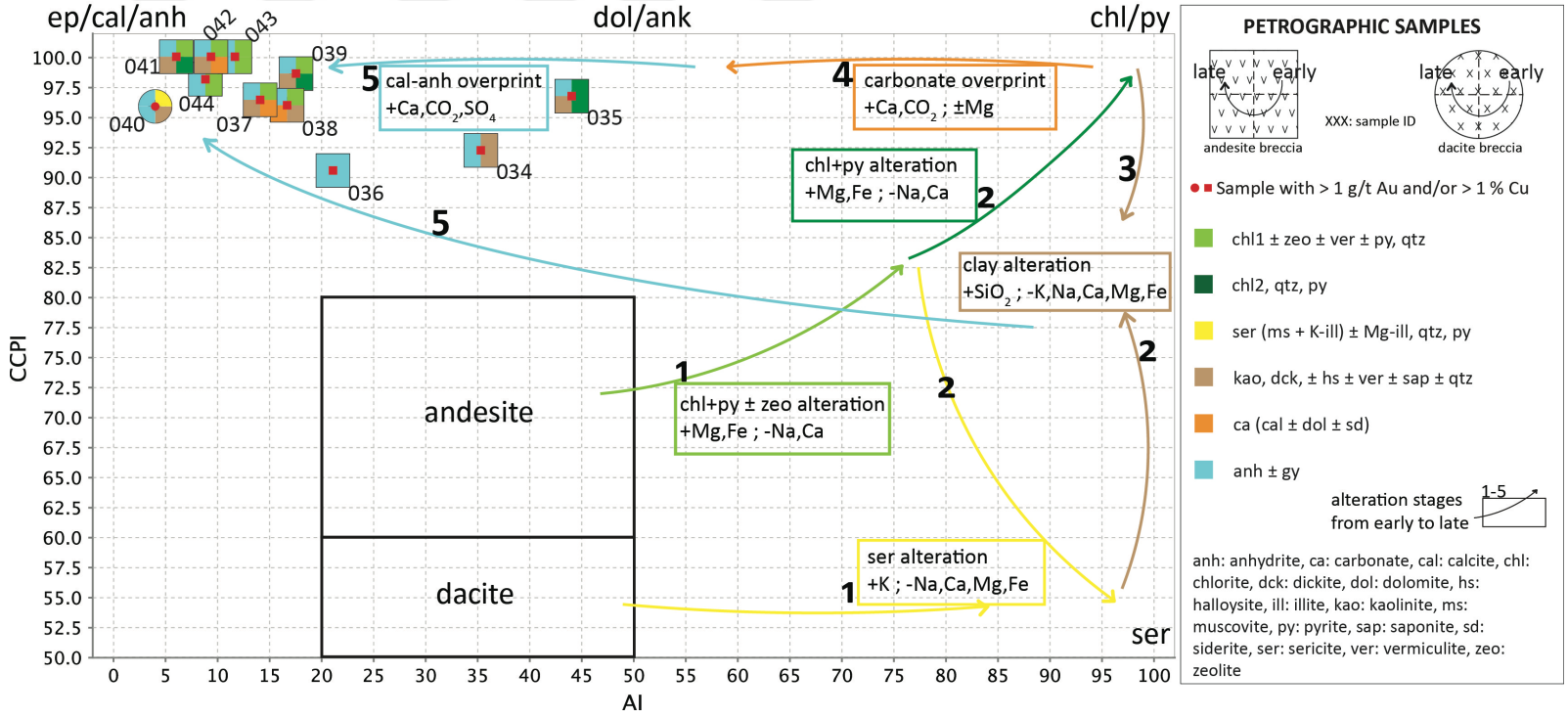


Figure 6.12. Alteration index (AI) versus chlorite-carbonate-pyrite index (CCPI) alteration box plot for drill core samples (HTD090) representing Main Zone mineralization, AI = 100 × (MgO + K_2O)/(MgO + K_2O + CaO + NaO) (Ishikawa et al., 1976), CCPI = 100 × (MgO + FeO)/(MgO + FeO + Na_2O + K_2O) (Large et al., 2001). anh: anhydrite, ca: carbonate, cal: calcite, chl: chlorite, dck: dickite, ep: epidote, dol: dolomite, ill: illite, kao: kaolinite, ms: muscovite, py: pyrite, sd: siderite, ser: sericite, ver: vermiculite, zeo: zeolite

6.2. Hydrothermal Alteration at South Zone

South Zone mineralization is hosted by the dacite breccia and the volcanosedimentary rock. Whereas gold and copper mineralization is confined within the dacite breccia, zinc mineralization displays tabular, stratabound-type ore bodies within the volcanosedimentary rock. Dacite breccia is monomictic, matrix to clast-supported breccia with dacite clasts displaying spherulitic texture. On the other hand, volcanosedimentary rock consists of dacitic lava flows, volcaniclastics and mass flow deposits.

Host volcanic rocks, gold-copper and zinc ore zones and associated hydrothermal alteration zones are shown in (Fig. 6.13). The drill hole HTD021 was logged and sampled. Thin section were examined and a temporal association between alteration phases were determined. These alteration phases (from early to late) are shown in the sample symbology on the drill hole trace (Fig. 6.13).

The hydrothermal alteration at South Zone is characterized by (i) early phase sericite-rich alteration; (ii) clay altereation, predominantly kaolinite and dickite accompanied by halloysite and palygorskite; (iii) zeolite alteration with $\pm$ chlorite and $\pm$ pyrite; and late (iv) carbonate, mostly dolomite and calcite and (v) anhydrite overprinting phases.

6.2.1. Early sericite-rich alteration

The early phase sericite-rich alteration is appears as light grey to light yellow in hand sample. It is distinguished by pervasive sericite (sericite-1) that is composed of fine-grained muscovite and K-illite, along with widespread fine-grained quartz (quartz-1) and occasional pyrite (pyrite-1) dissemination. In Hod Maden, this alteration is commonly found in association with felsic to intermediate volcanic rocks. Hence, early-phase hydrothermal alteration of the South Zone mineralization which is hosted by dacite breccia and volcanosedimentary rocks of dacitic origin is dominated by pervasive sericite and quartz. Sericite often occupies the spherules in dacite breccia clasts replacing the primary crystal fibers of feldspars. In addition, phenocrysts and groundmass are altered into sericite, pervasively. As the

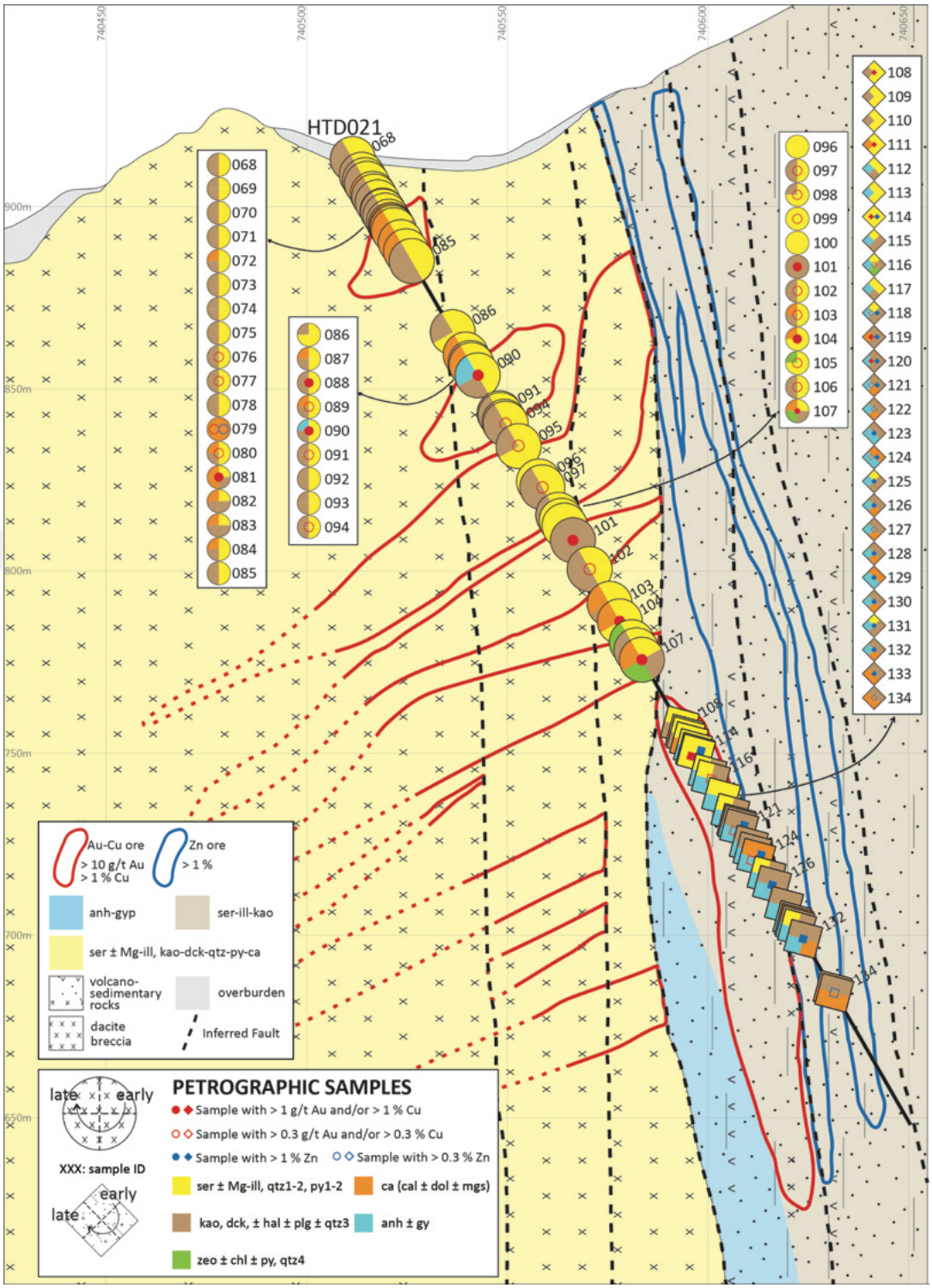


Figure 6.13. A cross section across the South Zone showing the spatial distribution of lithological units, Au-Cu and Zn ore zones and associated hydrothermal alteration assemblages. Notice the each petrographic sample indicates the present hydrothermal alterations and their temporal evolution from early to late phases.

groundmass is more susceptible to late phase hydrothermal activity, it can be altered into clay minerals. Petrographic investigation of early sericite-rich alteration, therefore, often observed as selectively on phenocrysts while groundmass is altered

into kaolinite after sericite (Fig. 6.14).

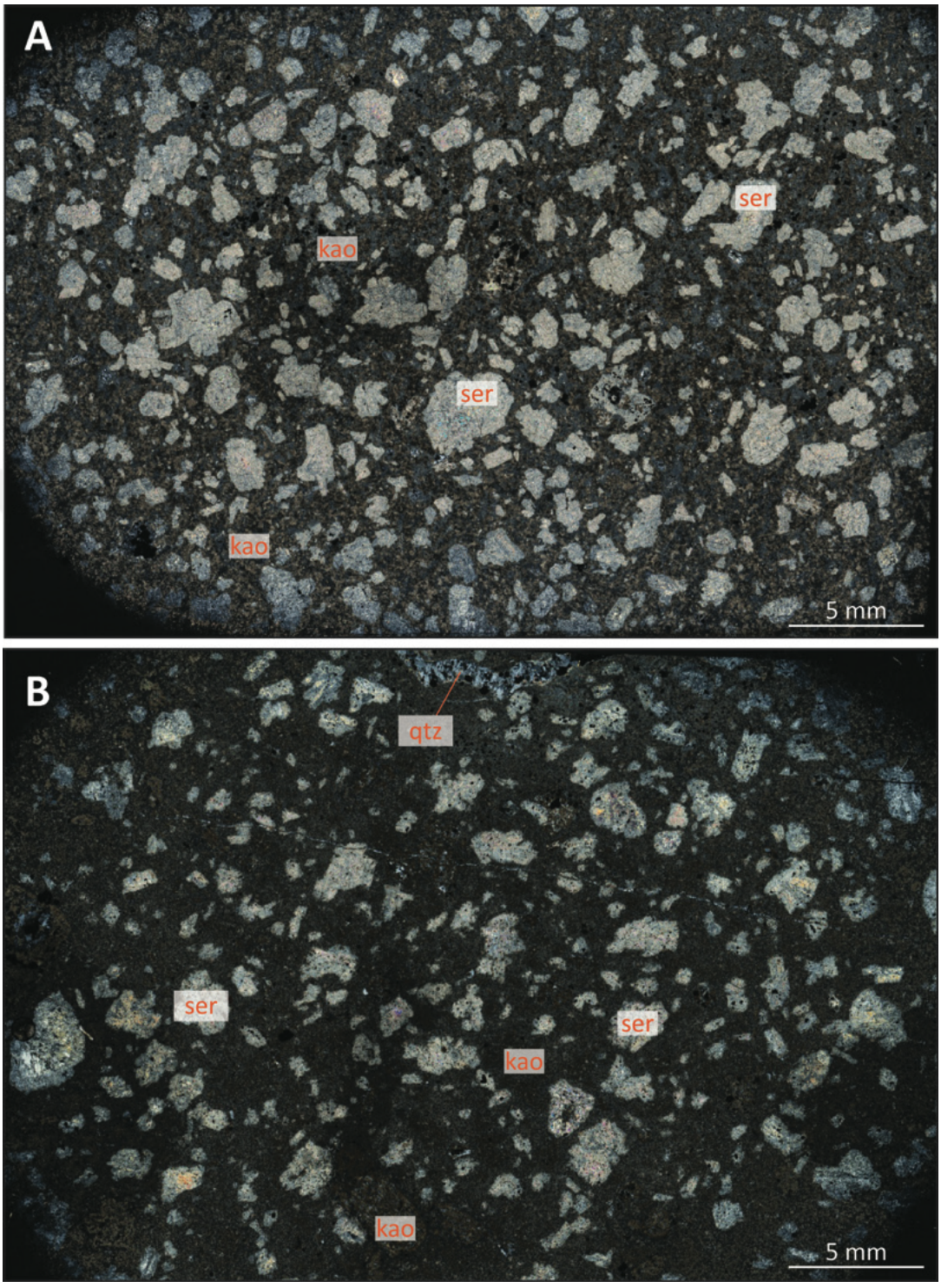


Figure 6.14. **Full thin section scan photomicrograph examples of samples displaying early sericite-rich alteration accompanied by later kaolinite overprint (XPL), (A) EB075, HTD021-15.9m; (B) EB077, HTD021-17.4m. kao: kaolinite, qtz: quartz, ser: sericite**

6.2.2. Clay alteration

Clay alteration is the most predominant alteration type together with sericite-rich alteration at South Zone. It can be observed from the shallow intervals of drill hole HTD021 and can be followed through the end of the hole. Both dacite breccia and the volcanosedimentary rocks display sericite-rich alteration which is replaced by clay alteration. The most abundant clay minerals identified are kaolinite and dickite. Additionally, SWIR-Terraspec studies have revealed the presence of halloysite, palygorskite, vermiculite, rectorite, and in smaller quantities, beidellite, nontronite, and montmorillonite. The temporal relationship between the early sericite-rich alteration and the subsequent clay alteration is clearly observed during the drill core logging process through hand sample examination. While the sericite-rich alteration appears in hues ranging from beige to grey, the clay minerals exhibit colors that vary from light to dark brown (Fig. 6.15 A). This temporal association is further confirmed during petrographic studies, where thin sections are examined under crossed-polarized light (XPL). Clay minerals, kaolinite and dickite in particular display dark brown color, whereas sericite crystals are observed in light brown to beige in color (Fig. 6.15 B).

6.2.3. Zeolite alteration

The segment of drill hole HTD021 (depth: 149.5 - 191.7m) focused on the lithological contact between the dacite breccia and volcanosedimentary rock is highly noteworthy. It contains crucial records of high-grade gold mineralization and elevated Zn-rich zones, mass flow deposits with sulfide clasts (EB108-110), evidence of deformation caused by the Hod Main Fault Zone, and specific zones (EB105, EB107, and EB116) with zeolite-bearing alteration assemblages (Fig. 6.13).

The light green color and radiating fan-like texture of the zeolite crystals (Fig. 6.16) corroborate the SWIR data, which suggests the presence of laumontite ($CaAl_2Si_4O_{12}.4H_2O$). The occurrence of Ca-zeolite also signifies the initiation or continuation of Ca-metasomatism, considering the subsequent presence of calcite

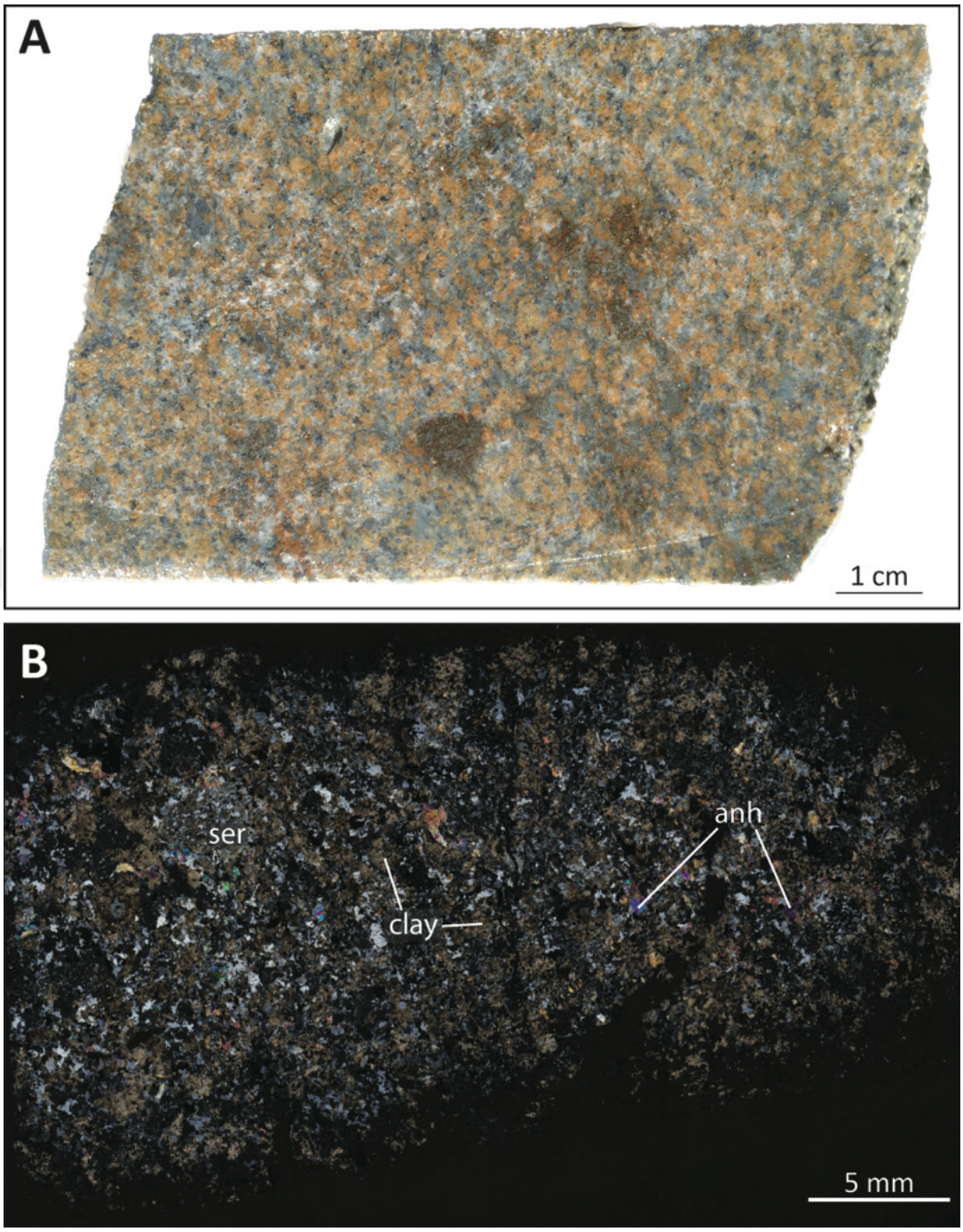


Figure 6.15. **(A) Drill core sample from HTD021-201m representing clay alteration replacing pre-existing sericite alteration on dacite breccia. Notice the brown clay minerals replacing the beige sericite, (B) Full thin section scan photomicrograph (XPL) of sample EB118, HTD021-202.1m. Dark brown minerals are annotated as clay minerals and SWIR work provides the presence of kaolinite, dickite, palygorskite and rectorite. anh: anhydrite, ser: sericite.**

and anhydrite overprinting events. It is noteworthy that zeolites commonly form as a result of low-temperature hydrothermal alteration processes involving the interaction of evolved seawater with (submarine) volcanic rocks. In such cases, drill

hole intervals with zeolite-bearing alteration assemblages may suggest the existence of a seafloor/sub-seafloor alteration zone.

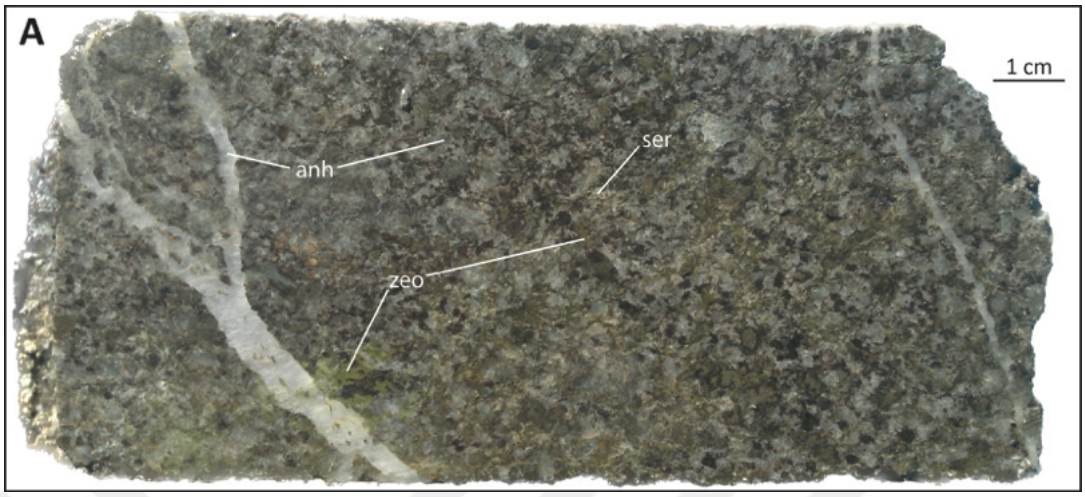


Figure 6.16. Drill core sample, EB116 from HTD021-191.7 m, representing zeolite (laumontite)-bearing alteration associations replacing volcanosedimantary rock. Notice the presence of pre-existing pervasive sericite alteration and late crosscutting anhydrite veinlets. anh: anhydrite, ser: sericite, zeo: zeolite.

6.2.4. Carbonate alteration

Carbonate alteration, characterized by dolomite and calcite, is associated with quartz-4 and pyrite-4 and often manifested as comb quartz-carbonate veins (Fig. 6.17). Furthermore, carbonate crystals are observed as open space fillings, occupying the interstitial spaces between euhedral quartz crystals and forms carbonate vein and veinlets cutting the pre-existing sericite and clay alterations.

Dolomite, the predominant carbonate mineral, shows a spatial association with ore minerals like chalcopyrite, sphalerite, and galena, alongside well-crystalline white quartz and grey silica. The mineralogy of carbonates is determined through SWIR data, Raman spectroscopy, and QEMSCAN data. Detailed spatial and temporal relationship between carbonates, quartz and sulfides will be discussed in Chapter 8. Notably, carbonate mineralogy reflects the cation activity in the ore-forming hydrothermal fluids and often indicates Mg-metasomatism (in the case of dolomite precipitation) and Ca-metasomatism (in the case of calcite precipitation accompanied by anhydrite and Ca-zeolites).

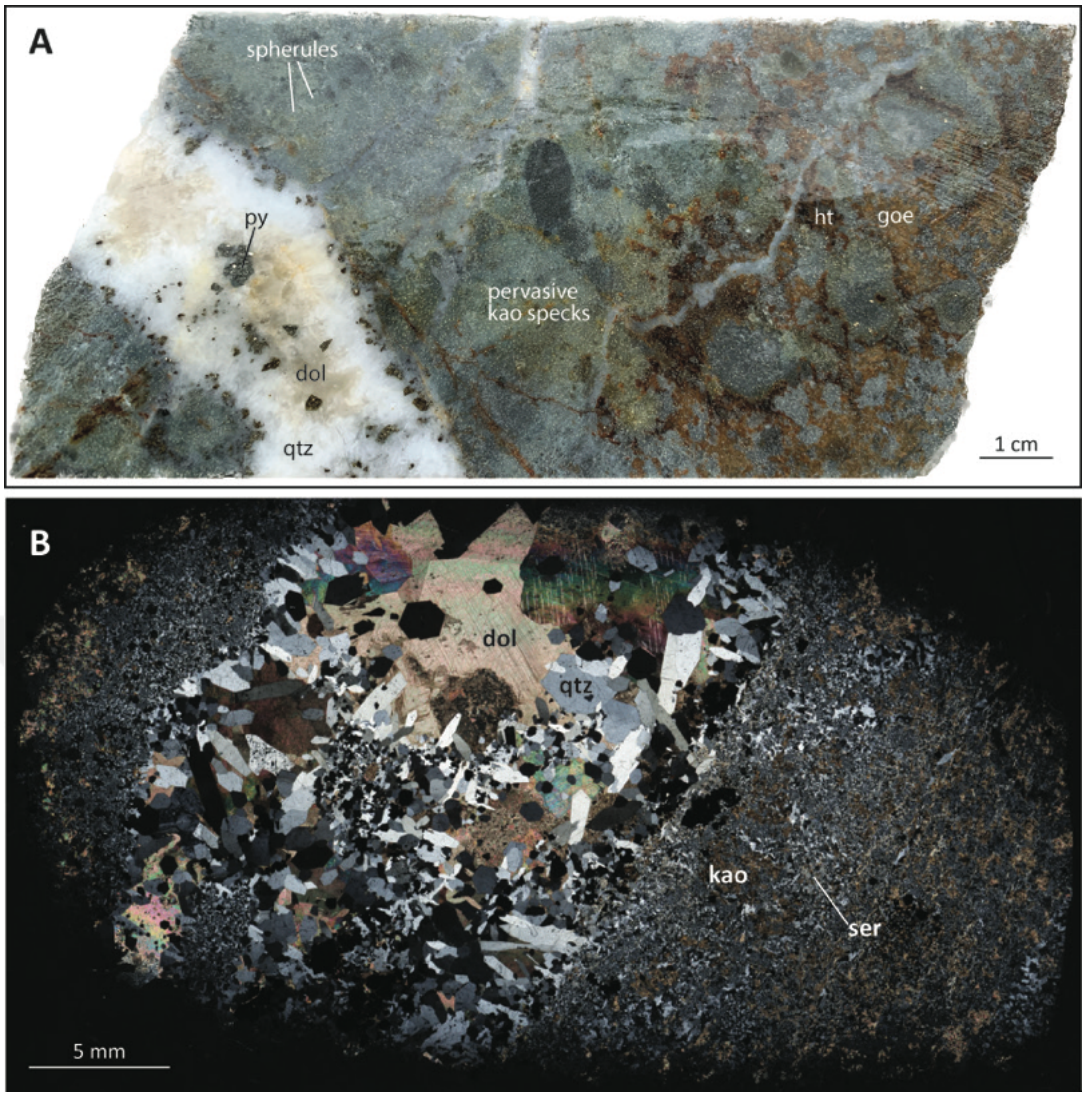


Figure 6.17. **(A) Drill core sample from HTD027-126.5m representing coarse comb quartz (quartz-4)-dolomite-pyrite vein cutting the spherulitic dacite breccia and pre-existing sericite and kaolinite alteration, (B) Full thin section scan photomicrograph (XPL) of sample EB072, HTD021-10.7m, comb quartz4-dolomite-pyrite vein cutting pre-existing sericite. and kaolinite alterations. dol: dolomite, goe: goethite, hm: hematite, kao: kaolinite, qtz: quartz, ser: sericite**

6.2.5. Late anhydrite overprint

Anhydrite is the latest hydrothermal alteration phase observed in South Zone, similar to Main Zone. However, the intensity of anhydrite alteration in South Zone is not as pronounced as in Main Zone. It is primarily observed as open space fillings or as patches overprinting pre-existing phases like sericite-rich alteration and clay alteration (Fig. 6.18). An interesting observation is that anhydrite alteration is predominantly present in samples representing volcanosedimentary rocks (Fig. 6.13), suggesting that the lithological contact defined by the Hod Main Fault Zone

may represent the paleo-seafloor, and the anhydrite in the volcanosedimentary rocks might have formed due to interactions with seawater. The presence of zeolites, which also indicate the seafloor environment, is evaluated in Chapter 6.2.3. Occasionally, calcite is associated with anhydrite, both indicating late-stage Ca-metasomatism. This association significantly influences the alteration trends of South Zone samples in the alteration box plots, as discussed in the following chapter Chapter 6.2.6.

6.2.6. Alteration trends at south zone

The graphic representation of mineralogical and chemical changes related to hydrothermal alteration phases at South Zone is achieved using the alteration box plot, which combines AI and CCPI alteration indices (equations 6.1 and 6.2; Fig. 6.19). A comprehensive examination of 73 samples was conducted using thin sections, enabling the determination of temporal relationships between different hydrothermal alteration phases. The resulting alteration assemblages were integrated into the symbology to indicate the sequence of alteration processes from early to late stages (Fig. 6.19). By evaluating the distribution of the samples, shifts in the alteration trends were identified, and the gain and loss of cations were also interpreted.

Both the dacite breccia and the volcanosedimentary rocks originate from dacitic lava flows, defining the initial composition of the least altered host volcanic rocks for South Zone mineralization as dacite in the alteration box plot. The earliest hydrothermal alteration observed during petrographic examination of the samples is sericite-rich alteration, characterized by pervasive fine-grained sericite-1 and quartz-1, along with pyrite-1 dissemination. This process shifts the alteration trend towards the right due to the gain of K and the loss of Na, Ca, Mg, and Fe (Fig. 6.19). Subsequently, sericite is replaced by clay minerals, predominantly kaolinite and dickite, along with quartz-2 and quartz-3. Other clay minerals like halloysite, palygorskite, vermiculite, rectorite, and in smaller quantities, beidellite, nontronite, and montmorillonite are present in smaller amounts. The clay alteration leads to the loss of K, Na, Ca, Mg, and Fe, resulting in an upward shift in the alteration trend (Fig. 6.19).

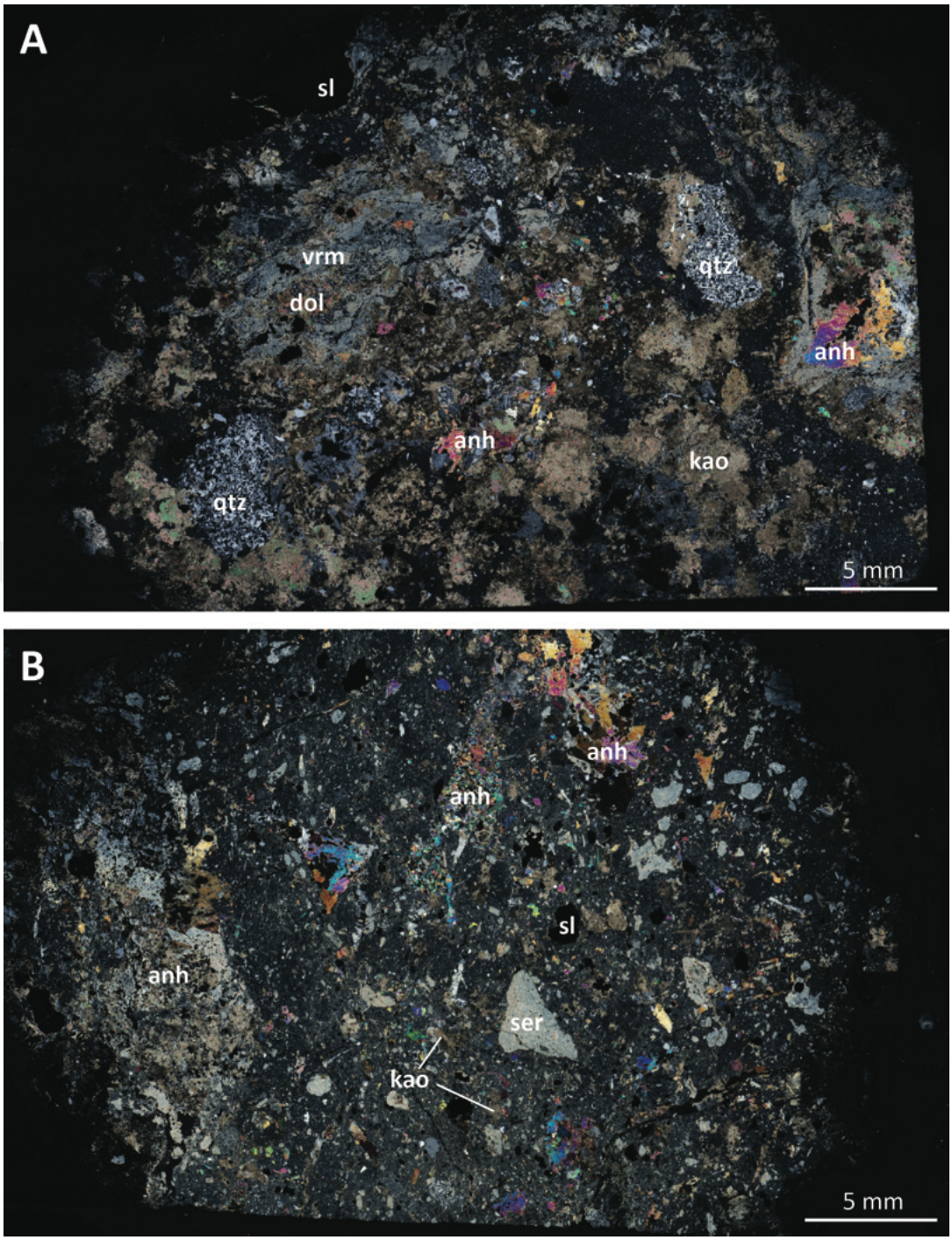


Figure 6.18. Full thin section scan photomicrograph examples of samples displaying late anhydrite overprint on sericite and clay altered volcanosedimentary rocks (XPL). (A) EB125ii, HTD021-221.4 m; (B) EB131, HTD021-237.6 m. anh: anhydrite, kao: kaolinite, qtz: quartz, ser: sericite, sl: sphalerite, vrm: vermiculite

Locally, zeolite-bearing alteration assemblages were identified, with zeolites like laumontite and chabazite confirmed by SWIR data. The presence of Ca-bearing zeolite causes a shift towards the upper-left part of the alteration box plot (Fig. 6.19). Carbonate alteration, mainly represented by dolomite and calcite, is observed

as comb quartz-4-carbonate veins or as patches and open space fillings. Dolomite precipitation increases the Mg and Ca content, shifting the alteration trend towards the top of the alteration box plot (Fig. 6.19). As calcite takes over and the late overprinting anhydrite phase dominates the hydrothermal activity, Ca increases further, and the alteration trend shifts towards the upper-left part of the alteration box plot (Fig. 6.19).

The distribution of the samples is coherent with the alteration trends. Samples exhibiting sericite and clay alteration tend to accumulate on the right-hand side of the plot, while those overprinted by carbonate and anhydrite phases are located in the upper-central and upper-left parts of the plot (Fig. 6.19). It is noteworthy to observe that the gold and copper-bearing dacite breccia samples and zinc-bearing volcanosedimentary rock samples are separated from each other. Clearly, gold and copper mineralization is confined to sericite and clay-altered dacite breccia zones, whereas zinc mineralization is spatially associated with clay, carbonate, and anhydrite minerals (Fig. 6.19).

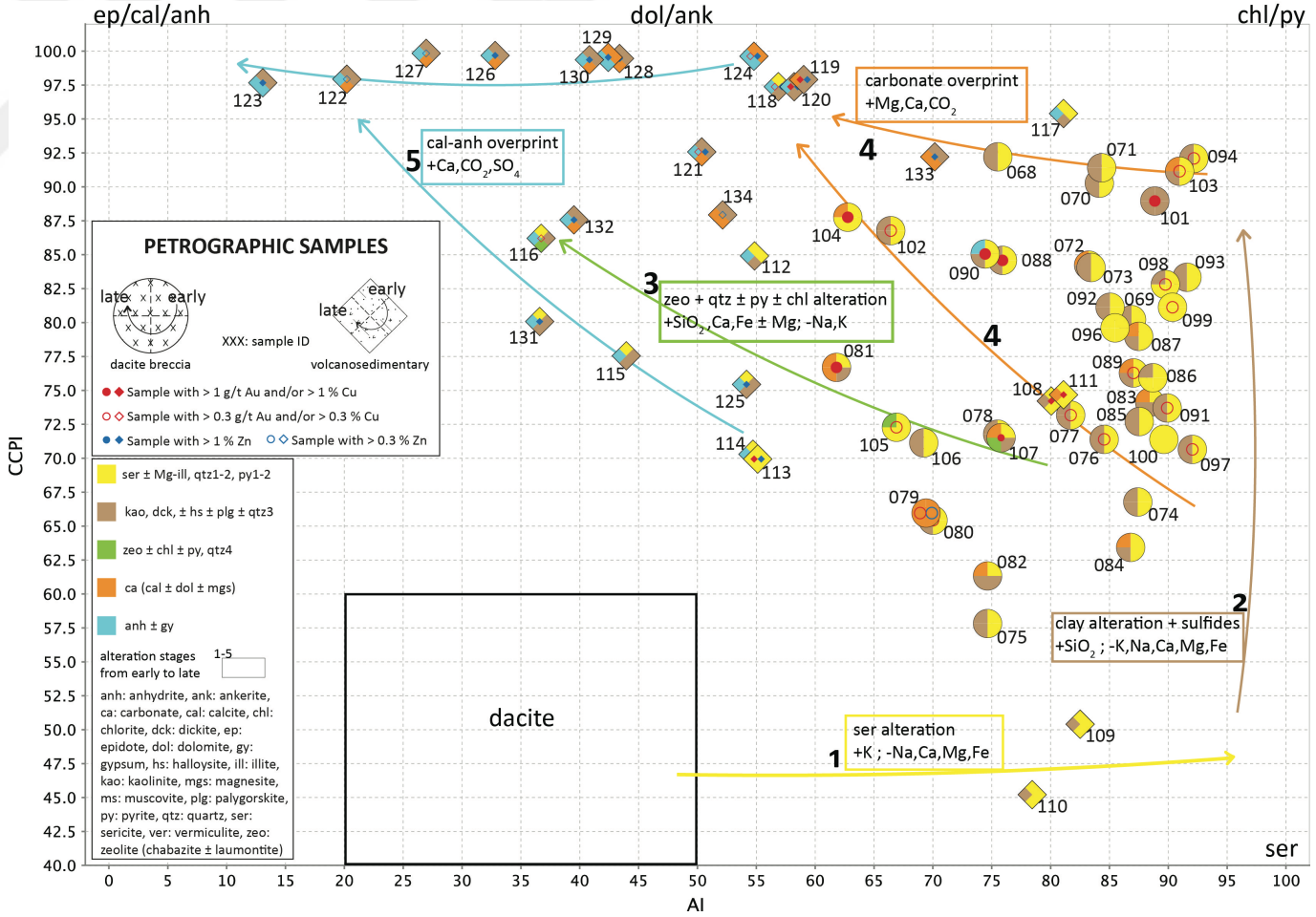


Figure 6.19. Alteration index (AI) versus chlorite-carbonate-pyrite index (CCPI) alteration box plot for drill core samples (HTD021) representing South Zone mineralization, AI = 100 × (MgO + K_2O)/(MgO + K_2O + CaO + Na_2O) (Ishikawa et al., 1976), CCPI = 100 × (MgO + FeO)/(MgO + FeO + Na_2O + K_2O) (Large et al., 2001)

6.3. Hydrothermal Alteration at Old Workings Zone

Host volcanic rocks including andesite breccia (with local massive andesite porphyry) and rhyodacite with banded lava flows, gold-zinc ore zones and associated hydrothermal alteration zones are shown in Figure. 6.20). The drill hole HTD222 was logged and sampled. Thin sections were examined and the temporal association between alteration phases were determined. These alteration phases (from early to late) are shown in the sample symbology on the drill hole trace (Fig. 6.20).

The hydrothermal alteration at the old workings zone is characterized by (i) early chlorite1-rich alteration on andesite breccia occasionally followed by chlorite2 alteration and early sericite1-rich alteration on rhyodacite; (ii) Mg-illite and sericite2-rich alteration both on andesite breccia and rhtodacite; (iii) clay alteration predominantly vermiculite and palygorskite accompanied by montmorillonite on both lithologies; (iv) carbonate, mostly dolomite and rhodocrosite and occasionally calcite with late (v) epidote and anhydrite overprinting phases accompanied by occasional calcite.

The earliest hydrothermal alteration phase identified on the andesitic rocks within the old workings zone is characterized by the presence of fine-grained chlorite1 along with disseminated pyrite1. The key distinction between the chlorite1-rich alterations observed in the main zone and those in the old workings zone lies in the relatively less pronounced occurrence of quartz1 alteration in the latter. Both the groundmass of andesite porphyry clasts within the andesite breccia and the matrix of the andesite breccia itself (displayed as either a monomictic, matrix to clast supported volcanic breccia containing rounded andesite clasts or as hyaloclastites with angular andesite clasts featuring curviplanar edges) are altered in chlorite1 (Fig. 6.21. A-D).

Plagioclase phenocrysts of the andesite porphyry clasts of the andesite breccia are pervasively altered into sericite1 (Fig. 6.21. C, D). Both the groundmass of the andesite porphyry clasts and the matrix of the andesite breccia are later altered into Mg-illite. Ihis alteration to Mg-illite is visible in hand samples as small specks or disseminations (Fig. 6.21. B), forming over the earlier chlorite1 and sericite1 phases, and manifesting as pervasive alteration in the groundmass of the andesite porphyry

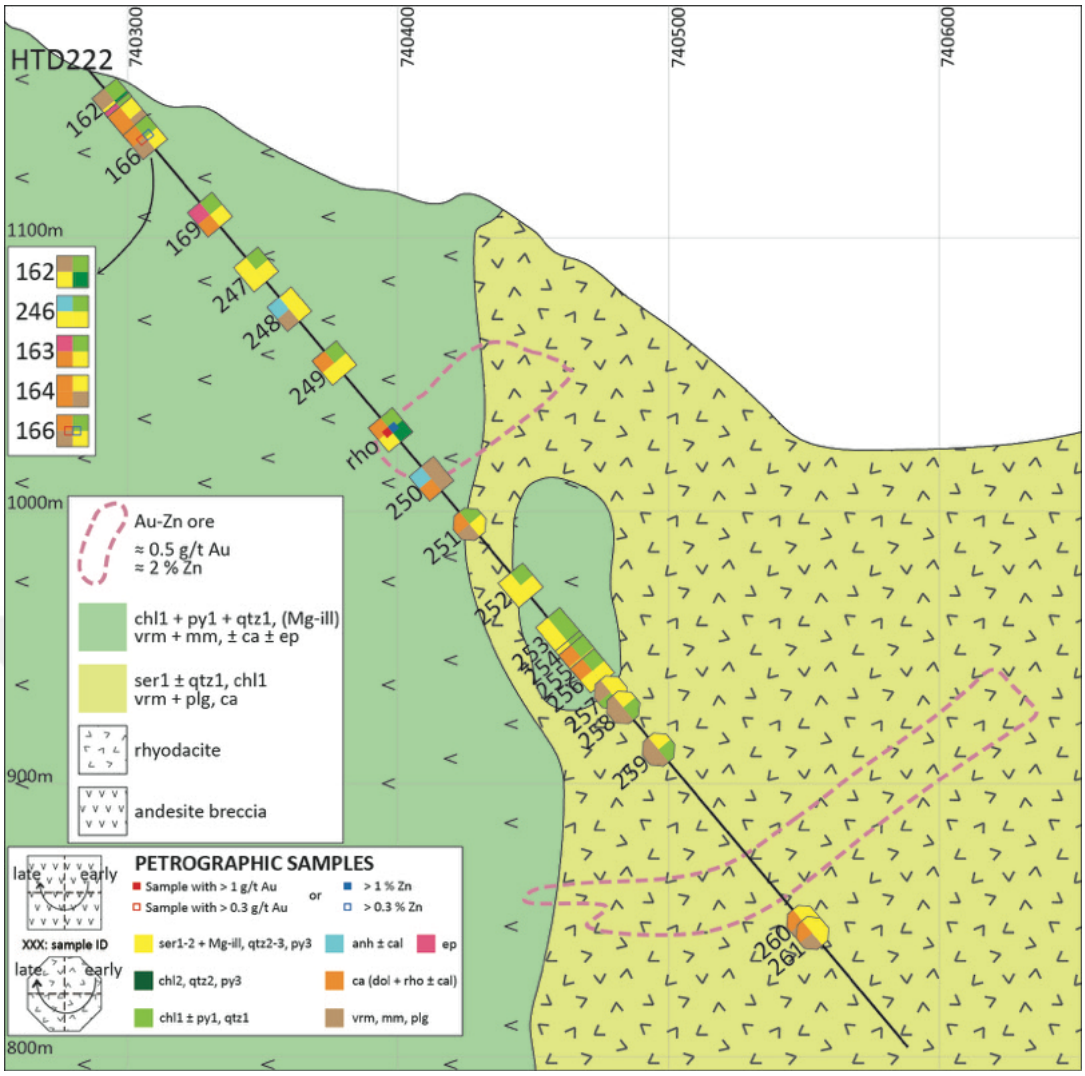


Figure 6.20. A cross section across the old workings zone showing the spatial distribution of lithological units, Au-Zn ore zones and associated hydrothermal alteration assemblages. Notice the each petrographic sample indicates the present hydrothermal alterations and their temporal evolution from early to late phases. Abbreviations: anh: anhydrite, ca: carbonate, cal: calcite, chl: chlorite, dol: dolomite, ep: epidote, ill: illite, mm: montmorillonite, plg: palygorskite, py: pyrite, rho: rhodochrosite, qtz: quartz, ser: sericite, vrm: vermiculite

clasts (Fig. 6.21. C, D). While sericite1 alteration appears to selectively alter the plagioclase phenocrysts, it remains unaffected by the later Mg-illite alteration, which is confined solely to the groundmass.

Subsequent to the initial alterations of chlorite1, sericite1, and Mg-illite, comb quartz4 veins become apparent as they intersect the host andesite breccia and the pre-existing alteration phases (Fig. 6.22). These quartz4 veins are accompanied by dolomite, which fills the open spaces within the central portion of the comb quartz vein. Both the quartz4 and dolomite phases are then subjected to an overprinting epidote alteration (Fig. 6.22). The epidote crystals exhibit prismatic and acicular

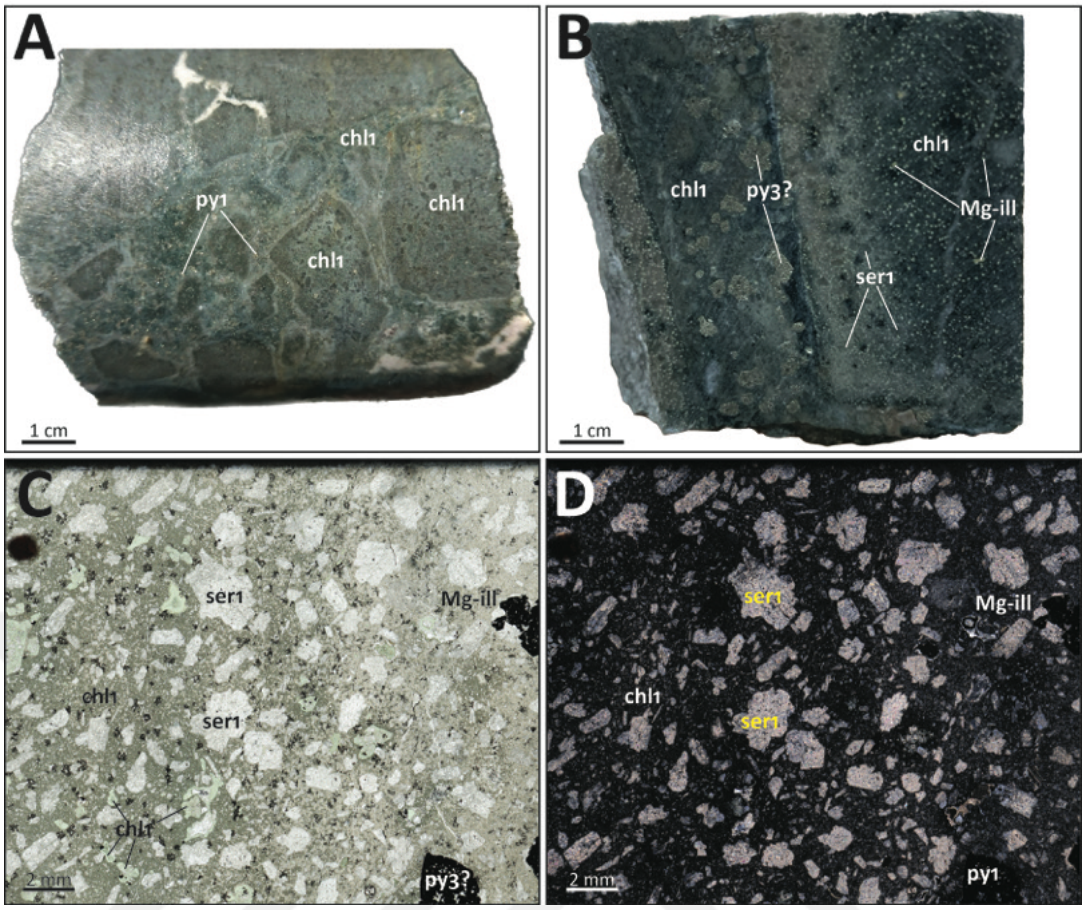


Figure 6.21. A-B) Drill core samples from drill hole HTD222-4.8 m and HTD222-143.8 m (sample EB249), respectively, targetting the old workings zone mineralization with early chlorite1-rich alteration overprinted by sericite1 and Mg-illite; (C-D) Photomicrographs of sample EB249 under PPL and XPL, respectively, displaying the early chlorite1 alteration on the groundmass of andesite porphyry clasts of andesite breccia and sericite1 alteration selectively pervasive on plagioclase phenocrysts and later Mg-illite overprint on the groundmass (abbreviations are as in Figure 6.20).

forms, establishing patches over dolomite and disseminations across the quartz4 crystals (Fig. 6.22). A fault offsets the comb quartz vein, dolomite and epidote alterations (Fig. 6.22). Subsequently, this fault plane undergoes infilling by calcite (Fig. 6.22).

Sample distribution of drill hole HTD222 in the alteration box plot resembles to the characteristic of HTD029 alteration trends (Fig. 6.11, 6.23). That is expected as both of the drill holes predominantly target the similar host rocks (andesite breccia) with a few differences. It is evident that samples from HTD222 are concentrated in the right part of the alteration box plot (Fig. 6.23). The hydrothermal alteration is characterized by early (i) chlorite1-rich alteration, (ii) chlorite2-rich alteration accompanied by pyrite and chalcopyrite, (iii) sericite2 and Mg-illite alteration (iv)

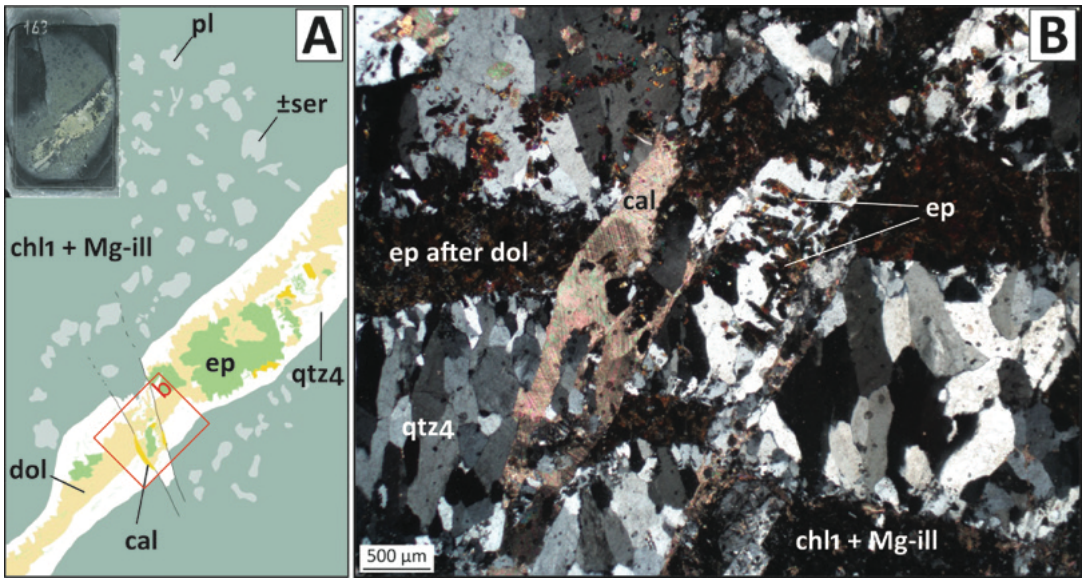


Figure 6.22. Sample EB163 displaying early pervasive chlorite1 and occasional selective sericite1 alteration on plagioclase phenocrysts cut by comb quartz4-dolomite-epidote-calcite vein, (A) Full thin section sketch, (B) Photomicrograph of the microfault displaying present hydrothermal alteration associations, XPL

carbonate, predominantly dolomite and rhodochrosite and (v) epidote and anhydrite occasionally accompanied with calcite. Presence of late calcite and epidote causes a shift in the alteration trend towards upper left part of the alteration box plot due to the addition of Ca and Fe^{3+} (Fig. 6.23).

Rhyodacite on the other hand, is altered into (i) sericite-rich assemblage which are later replaced by (ii) clay minerals, predominantly Mg-ill, palygorskite and vermiculite. Sericite-rich alteration results in an increase in K and a depletion in Na, Ca, Mg and Fe. This causes the altertion trend to shift towards right-hand side as AI increases (Fig. 6.23). The influence of clay alteration, however, causes an abrupt decrease in K that leads the CCPI values go up and the alteration trend shifts towards upwards (Fig. 6.23). Clay alteration is locally followed by carbonate, predominantly dolomite and calcite overprinting events that results in a shift in the alteration trend towards the upper left part of the alteration box plot (Fig. 6.23).

Across both host rocks and the overall sample distribution, a clear concentration of samples is observable within the central region of the alteration box plot (CCPI $<$ 77). This concentration signifies that the intensity of the hydrothermal alteration is notably lower compared to the alterations present in the main zone and south zone. This observation is also corroborated by the absence of samples with elevated Au-Cu or Au-Zn grades (Fig. 6.23).

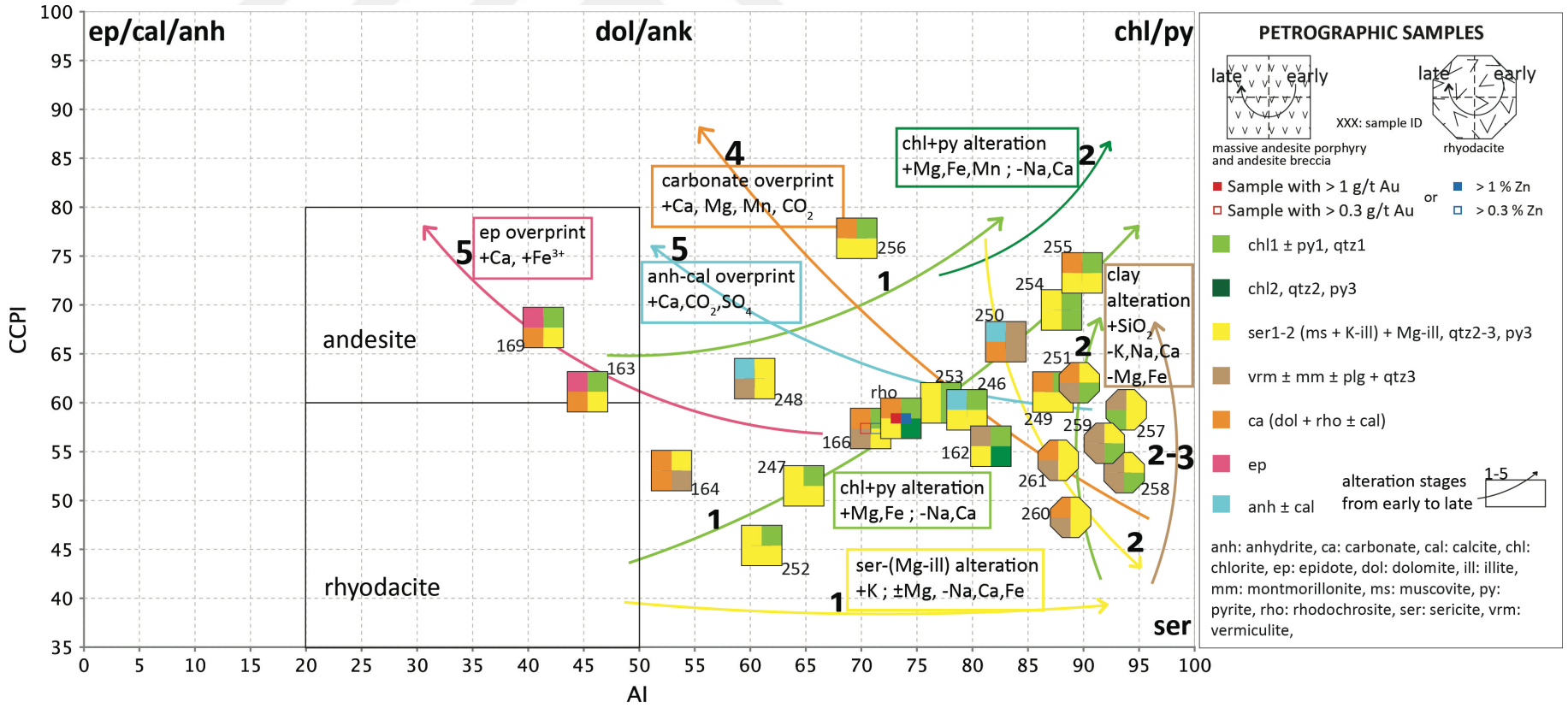


Figure 6.23. Alteration index (AI) versus chlorite-carbonate-pyrite index (CCPI) alteration box plot for drill core samples (HTD222) representing old workings zone mineralization, AI = 100 × (MgO + K_2O)/(MgO + K_2O + CaO + Na_2O) (Ishikawa et al., 1976), CCPI = 100 × (MgO + FeO)/(MgO + FeO + Na_2O + K_2O) (Large et al., 2001)

7. CHLORITE MINERAL CHEMISTRY

The chemical compositions of hydrothermal alteration minerals were analyzed using a scanning electron microprobe (JEOL 8200 Superprobe) at the UNIGE. Chlorite's mineral chemistry can be studied to see how the physical and chemical properties of the hydrothermal fluids have changed through time. The temperatures of the hydrothermal fluids can be empirically estimated from the reported mineral assemblages. Furthermore, a quantitative estimation of temperatures can be obtained through the application of chlorite composition thermometry.

Electron microprobe data from 12 samples (264 points) obtained from the Main Zone (n=11) and Old Workings Zone (n=1) are presented in (Table. 7.1). The analyzed chlorites in this study can be classified into two assemblages: "chlorite1," which represents the early and pervasive chlorite alteration, and "chlorite2" which is temporally and spatially associated to copper and gold mineralization (see the previous chapter). The chlorites from the early alteration phase are fine-grained and exhibit a light green color, while the chlorites related to mineralization are coarser-grained, flaky and typically dark green to black in color. Appendix-B2 includes scanned sections and photomicrographs that illustrate the plane-polarized, cross-polarized, and reflected light characteristics of these chlorites under a polarized microscope, as well as scanning electron microscopy images. Additionally, the electron microprobe readings are accompanied by the corresponding beam locations in Appendix-B2.

Table 7.1. Average chlorite compositions and temperature calculations

Sample ID	EB043	EB162	EB189	EB193	EB193	EB196	EB197	EB200	EB201	EB206	EB207	EB212	EB281	EB281
Chlorite classification	brunsvigite	pycnochlorite	ripidolite	ripidolite	ripidolite	ripidolite	ripidolite	ripidolite	ripidolite	ripidolite	ripidolite	ripidolite	pycnochlorite	ripidolite
Chlorite phase	chlorite1	chlorite2	chlorite2	chlorite1	chlorite2	chlorite2	chlorite2	chlorite2	chlorite2	chlorite2	chlorite2	chlorite1	chlorite1	chlorite2
Ore Zone	Main	OWZ	Main	Main	Main	Main	Main	Main	Main	Main	Main	Main	Main	Main
Drill Hole	HTD090	HTD222	HTD029	HTD029	HTD029	HTD029	HTD029	HTD029	HTD029	HTD030A	HTD030A	HTD030A	HTD088	HTD088
SWIR-FeOH (nm)	Null	Null	2257	Null	Null	2254	Null	2257	Null	2258	2258	2255	2258	2258
SiO_2	27.64	27.75	25.92	26.02	25.32	26.01	25.23	25.76	25.84	26.77	25.92	27.18	28.65	27.30
TiO_2	0.03	0.01	0.04	0.03	0.02	0.02	0.02	0.00	0.02	0.02	0.02	0.01	0.04	0.06
Al_2O_3	22.29	20.75	21.55	21.00	19.72	21.34	21.03	20.66	21.22	22.06	20.58	21.30	23.86	22.70
FeO	23.99	20.52	28.50	27.19	35.47	28.64	32.63	33.42	27.84	27.21	28.75	23.44	18.02	23.86
MnO	0.56	1.88	0.66	0.78	0.64	0.64	0.80	0.51	0.81	0.89	0.73	0.56	0.45	0.63
MgO	13.27	16.78	12.08	13.26	7.80	12.43	10.07	9.52	13.19	11.73	13.07	16.17	17.43	15.08
CaO	0.06	0.08	0.06	0.05	0.04	0.04	0.04	0.02	0.05	0.04	0.08	0.05	0.05	0.04
Na_2O	0.02	0.01	0.09	0.02	0.02	0.02	0.01	0.01	0.01	0.02	0.01	0.01	0.01	0.01
K_2O	0.45	0.11	0.05	0.01	0.05	0.17	0.01	0.03	0.01	0.07	0.01	0.18	0.04	0.02
Cr_2O_3	0.01	0.01	0.01	0.00	0.00	0.01	0.01	0.01	0.01	0.01	0.01	0.01	0.01	0.01
Total	88.33	87.89	88.96	88.38	89.09	89.32	89.84	89.93	88.89	88.81	89.18	88.92	88.55	89.71
Number of cations on the basis of 28-oxygen														
Si^{iv}	5.66	5.69	5.46	5.49	5.55	5.46	5.40	5.51	5.44	5.57	5.47	5.56	5.64	5.52
Al^{iv}	2.34	2.32	2.54	2.51	2.45	2.54	2.60	2.49	2.56	2.43	2.53	2.44	2.36	2.48
Al^{vi}	3.10	2.71	2.82	2.72	2.65	2.76	2.71	2.72	2.70	3.02	2.60	2.71	3.22	2.95
Mg^{vi}	4.05	5.12	3.79	4.17	2.55	3.89	3.21	3.03	4.13	3.64	4.11	4.93	5.11	4.54
Fe^{vi}	4.11	3.52	5.02	4.80	6.50	5.03	5.84	5.97	4.90	4.74	5.08	4.01	2.97	4.03
Mn^{vi}	0.10	0.33	0.12	0.14	0.12	0.11	0.15	0.09	0.14	0.16	0.13	0.10	0.07	0.11
Fe/(Fe+Mg)	0.50	0.407	0.57	0.54	0.72	0.56	0.65	0.66	0.54	0.57	0.55	0.45	0.37	0.47
T (°C) - (Cathelineau and Nieva, 1985)	330.1		330.0			328.9	341.7	331.6	330.1	317.0	326.9	309.8	295.7	316.1
T (°C) - (Cathelineau, 1988)	314.2	311.0	347.7	342.6	332.7	346.8	357.0	339.5	351.0	328.8	345.1	330.7	318.6	337.9
T (°C) - (Jowett, 1991)	319.0	313.0	354.8	348.7	344.8	353.7	366.6	349.8	357.3	335.6	351.8	334.1	318.4	341.5

OWZ: Old workings zone

Chlorites display a range of compositions, with Mg-rich chlorite predominating in the early phase alterations (chlorite1) and Fe-rich chlorite (chlorite2) associated with mineralization events. Apart from the early phase samples, chlorites exhibit ripidolite compositions with Fe/(Fe + Mg) values ranging from 0.45 to 0.66 (Table. 7.1). Sample EB281 comprises two distinct populations of chlorite compositions: Mg-rich pycnochlorite in the early phase with an average Fe/(Fe+Mg) value of 0.37, and Fe-rich ripidolite in the mineralization phase with an average Fe/(Fe+Mg) value of 0.47.

The non-stoichiometric properties of chlorite make it an intriguing geothermometer, as the composition of chlorite holds valuable insights into the specific physicochemical conditions present during its formation. A comprehensive evaluation of temperature estimation techniques utilizing chlorite chemistry was conducted (Hayes, 1970; Walshe, 1986; Cathelineau, 1988; Kranidiotis and MacLean, 1987; De Caritat et al., 1993) and multiple calculation methods for compositional geothermometers were applied to the chlorite analyses carried out in this study. The outcomes of this comparative analysis demonstrate that no individual chlorite geothermometer exhibits satisfactory performance across the entire spectrum of natural conditions, including varying temperatures, bulk rock composition, coexisting mineral assemblages, Fe/(Fe + Mg) ratios, fO_2 levels, and so on. Consequently, chlorite geothermometry results from three distinct approaches were utilized to account for these limitations (Cathelineau and Nieva, 1985; Cathelineau, 1988; Jowett, 1991).

Prior to the microprobe work, a petrographic study (see the previous chapter and Appendix-B2) revealed that chlorites in both Main Zone and Old Workings Zone, whether in the early phase or during later mineralization events, are spatially associated with quartz and occasionally Al-rich silicates such as sericites and zeolites. Chlorite, in assemblage with quartz and an additional Al-rich mineral phase, is considered to lie along the chlorite Al-saturation boundary (Kranidiotis and MacLean, 1987) and a correction is required for the calculated tetrahedral aluminum Al^{iv} based on a 28-oxygen formula (eq. 7.1). The temperature of chlorite precipitation can be estimated based on the Al^{iv} concentration of the chlorites, using the equation (eq. 7.2) of Cathelineau and Nieva (1985).

$$\mathrm{Al}^{\mathrm{iv}}_{\mathrm{corrected}} = \mathrm{Al}^{\mathrm{iv}}_{28-\mathrm{oxygen}} + 0{,}7 \cdot \left(\frac{\mathrm{Fe}^{2+}_{28-\mathrm{oxygen}}}{\mathrm{Fe}^{2+}_{28-\mathrm{oxygen}} + \mathrm{Mg}^{2+}_{28-\mathrm{oxygen}}}\right) \tag{7.1}$$

$$\mathrm{T}\ ^{\circ}\mathrm{C} = 106 \cdot \mathrm{Al}^{\mathrm{iv}}_{\mathrm{corrected}} + 18 \tag{7.2}$$

Cathelineau (1988) proposed that Equation 7.3 has the potential to serve as a widely applicable chlorite geothermometer in various geological settings, including diagenetic, hydrothermal, and metamorphic environments. This is due to the observation that the $\mathrm{Al}^{\mathrm{iv}}_{14-\mathrm{oxygen}}$ value, which is crucial for the equation, seems to be unaffected by rock lithology (demonstrated in both Los Azufres andesites and Salton Sea feldspathic sandstone) and fluid composition.

Jowett (1991) proposed a correction approach comparable to Kranidiotis and MacLean (1987), which involved an isothermal normalization of Fe/(Fe + Mg) based on chlorite compositions from Salton Sea and Los Azufres (eq. 7.4).

$$\mathrm{T}\ ^{\circ}\mathrm{C} = 321.98 \cdot \mathrm{Al}^{\mathrm{iv}}_{14-\mathrm{oxygen}} - 61.92 \tag{7.3}$$

$$\mathrm{T}\ ^{\circ}\mathrm{C} = 319 \cdot \left(\mathrm{Al}^{\mathrm{iv}}_{14-\mathrm{oxygen}} + 0.1 \cdot \left(\frac{\mathrm{Fe}^{2+}_{14-\mathrm{oxygen}}}{\mathrm{Fe}^{2+}_{14-\mathrm{oxygen}} + \mathrm{Mg}^{2+}_{14-\mathrm{oxygen}}}\right)\right) - 69 \tag{7.4}$$

The estimated temperatures (eq. 7.2, 7.3 and 7.4) for chlorite precipitation in Hod Maden Main Zone mineralization (Table. 7.1; Appendix-B2) are 307.1 ± 11.5 °C for the early phase chlorites and 338.2 ± 28.4 °C for chlorites associated with the mineralization events. (Table. 7.1).

8. MINERALIZATION

The Hod Maden is a high-grade gold-copper deposit. It contains ∼4 Moz of AuEq and represents one of the highest-grade gold-copper (8.8 g/t Au and 1.5% Cu) discoveries made globally in recent years (Alizade and Aksoy, 2019; Laskowski, 2021). The orebody is made up of north-north-south striking mineralization comprising two main sections: a northern area known as the main zone and a continuous southern zone (Fig. 1.2 A, B). Additionally, there is a third mineralized area located 500 m further south known as the old workings zone (Fig. 1.2 A). The bulk of the orebody lies beneath the main zone and south zone contains limited economic mineralization. Hod Maden deposit also comprises a stratabound and disseminated Zn ± Pb (sphalerite ± galena) mineralization with a resource of 2.8 Mt @ 4.0% Zn that flanks the gold-copper mineralization to the east and locally to the west (Laskowski, 2021).

The main zone deposit is distinguished by its sub-vertical orientation, stretching around 400 meters in length (N-S), and possessing a true thickness of 50-70 meters, while extending more than 300 meters down-dip. On the other hand, the south zone is also sub-vertical, approximately 200 meters in length, and has a depth of 300 meters, but it exhibits notably reduced thickness and sporadic occurrences of economic mineralization. Main zone and south zone ore bodies are hosted by chlorite2-altered andesite breccia and sericite-2 altered dacite breccia, respectively. Moreover, old workings zone mineralization is hosted by chlorite1 altered andesite breccia and silicified rhyodacite dome.

8.1. Main Zone Mineralization

Main Zone exhibits two primary high-grade gold and copper mineralization styles. The first is massive (to semimassive) sulfide mineralization consiting of gold-bearing pyrite2 and chalcopyrite1 with secondary chalcocite (in much lesser

amount). It represents the highest-grade mineralization (typically >15 g/t Au but locally >100 g/t Au) at Hod Maden and lies along the eastern margin of the Main Zone (Fig. 6.1). The second style is multiphase breccia characterized by (i) chlorite2, pyrite3, chalcopyrite2 and quartz2; (ii) quartz3, clay minerals (kaolinite, dickite, vermiculite, palygorskite, halloysite), jasper-hematite and carbonates predominantly siderite and (iv) late comb quartz4-dolomite-pyrite4-chalcopyrite3 phases. Pervasive anhydrite alteration and occasioaly calcite postdates and overprints all the pre-existing mineralization phases.

8.1.1. Massive (to semi-massive) sulfide mineralization

The highest-grade gold and copper mineralization of Hod Maden is spatially associated with massive (to semi-massive) sulfide orebody. It is marked by a pyrite2 content >60%, along with the presence of significant chalcopyrite (Fig. 8.1). Upon close inspection of the drill core with a hand lens, it can be observed that chalcopyrite1 occasionally replaces pyrite2. The orebody exhibits a distinct comma-like, lens-shaped, sigmoidal morphology, occurring between the andesite breccia with chlorite2-rich alteration and the volcanosedimentary rocks (Fig. 6.1). The thickness of the massive sulfide ore body is greatest near the surface and gradually decreases with depth. The mineralization is not only constrained by the particular lithologies but is also confined by the fault segments of the Hod main fault zone (Fig. 6.1). The massive sulfide ore body undergoes deformation due to its spatial association with the fault zone. The deformation is evident in the form of brecciation and fractures (Fig. 8.1). The fractures and open spaces are predominantly filled with anhydrite patches (Fig. 8.1 B) or veinlets (Fig. 8.1 C) . Furthermore, SWIR data indicates the presence of kaolinite, which is closely associated with the massive sulfide lens and major fault planes.

8.1.2. Gold mineralization associated with chlorite2-rich alteration

Following the massive sulfide orebody, a significant portion of the remaining high-grade gold-copper mineralization in the Main Zone is hosted by andesite

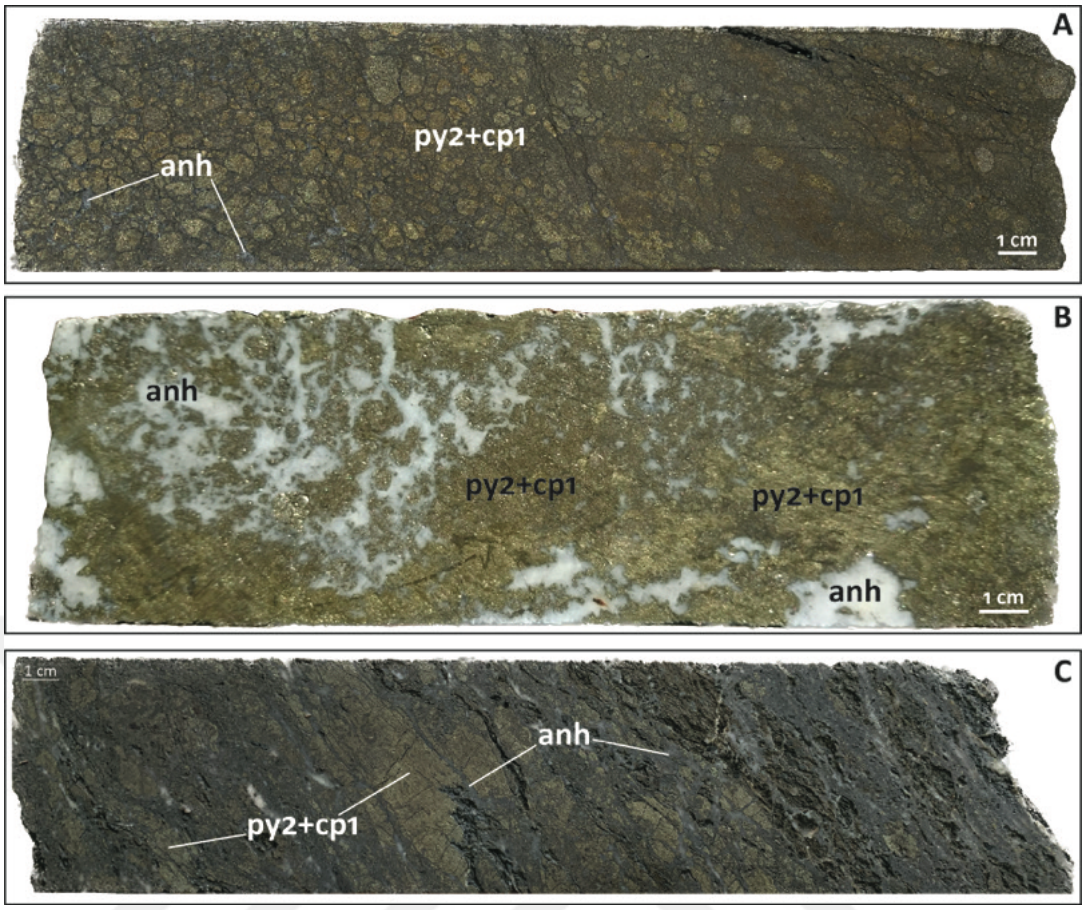


Figure 8.1. **(A) Deformed and brecciated massive sulfide mineralization consisting of pyrite and chalcopyrite, drill hole HTG02-79.2 m, (B) Brecciated semi-massive chalcopyrite-pyrite mineralization, drill hole HTD029-557.3 m. Notice that matrix is occupied by anhydrite. (C) Deformed and brecciated massive sulfide mineralization consisting of pyrite and chalcopyrite with anhydrite overprint occupying fractures, drill hole HTD05-149 m. Abbreviations: anh: anhydrite, cp: chalcopyrite, py: pyrite**

breccia, exhibiting intense chlorite-2-rich alteration (Fig. 6.1). This study extensively documents the spatial and temporal associations between the chlorite-2-bearing alteration phases and the pyrite-3, chalcopyrite-2, and quartz-2 assemblage, which are characteristic of the high-grade gold-copper mineralization. The investigation of these relationships is documented through various methods, including drill core logging (Fig. 8.2 A) and thin section petrography (Fig. 8.2 B-E). Furthermore, the scanning electron microscopy (SEM) images acquired during the electron probe microanalysis (EPMA) mineral chemistry studies on chlorites (Fig. 6.5), and the backscattered electron (BSE) and quantitative evaluation of minerals by scanning electron microscopy (QEMSCAN) images of gold-bearing grains confirm the spatio-temporal relationship between chlorite-2 alteration and gold-copper mineralization (Fig. 8.3).

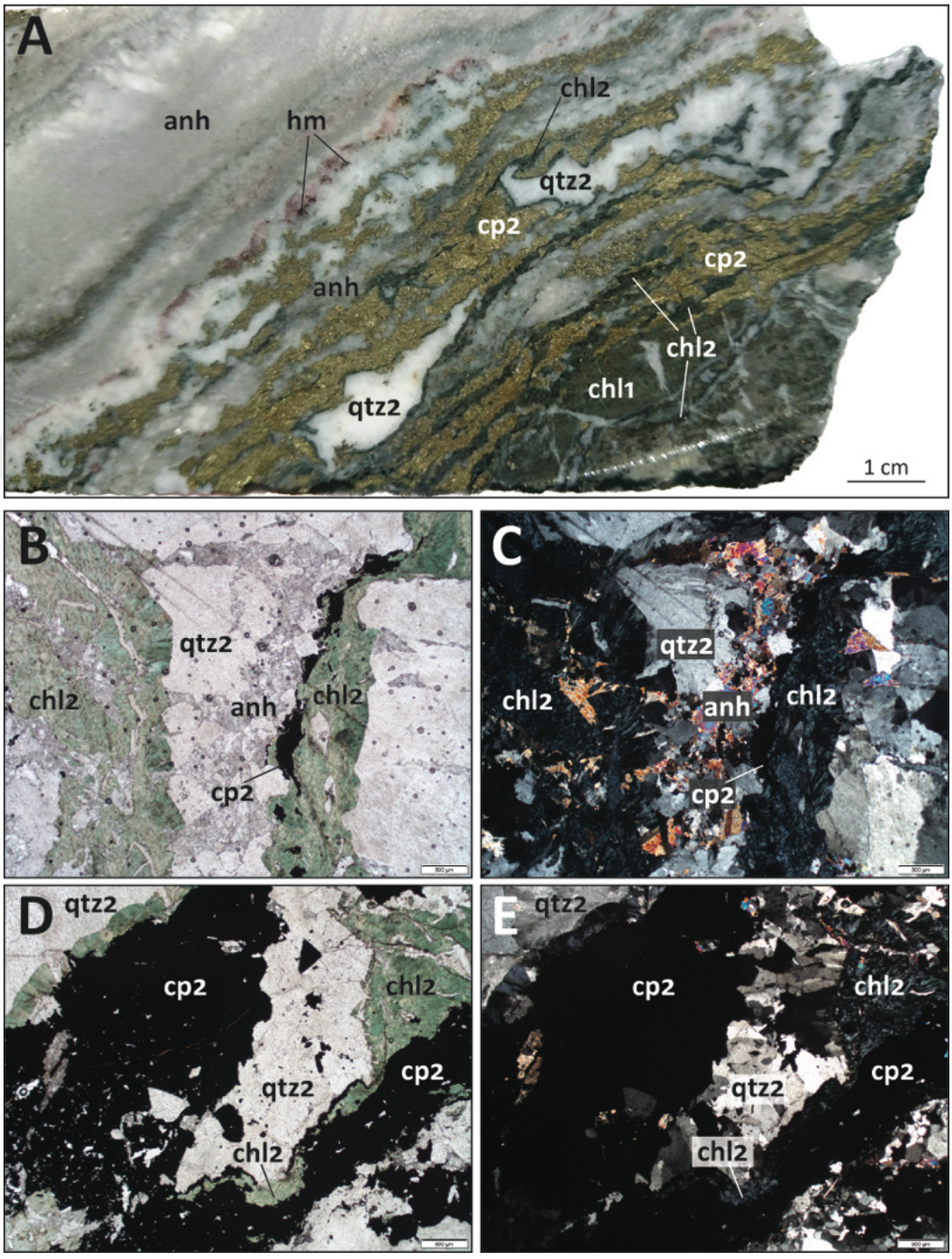


Figure 8.2. **Sample EB197, drill hole HTD029-507.1 m, representing Main Zone chalcopyrite2 (±pyrite3) mineralization associated with chlorite2-quartz2 phase and overprinted by anhydrite. Notice the presence of hematite. (A) drill core sample, (B, D) Photomicrograph in PPL and (C, E) in XPL. Abbreviations: anh: anhydrite, cp: chalcopyrite, chl: chlorite, hm: hematite, qtz: quartz**

In Figure 8.2 A, andesite breccia with early chlorite1-rich alteration is replaced by chlorite2-chalcopyrite2±pyrite3-quartz2 assemblage. Weak hematite overprint on chalcopyrite is present. A late anhydrite phase overprints all the pre-existing phases. Thin section photomicrographs of the same sample under PPL (Fig. 8.2 B, D) and XPL (Fig. 8.2 C, E) confirmed the spatial association of chalcopyrite2±pyrite3 mineralization and chlorite2 alteration.

BSE and QEMSCAN images of Au-bearing grains represent the gold mineralization associated with chlorite2-quartz2 (Fig. 8.3 A), with pyrite3 (Fig. 8.3 B, C) and quartz2-pyrite3-sericite3 (Fig. 8.3 D) assemblages. Gold particles were analyzed by manual energy dispersive spectroscopy (EDS) and they occur as native gold (Au^0) with no Ag ($\leq 4\%$) or Te (Fig. 8.3; Meng, 2019).

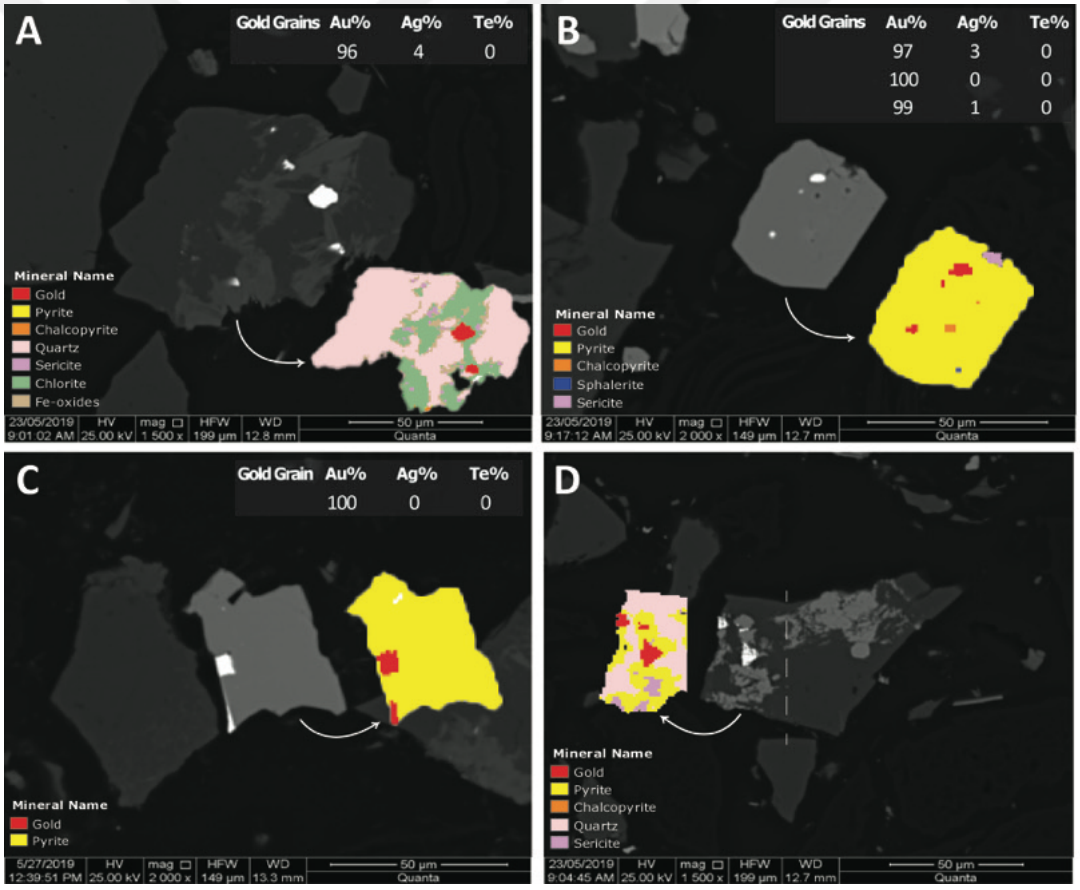


Figure 8.3. BSE and QEMSCAN images of gold grains characterizing main zone mineralization from selected composite samples representing drill hole intervals (Meng, 2019), (A) and (B) HTD110, 190-220 m, (C) HTD111, 358-370, (D) HTD110, 190-220 m

8.1.3. Gold mineralization associated with chalcopyrite-2

Gold mineralization is found to be in spatial association with the massive sulfide lens, representing the earliest mineralization phase, and with the subsequent chlorite2-quartz2-pyrite-3 assemblage. Within this assemblage, gold particles are observed in chlorite2-quartz2, pyrite3 and pyrite3-quartz2 grains. In addition to these two gold mineralization phase, ore microscopy studies revealed that a chalcopyrite phase (chalcopyrite2) replaces pyrite3. The reflected light photomicrograph of the polished sample (EB197, HTD029-507.1 m) shows deformation of pyrite3, and fractures are filled with chalcopyrite2 (Fig. 8.3 A). Moreover, detailed BSE and QEMSCAN images reveal that chalcopyrite2 replaces pyrite3 as patches or veinlets, and gold particles are observed to precipitate along with chalcopyrite2 (Fig. 8.3 B-D). Gold particles from a composite sample characterizing a 30 m-interval of HTD110 representing main zone andesite-breccia hosted multiphase mineralization were analyzed by manual EDS and resulted in 95 %Au and 95 %Ag with no Te. Whereas, gold particles representing a composite sample targetting a 13 m-interval of HTD090 (Fig. 6.1) have 88-85 %Au and 15-12 %Ag with no Te.

8.1.4. Gold mineralization associated with Fe-oxide assemblage

In the preceding subchapters focusing on the main zone mineralization phases, the Au-Cu mineralization related to (i) massive sulfides, (ii) chlorite2-pyrite3-quartz2, and (iii) chalcopyrite2 associations were reported. Apart from these Au-Cu associations, there is evidence of an oxidation event leading to the overprinting of hematite and goethite on pre-existing pyrite3 and chalcopyrite2. It is well documented in the hydrothermal alteration chapter that chlorite2-pyrite3-chalcopyrite2 assemblage is overprinted by quartz3-sericite-clay minerals (predominantly kaolinite, dickite and saponite) accompanied by hematite and goethite ±siderite (Fig. 6.7). While chlorites are partly or pervasively altered into sericite and clay minerals, sulfide minerals (pyrite3 and chalcopyrite2) are altered into hematite and goethite ±siderite. Figure 8.5 A, B, clearly displays the hematite-goethite accompanied by quartz3 replacement over pyrite3 and

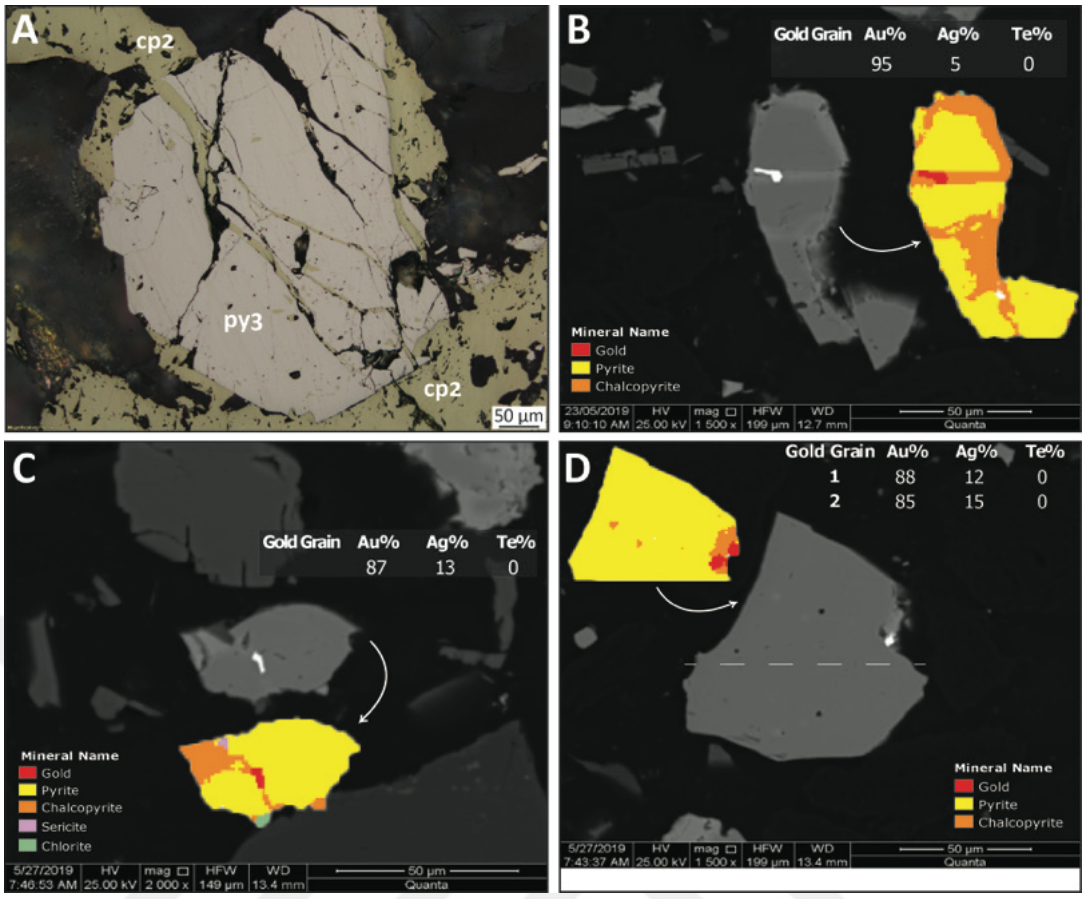


Figure 8.4. **(A) Polished sample (EB197, HTD029-507.1 m) reflected light photomicrograph representing chalcopyrite2 replacing fractures along pyrite3 (B, C and D) BSE and QEMSCAN images of gold grains from composite samples from (B) HTD110-190-220 m, (C, D) HTD090-290-303 m representing main zone gold mineralization associated with chalcopyrite2 replacing pyrite3**

chalcopyrite2. Hematite and goethite are formed commonly in rosettes; radiating fibrous crystals (Fig. 8.5 A, B and D). The spatial relationship of gold particles with goethite and chalcopyrite2±pyrite±siderite association (Fig. 8.5 C) and quartz3-goethite-siderite association is shown (Fig. 8.5 D). Gold particles from a composite sample characterizing a 12 m-interval of HTD111 representing main zone andesite-breccia hosted multiphase mineralization were analyzed by manual EDS and resulted in ∼100 %Au with with no Ag ($\leq 2\%$) or Te.

8.1.5. Geologic and geochemical profiles of main zone mineralization

Drill hole data, comprising lithological and petrographic descriptions of core samples, as well as geochemical data containing concentrations of Au, Ag, Cu, Pb,

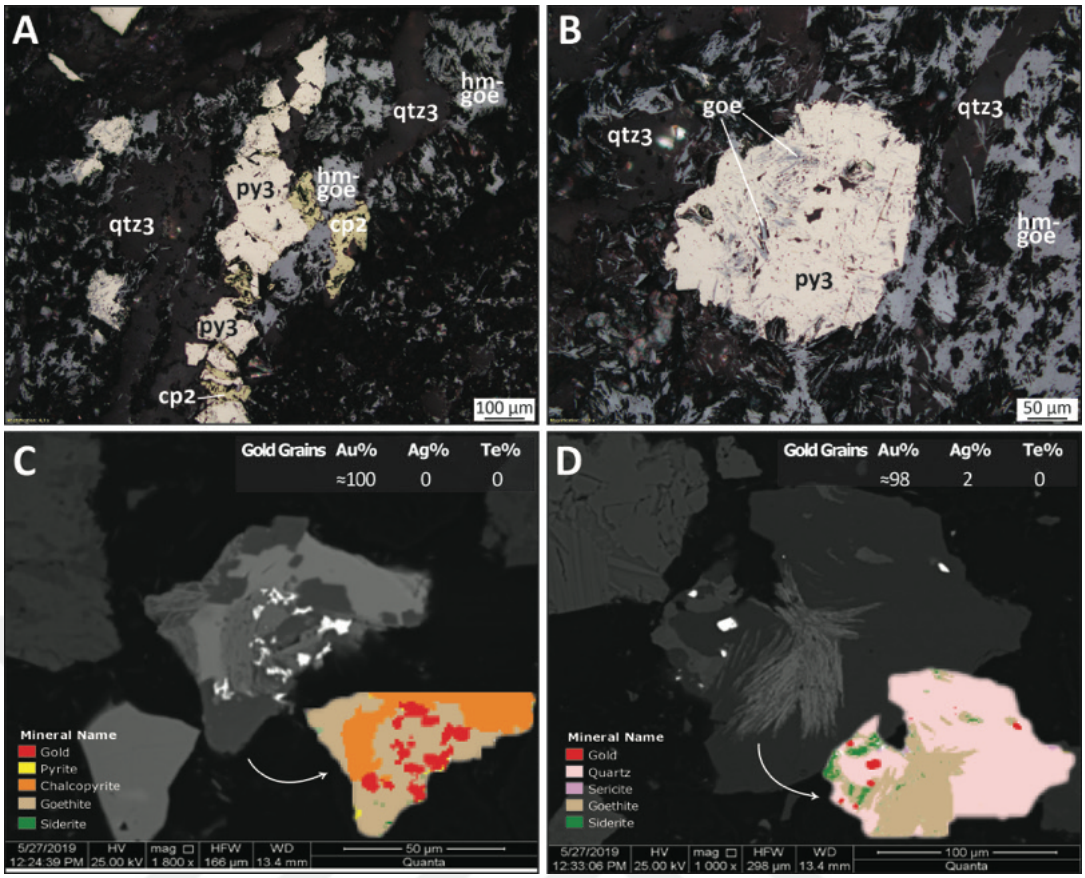


Figure 8.5. **(A, B) Polished samples (EB198, HTD029-521.7 m) reflected light photomicrographs representing main zone mineralization, goethite overprint on pre-existing pyrite3-chalcopyrite2 and chalcoyprite2, respectively. (C, D) BSE and QEMSCAN images of gold grains associated with goethite, siderite and quartz3 phases characterizing main zone mineralization from selected composite samples, HTD111, 358-370**

Zn, and alteration indices such as AI alteration index (AI = 100 × [MgO + K_2O]/[MgO + K_2O + CaO + NaO]; Ishikawa et al., 1976), chlorite-carbonate-pyrite index (CCPI = 100 × [MgO + FeO]/[MgO + FeO + Na_2O + K_2O]; Large et al., 2001), Ba/K_2O index [(Ba/100)/((Ba/100) + K_2O) × 100; Yergeau et al., 2022], Na/alkalis index (Na_2O/[Na_2O + K_2O + CaO] × 100; Yergeau et al., 2022), and MnO/MgO index ([MnO × 10]/[(MnO × 10) + MgO] × 100; Yergeau et al., 2022), have been utilized to generate geologic and geochemical profiles. The Na/alkalis index traces Na enrichment or depletion relative to the other alkalis as a proxy for the alteration intensity and type of clay alteration; the Ba/K_2O index traces Ba enrichment relative to K, as a proxy for the precipitation of Ba-rich sulfates or phyllosilicates; the MnO/MgO index represents the presence of Mn-rich carbonates (mainly rhodochrosite) and phyllosilicates, predominantly chlorite.

The profiles depict the changes in chemistry concerning metal grades, lithological

variations, and hydrothermal alteration phases, aiming to illustrate the evolution of hydrothermal alterations and their connection with mineralization phases. The assay values for metals and the calculated indices are presented in the table provided in the Appendix-A4.

The mineralization at the Main zone is investigated using three drill holes: HTD018, HTD029, and HTD090 (Fig. 6.1). Geologic and geochemical profiles are created for each drill hole, building upon the alteration box plots (Fig. 6.10, 6.11, 6.12). The previous hydrothermal alteration chapter has already revealed the changes in alteration trends over time, and in this chapter, the findings with assay values and additional indices will be complemented to illustrate the evolution of mineralization and associated hydrothermal alteration phases.

The geologic and geochemical profiles of drill hole HTD018 and HTD029 (traces shown in Fig. 6.1) reveal the spatial association of high-grade Au (up to 40.3 g/t) and Cu (up to 7.5%) mineralization with andesite breccia exhibiting intense chlorite2-rich alteration, accompanied by quartz2-3, clay, and Fe-oxide phases (Fig. 8.6, 8.7). Within this interval of high-grade Au-Cu mineralization, CCPI values are high, AI values are low, and the Ba/K_2O index values are relatively elevated (Fig. 8.6, 8.7). The Na/alkalis index values are depleted, suggesting that the intense hydrothermal alterations in these zones have caused advanced Na-leaching. However, it is noteworthy to highlight the elevated Na/alkalis values in unmineralized andesite breccia with chlorite1-rich alteration (Fig. 8.6, 8.7). This strong MnO/MgO index is in agreement with the distal alteration characterized by Mn-rich carbonates and chlorite. Zn mineralization is hosted by sericite-clay altered dacite breccia. While Pb values increase abruptly along with Zn values, the Pb grades remain low (below 0.15%, Fig. 8.6). Additionally, MnO/MgO index values increase parallel to the Pb-Zn values in the dacite breccia (Fig. 8.6).

The profiles of drill hole HTD090 (traces shown in Fig. 6.1) share similar characteristics with the profiles of HTD018 and HTD029. High grade Au-Cu mineralization (up to 66.1 g/t Au and 5.5 % Cu) is spatially associated with andesite breccia with chlorite2-rich alteration and presence of significant clay minerals and hematite-goethite. The Au-Cu mineralization is concordant with increased CCPI and decreased AI values, and elevated Ba/K_2O index values (Fig. 8.8). High grade

Zn-Pb mineralization (up to 27.7 % Zn and 3.3 % Pb) is hosted by volcanosedimentary rocks with anhydrite-gypsum alteration (Fig. 8.8). This interval also in agreement with the increase in Ag grades (up to 58 g/t) and MnO/MgO index values (Fig. 8.8). Abrupt enrichment in Na/alkalis index towards the alteration boundary within the volcanosedimentary rocks (depth: 110-125 m) is noteable (Fig. 8.8).

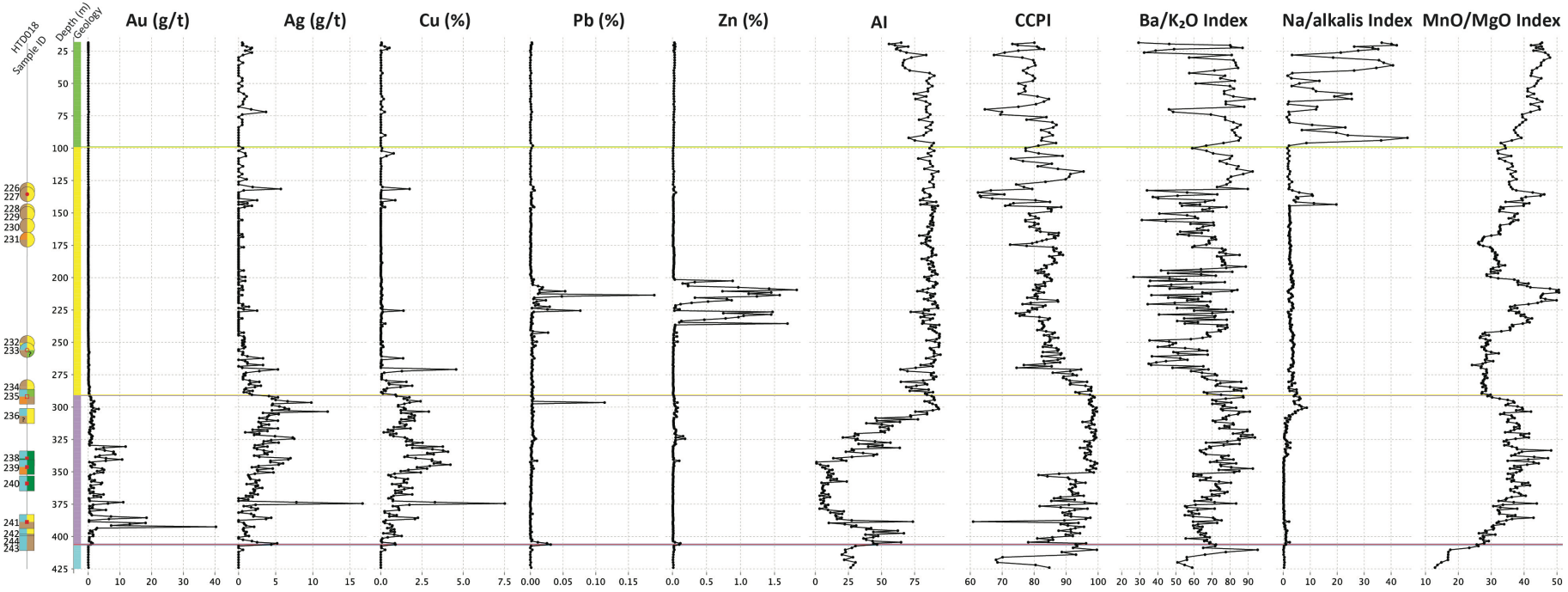


Figure 8.6. **Geologic and geochemical profiles of drill hole HTD018 (trace and legend shown on Fig. 6.1) that intersects Main Zone mineralization. The location and distribution of the analyzed samples and results are indicated by black horizontal lines. All the lithogeochemical data and Au, Ag, Cu, Zn and Pb assay values are from Artmin Madencilik. AI = alteration index (Ishikawa et al., 1976), CCPI = chlorite-carbonate-pyrite index (Large et al., 2001).**

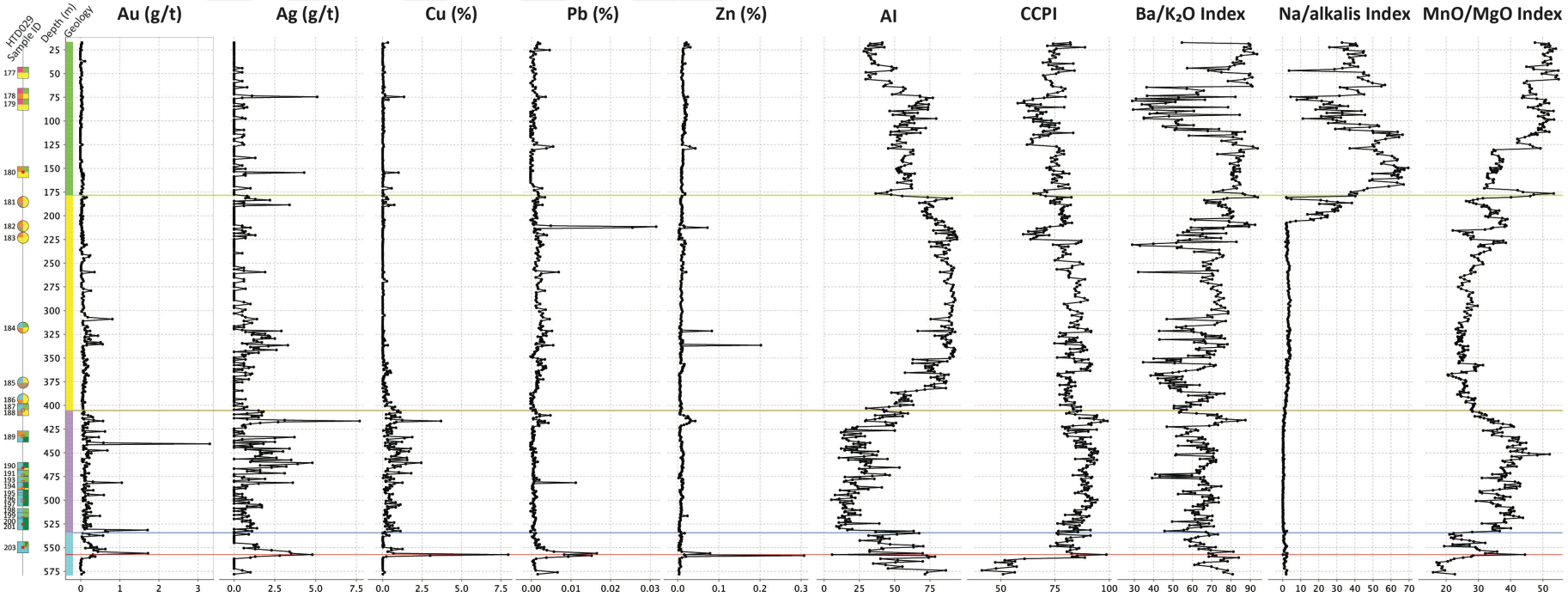


Figure 8.7. **Geologic and geochemical profiles of drill hole HTD029 (trace and legend shown on Fig. 6.1) that intersects Main Zone mineralization. The location and distribution of the analyzed samples and results are indicated by black horizontal lines. All the lithogeochemical data and Au, Ag, Cu, Zn and Pb assay values are from Artmin Madencilik. AI = alteration index (Ishikawa et al., 1976), CCPI = chlorite-carbonate-pyrite index (Large et al., 2001).**

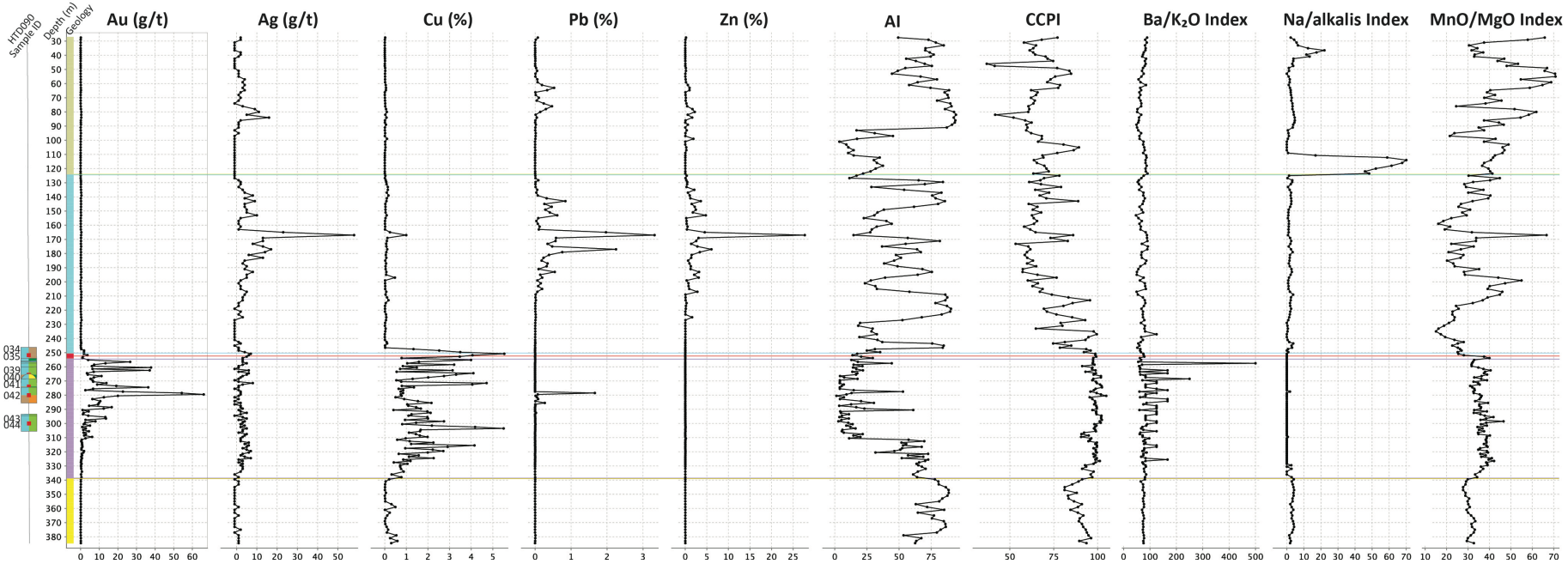


Figure 8.8. **Geologic and geochemical profiles of drill hole HTD090 (trace and legend shown on Fig. 6.1) that intersects Main Zone mineralization. The location and distribution of the analyzed samples and results are indicated by black horizontal lines. All the lithogeochemical data and Au, Ag, Cu, Zn and Pb assay values are from Artmin Madencilik. AI = alteration index (Ishikawa et al., 1976), CCPI = chlorite-carbonate-pyrite index (Large et al., 2001).**

8.2. South Zone Mineralization

South zone contains a supplementary quantity of Au-Cu (2.52 Mt @ 3.5 g/t Au + 0.3% Cu for 284,000 Oz Au + 7,500 t Cu or 341,000 Oz AuEq; Alizade and Aksoy, 2019) and Zn mineralization, distinct from the main zone . The Au-Cu mineralization is present in both dacite breccia and volcanosedimentary rocks, while Zn mineralization is exclusively hosted by the volcanosedimentary rocks (see Fig. 6.13). The orebody in the south zone is sub-vertical, spanning around 200 meters in length, and extending to a depth of 300 meters.

Dacitic host rock is characterized by a dacite breccia, a monomictic breccia, with clasts of spherulitic dacite lavas and syn-volcanic intrusions. Mineralized volcanosedimentary rocks, on the other hand, characterized by mass flow deposits with dacite and massive sulfide clasts, and dacitic lava flows and volcaniclastic rocks. The predominant hydrothermal alteration assemblages associated with Au-Cu mineralization consists of sericite2, quartz2-3 and clay minerals predominantly kaolinite and dickite.

In the south zone, the mineralization initiates with the deposition of sphalerite1 and galena1, which replaces the early sericite1-rich alteration. Subsequently, the intensity of silicification increases, and the dominance of quartz veining becomes more prominent. Elevated gold and copper grades are both temporally and spatially related to widespread silicification (quartz2) and the presence of zones with quartz3 veins and veinlets, along with sericite2 and kaolinite-dickite, respectively. Within this phase, sulfides like pyrite3 and chalcopyrite2 are hosted. Following this stage, the mineralization is occured as comb quartz4 veins containing sphalerite2-pyrite4-chalcopyrite3.

As anticipated, increased copper values are linked to areas with chalcopyrite enrichment, while zinc mineralization is attributed to the precipitation of sphalerite, and lead is associated with the presence of galena. To comprehensively understand the mineralization at the south zone, it is crucial to investigate and elucidate the spatial and temporal relationships of these ore minerals with the host dacite breccia and the associated hydrothermal alteration phases.

Sample EB124 is particularly noteworthy and proves to be highly beneficial as it

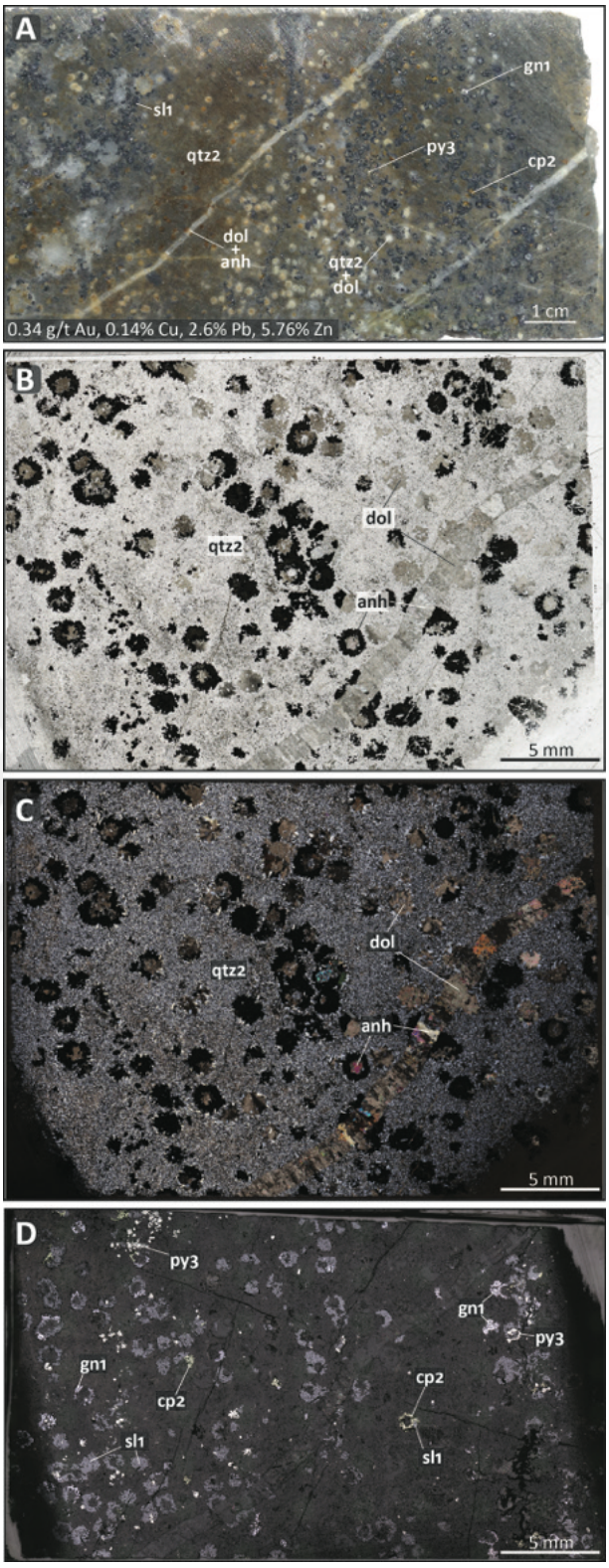


Figure 8.9. **Sample EB124 from drill hole HTD021-215.9 m, representing South Zone galena-sphalerite-pyrite-chalcopyrite mineralization accompanied by quartz, dolomite and anhydrite replacing spherulitic dacite breccia, (A) drill core slab, (B) full thin section scan photomicrograph (PPL), (C) full thin section scan photomicrograph (XPL), (D) polished section, reflected light image. anh: anhydrite, cp: chalcopyrite, dol: dolomite, gn: galena, py: pyrite, sl: sphalerite**

showcases the preserved original texture of the volcanosedimentary rocks, including the spherulitic texture characteristic of the dacitic lava flows (Fig. 8.9 A). Additionally, it presents the hydrothermal alteration minerals, such as quartz2, dolomite, and anhydrite (Fig. 8.9 B, C). The exceptional features of this sample enable clear observations of the crosscutting, replacement, and overprinting relationships between sphalerite1, galena1, pyrite3, and chalcopyrite2 (Fig. 8.9 D). The sample represents the 1-meter interval of the drill hole HTD021, 215-216 m, and the metal assay values are as follows: 0.34 g/t Au, 0.14%Cu, 2.6%Pb and 5.8%Zn (Fig. 8.9 A; Appendix A-4).As mentioned in the hydrothermal alteration chapter, the south zone experiences the replacement of dacitic rock spherules by the sericite1-quartz1-pyrite2 assemblage. In sample EB124, the earliest phase observed replacing the spherules is sphalerite1 (Fig. 8.9 A, D), followed by the subsequent replacement by galena1, pyrite3, and chalcopyrite2 in a sequential order (Fig. 8.9 D). Concurrently, the precipitation of sulfides is accompanied by the presence of quartz2 (Fig. 8.9 C). The later stages of the hydrothermal activity are characterized by the occurrence of dolomite and anhydrite, evident as open space fillings within the spherules or as dolomite-anhydrite veinlets that crosscut all the pre-existing mineralization and alteration phases (Fig. 8.9 A-C).

Sample EB079 (HTD021-20.3 m) is chosen to exemplify the late-stage mineralization, which is characterized by the presence of sphalerite2-pyrite4-chalcopyrite3 phase accompanied by comb quartz4 veins and dolomite with an open space filling characteristic. The earliest sulfide phase is the sphalerite2, which exhibits partial replacement by pyrite4 and chalcopyrite3 (Fig. 8.10 A). Both sphalerite2 and pyrite4 are further overprinted by quartz4-chalcopyrite2 phase (Fig. 8.9 A, B). Dolomite occupies the open spaces within the central part of the comb quartz4-sphalerite2-pyrite3-chalcopyrite2 vein. The growth zones of dolomite crystals are clearly visible through the optical cathodoluminescene images (Fig. 8.9 C). Occasionally, fine-grained, euhedral quartz4 crystals are observed to overprint dolomite, indicating local post-dolomite quartz precipitation (Fig. 8.9 C).

The investigation of gold mineralization, particularly in the south zone, involved the analysis of BSE and QEMSCAN images taken from composite samples representing specific intervals of drill holes targeting the mineralization (Meng,

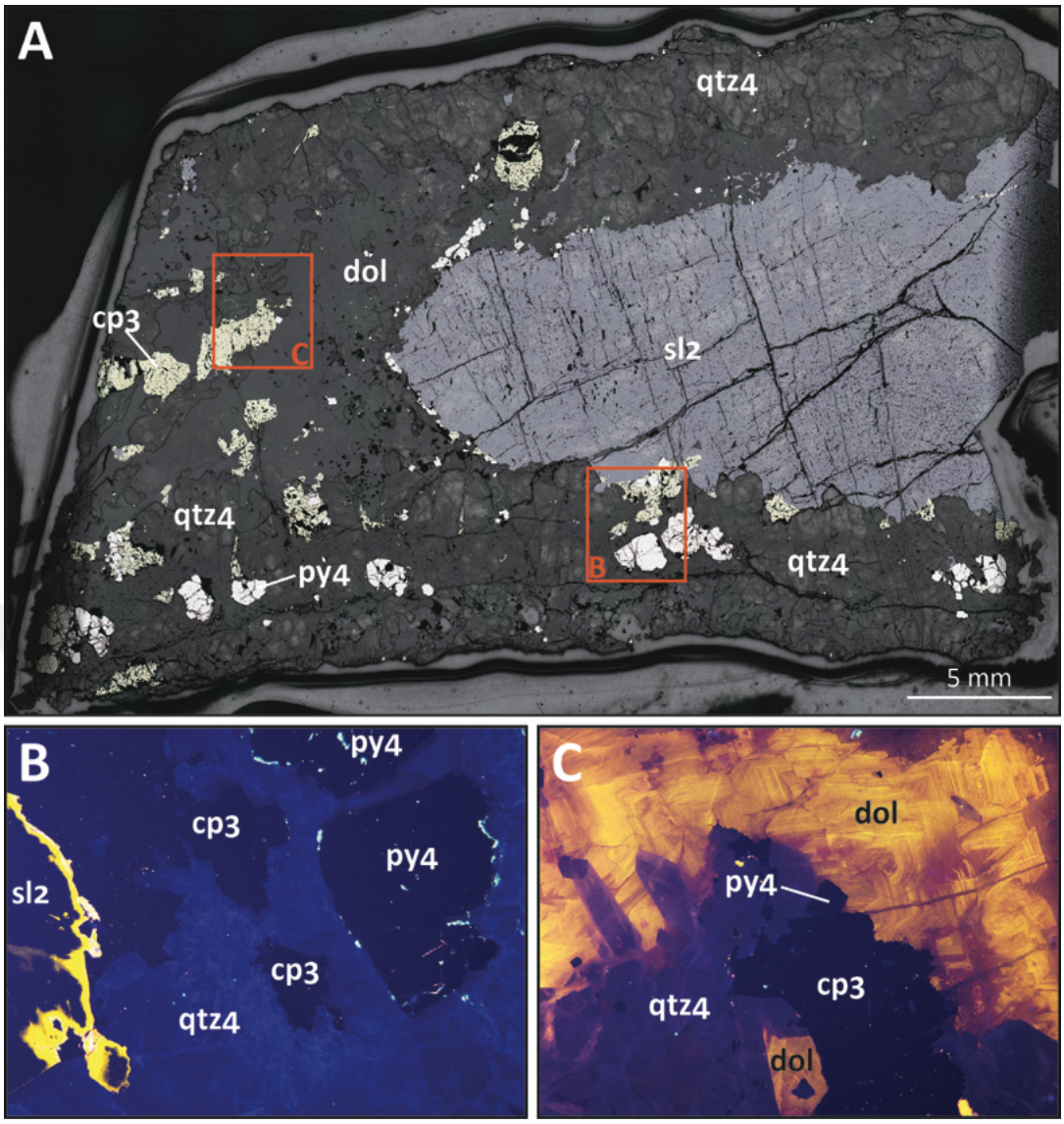


Figure 8.10. Sample EB079 from drill hole HTD021-20.3 m, representing South Zone sphalerite2-chalcopyrite2-pyrite4 mineralization associated with quartz4 and dolomite. (A) Polished sample, reflected light image, (B, C) Optical cathodoluminescence images. cp: chalcopyrite, dol: dolomite, py: pyrite, qtz: quartz, sl: sphalerite

2019). Similar to the main zone, gold mineralization in the south zone exhibits spatial and temporal associations with pyrite3, chalcopyrite2, and quartz3 phases in a specific order. The earliest Au mineralization is observed as gold particles enclosed within the pyrite3-sericite2 assemblage, which is later overprinted by chalcopyrite2 (Fig. 8.11 A). Subsequently, gold particles are found in association with the chalcopyrite2 phase, as evident in Figure 8.11 B, where chalcopyrite2 replaces the pyrite3-sericite2 assemblage. It is worth noting that sericite2 is overprinted by kaolinite and dolomite, while chalcopyrite2 is locally replaced by chalcocite/covellite (Fig. 8.11 B). The presence of sphalerite (sphalerite2?) along

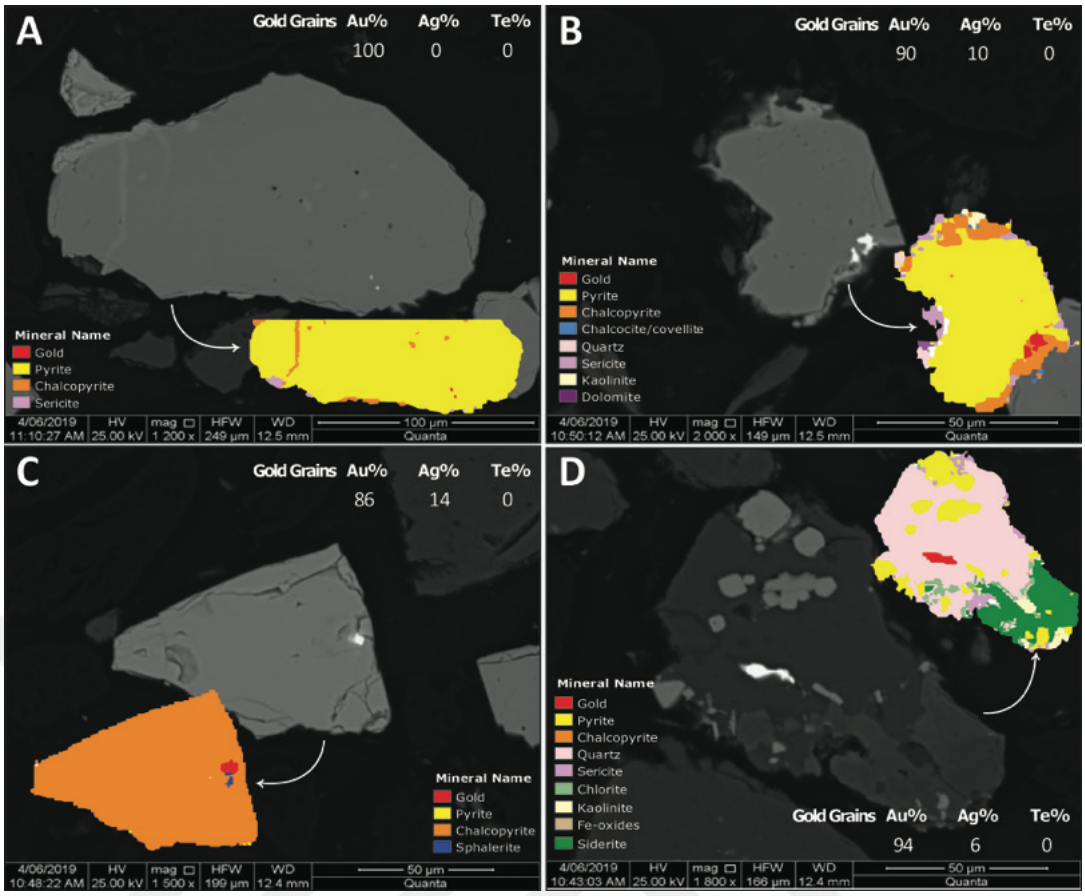


Figure 8.11. BSE and QEMSCAN images of gold grains characterizing south zone mineralization from selected composite samples representing drill hole HTD196, 42-57 m (Meng, 2019), (A) Gold particles enclosed within pyrite3, (B) gold particles associated with chalcopyrite2 replaces pyrite3, (C) gold particles associated with chalcopyrite2 and sphalerite2?, (D) gold particles associated with quartz3-pyrite3-sericite2-kaolinite-iron oxide-siderite

with gold particles along the fractures of chalcopyrite2 is also noteworthy, suggesting a potential late sphalerite2 precipitation as open space filling (Fig. 8.11 C). Additionally, gold is observed in association with the quartz3-pyrite3 phase. In the main zone Au mineralization, gold particles were found in association with sericite2 and clay minerals formed after chlorite2, accompanied by hematite-goethite and siderite (Fig. 8.5). Similarly, in the south zone, gold mineralization exhibited associations with the quartz3-pyrite3 phase, characterized by sericite2 and a kaolinite-iron oxide-siderite assemblage (Fig. 8.11 D). Manual EDS analysis was conducted on gold particles associated with different mineral phases (Meng, 2019). Gold particles linked with pyrite2 were found to be composed of 100%Au, with no Ag and Te detected. Gold particles associated with chalcopyrite2 showed a composition of 90-86 %Au and 10-14 %Ag, with no Te

detected. Gold particles associated with the quartz3-pyrite3 phase exhibited a composition of 94 %Au and 6 %Ag, with no Te present.

8.2.1. Geologic and geochemical profiles of south zone mineralization

The mineralization at the south zone is investigated using the drill hole HTD021 (Fig. 6.13). Geologic and geochemical profiles are created particularly for this drill hole, building upon the alteration box plot (Fig. 6.19). The previous hydrothermal alteration chapter has already revealed the changes in alteration trends over time, and in this chapter, the findings with assay values and additional indices (table provided in the Appendix-A4) will be complemented to illustrate the evolution of south zone mineralization and the associated hydrothermal alteration phases.

The geologic and geochemical profiles of drill hole HTD021 (traces shown in Fig. 6.13) reveal that high-grade Au and Cu mineralization are hosted by both dacite breccia (up to 9.6 g/t Au and Cu up to 2.6%) and volcanosedimentary rocks (up to 6.5 g/t Au and Cu up to 1.8%). Hydrothermal alteration minerals associated high-grade Au-Cu mineralization are sericite2-clay minerals, predominantly kaolinte and dickite and late carbonate and anhydrite overprint. High CCPI and low AI values indicate intense hydrothermal alteration and late carbonate and anhydrite overprint. These values are often concordant to the Au-Cu mineralization (8.12). Elevated Na/alkalis index values associated with shallow Au mineralization (HTD021, 14-24 m) is also noteworthy (8.12). This association can be explained by the presence of gold-bearing quartz veinlets without causing an intense alteration which often brings about Na-leaching. Pb-Zn mineralization, on the other hand, is confined to volcanosedimentary rocks. Low AI, high CCPI, decreased Ba/K_2O index values and increased MnO/MgO index values are in agreement with Pb-Zn mineralization (8.12). This strong MnO/MgO index is in agreement with the distal alteration characterized by Mn-rich carbonates and phyllosilicates. Ag assay values are low ($\leq$9 g/t). Elevated Ag values are concordant to both Au-Cu and Pb-Zn mineralization (8.12).

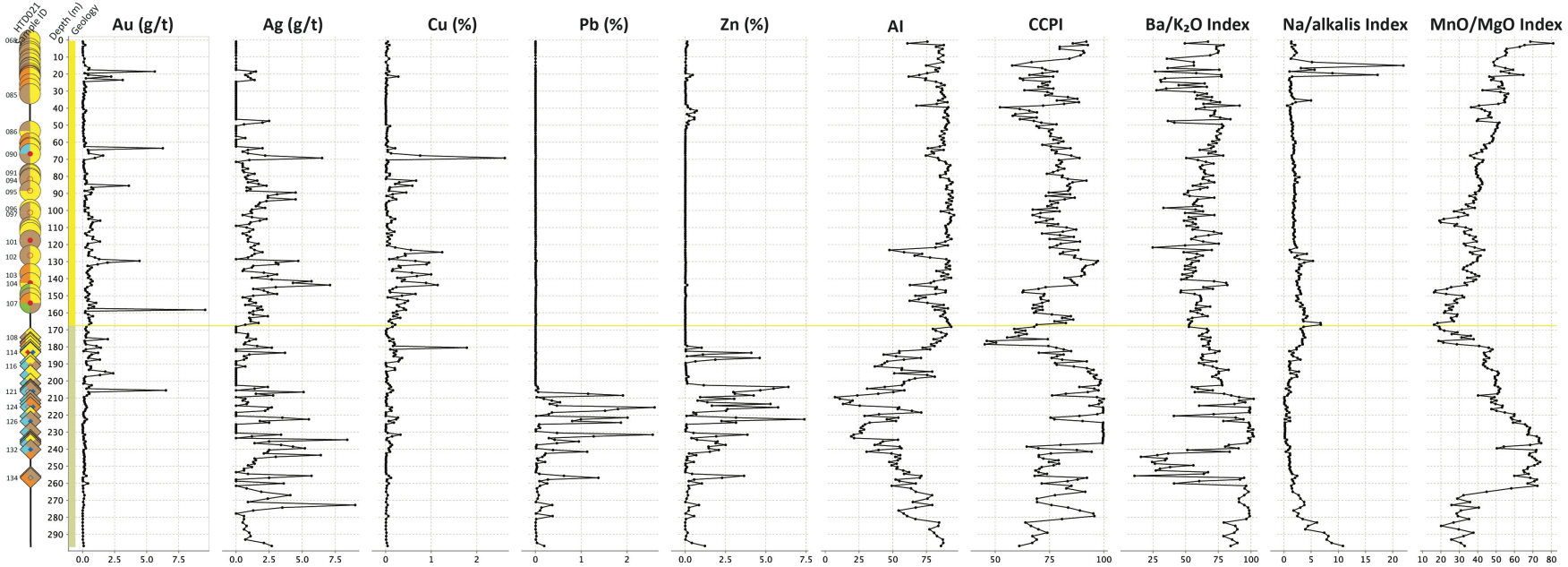


Figure 8.12. **Geologic and geochemical profiles of drill hole HTD021 (trace and legend shown on Fig. 6.1) that intersects South Zone mineralization. The location and distribution of the analyzed samples and results are indicated by black horizontal lines. All the lithogeochemical data and Au, Ag, Cu, Zn and Pb assay values are from Artmin Madencilik. AI = alteration index (Ishikawa et al., 1976), CCPI = chlorite-carbonate-pyrite index (Large et al., 2001).**

8.3. Old Workings Zone Mineralization

As suggested by its name, the ”old workings zone” has historical significance in terms of mining activity, and indeed, a majority of the prominent outcropped mineralization is located within this zone. The mineralization within this zone is characterized by veins containing quartz-sphalerite-pyrite-chalcopyrite±galena and finds its host within both the andesite breccia and rhyodacite lava flows. The host volcanic rocks, zones of gold-zinc ore, and the corresponding hydrothermal alteration areas are visually depicted in (Fig. 6.20).

The spatial and temporal relationship between the host andesite breccia, associated hydrothermal alteration assemblages and the mineralization is well observed through the logging of drill hole HTD222 (particularly depth interval of 142-143 m) and petrographic investigation of sample EB162 from HTD222-14.9 m. It is evident that early pervasive chlorite1-rich alteration on the andesite breccia is the most predominant alteration (Fig. 8.13. A). Chlorite2-quartz2-pyrite3±chalcopyrite2 phase either cuts through the andesite breccia or occupy the matrix between andesite breccia clasts (Fig. 8.13. A, B). This mineralization pattern remains consistent throughout the andesite breccia. Importantly, this pattern is clearly evident in both the drill cores (at the scale of centimeters) and thin sections (at the scale of millimeters) (Fig. 8.13. A-D). Furthermore, there is an overlay of Mg-illite alteration onto the chlorite1-rich alteration, predominantly affecting the groundmass of the andesite porphyry clasts within the andesite breccia.

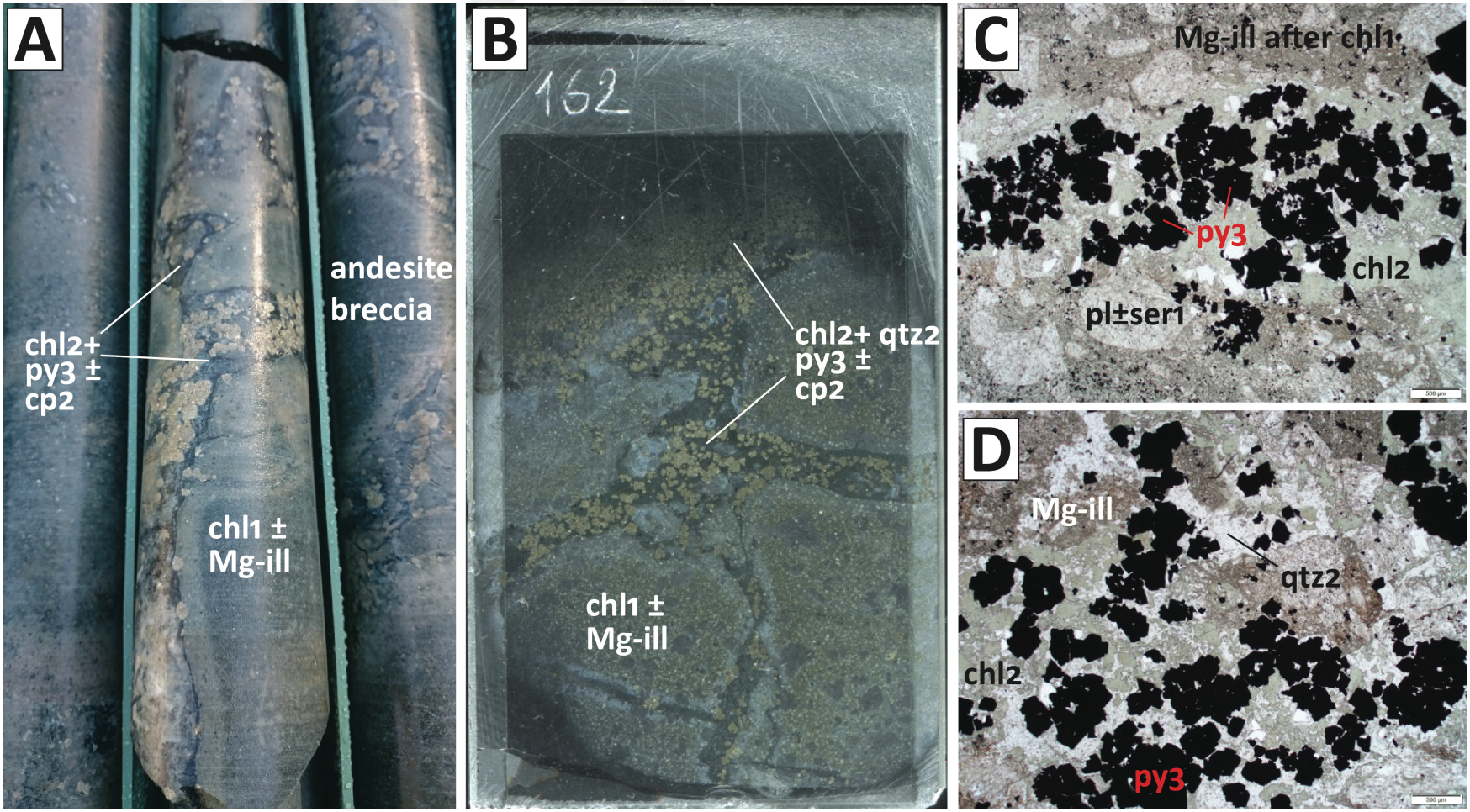


Figure 8.13. Old workings zone mineralization occured as chlorite2-quartz2-pyrite3±chalcopyrite2 veins and patches replacing the chlorite1-altered andesite breccia, (A) drill core photo from HTD222-142.5 m, (B) Full thin section scan of sample EB162, (C-D) Photomicrographs of sample EB162, PPL.

The mineralization at the old workings zone is investigated using the drill hole: HTD222 (Fig. 6.20). Geologic and geochemical profiles are created for this drill hole, building upon the alteration box plots (Fig. 6.23, 8.14). The hydrothermal alteration section has already demonstrated alterations in trends across time. In this particular section, the outcomes, along with assay results and supplementary indices, will be combined to provide a comprehensive depiction of the progression of mineralization and the correlated hydrothermal alteration phases.

The geologic and geochemical profiles of drill hole HTD222 (traces shown in Fig. 6.20) reveal that Au and Zn mineralization are hosted by both andesite breccia (up to 1.5 g/t Au and Zn up to 2.6%) and rhyodacite (up to 0.3 g/t Au and Zn up to 0.8%). Hydrothermal alteration minerals associated Au-Zn mineralization are quartz2-chlorite2, quartz3-4 veins accompanied by carbonate (dolomite, rhodochrosite)±anhydrite and epidote-calcite overprint. Low CCPI values (<77) indicate the lack of intense hydrothermal alteration. The occasional increase in CCPI is due to the epidote, and late calcite±anhydrite overprint. Elevated AI values, on the other hand, is associated with the sericite1-2 alteration both on andesite breccia and the rhyodacite. It is noteworthy that Na/alkalis index values abruptly decreases with respect to the rhyodacite and the associated hydrothermal alteration (8.14). The Au-Zn mineralization hosted by the rhyodacite (402-407m) is consistent with low Na/alkalis index values, slightly increased AI, Ba/K_2O and MnO-MgO index values. The Au-Zn mineralization hosted by andesite breccia is similarly consistent with increased MnO-MgO index values. This strong MnO/MgO index is in agreement with the distal alteration characterized by Mn-rich carbonates and chlorite2 minerals (Table. 7.1).

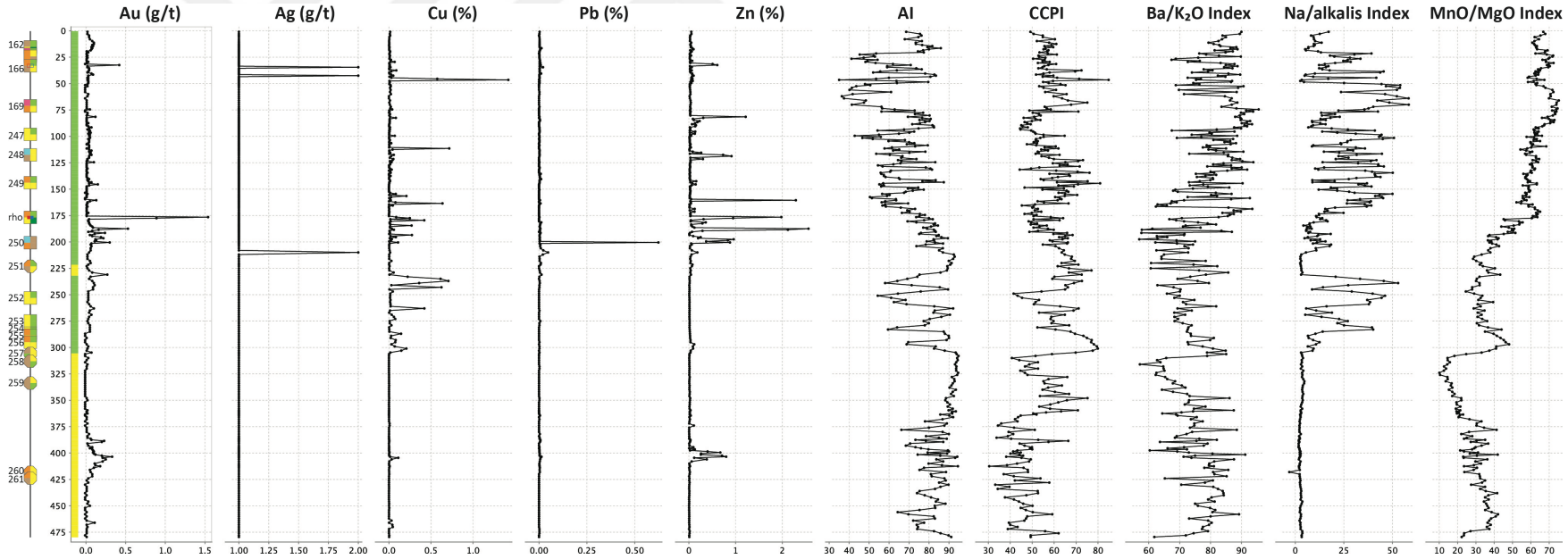


Figure 8.14. **Geologic and geochemical profiles of drill hole HTD222 (trace and legend shown on Fig. 6.20) that intersects old workings zone mineralization. The location and distribution of the analyzed samples and results are indicated by black horizontal lines. All the lithogeochemical data and Au, Ag, Cu, Zn and Pb assay values are from Artmin Madencilik. AI = alteration index (Ishikawa et al., 1976), CCPI = chlorite-carbonate-pyrite index (Large et al., 2001).**

9. GEOCHRONOLOGY

9.1. U-Pb Geochronology

Sample EB056, which represents columnar dacite of Kızılkaya Formation, exhibits an interpreted $^{206}Pb/^{238}U$ weighted mean age of 84.78 ± 0.43 Ma based on 34 concordant zircon spot analyses (Fig. 9.1 A, B, C). The mean square of weighted deviates (MSWD) value is 0.85. Within this sample, there are four outlier ages at 87.1 ± 1.7, 81.7 ± 2.0, 91.3 ± 2.8, and 93.2 ± 3.4 Ma (Fig. 9.1 A, B). While no discordant zircons were found, one zircon with two spot analyses reveals contrasting ages of 82.3 ± 2.2 Ma for the core and 87.9 ± 3.0 Ma for the rim (N:23-24; Fig. 9.1 C). This particular zircon, along with the other four outliers, is excluded from the analysis.

Sample EB142 from the rhyodacite in the Kızılkaya Formation is dated at 84.00 ± 0.44 Ma based on the analyses of 31 concordant zircon spot analyses (Fig. 9.1 D, E, F). MSWD value is 1.50. One discordant (N:17 at 84.4 ± 1.4 Ma) and seven outlying zircon spot analysis (at 81.5 ± 1.9, 87.2 ± 1.6, 87.3 ± 1.4, 87.0 ± 2.0, 81.6 ± 1.4, 79.3 ± 2.5 and 71.9 ± 4.3 Ma) are discarded (Fig. 9.1 D, E, F).

Sample EB275 representing the volcanic clasts (Hızarlıdere volcanics) of Öğdem Formation's red conglomerate unit yields an interpreted $^{206}Pb/^{238}U$ weighted mean age of 165.65 ± 0.69 Ma based on 28 concordant zircon spot analyses (Fig. 9.1 G, H, I). This age is conformable with the stratigraphic age of the Hızarlıdere Formation. MSWD value is 1.40. This sample also has two xenocrystic zircons with three concordant zircon spot analysis at 302. 7 ± 4.5 Ma (N:4), 298.7 ± 3.8 Ma (N:5) and 622.0 ± 5.7 Ma (N:30; (Fig. 9.1 G, H, I)). Five discordant (N:3, 25, 35, 39 and 40) and four outlying zircon spot analyses (N:8, 20, 23 and 29) are rejected (Fig. 9.1 G, H, I).

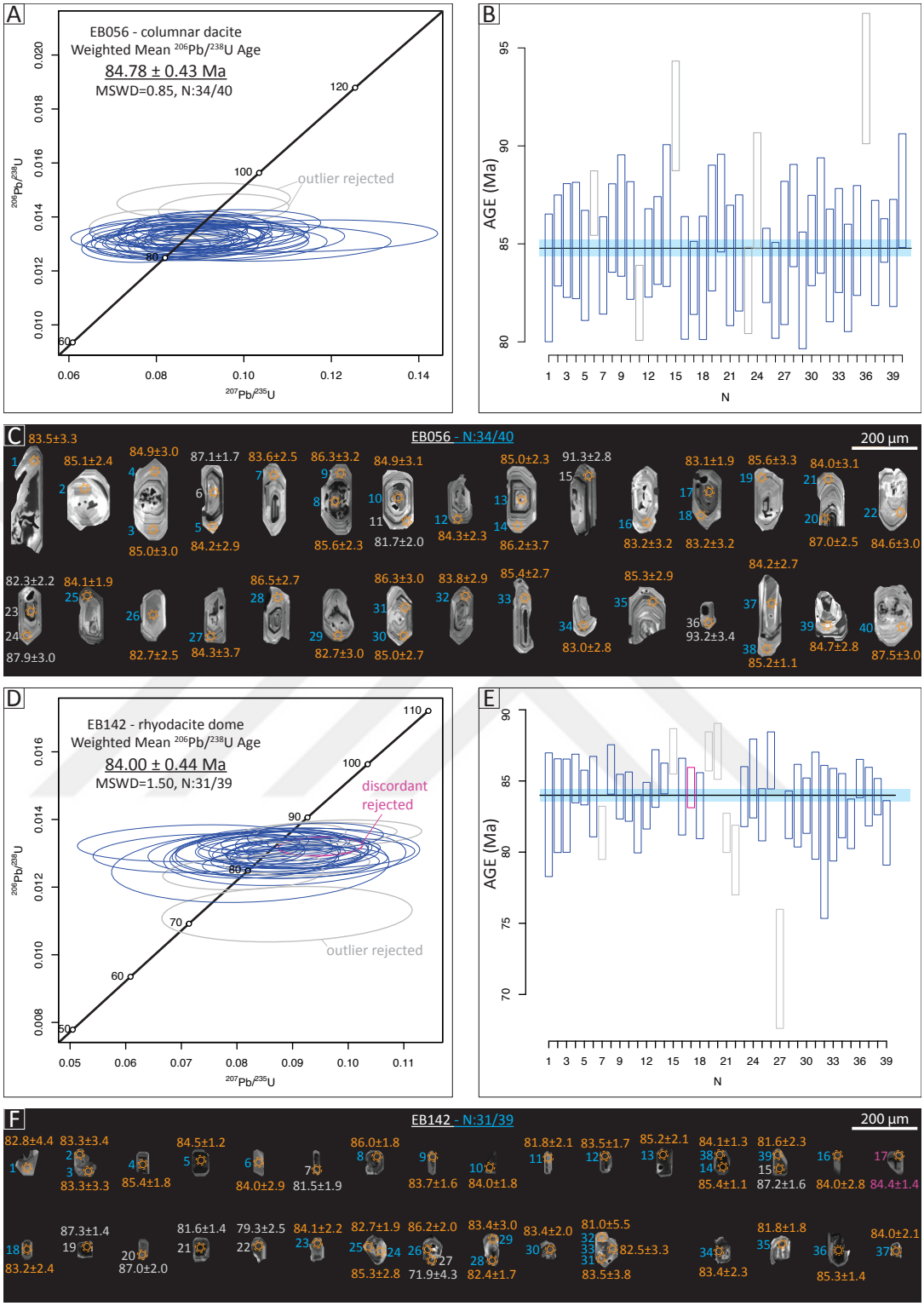


Figure 9.1. **$^{206}Pb/^{238}U$ vs. $^{207}Pb/^{235}U$ Concordia, $^{206}Pb/^{238}U$ weighted mean histogram diagrams and zircon cathodoluminescence images with laser spot locations (orange circles), spot $^{206}Pb/^{238}U$ ages (orange if accepted, grey if outlying, and pale pink if discordant). Blue numbers indicate the zircon number (N) in the weighted mean age diagram). (A), (B) and (C) from the columnar dacite, EB056; (D), (E) and (F) from rhyodacite EB142; (G), (H) and (I) from red conglomerate unit with volcanic clasts**

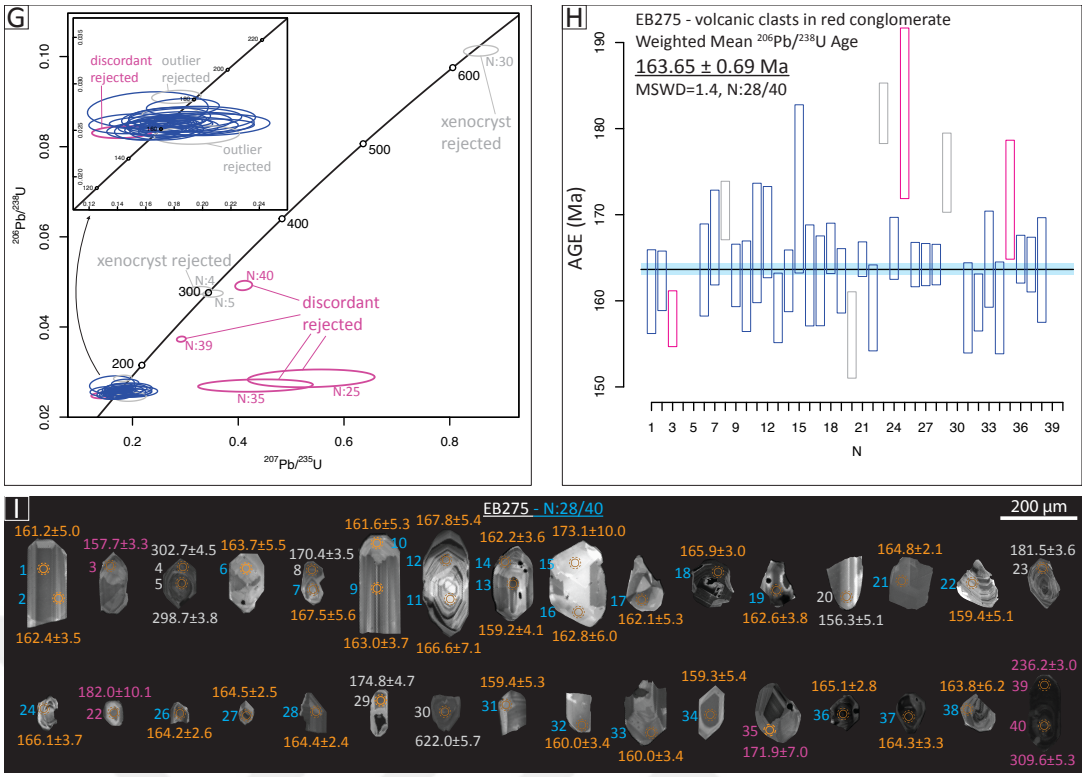


Figure 9.1. (Cont.)

9.2. Ar-Ar Geochronology

Samples EB078 and EB232 are selected for the Ar-Ar geochronology. EB078, from drill hole HTD021, represents a sericite2-pyrite vein crosscutting sericite1-2 altered dacite breccia from the south zone mineralization. EB232, on the other hand, is from the drill hole HTD018 and represents the spherulitc dacite with sericite2 alteration of the main zone mineralization. Each sample has two aliquots having different size fractions. Aliquots named as ”A” indicate sericite samples with >2µm size fraction and aliquots named as ”B” indicate sericite samples with <2µm size fraction.

Data tables and associated Ar-spectra graphs are provided in the Appendix-D1. As single crystal or single mineral $^{40}Ar/^{39}Ar$ analysis on these samples is not possible due to the fine-grained nature of the hydrothermal sericites, the samples yield complex 40Ar/39Ar age spectra (Fig. 9.2. A-D). In addition, local kaolinite overprints on sericites are present. Hence, the obtained complex 40Ar/39Ar age spectra were the most likely result.

The argon age spectra do not yield any isochron or inverse isochron ages due to

the fact that the samples do not yield isochrons (the steps all have different dates). The inverse isochron data is presented in Appendix-A4 to emphasize the absence of isochrons. However, the interpretation of the age spectra offers valuable insights:

For the sample EB078, the oldest steps yield dates of 84.6 $\pm$ 0.5 Ma (aliquot A) and 87.2 $\pm$ 0.4 Ma (aliquot B). The subsequent steps at lower temperatures produce younger dates. This clearly indicates alteration; the oldest step dates at the high-temperature end likely represent the age of the sericite, while the younger steps probably correspond to the time of alteration (although they may not record it accurately - it is a mixing line).

Similarly, for the sample EB232, the oldest steps yield dates of 83.5 $\pm$ 0.7 Ma (aliquot A) and 82.1 $\pm$ 0.3 Ma. The interpretation remains consistent with the aforementioned data, where the oldest steps reflect the age of the sericite, and the subsequent steps demonstrate evidence of alteration.

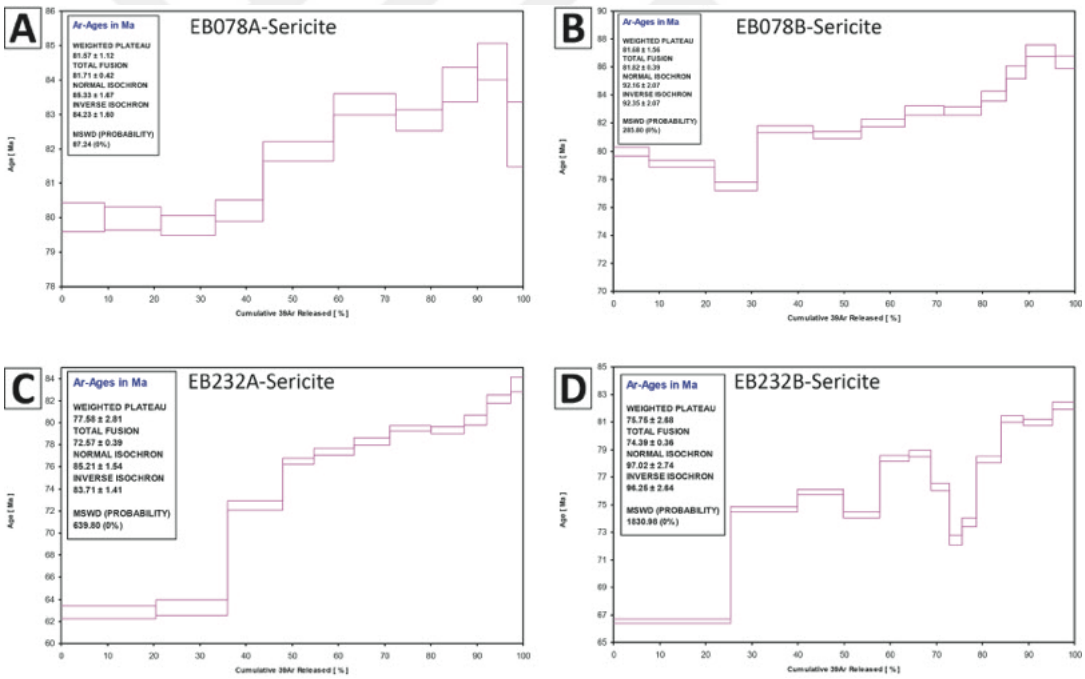


Figure 9.2. $^{40}Ar/^{39}Ar$ age spectra for analyzed sericite, (A-B) EB078, south zone mineralization; (C-D) EB232, main zone mineralization. MSWD: mean square of weighted deviates

10. STABLE ISOTOPES

Analyzing the stable isotope ratios of ore minerals and hydrothermal alteration assemblages provides a means to identify the source of the fluids responsible for these minerals and to deduce the origin and evolution of the metal-bearing fluids. In the pursuit of understanding the source and developmental trajectory of metal-carrying hydrothermal fluids in the Hod Maden deposit, stable isotope samples were gathered from diverse ore zones and their corresponding hydrothermal alteration assemblages. Distinct samples of ore minerals, namely chalcopyrite, sphalerite, and pyrite representing the mineralization phase, along with anhydrite representing the post-mineralization phase, were subjected to analysis to determine their sulfur isotopic composition (δ^{34}S values). For deciphering the oxygen and deuterium isotope compositions (δ^{18}O and δD values), samples of hydrothermal alteration minerals associated to mineralization, such as chlorite (mainly chlorite2), sericite2, Mg-illite, and kaolinite, were investigated.

10.1. Sulfur Isotope Analysis

Sulfides minerals comprising of pyrite2 (n=1, main zone), pyrite3 (n=1, south zone; n=2, old workings zone), pyrite4 (n=3, main zone); chalcopyrite2 (n=12, main zone; n=2 south zone), chalcopyrite3 (n=7, main zone; n=3, south zone, n=1, old workings zone), sphalerite1 (n=2, south zone), sphalerite2 (n=3, old workings zone; n=2, south zone), sphalerite3 (n=1, south zone; n=1, old workings zone) and anhydrites (n=13, main zone; n=2, south zone) were analyzed for the δ^{34}S values. The δ^{34}S values for sulfides range from -2.4 to +5.7 ‰ whereas δ^{34}S values for sulfates range between 16.1 and 20.7 ‰ (Appendix-C1, Fig.10.1).

The δ^{34}S values of chalcopyrite2 in the main zone vary between -2.4 ‰ and 3.2 ‰, while in the south zone, the δ^{34}S values of chalcopyrite2 range from 2.3 ‰ to 3.3 ‰. For chalcopyrite3, the δ^{34}S values in the main zone range from 0.3 ‰ to 4.9 ‰,

whereas in the south zone, they range from -0.8 ‰ to 1.59 ‰. The δ^{34}S value of chalcopyrite3 from the old workings zone is 1.1 ‰.

In the main zone, the δ^{34}S value of pyrite2 is 4.4 ‰. In the south zone, the δ^{34}S value of pyrite3 is 2.3 ‰, while in the old workings zone, the δ^{34}S values of pyrite3 range from 2.2 ‰ to 2.4 ‰. The δ^{34}S values of pyrite4 in the main zone vary between -0.7 ‰ and 3.3 ‰.

The δ^{34}S values of sphalerite1 in the south zone fluctuate between 1.6 ‰ and 1.8 ‰. The δ^{34}S values of sphalerite2 in the south zone vary from 1.6 ‰ to 2.4 ‰, whereas in the old workings zone, the δ^{34}S values of sphalerite2 range from -0.3 ‰ to 0.3 ‰. In the main zone, the δ^{34}S value of sphalerite3 is 3.9 ‰, while in the old workings zone, the δ^{34}S value of sphalerite3 is -1.7 ‰.

The δ^{34}S of anhydrites within the Hod Maden deposits varies between 17.1 ‰ and 20.7 ‰. Specifically, in the main zone, the δ^{34}S values of anhydrites range from 17.1 ‰ to 19.9 ‰, whereas in the south zone, these values extend from 19.1 ‰ to 20.7 ‰.

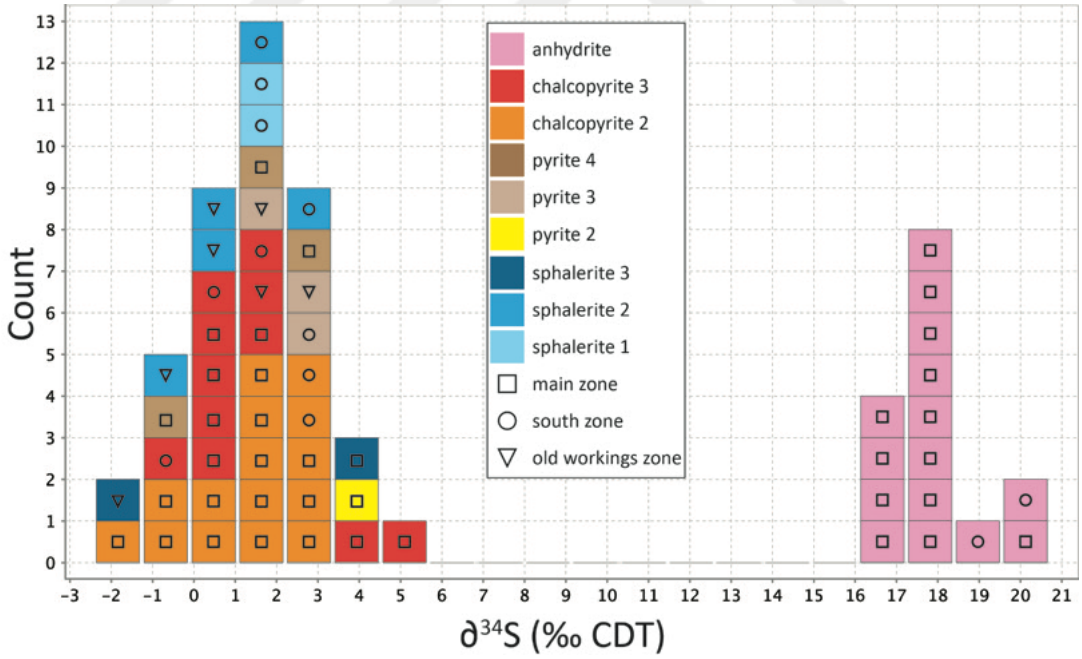


Figure 10.1. Histogram of measured δ^{34}S values in chalcopyrite, pyrite, sphalerite and anhydrite, CDT: Canyon Diablo Troilite

10.2. Oxygen and Deuterium Isotope Analysis

A total of 28 phyllosilicate minerals including chlorite1 (n=6 at main zone, n=1 at old workings zone), chlorite2 (n=13 at main zone, n=1 at old workings zone), sericite2 (n=1 at main zone, n=3 at south zone), Mg-illite (n=2 at old workings zone) and kaolinite (n=1 at main zone) were analyzed for the $\delta^{18}O_{mineral}$ and $\delta D_{mineral}$ values. $\delta^{18}O_{mineral}$ values range from 0.8 ‰ to 8.30 ‰, whereas $\delta D_{mineral}$ values range from -92 ‰ and -36 ‰ (Appendix-C2, C3).

For calculation of the oxygen and deuterium isotope compositions of the chlorite and sericite-forming fluids (including Mg-illite and kaolinite), the fractionation equations (reactions 11.1 and 10.2) of Cole and Ripley (1999) and equations (10.3 and 10.4) of Sheppard and Gilg (1996) are used.

$$10^{3}\ln\alpha_{(\mathrm{chlorite-water})} = \delta^{18}O_{\mathrm{chlorite}} - \delta^{18}O_{H_2O} = 2.69 \cdot 10^{9} \cdot T^{-3} - 6.34 \cdot 10^{6} \cdot T^{-2} + 2.97 \cdot 10^{3} \cdot T^{-1} \quad (10.1)$$

$$10^{3}\ln\alpha_{(\mathrm{chlorite-water})} = \delta D_{\mathrm{chlorite}} - \delta D_{H_2O} = -30 \text{ to } -40 \quad (10.2)$$

$$10^{3}\ln\alpha_{(\mathrm{sericite-water})} = \delta^{18}O_{\mathrm{sericite}} - \delta^{18}O_{H_2O} = 2.39 \cdot 10^{6} \cdot T^{-2} - 3.76 \quad (10.3)$$

$$10^{3}\ln\alpha_{(\mathrm{sericite-water})} = \delta D_{\mathrm{sericite}} - \delta D_{H_2O} = -25 \pm 5 \quad (10.4)$$

The temperatures utilized for temperature-dependent fractionation equations concerning chlorite are determined based on the chlorite's composition (Table 7.1). In cases where mineral chemistry data for that specific chlorite is unavailable, a temperature range of 338 ± 28°C is employed. This range encompasses the upper and lower temperatures of chlorite formation calculated from mineral chemistry data. These estimations align with the anticipated temperatures (300-375°C) for the

precipitation of Cu ± Au sulfides from a hydrothermal fluid (Large, 1992). Given the petrographic analysis indicating that sericite and clay minerals replace chlorite phases as temperatures decrease, the sericite2 and Mg-illite phases are assigned a temperature range of 225 ± 25°C, whereas a temperature range of 175 ± 25°C is assigned to kaolinite.

The calculated $\delta^{18}O_{water}$ values originating from chlorite1 span between 2.5 ‰ and 4.0 ‰, while the δD_{water} values associated with chlorite1 cover a range of -18 ‰ to -14 ‰ (Fig. 10.2). For chlorite2, the $\delta^{18}O_{water}$ values vary from 1.0 ‰ to 3.2 ‰, and the corresponding δD_{water} values range from -24 ‰ to -8 ‰ (excluding the δD_{water} value of sample EB043 due to issues with duplicate δD analysis; Fig. 10.2). Moving to sericite2, the calculated $\delta^{18}O_{water}$ values extend from -0.8 ‰ to 1.0 ‰, while the δD_{water} values span from -20 ‰ to -11 ‰ (Fig. 10.2). Finally, for Mg-illite and kaolinite, the calculated $\delta^{18}O_{water}$ values fall within the range of -1.7 ‰ to 1.7 ‰, and the corresponding δD_{water} values are distributed between -37 ‰ and -15 ‰ (Fig. 10.2).

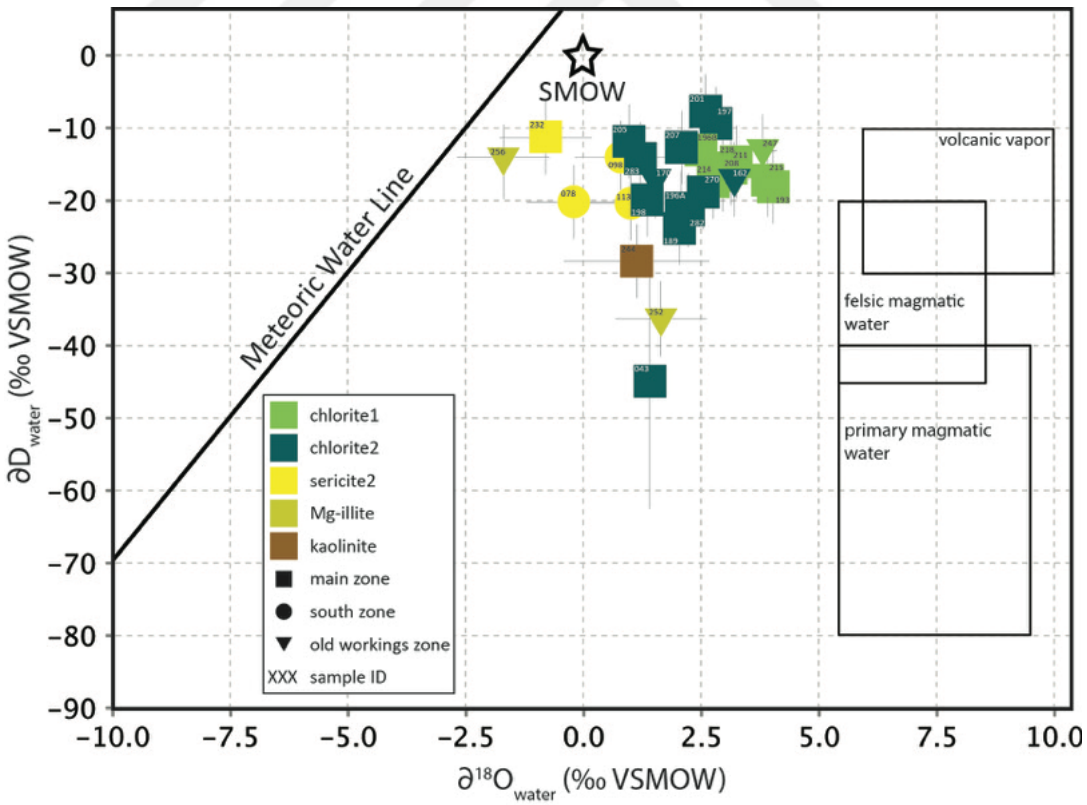


Figure 10.2. Calculated $\delta^{18}O_{water}$ vs. δD_{water} of hydrothermal fluids responsible for chlorite1, chlorite2, sericite2, Mg-illite and kaolinite alterations, VSMOW: Vienna Standard Mean Ocean Water, Meteoric water line (Craig, 1961), felsic magmatic water (Taylor, 1992), primary magmatic water (Taylor, 1974), volcanic vapor (Giggenbach, 1992)

11. FLUID INCLUSIONS

The investigation into fluid inclusions is primarily focused on sample EB181 due to the presence of euhdral quartz crystals (in comb quartz4 veins), which allows for the identification of primary, secondary, or pseudo-secondary fluid inclusions. The distinct crystalline structure of the quartz crystals provides growth zones, aiding in the interpretation of fluid inclusion alignment (Fig. 11.1).

The melting (T_{ice}) and homogenization temperatures (T_h) are measured on the primary fluid inclusions. While T_{ice} values range from -5 °C to -2 °C, T_h values vary between 120 °C and 170 °C.

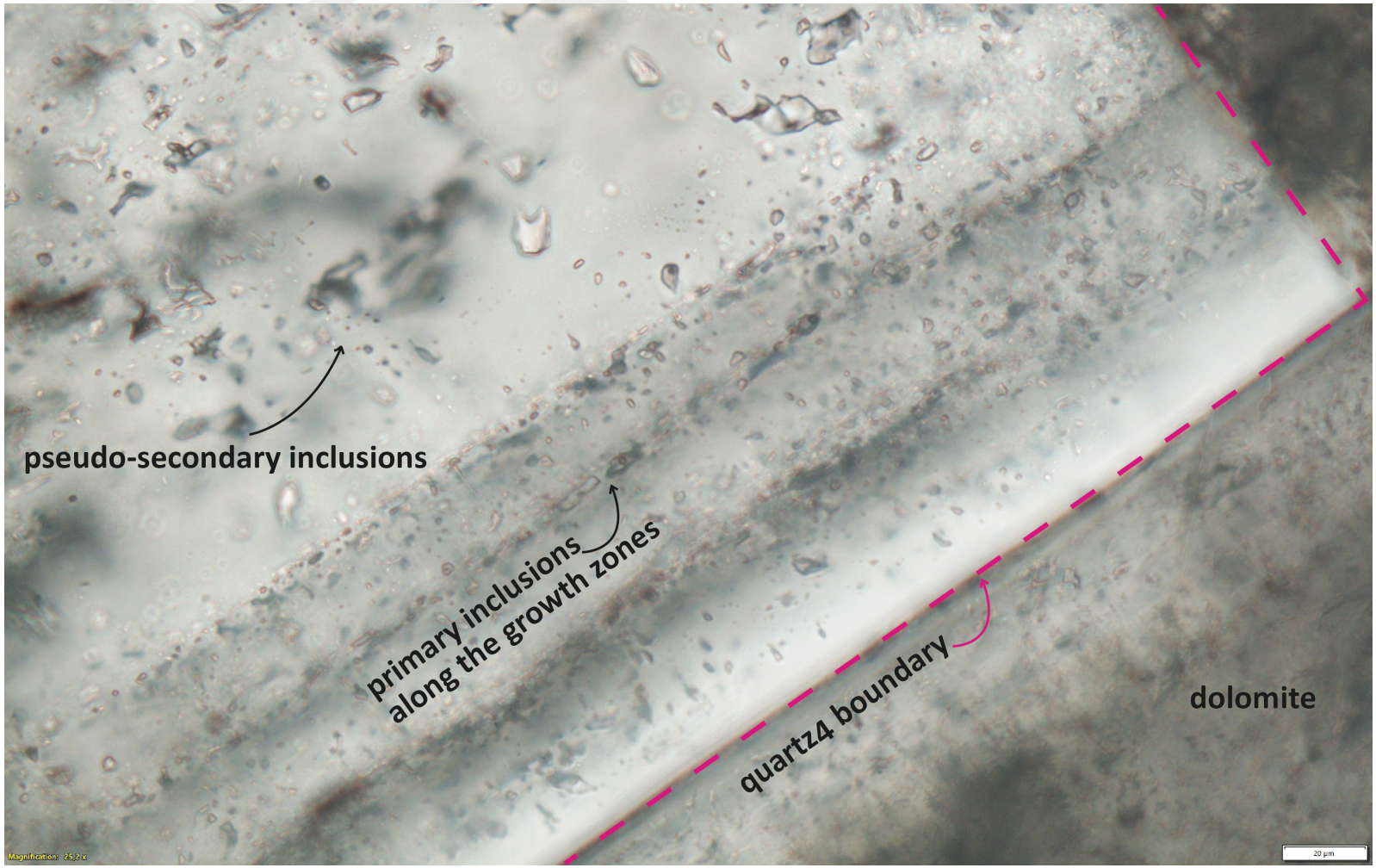


Figure 11.1. Primary and pseudo-secondary fluid inclusions in a quartz4 crystal of the comb quartz4 vein in sample EB181. Notice the euhedral habit and the growth zones of the quartz4 crystal.

12. DISCUSSION

12.1. Revised Age of the Dacitic Units

"Maden Dasiti" (Mine Dacite) has been used to refer to the discussed dacitic units by Şatır and Ereren (1976) and Konak and Hakyemez (2009) because the Hod Maden mineralization is spatially associated with the dacite and rhyodacite units in the region. Additionally, they concluded that the dacitic units are Eocene in age, based on their observations of field crosscutting relationships. The fact that the dacitic rocks crosscut the volcanosedimentary and andesite breccia units of the Çatak Formation do not necessarily imply that the dacitic units are Eocene in age. Rather, their spherulitic texture, which arose from the rapid cooling of lavas as a result of interactions with seawater, as well as the presence of local mass flow deposits containing sulfide clasts resulting from a sequence of collapse and redeposition on the seafloor, suggest that the units were formed in a submarine environment during Santonian.

12.2. Delineation of "Unnamed Volcanosedimentary Rocks"

Prior to this study, the eastern segment of Hod stratigraphy, characterized by Late Cretaceous units, was vaguely reported. This may be due to several reasons: (i) the area is located at the intersection of four 1/25000 quadrangles (F47c4, F47c3, G47b1 and G47b2); (ii) the lithological units are intensely altered, making it difficult to determine the rock type, to identify petrographic characteristics and to clarify lithological boundaries; (iii) the steeply dipping nature of lithologies and the structural framework of the area make it challenging to correlate the units and/or formations with their counterparts in the region; (iv) the morphology and vegetation of the region make some areas inaccessible for mapping and sampling. Earlier research provided beneficial, yet incomplete information on Late Cretaceous units,

either reporting them as a package without thorough petrographic analysis or describing individual lithologies without regional geology context and proper stratigraphy. However, this study utilized field mapping, drill core logging, petrographic analysis accompanied by short-wave infrared (SWIR) data to delineate the Late Cretaceous units into the Turonian Çatak Formation, Santonian Kızılkaya Formation, and Santonian-Campanian Evliyatepe Formation. The identification was achieved by comparing morphological, compositional, and petrographic characteristics of these units with reported data and by considering their field relationships. For instance, Kızılkaya Formation comprises four distinct lithological units. Felsic to intermediate volcanism causes submarine spherulitic dacite breccia, stratified volcanosedimentary unit, and flow-banded rhyodacite dome in the central part, whereas, in the south, it forms columnar dacites with large quartz phenocrysts. On the other hand, the presence of amygdaloidal texture with chlorite, zeolite, vermiculite, and carbonate-bearing amygdales in mafic submarine and locally subaerial lava flows of Çatak and Evliyatepe formations provide excellent examples of textural interpretation on altered volcanic rocks and the significance of hydrothermal alteration assemblages.

12.3. Physico-Chemical Conditions of Gold Precipitation

According to Gammons and Williams-Jones (1995), the solubility of gold can be enhanced by reducing the pH in oxidizing fluids, as shown in reaction (12.1). The presence of reduced hydrothermal fluids mixing with oxygenated sulfate-rich seawater likely leads to the deposition of gold. This process causes the oxidation of $Au(HS)_2^-$ and a consequent reduction in the content of H_2S (Hannington and Scott, 1989; Huston et al., 1992).

Hannington and Scott (1989b) suggested that there is a negative correlation between Au concentration and sulfidation which is controlled by the reaction (12.2). Chlorite and sericite precipitation controls the pH of the system as chlorite is a stable phase under alkaline conditions, sericite forms as a result of H^+ metasomatism which requires more acidic conditions. Gold and chlorite2 association and subsequent sericite2 and clay alteration, predominantly kaolinite and dickite can be interpreted

in this regard. Pervasive chlorite precipitation can result in an increase in the activity of H^+ ions which can cause gold precipitation due to the destruction of gold bi-sulfide complexes (equations 12.2 and 12.5).

$$Au_{(s)} + 2H_2S_{(aq)} + 1/4O_{2(g)} \rightleftharpoons Au(HS)_2{}^- + H^+ + 1/2H_2O \quad (12.1)$$

$$4Au + S_{2(g)} + 6H_2S_{(aq)} \rightleftharpoons 4Au(HS)_2{}^- + 4H^+ \quad (12.2)$$

$$AuCl_2{}^- + 2H_2O \rightleftharpoons 4Au + 8Cl^- + 4H^+ + O_{2(g)} \quad (12.3)$$

$$CuCl^0 + FeS_2 + 2\,H_2O \rightleftharpoons \underset{\text{chalcopyrite}}{4CuFeS_2} + 4Cl^- + 4H^+ + O_{2(g)} \quad (12.4)$$

$$3\,\underset{\text{chlorite}}{Mg_5Al_2Si_3O_{10}(OH)_8} + 2\,K^+ + 28\,H^+ \rightleftharpoons \quad (12.5)$$
$$2\,\underset{\text{muscovite}}{KAl_3Si_3O_{10}(OH)_2} + 3\,SiO_2 + 15\,Mg^{2+} + 24\,H_2O$$

$$3\,Mg^{2+}_{(aq)} + 4\,Si(OH)^4_{(aq)} \rightleftharpoons Mg_3\,Si_4O_{10}(OH)_{2(s)} + 4\,H_2O + 6\,H^+ \quad (12.6)$$

High Cu/Zn ratios are indicative of either high-temperature (>300–350°C) leaching or contribution of “independent” Cu. While hydrothermal leaching tends to result in higher Zn concentrations compared to Cu, magmatic processes tend to enrich Cu over Zn in magmatic-hydrothermal fluids (Stanton 1991, 1994; Huston, 2011).

12.4. Elevated Gold Grades of the Hod Maden Au-Cu Deposit

The remarkable elevation of gold grades within the Hod Maden Au-Cu deposit can be attributed to a series of intricate and distinct multiphase gold precipitation phases, each of which contributes to the overall gold enrichment of the Hod Maden

mineralization. Firstly, the association of elevated gold grades with chlorite2, highlights the significance of specific alteration processes in promoting gold enrichment. Secondly, the correlation between elevated gold grades and quartz2, an accompanying mineral phase, highlights the complexity of the mineralization process. Additionally, the presence of elevated gold grades associated with pyrite3 emphasizes the role of sulfide minerals in hosting and transporting gold within the deposit. Furthermore, the association of elevated gold grades with chalcopyrite2, characterizes the assocation of various base metal sulfides in the deposit's mineralization process. The notable presence of Fe-oxide minerals, such as hematite-goethite, and accompanying siderite, which are linked to elevated gold grades, further adds to the multi-phase nature of the gold enrichment process. This visual representation is aptly captured in Figure 8.5, illustrating the association of gold with Fe-oxide and siderite. Lastly, the correlation between elevated gold grades and quartz-3 highlights the multifaceted and dynamic hydrothermal conditions that have contributed to the gold enrichment within the Hod Maden Au-Cu deposits. Collectively, these distinct gold precipitation phases provide insights into the complex interplay of mineralogical and hydrothermal processes that have culminated in the elevated gold grades characteristic of the Hod Maden deposit, solidifying its position as a significant and unique source of precious metal mineralization.

12.5. Mineral Deposit Type of Hod Maden Mineralization

The Hod Maden deposit exhibits key characteristics of a gold-rich volcanogenic massive sulfide (VMS) deposit, as supported by several compelling pieces of evidence.

Submarine Volcanic Host Rocks: The deposit is situated within submarine volcanic host rocks, a common feature of VMS deposits. This geological context is consistent with the formation of hydrothermal systems associated with submarine volcanic activity.

Lithological Control: The distribution of ore bodies is intricately linked to specific

lithological units. The presence of gold and mineralization is tightly confined to certain lithologies, particularly the andesite breccia. This lithological control is a hallmark of VMS deposits where mineralization is often concentrated in specific rock types.

Subseafloor Replacement: The mode of mineralization at Hod Maden is suggestive of subseafloor replacement. The deposit displays evidence of minerals replacing the original rock matrix, which is a common process in VMS deposits formed beneath the seafloor.

Favorable Horizon and Hiatus in Volcanism: The presence of anhydrite, jasper, and volcanosedimentary sequences within the deposit indicates a specific stratigraphic horizon and periods of volcanic hiatus. Such conditions are conducive to the development of VMS systems, where ore-forming fluids can interact with sedimentary and volcanic units in a controlled manner.

Asymmetric Hydrothermal Alteration: The deposit showcases an asymmetric pattern of hydrothermal alteration, with more intense alteration occurring in the stratigraphic footwall. This phenomenon aligns with the alteration zonation typically observed in VMS deposits.

Evolved Seawater Signature: The isotopic composition and trace element ratios of the mineralizing fluids suggest an evolved seawater signature. This signature is consistent with the involvement of hydrothermal fluids that interacted with seawater, a characteristic feature of many VMS systems.

Mg-Metasomatism and Chlorite-Rich Ore Zones: The presence of Mg-metasomatism and chlorite-rich ore zones points to hydrothermal alteration processes characteristic of VMS deposits. Chlorite-rich alteration zones are often associated with precious metal enrichment in these types of deposits.

Collectively, these pieces of evidence strongly support the classification of the Hod Maden deposit as a gold-rich VMS deposit. The submarine volcanic setting, lithological control, subseafloor replacement, favorable stratigraphic conditions, alteration patterns, isotopic signatures, and specific mineralization characteristics all align with the attributes commonly observed in VMS deposits, reinforcing the argument for its classification as a gold-rich VMS deposit.

12.6. Contribution to Exploration Programs Conducted in the Region

The eastern part of the eastern Pontides is an important area for mineral exploration, especially for VMS Cu and epithermal systems. To conduct a successful exploration program, several essential characteristics of a particular area must be identified, including tectonic setting, stratigraphy, host rock type and age, magma composition, structural kinematic association, deposit and commodity type, ore and gangue mineral assemblages and textures. This study offers detailed information on these features for Hod region, including spatial and temporal distribution of lithological units and their stratigraphic relationships, host rock petrography, hydrothermal alteration assemblages including present ore and gangue minerals, and textural interpretation. One example is the spherulitic texture, observed in the dacite unit, which has been replaced by gold-bearing chalcopyrite and pyrite, as well as sericite, quartz, and dolomite (Fig. 4.3F). This example suggests that the exploration target for this type of mineralization is localized to areas where Santonian dacitic units are stratigraphically confined by mafic lava flows and volcaniclastic rocks, showing spherulitic/amygdaloidal textures with pervasive sericite alteration.

Alteration indices, alteration box plots and geological and geochemical profiles, easy to implement and apply in any exploration program.

13. CONCLUSIONS

Hod Maden deposit is located in eastern Pontides, NE Turkey, and represents one of the highest-grade gold-copper (4 Moz @11.1 g/t AuEq) discoveries made globally in recent years. It is hosted by Late Cretaceous volcanic sequences of Çatak and Kızılkaya formations which host several Kuroko-type VMS and epithermal deposits throughout the eastern Pontides. Hod Maden differs from them with significantly elevated gold grades and mineralization/alteration styles. Petrographic studies indicate a submarine environment for host volcanics and hydrothermal alteration mineralogy is mainly controlled by the host rock composition (chloritic alteration with andesitic host or sericitic-clay alteration with dacitic host). High grade Au mineralization is associated with the hydrothermal alteration sequence starting with an early stage pervasive fine-grained quartz and chlorite/sericite-clay alteration cut by fine-grained quartz veinlets followed by comb coarse-quartz veins bearing pyrite and chalcopyrite and with the late stage anhydrite, epidote and carbonate phase as overprint or open space filling.

The ore zones form three distinct ore bodies that are from north to south, main zone, south zone and old workings zone. Main zone consists gold and copper sulfide-quartz veins and zones of disseminated to semimassive sulfides. The ore zone is spatially associated with jasper-bearing, chlorite and zeolite altered amygdaloidal andesite breccia with occasional hyaloclastite and sericite – and clay (Mg-illite, kaolinite-dickite) altered spherulitic/amygdaloidal dacite breccia units. A late, intense anhydrite phase overprints the pre-existing volcanic and hydrothermal alteration textures. South zone consists of auriferous semimassive veins, zones of sulfide stringers and disseminated sulfides that are hosted in spherulitic/amygdaloidal, monomictic dacite breccia and mass flow deposits. Quartz-pyrite-chalcopyrite-sphalerite veins and clasts replaced by sulfides form the mineralized bodies. The alteration consists of an assemblage of sericite (finegrained muscovite, K- illite), clay (dickite, kaolinite, halloysite, montmorillonite) and late calcite, dolomite and anhydrite overprint. Old workings zone consists of copper and

zinc sulfide (chalcopyrite-pyrite-sphalerite)-quartz veins. The ore zone is hosted in amygdaloidal andesite breccia and rhyodacitic dome with banded lava flow and pyroclastic products (pumice-bearing crystal tuff). Quartz-sulfide veins are accompanied by pervasive chlorite, sericite and occasional dolomite, epidote, rhodochrosite alteration.

New zircon U-Pb dating clarifies that columnar dacites were (evaluated as the same volcanic phase with the host dacite breccias at the south zone) formed at 84.78 ± 0.43 Ma while the rhyodacitic unit of old workings zone has been dated at 84.00 ± 0.44 Ma. In addition, the volcanic clasts of a red conglomerate unit, a marker horizon in the region, yielded the age of 163.65 ± 0.69 Ma.

The majority of $\delta^{34}S$ values of sulfide minerals record minor deviations between -0.81 and +3.33 ‰ and represents a magmatic source (magmatic water and/or seawater interaction with pre-existing host volcanic rocks). The $\delta^{34}S$ values of anhydrites display variations between 17.06 and 19.93 ‰ and overlap with the sulfur isotopic composition of Late Cretaceous seawater sulfate. Hydrothermal fluids in equilibrium with chlorite and sericite have $\delta^{18}O_{water}$ between -2.7 to +4.3 ‰ and δD_{water} ‰ values between -33 to -3 that define a trend between evolved seawater and a magmatic fluid as a result of fluid-rock interactions and a magmatic water input.

REFERENCES

Akdoğan, R., Okay, A. I., and Dunkl, I. (2018). Triassic-Jurassic arc magmatism in the Pontides as revealed by the U-Pb detrital zircon ages in the Jurassic sandstones of northeastern Turkey. *Turkish J Earth Sci*, 27(2):89–109.

Akıncı, Ö. T. (1984). The Eastern Pontide volcano-sedimentary belt and associated massive sulphide deposits. *Geol Soc Spec Publ*, 17(1):415–428.

Alizade, F. and Aksoy, M. (2019). Hod Maden gold/copper deposit: Turkey. In *Tech Session Abstracts*. PDAC The World's Premier Mineral Exploration and Mining Convention.

Alkan, H., Çınar, H., Oreshin, S., and Vinnik, L. (2019). Investigation of the crustal and upper-mantle structure of the eastern Pontides orogenic belt (NE, Turkey): a receiver-function study. *J Seismol*, 23(3):473–491.

Aydın, F., Oğuz Saka, S., Şen, C., Dokuz, A., Aiglsperger, T., Uysal, İ., Kandemir, R., Karslı, O., Sarı, B., and Başer, R. (2020). Temporal, geochemical and geodynamic evolution of the Late Cretaceous subduction zone volcanism in the eastern Sakarya Zone, NE Turkey: Implications for mantle-crust interaction in an arc setting. *J Asian Earth Sci*, 192:104217.

Aydın, F., Şen, C., Dokuz, A., Kandemir, R., and Sarı, B. (2016). Petrology and genesis of the Late Cretaceous volcanism in northeastern Turkey: new evidence for the Late Mesozoic geodynamic evolution of the eastern Pontides. Technical report, Tübitak Project No: 112Y365.

Bozkurt, E. (2017). Draft report on structures of the Hot Maden Property. Technical report, Artmin Madencilik.

Boztuğ, D., Jonckheere, R., Wagner, G., and Yeğingil, Z. (2004). Slow Senonian and fast Palaeocene–Early Eocene uplift of the granitoids in the Central Eastern Pontides, Turkey: apatite fission-track results. *Tectonophysics*, 382(3):213–228.

Burke, E. A. J. (2001). Raman microspectrometry of fluid inclusions. *Lithos*, 55(1-4):139–158.

Callan, N. (2013). Report on Geological Mapping and Prospect Evaluation, Hot Maden Property, Artvin District, NE Turkey. Technical report, NJC Geological and Exploration Services EIRL.

Cathelineau, M. (1988). Cation site occupancy in chlorites and illites as a function of temperature. *Clay Miner*, 23:471–485.

Cathelineau, M. and Nieva, D. (1985). A chlorite solid solution geothermometer. The Los Azufres (Mexico) geothermal system. *Contrib Minera Petrol*, 91:235–244.

Çekiç, Y., Gümüşel, A., Topcu, T., Yağcı, A., Özdoğan, K., Yılmaz, H., and Kırcı, M. (1984). Artvin F47 a1,a2,a3,a4-b1,b2,b3,b4-c3-c4-d1-d3,d4 paftalarının polimetalik masif sülfit cevheri prospeksiyonu raporu. Technical report, Maden Tetkik ve Arama Enstitüsü.

Çiftçi, E. and Hagni, R. D. (2005). Mineralogy of the Lahanos deposit a Kuroko-type volcanogenic massive sulfide deposit from the eastern Pontides (Giresun-NE Turkey). *Türkiye Jeoloji Bülteni*, 48(1):55–64.

Cole, D. R. and Ripley, E. M. (1999). Oxygen isotope fractionation between chlorite and water from 170 to 350 °C: a preliminary assessment based on partial exchange and fluid/rock experiments. *Geochim Cosmochim Acta*, 63(3):449–457.

Craig, H. (1961). Isotopic variations in meteoric waters. *Science*, 133(3465):1702–1703.

De Caritat, P., Hutcheon, I., and Walshe, J. L. (1993). Chlorite geothermometry: A review. *Clays Clay Miner*, 41(2):219–239.

Doyuran, M. (1970). Artvin-Hot Köyü'ne Bağlı Belizor Meydan mahalleleri civarı'nın jeolojisi ve burada bulunan Pb-Zn-Cu-Py damarlarının etüdü. Technical report, Maden Tetkik ve Arama Enstitüsü.

Eyüboğlu, Y. (2010). Late Cretaceous high-K volcanism in the eastern Pontide orogenic belt: implications for the geodynamic evolution of NE Turkey. *Int Geol Rev*, 52(2-3):142–186.

Eyuboglu, Y., Chung, S.-L., Santosh, M., Dudas, F. O., and Akaryalı, E. (2011). Transition from shoshonitic to adakitic magmatism in the eastern Pontides, NE Turkey: Implications for slab window melting. *Gondwana Res*, 19(2):413–429.

Fowler, A. D., Jensen, L. S., and Peloquin, S. A. (1987). Varioles in Archean basalts. *Can Mineral*, 25:275–289.

Galley, A. G., Hannington, M. D., and Jonasson, I. R. (2007). Volcanogenic massive sulphide deposits. In Goodfellow, W. D., editor, *Mineral deposits of Canada: A synthesis of major deposit-types, district metallogeny, the evolution of geological provinces, and exploration methods*, pages 141–161. Geological Association of Canada, Mineral Deposits Division.

Genna, D., Gaboury, D., and Roy, G. (2014). The Key Tuffite, Matagami Camp, Abitibi Greenstone Belt, Canada: petrogenesis and implications for VMS formation and exploration. *Miner Deposita*, 49(4):489–512.

Giggenbach, W. (1992). Isotopic shifts in waters from geothermal and volcanic systems along convergent plate boundaries and their origin. *Earth and Planetary Science Letters*, 113(4):495–510.

Griffin, W., Belousova, E., Shee, S., Pearson, N., and O'Reilly, S. (2004). Archean crustal evolution in the northern Yilgarn Craton: U–Pb and Hf-isotope

evidence from detrital zircons. *Precambrian Res*, 131(3):231–282. Archaean Tectonics, Volume 2.

Grosjean, M., Moritz, R., Rezeau, H., Hovakimyan, S., Ulianov, A., Chiaradia, M., and Melkonyan, R. (2022). Arabia-Eurasia convergence and collision control on Cenozoic juvenile K-rich magmatism in the South Armenian block, Lesser Caucasus. *Earth Sci Rev*, 226:103949.

Hayes, J. B. (1970). Polytypism of chlorite in sedimentary rocks. *Clays Clay Miner*, 18:285–306.

Herrington, R., Maslennikov, V., Zaykov, V., Seravkin, I., Kosarev, A., Buschmann, B., Orgeval, J.-J., Holland, N., Tesalina, S., Nimis, P., and Armstrong, R. (2005). 6: Classification of VMS deposits: Lessons from the South Uralides. *Ore Geol Rev*, 27(1):203–237. Special Issue on Geodynamics and Ore Deposit Evolution in Europe.

Hollis, S. P., Cooper, M. R., Herrington, R. J., Roberts, S., Earls, G., Verbeeten, A., Piercey, S. J., and Archibald, S. M. (2015). Distribution, mineralogy and geochemistry of silica-iron exhalites and related rocks from the Tyrone Igneous Complex: Implications for VMS mineralization in Northern Ireland. *J Geochem Explor*, 159:148–168.

Honnorez, J. and Kirst, P. (1975). Submarine basaltic volcanism: morphometric parameters for discriminating hyaloclastites from hyalotuffs. *Bull Volcanol*, 39:441–465.

Ishikawa, Y., Sawaguchi, T., Shin-ichi, I., and Horiuchi, M. (1976). Delineation of prospecting targets for Kuroko deposits based on modes of volcanism and underlying dacite and alteration haloes. *Min Geol*, 26:105–117.

Jackson, S. E., Pearson, N. J., Griffin, W. L., and Belousova, E. A. (2004). The application of laser ablation-inductively coupled plasma-mass spectrometry to in situ U-Pb zircon geochronology. *Chem Geol*, 211(1):47–69.

Jowett, E. C. (1991). Fitting iron and magnesium into the hydrothermal chlorite geothermometer. In *GAC/MAC/SEG Joint Annual Meeting*, volume 16, page A62.

Kalogeropoulos, S. I. and Scott, S. D. (1983). Mineralogy and geochemistry of tuffaceous exhalites (tetsusekiei) of the Fukazawa Mine, Hokuroku District, Japan. In Ohmoto, H. and Skinner, B. J., editors, *The Kuroko and Related Volcanogenic Massive Sulfide Deposits*, volume 5. Society of Economic Geologists.

Kanar, F. (2016). *Zeytinlik (Artvin) civarının jeolojisi ve tektoniği*. PhD thesis, Bozok University.

Kandemir, Ö., Akbayram, K., Çobankaya, M., Kanar, F., Pehlivan, Ş., Tok, T., Hakyemez, A., Ekmekçi, E., Danacı, F., and Temiz, U. (2019). From arc evolution to arc-continent collision: Late Cretaceous-middle Eocene geology of the Eastern Pontides, northeastern Turkey. *Geol Soc Am Bull*, 131(11-12):1889–1906.

Kandemir, Ö., Kanar, F., Çobankaya, M., Pehlivan, Ş., Tok, T., Akbayram, K., and Atıcı, G. (2017). Artvin Borçka-Yusufeli arasında kalan alanın jeolojisi. Technical report, Maden Tetkik ve Arama Genel Müdürlüğü.

Karslı, O., Ketenci, M., Uysal, İ., Dokuz, A., Aydın, F., Chen, B., Kandemir, R., and Wijbrans, J. (2011). Adakite-like granitoid porphyries in the eastern Pontides, NE Turkey: Potential parental melts and geodynamic implications. *Lithos*, 127(1):354–372.

Kasemann, S., Meixner, A., Rocholl, A., Vennemann, T., Rosner, M., Schmitt, A. K., and Wiedenbeck, M. (2001). Boron and oxygen isotope composition of certified reference materials NIST SRM 610/612 and reference materials JB-2 and JR-2. *Geostand newsl*, 25(2-3):405–416.

Kaygusuz, A. and Aydınçakır, E. (2011). Petrogenesis of a Late Cretaceous composite pluton from the eastern Pontides: the Dağbaşı pluton, NE Turkey. *N Jb Miner Abh*, 188(3):211–233.

Kaygusuz, A., Siebel, W., İlbeyli, N., Arslan, M., Satır, M., and Şen, C. (2010). Insight into magma genesis at convergent plate margins - a case study from the eastern Pontides (NE Turkey). *N. Jb. Miner. Abh*, 187(3):265–287.

Kokelaar, P. (1986). Magma-water interactions in subaquesous and emrgent basaltic magmatism. *Bull Volcanol*, 48:275–291.

Konak, N. and Hakyemez, H. Y. (2009). 1:100 000 ölçekli Türkiye jeoloji haritaları no:105 Tortum-G47 paftası. Technical report, Maden Tetkik ve Arama Genel Müdürlüğü.

Konak, N., Hakyemez, H. Y., Bilgiç, T., Bilgin, R., Hepşen, N., and Ercan, T. (2001). Kuzeydoğu Pontidlerin (Oltu- Olur-Şenkaya-Narman-Tortum-Uzundere-Yusufeli) jeolojisi. Technical Report 10489, Maden Tetkik ve Arama Genel Müdürlüğü.

Konak, N., Okay, A. I., and Hakyemez, H. Y. (2009). Tectonics and stratigraphy of the Eastern Pontides-field trip guide book 9th-14th October 2009. Technical report, Maden Tetkik ve Arama Genel Müdürlüğü.

Koppers, A. A. (2002). ArArCALC-software for 40Ar/39Ar age calculations. *Comput Geosci*, 28(5):605–619.

Kranidiotis, P. and MacLean, W. H. (1987). Systematics of chlorite alteration at the Phelps Dodge massive sulfide deposit, Matagami, Quebec. *Econ. Geol.*, 82:1898–1911.

Kuiper, K. F., Deino, A., Hilgen, F. J., Krijgsman, W., Renne, P. R., and Wijbrans, J. R. (2008). Synchronizing rock clocks of earth history. *Science*, 320(5875):500–504.

Kuşcu, İ., Tosdal, R. M., and Gençalioğlu-Kuşcu, G. (2019). Porphyry-Cu deposits of Turkey. In Pirajno, F., Ünlü, T., Dönmez, C., and Şahin, M. B., editors, *Mineral Resources of Turkey*, page 749. Springer.

Large, R. R. (1992). Australian volcanic-hosted massive sulfide deposits; features, styles, and genetic models. *Econ Geol*, 87(3):471–510.

Large, R. R., McPhie, J., Gemmel, J. B., Herrmann, W., and Davidson, G. J. (2001). The spectrum of ore deposit types, volcanic environments, alteration halos, and related exploration vectors in submarine volcanic successions: some examples from Australia. *Econ Geol*, 96:913–938.

Laskowski, K. (2021). Hod maden feasibility study: November 2021. Technical report, Sandstorm Gold Royalties.

Leistel, J. M., Marcoux, E., Thiéblemont, D., Quesada, C., Sánchez, A., Almodóvar, G. R., Pascual, E., and Sáez, R. (1997). The volcanic-hosted massive sulphide deposits of the Iberian Pyrite Belt: Review and preface to the Thematic Issue. *Miner Deposita*, 33(1):2–30.

Maslennikov, V., Ayupova, N., Herrington, R., Danyushevskiy, L., and Large, R. (2012). Ferruginous and manganiferous haloes around massive sulphide deposits of the Urals. *Ore Geol Rev*, 47:5–41. Manganese Metallogenesis.

McPhie, J., Doyle, M., and Allen, R. (1993). *Volcanic textures: a guide to the interpretation of textures in volcanic rocks*. CODES Key Centre.

Meng, Q. (2019). Quantitative automated mineralogical analysis conducted on variability composites from the Hod Maden project for Artmin Madencilik. Technical report, ALS Metallurgy Mineralogy.

Moritz, R., Melkonyan, R., Selby, D., Popkhadze, N., Gugushvili, V., Tayan, R., and Ramazanov, V. (2016). Metallogeny of the Lesser Caucasus: From Arc Construction to Postcollision Evolution. In *Tectonics and Metallogeny of the Tethyan Orogenic Belt*. Society of Economic Geologists.

Moritz, R., Popkhadze, N., Hässig, M., Golay, T., Lavoie, J., Gugushvili, V., Ulianov, A., Ovtcharova, M., Grosjean, M., Chiaradia, M., and Dumitrica, P. (2020). At the crossroads of the Lesser Caucasus and the Eastern Pontides: Late Cretaceous to early Eocene magmatic and geodynamic evolution of the Bolnisi district, Georgia. *Lithos*, 378-379:105872.

MTA (2002). 1:500,000-scale map of Turkey. Technical report, Maden Tetkik ve Arama Genel Müdürlüğü.

Nikishin, A. M., Khotylev, A. O., Bychkov, A. Y., Kopaevich, L. F., Petrov, E. I., and Yapaskurt, V. O. (2013). Cretaceous volcanic belts and the evolution of the Black Sea Basin. *Moscow Uni Geol Bull*, 68(3):141–154.

Nikishin, A. M., Okay, A., Tüysüz, O., Demirer, A., Wannier, M., Amelin, N., and Petrov, E. (2015). The Black Sea basins structure and history: New model based on new deep penetration regional seismic data. Part 2: Tectonic history and paleogeography. *Mar Pet Geol*, 59:656–670.

Okay, A. I. (1989). Tectonic units and sutures in the Pontides, northern Turkey. In Şengör, A. M. C., editor, *Tectonic Evolution of the Tethyan Region*, pages 109–116. Springer Netherlands, Dordrecht.

Okay, A. I. (2008). Geology of Turkey: A synopsis. *Anschnitt*, 21:19–42.

Okay, A. I. and Şahintürk, Ö. (1997). Geology and tectonic evolution of the Pontides. In Robinson, A., editor, *AAPG Memoir 68: Regional and petroleum geology of the Black Sea and surrounding region*, pages 183–226. AAPG Special Volumes.

Okay, A. I. and Nikishin, A. M. (2015). Tectonic evolution of the southern margin of Laurasia in the Black Sea region. *Int Geol Rev*, 57(5-8):1051–1076.

Okay, A. I., Şengör, A. M. C., and Görür, N. (1994). Kinematic history of the opening of the Black Sea and its effect on the surrounding regions. *Geology*, 22(3):267–270.

Okay, A. I., Sunal, G., Sherlock, S., Kylander-Clark, A. R. C., and Özcan, E. (2020). İzmir-Ankara suture as a Triassic to Cretaceous plate boundary-data from central Anatolia. *Tectonics*, 39(5):e2019TC005849. e2019TC005849 2019TC005849.

Ovalıoğlu, R. (1966). Hot-(Artvin) Cu-Pb-Zn zuhurları. Technical report, Maden Tetkik ve Arama Enstitüsü.

Peter, J. M. and Goodfellow, W. D. (1996). Mineralogy, bulk and rare earth element geochemistry of massive sulphide-associated hydrothermal sediments of the Brunswick Horizon, Bathurst Mining Camp, New Brunswick. *Can J Earth Sci*, 33(2):252–283.

Pichler, H. (1965). Acid hyaloclastites. *Bull Volcanol*, 28(293-310).

Rittmann, A. (1962). *Volcanoes and their activity*. John Wiley and Sons.

Robinson, A. G., Banks, C. J., Rutherford, M. M., and Hirst, J. P. P. (1995). Stratigraphic and structural development of the Eastern Pontides, Turkey. *J Geol Soc*, 152(5):861–872.

Rumble, D. I. and Hoering, T. C. (1994). Analysis for oxygen and sulfur isotope ratios in oxide and sulfide minerals by spot heating with a carbon dioxide laser in a fluorine atmosphere. *Acc Chem Res*, 27(8):237–241.

Şatır, F. and Ereren, M. (1976). Artvin-Yukarımadenköy (Hot) ile yakın yöresindeki piritli Cu-Zn-Pb cevherleşmesine ait jeoloji raporu. Technical report, Maden Tetkik ve Arama Enstitüsü.

Schrötter, H. W. and Klöckner, H. W. (1979). Raman scattering cross sections in gases and liquids. In Weber, A., editor, *Raman Spectroscopy of Gases and Liquids. Topics in Current Physics*, volume 11. Springer.

Şengör, A. and Yilmaz, Y. (1981). Tethyan evolution of Turkey: A plate tectonic approach. *Tectonophysics*, 75(3):181–241.

Sharp, Z. D. (1990). A laser-based microanalytical method for the in situ determination of oxygen isotope ratios of silicates and oxides. *Geochim Cosmochim Acta*, 54(5):1353–1357.

Sheppard, S. and Gilg, H. (1996). Stable isotope geochemistry of clay minerals: ”the story of sloppy, sticky, lumpy and tough” cairns-smith (1971). *Clay Miner*, 31(1):1–24.

Silvestri, S. C. (1963). Proposal for a genetic classification of hyaloclastites. *Bull Volcanol*, 25:315–321.

Sláma, J., Košler, J., Condon, D. J., Crowley, J. L., Gerdes, A., Hanchar, J. M., Horstwood, M. S., Morris, G. A., Nasdala, L., Norberg, N., Schaltegger, U., Schoene, B., Tubrett, M. N., and Whitehouse, M. J. (2008). Plešovice zircon — A new natural reference material for U-Pb and Hf isotopic microanalysis. *Chem Geol*, 249(1):1–35.

Soycan, H. (2017). *Doğu Pontidler (Trabzon, Bayburt, Erzurum ve Artvin) Orta Jura ve Üst Kretase volkano-sedimanter istiflerinin radyolarya taksonomisi, biyostratigrafisi ve çökel ortamları*. PhD thesis, Hacettepe University.

Spangenberg, J. E., Saintlian, N. J., and Palinkas, S. S. (2022). Safe, accurate, and precise sulfur isotope analyses of arsenides, sulfarsenides, and arsenic and mercury sulfides by conversion to barium sulfate before EA/IRMS. *Anal Bioanal Chem.*, 414(6):2163–2179.

Sterner, S. and Bodnar, R. J. (1984). Synthetic fluid inclusions in natural quartz I. Compositional types synthesized and applications to experimental geochemistry. *Geochim Cosmochim Acta*, 48(12):2659–2668.

Taylor, B. E. (1992). Hydrogen isotope composition of magmatic water. In *Annual meeting of the Geological Society of America (GSA)*.

Taylor, H. P. J. (1974). The application of oxygen and hydrogen isotope studies to problems of hydrothermal alteration and ore deposition. *Econ Geol*, 69:843–883.

Temizel, İ. and Kurt, A. (2019). Geç Kretase yaşlı Bozat (Giresun, KD Türkiye) Plütonu'nun petrografik, jeokimyasal ve petrolojik özellikleri. *Gümüşhane Üniv J Sci Technol*, 9(3):454–472.

Topal, E. and Tezcan, E. (2018). Hod Maden Project Geological Report. Technical report, Artmin Madencilik.

Topuz, G., Altherr, R., Schwarz, W. H., Siebel, W., Satır, M., and Dokuz, A. (2005). Post-collisional plutonism with adakite-like signatures: the Eocene Saraycık granodiorite (Eastern Pontides, Turkey). *Contributions to Mineralogy and Petrology*, 150(4):441–455.

Tsutsumi, M. and Ohmoto, H. (1983). A preliminary oxygen isotope study of tetsusekiei ores associated with the Kuroko deposits in the Hokuroku District, Japan. In Ohmoto, H. and Skinner, B. J., editors, *The Kuroko and Related Volcanogenic Massive Sulfide Deposits*, volume 5. Society of Economic Geologists.

Ulianov, A., Müntener, O., Schaltegger, U., and Bussy, F. (2012). The data treatment dependent variability of U-Pb zircon ages obtained using mono-collector, sector field, laser ablation ICPMS. *J Anal At Spectrom*, 27:663–676.

Ustaömer, T., Robertson, A. H. F., Ustaömer, P. A., Gerdes, A., and Peytcheva, I. (2013). Constraints on Variscan and Cimmerian magmatism and metamorphism in the Pontides (Yusufeli–Artvin area), NE Turkey from U–Pb dating and granite geochemistry. *Geol Soc Spec Publ*, 372(1):49–74.

Ustaömer, T., Ustaömer, P. A., Robertson, A. H. F., and Gerdes, A. (2016). Implications of U-Pb and Lu-Hf isotopic analysis of detrital zircons for the depositional age, provenance and tectonic setting of the Permian–Triassic Palaeotethyan Karakaya Complex, NW Turkey. *Int J Earth Sci*, 105(1):7–38.

Walshe, J. L. (1986). A six-component chlorite solid solution model and the conditions of chlorite formation in hydrothermal and geothermal systems. *Econ Geol*, 81:681–703.

Yamagishi, H. (1987). Studies on the Neogene subaqueous lavas and hyaloclastites in southwest Hokkaido. *Rep Geol Surv Hokkaido*, 59:55–117.

Yergeau, D., Mercier-Langevin, P., Dubé, B., McNicoll, V., Jackson, S. E., Malo, M., and Savoie, A. (2022). The Westwood Deposit, Southern Abitibi Greenstone Belt, Canada: An Archean Au-rich polymetallic magmatic-hydrothermal system—part II. Hydrothermal alteration, mineralization, and geologic model. *Economic Geology*, 117(3):577–608.

Yılmaz, S. and Boztuğ, D. (1996). Space and time relations of three plutonic phases in the eastern Pontides, Turkey. *Int Geol Rev*, 38(10):935–956.

Yılmaz, Y., Tüysüz, O., Yiğitbaş, E., and Şengör, A. M. C. (1997). Geology and tectonic evolution of the Pontides. In Robinson, A. G., editor, *AAPG Memoir 68: Regional and petroleum geology of the Black Sea and surrounding region*, chapter 11, pages 183–226. AAPG Special Volumes.

Yılmaz, Y., Yiğitbaş, E., and Çemen, İ. (2022). Tectonic development of the Ankara-Erzincan suture and the eastern Pontide mountains, northeast Anatolia, Turkey. *Authorea Preprints*.

APPENDICES

Appendix A1 - Sample Database (.xlsx)

Appendix A2 - Petrographic Report (HTD090 drill hole example) (.pdf)

Appendix A3 - Shortwave Infrared Spectroscopy Results (.xlsx)

Appendix A4 - Drill Hole Data for Geologic and Geochemical Profiles (.xlsx)

Appendix B1 - Electron Microprobe Results (.pdf)

Appendix B2 - Chlorite Chemistry Beam Locations (.pdf)

Appendix C1 - S-Isotope Results (.xlsx)

Appendix C2 - O-Isotope Results (.xlsx)

Appendix C3 - H-Isotope Results (.xlsx)

Appendix D1 - Ar-Ar Geochronology Results (.xls)

CURRICULUM VITAE

Personal Information

Name and Surname: M** E** B**

Nationality: ***

Phone: ***

E-mail: e***@mu.edu.tr

Education

2016-2023 **PhD**, Geological Engineering, Muğla Sıtkı Koçman Üniversitesi, Muğla (Economic Geology)
(Education language: English) (Grade: 4.00/4.00)
Thesis: Characteristics, Genesis and Triggers for the Formation of Hod Maden Au-Cu Mineralization System, NE Turkey
Supervisor: Prof. Dr. İlkay KUŞCU

2011-2015 **MSc**, Geological Engineering, Muğla Sıtkı Koçman Üniversitesi, Muğla (Economic Geology)
(Education language: English) (Grade: 3.94/4.00)
Thesis: Geochemical and Geochronological Characterization of the Early-Middle Eocene Magmatism and Related Epithermal Systems of the Eastern Pontides, Turkey
Supervisor: Prof. Dr. İlkay KUŞCU

2006-2011 **BSc**, Mining Engineering, Middle East Technical University, Ankara
(Education language: English) (Grade: 2.28/4.00)

2002-2006 High School, Ayrancı Lisesi, Ankara

Research Interests

- Hydrothermal alteration and mineralization
- Volcanogenic massive sulfide (VMS) deposits
- Epithermal deposits

Academic Experience

- 2012- Present, Research/Teaching Assistant, Department of Geological Engineering, Muğla Sıtkı Koçman University
- 2021-2022, Visiting International Researcher, Mineral Resources and Geofluids, University of Geneva
- 2013-2014, Visiting International Researcher, Mineral Deposit Research Unit, University of British Columbia

Papers

- Bilir, M. E., Kuşcu İ., Topal, E., Moritz, R. (2023). Geology and Stratigraphy of Hod (Artvin) Region, Eastern Pontides, NE Turkey. *Muğla j sci technol*, 9(2):25-35.

Abstracts

- Bilir, M. E., Kuşcu İ., Topal, E., Moritz, R. (2023). Hod Maden Au-Cu Yatağı, Doğu Pontidler, KD Türkiye: Denizaltı Volkanik Kayaç Dokuları ile Hidrotermal Alterasyon ve Cevherleşme. 75. Türkiye Jeoloji Kurultayı

- Bilir, M. E., Kuşcu, İ., Topal, E., Ulianov, A., Spikings, R. A., Vennemann, T., Putlitz, B., Spangenberg, J., Moritz, R. (2023). Hod Maden Au-Cu Yatağı, Doğu Pontidler, KD Türkiye: Hidrotermal Alterasyon ve Cevherleşmenin Jeokimyasal ve İzotopik Karakterizasyonu. 75. Türkiye Jeoloji Kurultayı

- Antoine, C., Spikings, R. A., Paul, A. N., Bilir, M. E., Bégué, F. and Schaltegger, U. (2022). Diffusion vs fluids: Ar distribution, chemical composition, oxygen isotopes and 40Ar/39Ar geochronology of muscovite crystals from Ecuador and Colombia. Swiss Geoscience Meeting

- Bilir, M. E., Kuşcu, İ., Moritz, R., Ulianov, A., Vennemann, T., Putlitz, B., Spangenberg, J. and Topal, E. (2022). Hod Maden Deposit, Eastern Pontides, NE Turkey: A Cretaceous Au- rich VMS System - Geochemical and Isotopic Characterization of Hydrothermal Alteration and Mineralization. SMRS 2022 - Sustainable Mineral Resources Supply: Challenges for Future Generations

- Bilir, M. E., Kuşcu, İ., Moritz, R. and Topal, E. (2022). Submarine Volcanic Rock Textures, Hydrothermal Alteration Assemblages and Mineralization of Hod Maden Au-Cu Deposit, Eastern Pontides, NE Turkey. SMRS 2022 - Sustainable Mineral Resources Supply: Challenges for Future Generations

- Bilir, M. E. and Kuşcu, İ. (2017). Magmatic-Hydrothermal Controls and Triggers for Porphyry Copper Deposits. 70. Türkiye Jeoloji Kurultayı

- Bilir, M. E. and Kuşcu, İ. (2016). Geochemical and Geochronological Characterization of the Early-Middle Eocene Magmatism and Related Epithermal Systems of the Eastern Pontides, Turkey. SEG 2016: Tethyan Tectonics and Metallogeny

- Bilir, M. E., Kuşcu, İ., Miskovic, A. and Hart C. J. R. (2014). The Early-Middle Eocene Magmatism and Related Epithermal Systems of the Eastern Pontides, NE Turkey. 8th International Symposium on Eastern Mediterranean Geology, 13-17 October, Muğla, Turkey, Abstracts

- Bilir, M. E., Kuşcu, İ., Miskovic, A. and Hart C. J. R. (2014). The Early-Middle Eocene Epithermal Systems of the Eastern Turkish Pontides: An Overview, Mineral Exploration Roundup

- Bilir, M. E. and Kuşcu, İ. (2014). The Early-Middle Eocene Magmatism and Related Epithermal Systems of the Eastern Turkish Pontides. 67. Türkiye Jeoloji Kurultayı, 06-10 Nisan, Ankara, Bildiri Kitapçığı

- Kuşcu, İ., Bilir, M. E. (2013). Field Evidence of Mechanisms that Control Ore Deposition in Hydrothermal Systems and Examples on Epithermal Gold Deposits of Turkey. 66. Türkiye Jeoloji Kurultayı, 14-18 Nisan, Ankara, Bildiri Kitapçığı